TUM School of Computation, Information and Technology
Technical University of Munich

Engineering of hybrid organic-inorganic silicon quantum dot light-emitting diodes

Josef Nepomuk Mock

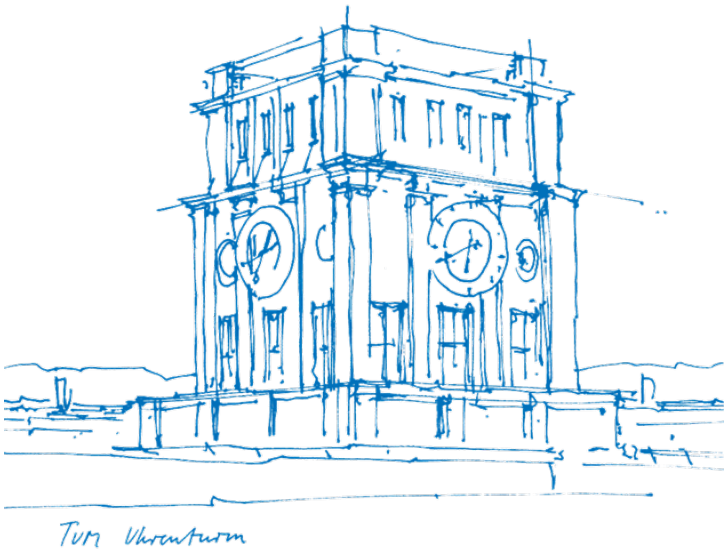

TUM School of Computation, Information and Technology
Technische Universität München

Engineering of hybrid organic-inorganic silicon quantum dot light-emitting diodes

Josef Nepomuk Mock

Vollständiger Abdruck der von der TUM School of Computation, Information and Technology der Technischen Universität München zur Erlangung des akademischen Grades eines

Doktors der Ingenieurwissenschaften (Dr.-Ing.)

genehmigten Dissertation.

Vorsitz:

Prof. Dr.-Ing. Werner Hemmert

Prüfer*innen der Dissertation:

1. Priv.-Doz. Dr.-Ing. habil. Markus Becherer
2. Prof. Dr. Alkiviathes Meldrum

Die Dissertation wurde am 26.09.2022 bei der Technischen Universität München eingereicht und durch die TUM School of Computation, Information and Technology am 27.01.2023 angenommen.

Für meine Eltern, Sonja und Josef Mock
Danke für euren Rat, Geduld und Unterstützung.

Abstract

Light is absolutely essential in today's society and quantum dots are pushing into the main technologies as next-generation light source. Quantum dots are semiconducting particles with sizes of a few nm, and when incorporated into light-emitting diodes, they have significant improvements over conventional organic and inorganic light-emitting diodes. They combine the long-living inorganic emitting material with the solution-processability of organic LEDs. So far, mainly toxic and rare materials have been researched as quantum dots and therefore alternatives are needed.

Silicon is the abundant and environment-friendly and the work horse of semiconducting industry. By shrinking it to the nanoscale, it starts to show photoluminescence and can be employed in optoelectronic devices. In this work, surface functionalized silicon quantum dots (SiQDs) were utilized as active material in LEDs. The SiQD-LEDs turned on at voltages between $1.5\,\mathrm{V}$ to $2\,\mathrm{V}$, reached high irradiance values of several hundred µW cm^{-2}, and peak external quantum efficiency (EQE) values around $1\,\%$. The electroluminescence showed an red emission peak at approx. $710\,\mathrm{nm}$ with a full width at half maximum of up to $140\,\mathrm{nm}$. The electroluminescence spectrum shifted blue and broadened with increasing voltages, which is commonly attributed to the size distribution of the SiQDs. The alkyl surface ligands on the SiQDs, hexyl, octyl, and dodecyl, ensure colloidal stability, but also introduce an insulating tunneling barrier, thus reducing the device current. The irradiance also attenuated with the ligand length, but interestingly, the SiQD-Oct showed superior irradiance for higher voltages. An improved ratio between the charge transport properties and the charge carrier localization was achieved. This effect was also observed in the EQE of the SiQD-LEDs, where the EQE of the octyl LED was the highest with $1.48\,\%$, followed by hexyl with $1.33\,\%$, and dodecyl with $0.92\,\%$. The spectral blue-shift was also ligand-dependent, and through increasing ligand length, the excitation of the SiQDs needs higher voltages, hence higher band gap SiQDs can be excited.

Capacitance-voltage measurements were conducted to gain insights into the charge carrier dynamics inside the SiQD-LEDs. A negative capacitance was observed for SiQD-Hex and SiQD-Dodec LEDs, which was explained by the presence of trap states and the demarcation energy. In SiQD-LEDs, the injected charge carriers accumulate inside the SiQD-LED until the turn-on voltage is reached. At the same time, thermally re-emitted charge carriers contribute to the charge accumulation and when the recombination starts, the charge carriers are recombined irreversibly. A negative capacitance was observed when the equilibrium was not established within one modulation cycle. The demarcation energy is frequency and temperature dependent and controls how many trap states are charged and discharged within one modulation cycle. For the SiQD-Hex LED, the charge carriers showed less charge accumulation with increasing frequency and temperature, whereas the SiQD-Dodec sample showed increased charge accumulation and a bigger negative capacitance with temperature. This was due to the better charge confinement of the long ligand, which demonstrates that ligands become essential when designing a SiQD-LED.

The broadband SiQD-LED emission was drastically reduced by implementing them into Fabry-Pérot resonators to build SiQD-cavity LEDs (cLEDs). The cavity consisted of a two parallel mirror alignment, where light constructively and destructively interfered between the semi-transparent Ag and the thicker highly reflective Ag electrode, resulting in a narrow and highly directed outcoupling emission cone at a certain wavelength. In the presented cLEDs, narrow bandwidth emission of $24\,\mathrm{nm}$ was achieved. By tuning the distance between the two mirrors, the cLED color was tailored from red-orange until infrared. The SiQD-cLEDs showed superior emission wavelength stability over the normal SiQD-LEDs with increasing driving voltages. The results demonstrate a road for possible improvements potential of the SiQD-LEDs which are desired for the next-generation QLEDs.

Kurzfassung

Lichttechnik ist aus der heutigen Gesellschaft nicht mehr wegzudenken. Heutzutage kommen hybride Quantenpunkt-Leuchtdioden (QLEDs) auf den Markt, die das langlebige anorganische Leuchtmaterial mit der lösungsbasierten Verarbeitung organischer LEDs kombinieren. Quantenpunkte sind halbleitende Partikel mit einer Größe von wenigen nm, wobei Silizium-Quantenpunkte (SiQDs) der umweltfreundlichste und verfügbarste Kandidat unter ihnen sind. Wenn das nicht leuchtende Silizium in den Nanobereich schrumpft beginnt es Photolumineszenz zu zeigen und kann in optoelektronischen Bauteilen eingesetzt werden.

Licht ist in der heutigen Gesellschaft absolut unverzichtbar und Quantenpunkte drängen als Lichtquelle der nächsten Generation in die vorherrschenden Technologien. Quantenpunkte sind halbleitende Teilchen mit einer Größe von wenigen nm und wenn sie in Leuchtdioden eingebaut werden weisen sie deutliche Verbesserungen gegenüber herkömmlichen organischen und anorganischen Leuchtdioden auf. Sie kombinieren langlebige anorganische Leuchtmaterialien mit den lösungsbasierten Herstellungsverfahren organischer LEDs. Da bisher hauptsächlich giftige und rare Materialien als Quantenpunkte erforscht wurden, werden daher Alternativen dazu benötigt.

Silizium ist verfügbar, umweltfreundlich und das wichtigste Material der Halbleiterindustrie. Wenn es zur nanoskala geschrumpft wird, beginnt es Photolumineszenz zu zeigen und kann deshalb in optoelektronischen Bauteilen eingesetzt werden. In dieser Arbeit wurden oberflächenfunktionalisierte Silizium Quantenpunkte (SiQDs) verwendet. Die SiQD-LEDs begannen bei Spannungen im Bereich von 1.5 V to 2 V zu leuchten, erreichten hohe Bestrahlungsstärken von mehreren hundert µW cm^{-2} und besaßen Spitzenwerte der externen Quanteneffizienz (EQE) von etwa 1 %. Die Elektrolumineszenz zeigte ein rotes Emissionsmaximum bei ca. 710 nm mit einer Halbwertsbreite von bis zu 140 nm. Das Elektrolumineszenzspektrum verschob sich ins Blaue und verbreiterte sich mit zunehmender Spannung, was gemeinhin auf die Größenverteilung der SiQDs zurückgeführt wird. Die Alkylgruppen auf der SiQD-Oberfläche sind notwendig für die Lösbarkeit, stellen jedoch eine isolierende Tunnelbarriere dar, so dass der Diodenstrom abnimmt und die Bestrahlungsstärke sich ebenfalls änderte. Interessanterweise zeigten die SiQD-Oct LEDs eine verbesserte Bestrahlungsstärke für höhere Spannungen, wo ein optimiertes Verhältnis zwischen den Ladungstransporteigenschaften und der Ladungsträgerlokalisierung auftrat. Dieser Effekt wurde auch bei der EQE der SiQD-LEDs beobachtet, wobei die EQE der Octyl-LED mit 1.48 % am höchsten war, gefolgt von Hexyl mit 1.33 % und Dodecyl mit 0.92 %. Die spektrale Blauverschiebung war auch ligandenabhängig, und mit zunehmender Ligandenlänge benötigt die Anregung der SiQDs höhere Spannungen, so dass SiQDs mit größerer Bandlücke angeregt werden können.

Um Einblicke in die Ladungsträgerdynamik innerhalb der SiQD-LEDs zu erhalten wurden Kapazitäts-Spannungs Messungen für SiQD-Hex- und SiQD-Dodec-LEDs durchgeführt. Dabei wurde eine negative Kapazität beobachtet, was durch das Vorhandensein von Defektzuständen und die Abgrenzungsenergie erklärt werden konnte. In den SiQD-LEDs akkumulieren die injizierten Ladungsträger im Inneren der SiQD-LEDs bis die Einschaltspannung erreicht ist und gleichzeitig tragen thermisch reemittierte Ladungsträger zur Ladungsakkumulation bei. Wenn nun die Rekombination beginnt, rekombinieren diese Ladungsträger irreversibel. Eine negative Kapazität tritt auf, wenn das Gleichgewicht nicht innerhalb eines Modulationszyklus wieder hergestellt wurde. Die Abgrenzungsenergie ist frequenz- und temperaturabhängig und bestimmt, wie viele Defektzustände innerhalb eines Modulationszyklus geladen und entladen werden. Bei der hexyl SiQD-LED akkumulierte weniger Ladung mit zunehmender Frequenz und Temperatur, währenddesen die dodecyl SiQD-LED eine erhöhte Ladungsakkumulation und eine größere negative Kapazität mit dem Temperaturanstieg offenbarte. Dieses Verhalten ist auf die höhere Lokalisierung der Ladungsträger

durch den langen Liganden zurückzuführen. Dies zeigt, dass Liganden beim Entwurf einer SiQD-LED von entscheidender Bedeutung sind.

Die breitbandige Emission von SiQD-LEDs wurde durch ihre Implementierung in Fabry-Pérot Resonatoren in Angriff genommen, um SiQD-Resonator-LEDs (cLEDs) zu bauen. Der Resonator bestand aus zwei parallel angeordneten Spiegeln, in denen das Licht konstruktiv und destruktiv zwischen dem halbtransparenten Ag Spiegel und der dickeren hochreflektierenden Ag-Elektrode interferierte und zu einem schmalen und stark gerichteten Auskopplungs-Emissionskegel bei einer bestimmten Wellenlänge führte. Bei den vorgestellten cLEDs wurde eine schmalbandige Emission von ca. 24 nm erreicht. Durch die Anpassung des Abstands zwischen den beiden Spiegeln konnte die Emissionsfarbe der cLEDs von rotorange bis infrarot angepasst werden. Ferner zeigten die SiQD-cLEDs mit zunehmender Ansteuerspannung eine höhere Stabilität der Emissionswellenlängen als die herkömmlichen SiQD-LEDs. Die Ergebnisse zeigen einen Weg für mögliche Verbesserungspotenziale der SiQD-LEDs auf, die für die QLEDs der nächsten Generation benötigt werden.

Contents

List of Abbreviations

AFM	Atomic force microscope
CCs	Charge carriers
cLED	Cavity light-emitting diode
DBR	Distributed Bragg reflectors
DCB	Dichlorbenzene
DFB	Distributed feedback
DLS	Dynamic light scattering
DOS	Density of states
EBL	Electron blocking layer
EIL	Electron injection layer
EL	Electroluminescence
EML	Emissive layer
EQE	External quantum efficiency
ETL	Electron transport layer
FP	Fabry-Pérot
FSR	Free spectral range
FTIR	Fourier transform infrared spectrometer
FWHM	Full width at half maximum
HBL	Hole blocking layer
HIL	Hole injection layer
HOMO	Highest occupied molecul orbital
HS	Hydrosililation
HSQ	Hydrogen silsesquioxane
HTL	Hole transport layer
IQE	Internal Quantum efficiency
ITO	Indium tin oxide
LED	Light-emitting diode

LUMO	Lowest unoccupied molecul orbital
MO	Molecule orbital
NC	Negatice capacitance
OLED	Organic light-emitting diode
OLR	Organolithium reagents
PEDOT:PSS	Poly(3,4-ethylenedioxythiophene) polystyrene sulfonate
PEI	Polyethylenimine
PL	Photoluminescence
Poly-TPD	Poly(N,N-bis-4-butylphenyl-N,N-bisphenyl)benzidine
PTFE	Polytetrafluoroethylene
PVD	Physical vapor deposition
PVK	Poly[9-vinylcarbazole]
PVK	poly(9-vinylcarbazole)
QDs	Quantum dots
QLED	Quantum dot light-emitting diode
QY	Quantum yield
RTE	Resistive thermal evaporation
SCLC	Space-charge limited current
SiQDs	Silicon quantum dots
SNOM	Scanning near-field optical microscope
SPM	Scanning probe microscope
STM	Scanning tunneling microscope
TCE	Transparent conducting electrode
TEM	Transmission electron microscopy
TGA	Thermal gravimetric analysis
UPS	Ultraviolet photoelectron spectroscopy
XPS	X-ray photoelectron spectroscopy
ZnO	Zinc oxide

1 Introduction

Light technology has become indispensable in today's society. People turn on light when it becomes dark; they use it to communicate, they use light for manufacturing, or probably most important nowadays, they use it for display applications. Light technology as we know it today has undergone many changes and improvements over the years. For a very long time, humanity had only fire as lighting and with oil lamps and candles, people lived for centuries. Edison's development of the light bulb in 1879 brought a new kind of lighting available to most people. In the year 2005, $6.5\,\%$ of the globally primary energy was used for artificial lighting and in 2015 in the EU the electrical energy consumption was even $12.4\,\%$, equivalent to $336\,\mathrm{TW\,h}$.[1, 2] To save some of the 132 million tons of CO_2 equivalent greenhouse gas emissions, the European Union decided to prohibit the production of light bulbs from 2012 because of their low efficiency.[3]

Many alternatives to light bulbs have already been developed for a longer time, but the most prominent is the light-emitting diode (LED). LEDs convert electrical energy directly into light via electroluminescence (EL), which is much more efficient than the glow of a filament, which mainly produces heat. Henry Joseph Round observed the first EL in SiC in 1907 and afterward, in the 1920s, Oleg Lossev made the first scientific explanation of EL in p-n-junctions.[4, 5] From the explanation by Lossev, it took until 1962 until the first practical LED, made of a $GaAs_{1-x}P_x$ p-n junction, was fabricated by Nick Holonyak.[6] The LED development progressed rapidly over the next few years, and more efficient, versatile colors (red, amber, green), higher power, and more reliable LEDs were introduced.[7, 8] Mainly new material combinations of different semiconductors drove the development, but a blue emitting LED was still missing for efficient white light production. Nakamura succeeded in building a blue GaN LED in 1994, which later awarded him the Nobel prize in physics for an invention of most substantial benefit to mankind.[9, 10] This development was substantial because white light is mainly generated by mixing blue, green, and red LEDs or by adding a phosphor layer to modify the blue emission spectrum.[11] In the last twenty years, the versatility and improvements of LEDs in color and power made them popular for display applications in, for example, TVs and smartphones. In addition, the demand for lighting applications is growing and more efficiency is essential to reduce the increasing energy usage for it.[12]

More recently, a new kind of LED was developed, the organic LEDs (OLEDs) constituting of organic semiconducting materials. The first step toward OLEDs was already done in 1906 by Pochettino, who discovered the photoelectric effect in anthracene crystals.[13] Similar to the solid-state LEDs, it took years from the discovery of the effect toward a mass-production device. Bernanose made attempts in the 1950s,[14, 15] Pope in 1963,[16] and Helfrich in 1965 [17] to establish organic lighting. They all studied the fundamental aspects of light generation in organic semiconductors and proposed first device layouts. However, their proposed devices were not commercialized because of their excessive thickness and high operation voltages.[11] The first practical OLED was presented in 1987 by Tang and van Slyke.[18] They used amorphous Alq3 (tris(8-hydroxyquinolinato)aluminum) as active material that showed green EL emission at voltages below $10\,\mathrm{V}$.[18] Although Alq3 is an organic material, it was deposited via vacuum deposition, similar to all inorganic LEDs. In contrast to the vacuum deposition, Burroughes presented the first solution-processed OLED made of PPV (Poly(p-phenylen-vinylen)) in 1990.[19] His OLED was spin-coated and the material solution enabled cheap fabrication techniques like printing, spraying, or roll-to-roll processing.[20–22] All these solution-based manufacturing techniques also allow the fabrication of large areas and even flexible OLEDs.[23] Moreover, through new materials and transparent polymer electrodes, the whole device can be manufactured transparent, diffuse, or mirrored.[24] The wide variety of design features of OLEDs make them a great asset for the lighting and entertainment industry, which is a billion-dollar market nowadays. OLEDs are increasingly pushing into the market as their big advantages are the

energy savings,[25] color reproduction, high contrast and resolution, a large viewing angle, and speed of response. All of those justify the use of OLEDs in portable devices, monitors, and televisions.[24] In contrast to the many advantages, one big issue remains, the OLEDs' lifetime.[24]

People tried to combine the advantages of an active inorganic layer while preserving at the same time the solution processibility and flexibility of organic LEDs. Colloidal quantum dots(QDs) seem to meet these needs and are excessively researched since their first appearance in the 1980s.[26, 27] QDs are inorganic semiconducting nanocrystals with diameters below $20\,\mathrm{nm}$ and can be made from a wide range of materials.[28] QDs made from group II-VI (CdSe, CdS, PbS,[29] ZnP, ZnSe[30]), IV-VI (CdTe[31]), III-V (InP[30]), I-III-IV_2 (CuInS2 [32]), and IV (Ge,[33] Si,[34] C [35]) have been manufactured and integrated into numerous optoelectronic devices since. QD-LEDs, so-called QLEDs, have excellent performance factors and seem to justify the hopes placed on them. Nevertheless, most QDs are based on the toxic materials cadmium and lead or the rare indium. The EU also limited toxic materials in 2003 for electrical and electronic equipment, where alternatives do not exist.[36] For that reason, environmentally friendly quantum dots are an important growing research field, and silicon quantum dots (SiQDs) are one of the hot topics among them.

Silicon is the workhorse of the classical semiconductor industry, but through its indirect band gap, it is not well known to be suitable as a light emitting material. By shrinking the dimensions of silicon from bulk to the nano-scale, it starts to show photoluminescence (PL). Canham experimentally provided the first appearance of silicon PL in 1990.[37] He observed red luminescence from porous silicon at room temperature by electrochemical and chemical dissolution of silicon wafers. From there, the research community got excited by the dream of all silicon photonic chips. Nowadays, many research groups focus on silicon nanocrystals or quantum dots. Those SiQDs can be synthesized by various methods and exhibit a size of a few nm.

Silicon is non-toxic, biodegradable, and one of the most abundant elements in the earth's crust. Therefore, a wide variety of applications are possible in bioimaging, sensing, solar cells, photodetectors, field-effect transistors, non-linear optics, and light-emitting diodes. One key factor of the wide variety is that the band gap is not only tunable by the quantum size effect. The well-established surface chemistry of silicon allows for tuning the QD surface and changing the properties of the whole SiQD, e.g., the emission color or their colloidal stability.[38] Today some SiQDs yield a very high PL quantum yield (QY) of up to $90\,\%$.[39] For solution processability, most SiQDs are functionalized via hydrosilylation (HS) with alkyl ligands to ensure colloidal stability in solutions.

As already mentioned, the non-toxic silicon might replace the toxic QD devices. The first near-IR SiQD-LED ($\lambda \approx 853\,\mathrm{nm}$) was presented in 2010 by Cheng et al. with an external quantum efficiency (EQE) of $0.6\,\%$.[40] Many groups tested different approaches to fabricate more efficient SiQD pure emissive LEDs. The record EQE reported so far is also from Cheng with $8.6\,\%$ at a wavelength of around $850\,\mathrm{nm}$ emission.[41] In this study, they used vacuum-deposited Alq3 as an efficient hole blocking layer to facilitate recombination in the SiQD layer. Since 2011 no better SiQD-LEDs have been produced and alternative ways to improve their performance are researched. The classical approach is to exchange or add several transport layers.[42] Some good ideas like a SiQD white-light LED,[43], or all-inorganic SiQD-LEDs,[44], and inverted device structure have been presented.[45] Recently, Angi et al. showed that a lower surface coverage of the SiQDs is beneficial for the device performance.[46] They used an organolithium reagents (OLR) method developed by Höhlein et al. to functionalize every second Si atom with an organic ligand.[47] Using that method, Angi et al. could increase the charge transport through the SiQD-LED and the performance in terms of luminance more than threefold. Additionally, the EQE also improved by a factor of three to a peak value of $1.8 \times 10^{-2}\,\%$.[46] Moreover, the improved charge transport via π-π conjugated functionalizations in contrast to alkyl ligands have been presented by Liu.[48] They prepared two kinds, one with an octyl alkyl chain and one with phenylpropyl ligand. The conjugated ligand showed improved charge transport and irradiance, whereas the EQE was better for the Octyl sample.

All those studies show the awareness about the surface functionalization, but no one systematically investigated the length effect of the widely used alkyl ligands on SiQD-LEDs. This not only includes the

LED performance, it also includes the charge carrier dynamics, which is essential for an optimized device layout. Generally, only $I - V$ analysis has been performed but the frequency dependency is missing. Both studies can help to improve the device efficiency and performance with new functionalization and fabrication concepts. Furthermore, all SiQD-LEDs so far have a broad emission spectrum bigger than $100\,\mathrm{nm}$ in common. This broadband emission has to be drastically reduced, if SiQD-LEDs shall to be implemented into display applications. As the size separation approach of Maier-Flaig et al. did not fully succeed, we present with an implemented Fabry-Pérot structure a structural way to reduce the spectrum width.[49]

In the beginning, the fundamental theory necessary for the SiQD-LEDs is presented in chapter 2, followed by chapter 3, where the used materials are briefly described and fabrication as well as the characterization methods are explained.

Afterward, in chapter 4, the working principle and the state-of-the-art of the hybrid organic/inorganic SiQD-LEDs are presented. Further, the fabrication process is outlined. The properties of individual thin films are analyzed by a broad range of optical and tactile measurement methods. Eventually, a typical SiQD-LED using SiQDs with a hexyl functionalized surface is analyzed.

Many SiQD-LEDs with different alkyl chain length with six[46] eight,[48] ten,[50] and twelve[41] have been fabricated, but non of them has in-depth analyzed the direct length influence. In this context, a SiQD-LED study of different length alkyl ligands with hexyl, octyl, and dodecyl is presented in chapter 5. The charge transport through the LEDs and the EL spectra are analysed as a function of ligand length to find an optimum length.

For the implementation of SiQD-LEDs into display applications, high performance is needed, and the behavior at a high switching speed is crucial. Therefore, we measured the capacitance-voltage characteristic at varying frequencies and temperatures in chapter 6. With that, we found a negative capacitance in the SiQD-LEDs for the first time. In the chapter, we adopt an existing formalism of how a negative capacitance can occur and how it functions.

Chapter 7 focuses on the spectral component of the SiQD-LED. So far, SiQD LEDs with spectral bandwidths of more than $100\,\mathrm{nm}$ have been presented, even for size-separated SiQDs.[49] For industrial applications in displays, for example, a spectral resolution of less than $50\,\mathrm{nm}$ is required. For this purpose, the SiQD LEDs are embedded in a Fabry-Pérot resonator, which builds an optical cavity that couples out a much narrower spectrum than the ordinary LED.

Chapter 8 contains a summarizing conclusion of the achievements of this work. Therein, each chapter's main aspects and the benefit it provides are highlighted. Further research topics and possible ways for developing the SiQD-LED further are provided.

2 Theoretical Background

This chapter describes the theoretical background for an understanding of hybrid organic-inorganic SiQD-LEDs. First of all, the necessary physical semiconductor fundamentals are discussed. It describes inorganic semiconductors and how recombination occurs, while in the next section, organic semiconductors are discussed. It is essential to explain how semiconductors work and how charge transport and recombination occurs. The electrical behavior of a light-emitting diode can be explained based on those fundamentals. Finally, the unique features and the definition of silicon quantum dots are discussed. In this chapter, I mostly followed the explanations of the textbooks from Schubert,[8], Sze,[7], and Köhler and Bässler,[51] which are highly recommended for a much more detailed description of the theoretical background.

2.1 Inorganic semiconductors

Inorganic crystalline solids are the prevailing material system used in electronic devices such as LEDs and can be classified based on their energy band structure. Energy bands are a distribution of discrete energy states that are densely packed together. Depending on their energetic range and their occupancy, they can be classified as valence band E_V and conduction band E_C. Depending on the material, the bands can overlap or there is a band gap E_g in between them, which results in three groups of materials to distinguish from, insulators, semiconductors, and metals. Insulators have a band gap $E_\mathrm{g} > 4\,\mathrm{eV}$ and in semiconductors, the band gap is between $1\,\mathrm{eV}$ and $4\,\mathrm{eV}$. The material is classified as metal when the valence and conduction band overlaps. Semiconductors are essential for optoelectronics and are discussed further in this section. Usually, charge carriers are forbidden within the band gap but they can be excited to the conduction band with external energy. In the conduction band the charges are able to move freely thus increasing the charge transport. GaAs and Si are one of the most researched semiconductors in history and represent two kinds of semiconductors, direct and indirect semiconductor. The band structures are schematically plotted in Figure 2.1. In direct semiconductors, the valence band maximum and the conduction band minimum have the same momentum k, while for indirect semiconductors, the valence band maximum and conduction band minimum do not have the same momentum. This momentum difference is crucial for radiative processes.

2.1.1 Recombination in semiconductors

All semiconductors have electrons and holes as charge carriers in their system. The intrinsic carrier concentration n_i at a given temperature is

$$n_0 p_0 = n_\mathrm{i}^2 \tag{2.1}$$

where n_0 and p_0 are the electron and hole concentrations.[8] Excess carriers can be generated with external stimulation, such as light absorption or current injection. The additional holes and electrons can now form electron-hole pairs. Free electrons can recombine with holes under a photon's emission, called radiative recombination. All other recombination mechanisms which do not emit a photon are called non-radiative recombination. An example of radiative recombination is illustrated with the green arrow in a direct semiconductor in Figure 2.1. The radiative recombination of electron-hole pairs always needs to follow the energy conservation rule:

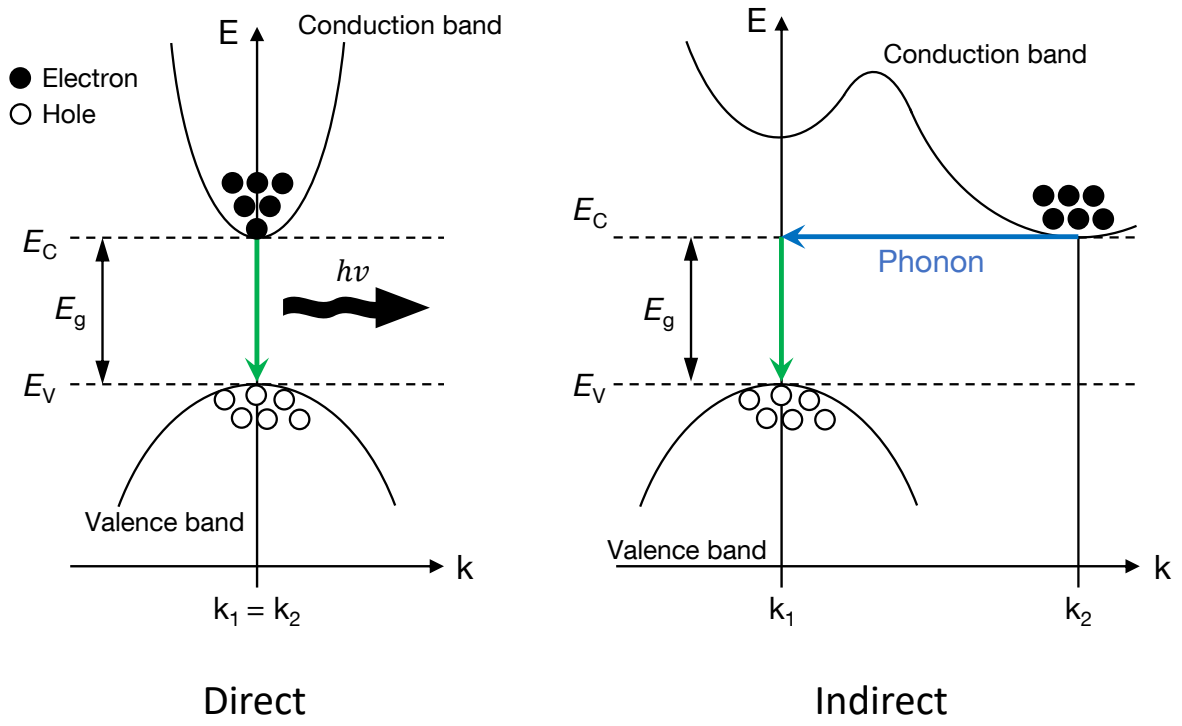

Figure 2.1 Schematic representation of a direct and indirect semiconductor. For the direct semiconductor, the valence band maximum and the conduction band minimum are located at the same momentum k, while this condition does not hold for indirect semiconductors. The green arrows indicate a band-to-band transition with the same momentum. The blue arrow in the indirect semiconductor represents a phonon, which is changing the momentum k to enable a band-to-band transition.

$$h\nu = E_\mathrm{e} - E_\mathrm{h} \approx E_\mathrm{g}. \tag{2.2}$$

The difference of kinetic energy of an electron and hole E_e and E_h is approximately the band gap energy E_g with the Planck constant h and the frequency ν. The photon energy $E_\mathrm{photon} = h\nu$ is approximately the band gap energy if its thermal energy $k_\mathrm{B}T$ is small compared with the band gap energy ($k_\mathrm{B}T \ll E_\mathrm{g}$).[8]

In addition to the energy conservation, the momentum has to be conserved in any physical process, thus in radiative transitions as well. This so-called k-selection rule is important for both indirect semiconductors but also for direct semiconductors. In the optical transition or in direct semiconductors, the wave vector of the valence band k_1 differs from the wave vector of the conduction band k_2 by the wave vector of a photon ($p_\mathrm{k} = \hbar k$).[7] p_k is negligibly small and therefore the k-selection rule in a radiative transition is generally written as [7]

$$k_1 = k_2. \tag{2.3}$$

In indirect semiconductors where the conduction band minimum has not the same k value as the valence band maxima, a phonon or other scattering agents are needed to provide the necessary momentum k_ph and therefore conserve the momentum.[7, 52] The phonon momentum is highlighted with a blue arrow in Figure 2.1. The additionally needed participant for momentum conservation makes the probability for interband transitions extremely small.

Despite radiative transitions, there are physical mechanisms where non-radiative recombination can occur. In optoelectronic devices, the non-radiative recombination decreases the efficiency and is therefore tried to minimize. Unwanted defects in the semiconductor are, among others, foreign atoms (impurities),

vacancies, dislocation, or stacking faults.[8, 53] If a defect causes an energetic state that lies in the band gap, it is called a trap state or recombination center.[54]

2.2 Organic semiconductors

Organic chemistry deals with carbon compounds, making carbon the backbone of organic semiconductors that are essential for organic electronics. This section covers the fundamental physical concept of orbitals at atomic and molecular states and their interaction to understand organic electronics. The interaction between the molecules can result in charge transport and, further, in semiconducting behavior that is important for optoelectronic devices.

2.2.1 Atomic orbitals and bonding

As organic chemistry is built on carbon-based materials, we explain the principle of atomic orbitals with carbon as an example. Due to Heisenberg's Uncertainty Principle,[55] the position of each electron around the nucleus of an atom has a certain probability distribution. This probability distribution is called an atomic orbital and is fully described by the electron's wave-function Ψ.[56, 57] Atoms can possess several orbitals. The electron configuration of carbon in the ground state is $1s^2 2s^2 2p_x^1 2p_y^1$. The spherical s orbitals and barbell-shaped p orbitals are displayed in Figure 2.2. The atom's electronic configuration should maximize the number of unpaired electrons in degenerated (same energy) orbitals according to Hund's rule.[58] By a simple overlap of s and p orbitals only two bonds would be allowed, which does not satisfy Hund's rule. Hence, the atomic orbitals are "mixing" and arranged via orbital hybridization that enables carbon to make up to four bonds.[51] Carbon can form sp, sp^2, or sp^3 hybrid orbitals shown in Figure 2.2. Two sp orbitals mix between two s and two p orbitals while in sp^2 orbitals three orbitals hybridize in the same plane with an angle of $120°$ between them.[51] In the sp^3 orbital, all corners of the tetrahedra arrange at an angle of $109.55°$.[51]

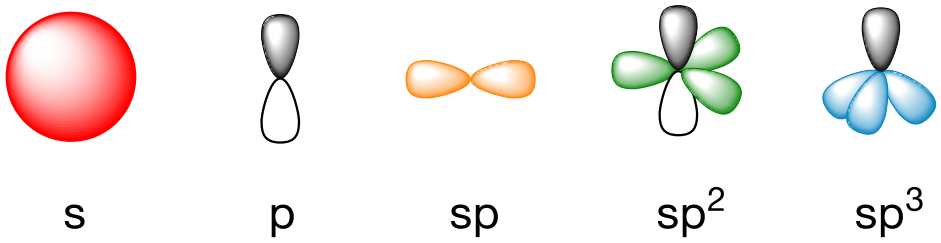

Figure 2.2 Schematic illustration of the spherical s and barbell shaped p orbital. The molecule orbitals with their hybridized orbitals sp, sp^2, and sp^3 are illustrated in orange, green, and blue color.

2.2.2 Molecule orbitals

Analog to "normal" waves, atomic orbitals can combine their wave functions either constructively (in phase) or destructively (out of phase).[58] The resulting combined orbital belongs to a pair of atoms and is a molecular orbital, also known as the linear combination of atomic orbitals (LCAO).[51, 58, 59] After combination, the electrons are equally found at any place on the molecule orbital and attract the nuclei, thus building an atomic bond, for example, a σ- or π- bond as illustrated in Figure 2.3a) in green and blue color, respectively. In-phase molecule orbitals are called bonding orbitals, while out-of-phase molecule orbitals do not have attraction forces to the nuclei and are called anti-bonding, denoted with a star.[51, 58, 59] An example of two p-orbitals is depicted in Figure 2.3b). The p-orbitals can build a π or π^* molecule orbital (MO). Their occupancy of the states is denoted with the green arrows. Generally, bonding orbitals have lower energy

than anti-bonding orbitals.[51] The low energy bonding orbitals are called highest occupied molecule orbital (HOMO), while the anti-bonding states are called lowest unoccupied molecule orbital (LUMO). The difference between those energy levels corresponds to the band gap and can be exploited for optoelectronics. For bigger molecules, as in a combination of multiple benzol rings with six π-bonds each, there are many bonding and anti-bonding orbitals that follow the Pauli exclusion principle.[59] With the combination of many molecule orbitals, band like structures form, as shown in Figure 2.3c).

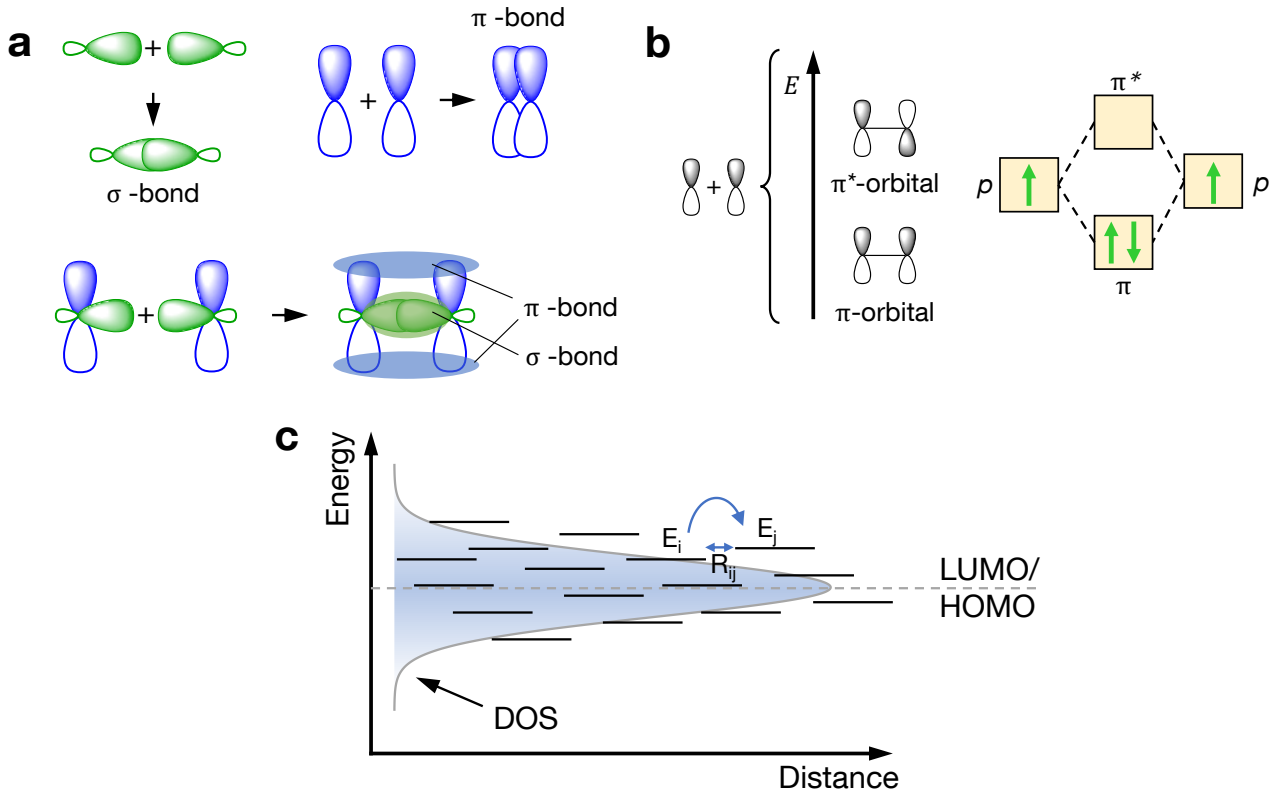

Figure 2.3 a) Bond formation of a σ- and π-bond or a combination of both within one molecule. b) The combination of two p-orbitals and their resulting molecule orbital with a bonding π-orbital and an anti-bonding π^*-orbital. c) Energy diagram of many bonding or anti-bonding energy states, building the HOMO and LUMO, respectively. Each line represents a single state, and the blue shaded area is the density of states (DOS).

2.2.3 Charge transport

Charge transport in organic semiconductors is complex because several different models are needed to describe it, for example, the band transport model, the polaronic transport model, and the disorder-based transport model for different regimes (e.g., low carrier density, high carrier density, space charge limited current, trap charged limited current, doped semiconductors, or strong coupling). Nevertheless, a unified theoretical formalism for the charge transport in organic semiconductors is still missing. In the book of Köhler and Bässler[51], a detailed description of each of them is provided, while in the following, a brief overview of the key aspects of charge transport in organics is given.

Inorganic semiconductors conduct current via the excitation of electrons from the valence band to the conduction band. The process is similar for organic semiconductors, where the electrons are excited from the bonding MO to the anti-bonding MO. Two kinds of charge transport for an excited charge carrier must be considered. There is *intra*-molecular charge transport within a single molecule, and *inter*-molecular charge transport between different molecules. The main difference between the classical crystalline semiconductors (covalent bondings) and the organic semiconductors is the weak van der Walls intermolecular

binding forces and the microscopic structural defects that inhibit free carrier movement due to potential barriers between the different molecules. This is the reason for the low charge transport compared to inorganic semiconductors. The weak atomic interactions lead to very narrow bands with an energetic width below 500 meV [60] so that the standard band transport can take place up to room temperature. At high temperatures, carriers get scattered due to molecular vibrations and charge inter-and intramolecular transport can only occur by a phonon-assisted tunneling mechanism called hopping [60, 61].

For π-conjugated systems, due to the overlap of the π-orbitals, the intra-molecular charge transport is also considered as delocalized, where the charge carriers can move freely. This often occurs in polymer chains or benzol rings, but defects in these systems also need to be overcome by hopping. The hopping states are discrete energy states with a Gaussian distribution around the HOMO and LUMO as depicted in Figure 2.3c).[60] Among the many models developed to describe hopping transport, the Miller-Abrahams model[62] is the most common one:

$$\omega_{i,j} = f_0 exp(-2\alpha R_{ij}) \begin{cases} \exp(-\frac{E_j - E_i}{k_B T}), & E_j - E_i \geq 0 \ (hop\ to\ higher\ state) \\ 1, & E_j - E_i \leq 0 \ (hop\ to\ lower\ state) \end{cases} \tag{2.4}$$

where ω_{ij} is the transition rate from localized state i to j and f_0 the attempt-to-escape frequency, which is typically assigned to the value 1×10^{14} Hz in literature.[63] R_{ij} the distance between the states and α the inverse localization length related to the tunneling probability [60, 62]. If a carrier absorbs a phonon to hop to a higher energetic state, the hopping rate must account for the tunneling probability. When a carrier hops to an energetically lower state, a phonon is emitted, and no additional energy is required [63].

2.3 Electrical properties of light-emitting diodes

The electric properties of LEDs will be described based on the book by Schubert,[8] where a more detailed description is provided. LEDs made out of inorganic semiconductors usually consist of a pn-junction as shown in Figure 2.4. The two doped regions (n-, p-doped) have majority charge carriers (electrons and holes) and build up a depletion region at the interface. By applying a reverse bias, this space charge region is even widened and no current is flowing. Under a forward bias, the space charge region is reduced and eventually removed, allowing the charge to flow while the current rises exponentially. This behavior can be described by the Shockley equation[64]

$$I = I_S(\exp{(\frac{qV}{k_B T})} - 1), \tag{2.5}$$

where I is the diode current, I_S the saturation current, V the voltage applied at the diode, k_B the Boltzmann constant, T the temperature, and q the elementary charge.

As already mentioned, the voltage strongly influences the diode behavior. The voltage at which the current strongly increases is called threshold voltage V_{th}. For highly doped pn-junctions ($E_C - E_F \ll E_g$) in the n-doped region and ($E_V - E_F \gg E_g$) in the p-doped region, the threshold voltage is approximately

$$V_{th} \approx \frac{E_g}{q} \tag{2.6}$$

The recombination of electrons from the n-doped region with holes from the p-doped region can occur under the emission of a photon in direct semiconductors. The pn-junction or diode is then called a LED. Furthermore, in ideal diodes, every electron that is injected into the active region generates a photon with the band gap energy, i.e., $h\nu \approx E_g$. Because of the energy conservation rule, the energy of the injected electron is equal to the photon energy

$$eV = h\nu \tag{2.7}$$

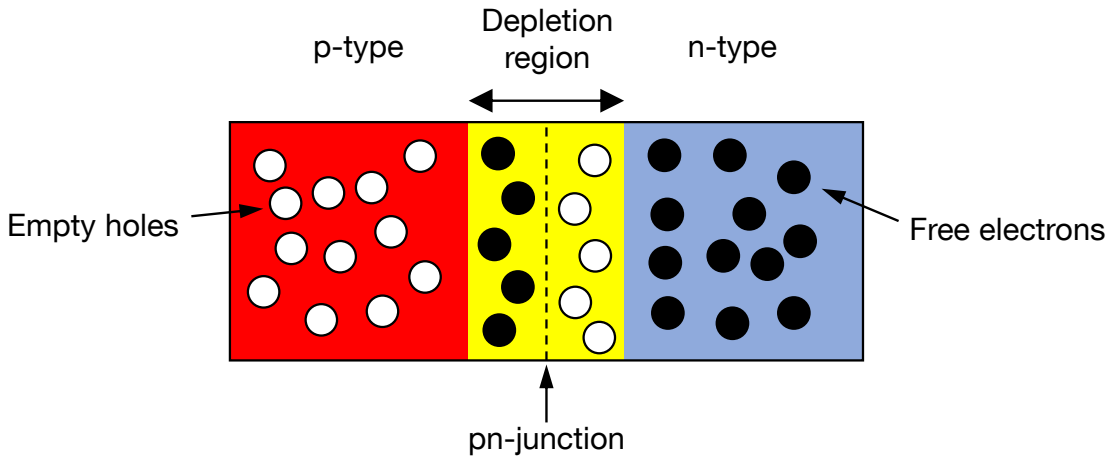

Figure 2.4 Schematic illustration of a semiconductor pn-junction. At the pn-junction of a p- and n-type semiconductor, a depletion region is building up.

The Shockley equation does account for this ideal case, although it does not apply for real diodes, where not every injected electron generates a photon. Therefore, it gets extended by an ideality factor η_{ideal} for the diode in order to account for it.

$$I = I_{\text{S}} \exp\left(\frac{qV}{\eta_{\text{ideal}} k_{\text{B}} T}\right) \tag{2.8}$$

where η_{ideal} is 1 for ideal diodes. In real diodes, the factor is $\eta_{\text{ideal}} = 1.1 - 2$ and higher.[8] Diodes often show parasitic resistances in form of a series resistance R_{S} or parallel resistance R_{P}. The effect of both resistances is demonstrated in Figure 2.5. The series resistance usually origins from a contact resistance or a high sheet resistance of the contacts. The parallel resistance can be caused by any current channel that bypasses the pn-junction. The bypass is mostly caused in the fabrication by imperfect layers. Taking R_{S} and R_{P} into account, the Shockley equation needs another modification and the $I - V$ characteristic is then given by

$$I - \frac{V - IR_{\text{S}}}{R_{\text{P}}} = I_{\text{S}} \exp\left(\frac{q(V - IR_{\text{S}})}{\eta_{\text{ideal}} k_{\text{B}} T}\right) \tag{2.9}$$

In the case of a very high parallel shunt resistance $R_{\text{P}} \to \infty$ and a very low series resistance $R_{\text{S}} \to 0$, the equation reduces to equation 2.8.

Capacitance characteristics of diodes

The total capacitance of a diode can be determined by the depletion capacitance C_{D} and diffusion capacitance C_{diff}. At zero applied bias, the depletion capacitance determines the diode capacitance and is given by the incremental depletion charge $\text{d}Q_{\text{D}}$ on each side of the junction upon an incremental change of the applied voltage $\text{d}V$.[7]

$$C_{\text{D}} = \frac{\text{d}Q_{\text{D}}}{\text{d}V} \tag{2.10}$$

When the diode is reverse-biased or for small forward biases, the depletion capacitance dominates as the carriers are pushed further apart and accumulate at the edge of the space charge region. This capacitance is directly related to the bias voltage and other junction parameters [65].

Under forward-bias conditions, the diffusion capacitance adds to the depletion capacitance because of the rearrangement of minority charges injected into the active region [7]. The diffusion capacitance is described by

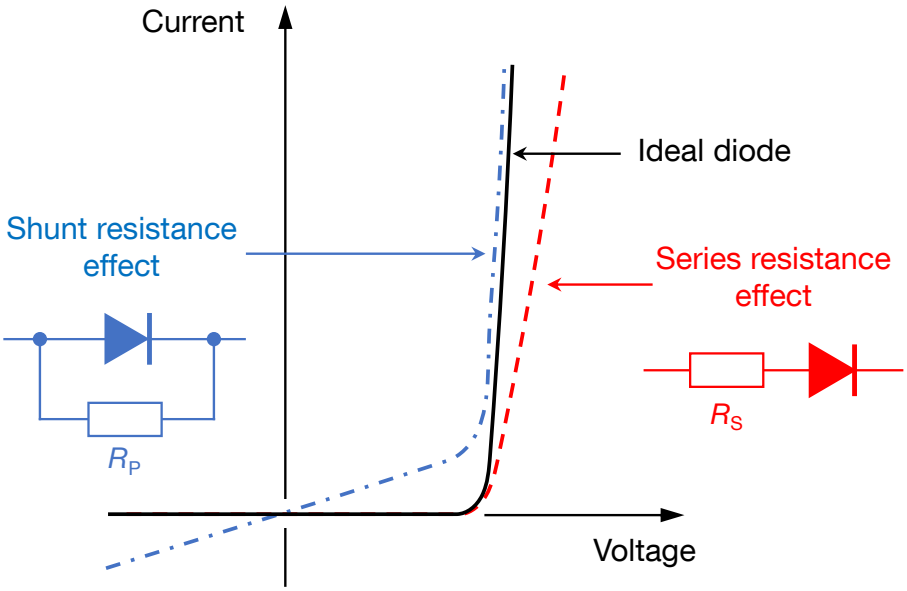

Figure 2.5 Effect of serial and shunt resistance on the $I - V$ characteristic of a diode. The figure is adapted from [8].

$$C_{\text{diff}} = \frac{q^2}{2k_{\text{B}}T} \cdot (L_{\text{p}} p_{\text{n0}} + L_{\text{n}} n_{\text{p0}}) \cdot \exp(\frac{qV_{\text{f}}}{k_{\text{B}}T}) \tag{2.11}$$

where C_{diff} is the diffusion capacitance, q is the elementary charge, k_{B} is the Boltzmann constant, T is the junction temperature, L_{p} and L_{n} are the diffusion lengths of holes and electrons, respectively. p_{n0} is the hole concentration in the n-doped region in thermal equilibrium, n_{p0} is the electron concentration in the p-doped region in thermal equilibrium, and V_{f} is the forward bias voltage. It can be seen from equation 2.11 that the diffusion capacitance is positive and always increases with bias voltage, which becomes important in subsection 6.2.1.[66] Furthermore, the diffusion capacitance is proportional to the DC current ($\propto \exp qV_{\text{f}}/k_{\text{B}}T$) and is therefore important at low frequencies and under forward bias.[7]

2.3.1 Organic light-emitting diodes

The working principle of OLEDs differs from inorganic diodes. The OLED usually consists of various organic layers that can be fabricated either from solution or evaporated at low temperatures. An OLED consists of a minimum of three layers, namely anode-, emissive-, and cathode-layer. At least one of the electrodes, either anode or cathode, has to be transparent to successfully transmit the generated photons out of the device. The electrodes are selected based on their work function, usually a high work function for the anode and a low work function for the cathode. The electrons and holes are injected directly into the emitting layer for recombination in such a device. In such single-layer devices, the efficiency (the ratio of the number of injected electrons to generated photons) is not very high because the electron and hole mobility within one material differs, which leads to recombination close to the electrode, where excited state quenching competes with luminescent decay.[8] As a consequence, using more layers has the advantage that the device performance can be optimized. In Figure 2.6 the energy diagram of such a multi-layer OLED device is schematically shown with all possible layer functions labeled. Starting at the anode side, followed by a hole injection layer (HIL) to ease hole injection into the device by minimizing the potential barrier, thus forming an ohmic contact. The HIL is usually followed by a hole transport layer (HTL) and/or an electron blocking layer (EBL). In both cases, the potential barrier of the HOMOs should be small to

achieve sufficient hole transport. At the same time, the EBL has the additional characteristic of blocking electrons with a low LUMO level. The LUMO level introduced a high potential barrier to the emissive layer (EML) where the recombination occurs. On top of the emissive layer is a hole blocking layer (HBL) and/or electron transport layer to confine the holes in the active layer while providing good electron mobility. The next layer is the electron injection layer (EIL) for good electron injection of the cathode. The cathode for electron delivery completes the device.

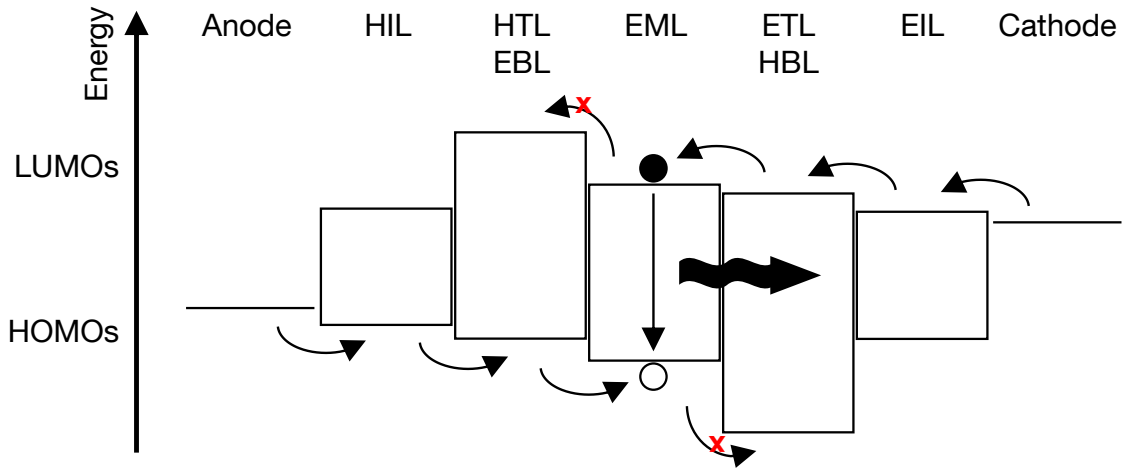

Figure 2.6 Schematic energy diagram showing the working principle of an OLED. The purpose of each individual layer is labeled at the top. The arrows indicate electron and hole movement from the anode and cathode to the EML, where they recombine under the emission of a photon.

2.4 Quantum dots

Quantum dots are now used in first industrial devices and have decisive advantages over organic semiconductors, such as a longer operating lifetime.[67–69] Therefore, this chapter explains the basics of QDs, why they are unique, and their particularities concerning LEDs. In this work, SiQDs are used because conventional QDs are based on toxic or rare materials such as Pb, Cd, or In.[70–72] Silicon is an indirect semiconductor and exhibits unique properties to show luminescence.

2.4.1 Quantum confinement effect

The size reduction of materials changes the physical properties of QDs, which are highly researched.[73] Quantum dots are structures on a nanometer-scale, where quantum mechanical effects are dominant [74]. Two main effects are responsible for the change. First, the ratio of atoms in the quantum dot core to surface atoms changes. Second, the quantum size effect leads to a discretization of the continuous conduction and valence bands in bulk into discrete energy levels. With appropriate methods, bulk semiconductor materials can be reduced to dimensions below the material-dependent Bohr radius.[75] This shrinking, the so-called quantum confinement effect or quantum size effect, leads to the discretization of the continuous conduction and valence bands in bulk into discrete energy levels, and the behavior of the nanostructure can be described by the particle in a box model. The band gap increases by further decreasing the

material's size because there are even fewer discrete states available. For small crystals, the energy for the lowest excited states is

$$E(R) = E_g + \frac{\hbar^2 \pi^2}{2R^2}[\frac{1}{m_e} + \frac{1}{m_h}] - \frac{1.8e^2}{\varepsilon_\infty R} \tag{2.12}$$

with R the radius of the quantum dot, m_e and m_h the effective mass of an electron and hole respectively.[76, 77] In this equation, a small term is neglected due to the dielectric discontinuity at the quantum dot surface.[76]

In Figure 2.7, the size-effect is illustrated from bulk material to quantum dots with varying sizes. The change of size and surface to volume ratio changes the optical, electrical, thermal, and photochemical properties of the nanometarial.[73]

The quantum effects are direct consequences of the confinement of the electron's wavefunction to the physical size of the nanomaterial and affect its optical, electrical, and photochemical properties [78]. Depending on the confinement along with one, two, or all three spatial directions, the nanostructures are termed quantum wells, quantum wires, and quantum dots, with the latter being also described as artificial atoms, nanocrystals, or colloidal particles.[75] For a more detailed description on the quantum confinement effect and how it is derived, please see [76, 77, 79]

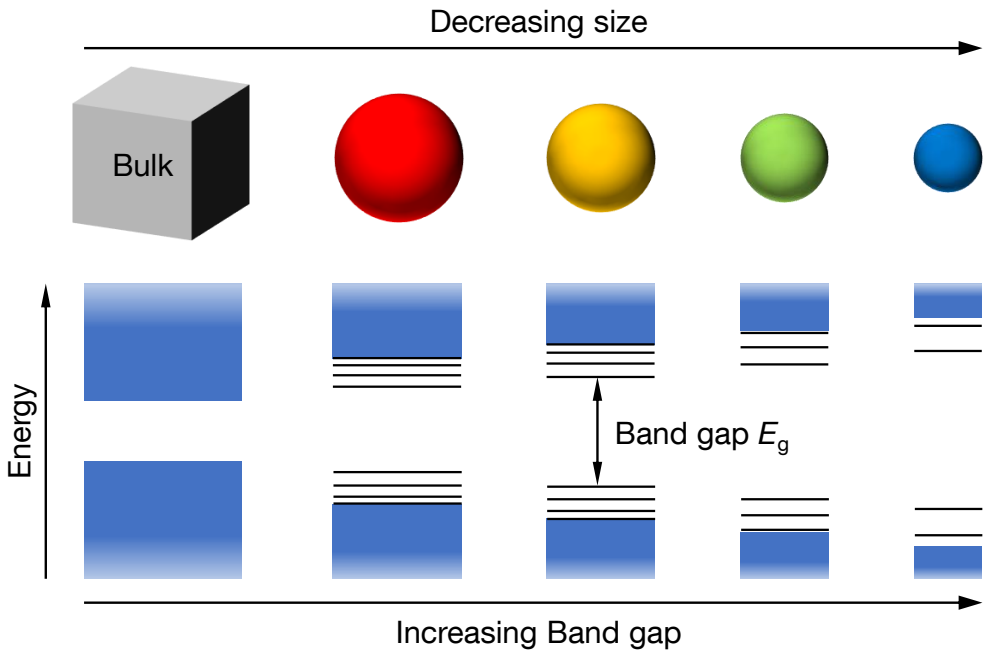

Figure 2.7 Schematic illustration of the quantum confinement effect in semiconductors. In bulk semiconductors, the conduction and valence band show continuous character but at nano-scale, the band gap becomes discretized. The band gap becomes bigger with further size reduction of the semiconductor.

2.4.2 Silicon quantum dots

Silicon is an indirect semiconductor that is only suitable for producing photonic products to a limited extent because its conduction band minimum and the valence band maximum do not have the same momentum.[80] In indirect semiconductors, a second quasiparticle usually provides the momentum (e.g., phonon) for a radiative transition between the bands to satisfy the momentum conservation rule. Only then can radiative recombination and the emission of a photon occur. Usually, those restrictions result in a low probability of photon emission.[81] Bulk silicon is a classic indirect semiconductor and is subject to these restrictions, as shown in Figure 2.8a), making it a poor material for optical applications.

However, if Si is scaled to the nano-scale, strong emission at room temperature has been observed.[37, 82–84] The quantum confinement of electron-hole pairs in nano-sized Si leads, in combination with the uncertainty principle of Heißenberg, to increased uncertainty of crystal momentum and the broadening of the wave vectors in the k-space (Figure 2.8b)). Consequently, the wave vectors of the electrons Ψ_e and holes Ψ_h overlap and establish a direct transition, which is referred to as "quasi-direct".[85, 86] This effect of Si enables a broad range of optical applications for silicon-based devices.

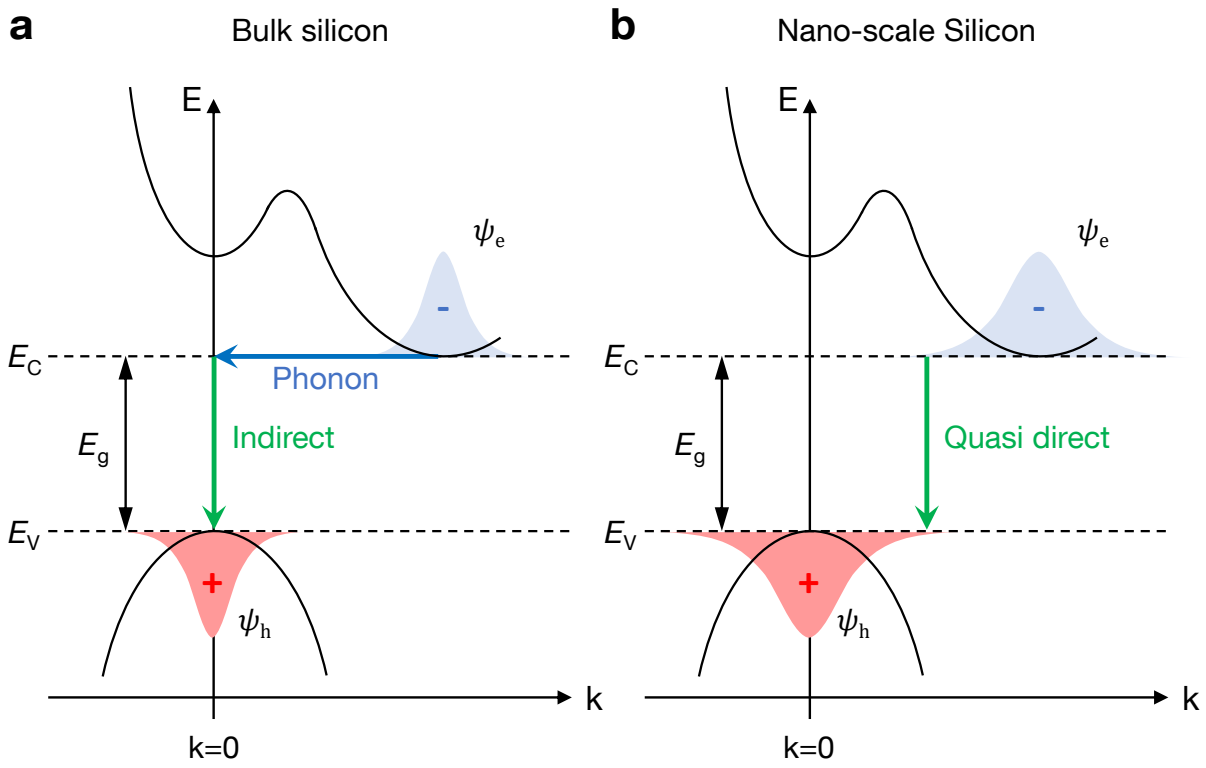

Figure 2.8 Schematic representation of the band structure of the indirect band gap of bulk silicon in a) and the quasi-direct band gap of nano-scale silicon in b). The conduction band minimum and the valence band maximum are at different k-vectors. At bulk silicon, a phonon-assisted process is needed for recombination. At the nano-scale, the wave vector for holes and electrons broadens, thus enabling a quasi-direct recombination transition. The wave vectors for holes Ψ_h and electrons Ψ_e are illustrated in red and blue colors, respectively.

3 Materials and Methods

This chapter provides a short description of the materials used to fabricate the SiQD-LEDs in this work. The fabrication methods are described afterwards, and the layer and device characterization is presented in the end.

3.1 Materials

Many materials can be used for SiQD-LEDs, but we have used only a few during this work. The used materials are all solution processible except the electrodes. That allows us to think about flexible devices in the future.

3.1.1 Indium tin oxide

ITO is the prevailing material for transparent conducting electrodes (TCE) in research and industrial applications because it combines high transparency, good electrical conductivity, and good adhesion on a substrate.[87] Indium tin oxide (ITO) usually consists of $90\,\%$ indium oxide (In_2O_3) and $10\,\%$ tin oxide (ZnO_2). In this composition, it has the lowest resistivity and is highly transparent in the visible range as a thin film.[88] The deposition of ITO is usually done via sputtering from ITO targets under elevated temperatures above $200\,$℃. At higher temperatures, the layer becomes more crystalline and charge transport improves.[88] Typical layer thicknesses for display applications are between $125\,\mathrm{nm}$ and $150\,\mathrm{nm}$ with high transparencies above $90\,\%$ and a low sheet resistance preferably less than $15\,\Omega/\square$.[88] The ITO layers we use for SiQD-LED fabrication were prepatterned and purchased from Xinyan Technology LTD (Hongkong). They have the typical layer thickness of about $120\,\mathrm{nm}$ and a sheet resistance of $15\,\Omega/\square$. For later work in chapter 7, we used homemade ITO substrates where the ITO was sputtered in an Alcatel model A 450 RF magnetron sputtering system.

3.1.2 PEDOT:PSS

PEDOT:PSS (Poly(3,4-ethylenedioxythiophene)-poly(styrenesulfonate)) is one of the most utilized conducting polymers. Its molecule structure is depicted in Figure 3.1a). It consists of the π-conjugated polymer PEDOT, a polymer for hole transport, and PSS, a water-dispersible polyelectrolite as a charge balancing counterion.[87] Both polymers can be mixed in different ratios n:m, from for example 1:2.5 to 1:20 for tuning the conductivity from $1\,\mathrm{S\,cm^{-1}}$ to $10^{-5}\,\mathrm{S\,cm^{-1}}$.[51] The typical mixing ratio of PEDOT:PSS for the usage as a hole transport layer in OLED or organic solar cell devices is 1:6, which yields a conductivity of $10^{-3}\,\mathrm{S\,cm^{-1}}$.[51] Used as a hole transport layer, the PEDOT:PSS layer smoothens the underlying ITO surface to prevent short circuits, acts as a diffusion barrier for oxygen atoms from the ITO, and improves the hole injection into the semiconducting polymer.[87, 89] In this work, we used the PEDOT:PSS Al4083 from Ossila (United Kingdom) with a PEDOT:PSS ration of 1:6 and further diluted it 1:3 with isopropanol for better wetting properties. The work function of this PEDOT:PSS solution lies between $5.0\,\mathrm{eV}$ to $5.2\,\mathrm{eV}$.[90]

3.1.3 Poly-TPD

Poly-TPD (Poly(N,N-bis-4-butylphenyl-N,N-bisphenyl)benzidine) is a blue-emitting conjugated polymer and its structure is shown in Figure 3.1b). The emission from this polymer at a wavelength of $420\,\mathrm{nm}$ is not

very efficient and therefore, it is mostly used as a hole transport layer in LEDs. If an LED is not properly adjusted, the blue emission can also lead to an undesirable side effect. Poly-TPD has its LUMO level at 2.3 eV and the HOMO level at 5.2 eV.[91] The deep HOMO energy level and the high hole mobility of $\mu_h = 2.1 \times 10^{-3}\,cm^2\,V^{-1}\,s^{-1}$ to $10^{-4}\,cm^2\,V^{-1}\,s^{-1}$ are ideal for hole transport, while the low LUMO energy level can efficiently block electrons.[92–94] The used Poly-TPD was purchased from Solaris Chem Inc. (Canada) with typical molecular weight M_W =100 kDa to 250 kDa and dissolved with $5\,mg\,mL^{-1}$ in dichlorbenzene (DCB).

3.1.4 Zinc Oxide

ZnO is an oxide-semiconductor with a wide band gap of 3.4 eV, typically n-type, and is therefore attractive as a blocking layer in organic devices.[95] Being an oxide provides immunity against oxidation, a usually highly transparency (>90 %), and a high electron mobility of ($\sim 2 \times 10^{-3}\,cm^2\,V^{-1}\,s^{-1}$).[42, 96, 97] Furthermore, ZnO can be processed from solution as inorganic nanocrystals without any surface ligands, which makes it suitable for flexible devices.[95] The conduction band of ZnO lies about -4.3 eV while the valence band is at -7.7 eV, a reasonable value for efficient hole blocking. The colloidal ZnO nanocrystals in this work were purchased from InfintyPV (Denmark), dispersed in isopropanol (5.6 wt%), and for final usage further diluted 1:3 with isopropanol.

3.1.5 Metal electrode

The top contact of the OLEDs and QLEDs is usually a non-transparent metal contact with a work function matching the underlying layer. The metal contact can be used as cathode or anode, depending on the device layout. The most common electrode materials are Al [43, 98] or Ag,[42, 48, 99] or a combination of those with Ca,[46] LiF,[41, 100] or MoO_3.[101, 102] All materials are deposited by physical vapor deposition and rates of 0.1 Å up to $3\,Å\,s^{-1}$. We used in this work a 100 nm thick Ag layer with a work function of 4.3 eV as the cathode.

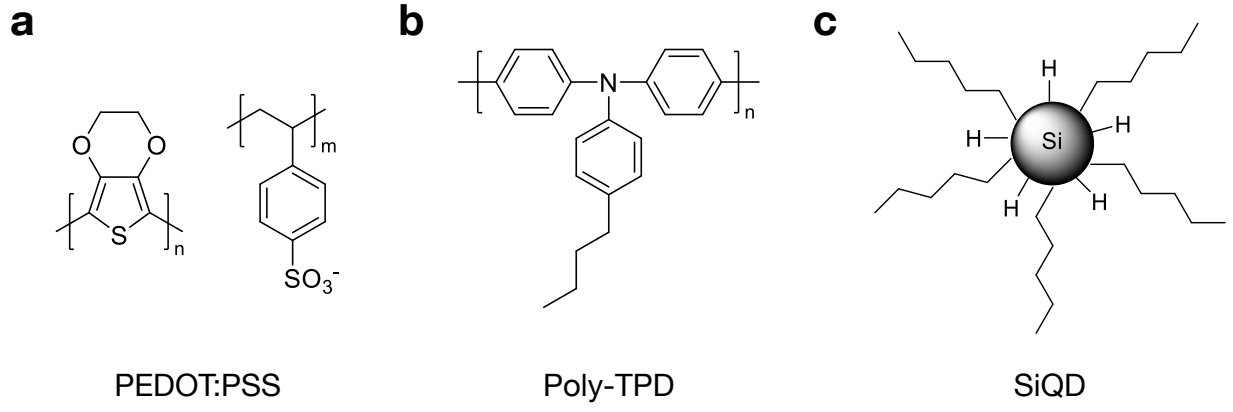

Figure 3.1 Polymer structure of a) PEDOT:PSS and b) Poly-TPD, which are used as HTL. c) Schematic representation of OLR functionalized SiQD, where every second H-termination was replaced by a hexyl group.

3.1.6 Silicon quantum dots

Nano-sized silicon starts to show photoluminescence at a size smaller than 4 nm because of the quantum confinement effect.[103] In combination with silicon's low cost, biocompatibility, and high abundance on earth, silicon quantum dots are a highly interesting research area.[104, 105] SiQDs can be synthesized with numerous methods, resulting in different quantum dot properties. There are three main synthesis groups, bottom-up gas-phase, top-down physical, and solution-phase approaches.

Most commonly used is the non-thermal plasma method in which the SiQDs agglomerate from the gas phase. Mangolini et al. use a mixture of argon and silane (SiH_4) to form SiQDs.[106, 107] In the self-assembly route, SiQDs can be synthesized via a one-step hydrothermal treatment based on a silane precursor.[108] Physical top-down approaches to obtain SiQDs are based on breaking down silicon or silicon-rich oxides, e.g., by etching or ball milling. The ball milling process is an easy process, but the drawbacks are the poor size control of the obtained nanoparticles and the high cost because high-quality Si wafers need to be milled.[109] The electrochemical etching of bulk silicon with HF electrolytes results in porous Si, which shows PL and was the method used by Canham to find PL in silicon for the first time.[37] Instead of using pure silicon, silicon-rich oxides are used to obtain SiQDs. Therein, the SiQDs are embedded into a SiO_x matrix through a disproportionation reaction. Liu et al. used amorphous SiO_x ($x < 2$) powder as starting material to synthesise SiQDs.[110] Freestanding SiQDs were obtained after annealing under argon flow at high temperatures and by HF-etching of the oxide layer.[110, 111] Instead of amorphous SiO_x powder, Hessel and co-workers used industrially available Hydrogen silsesquioxane (HSQ) in its polymeric form as the starting material for SiQD synthesis.[112] After thermal annealing of the HSQ at a temperature above $1100\,°C$, freestanding hydride-terminated SiQDs are obtained by HF-etching.[112]

SiQD synthesis and functionalization

In this thesis, all SiQDs were synthesized via the polymeric HSQ method proposed by Hessel et al..[112] The synthesis was done in the department of chemistry at TUM by Elisabeth Groß. In Figure 3.2a), the SiQD synthesis via this method is schematically depicted. The starting product is polymeric HSQ, which was annealed at temperatures of $1100\,°C$ under a slightly reducing atmosphere for $1\,h$.[99] As a result, an amber solid with SiQDs grown in a SiO_2 matrix was achieved during this time. The advantage of this method is the excellent control over the size of the SiQDs by adjusting the annealing temperature.[113] After cooling, the powder was ground and etched with a mixture of ethanol, Di-water, and HF to liberate free-standing H-terminated SiQDs.

To ensure colloidal stability, the SiQDs were functionalized with an organic ligand. The most common method is hydrosilylation, where every Si atom becomes functionalized with a functional group.[114, 115] An alternative functionalization method was developed by Höhlein et al., where only every second Si atom becomes functionalized. They used organolithium reagents to achieve partial surface functionalization. The corresponding reaction schematic is depicted in Figure 3.2b). The lithiated reagents are used to bind on the SiQD surface and in a second step, the Li is removed via HCl to get the Li free SiQD. From this schematic, it becomes clear that a maximum surface coverage of $50\,\%$ can be achieved. The lower surface coverage turned out to be more efficient in SiQD-LEDs.[46] For this reason, we employed the OLR method for this work. We used N-alkyl surface ligands with six (Figure 3.1c)), eight, and twelve carbon atoms on the SiQDs for the results in this thesis.

3.2 Fabrication methods

This section briefly describes the important fabrication methods used for the SiQD-LEDs, which are among others spin-coating, physical vapor deposition, and sputter deposition. All other fabrication steps are described in the fabrication chapter as they are part of the work flow.

3.2.1 Layer deposition via spin-coating

Spin-coating is a highly reproducible technique used for decades to deposit uniform and thin films on flat substrates. Commonly, spin-coating is used to cast photoresist on wafers for structuring via photolithography. However, spin-coated multi-layer systems are also the standard fabrication technique for solution-based materials due to the simplicity of the process. The simplicity makes it ideal for prototyping OLEDs

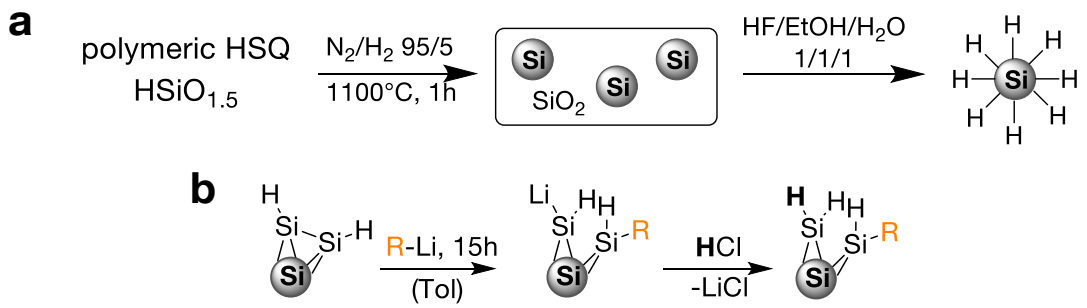

Figure 3.2 a) Schematic representation of the SiQD synthesis from polymeric HSQ. The SiQD grow within a SiO_2 matrix by annealing at 1100 ℃, followed by H-termination due to HF-etching. b) OLR reaction schematic for the hydride terminated SiQDs. After the functionalization, the lithium is removed by the workup with HCl. The R represents the alkyl group that is added. The figure is reprinted with permission from [99]

in a research environment. Typically, a few ml of material is dispersed on the substrate and brought to a set rotational speed. If the material is dispersed before the rotation starts, it is called *static spin-coating*. When the deposition starts shortly after the spin start, the process is called *dynamic spin-coating*.[116]

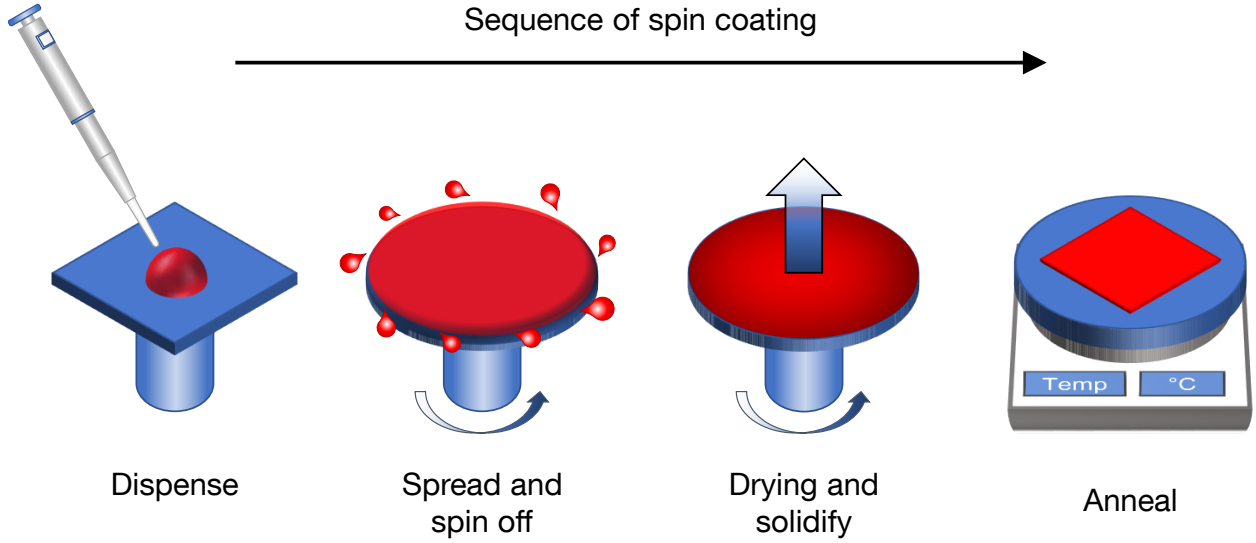

Figure 3.3 Sequence of a spin-coating process from left to right. The solution deposition is followed by a spreading and spinning off of excess material. Meanwhile dries the solvent and the film solidifies during spinning. The thin film becomes annealed after spinning to remove any residual solvent.

The spin-coating process is displayed in Figure 3.3 with its few steps. First, the material is dispensed onto the substrate. Only a few ml are used to cover substrates up to diameter with a few tens of cm in industry. Second, the centrifugal force spreads the material to a uniform thin film. The film thickness depends on the solution's concentration, the material's molar mass, and the rotational speed ω.[117] The final film thickness t for a solution with constant concentration and material is proportional to the inverse square root of the rotational speed: $t \propto 1/\sqrt{\omega}$.[117] A typical film thickness t curve as function of the rotation speed is shown in Figure 3.4. While spinning, most of the deposited material gets spun off so that only a small percentage of the initial material remains on the substrate. The next step in Figure 3.3, drying and solidifying, depicts the solvent evaporation from the film. As the solution solidifies, the film thinning stops and eventually forms a stable film thickness for further handling. The described steps typically take 20 s to 30 s after solution deposition. Usually, the spin-cast film becomes further annealed to remove any residual solvent in the thin film.

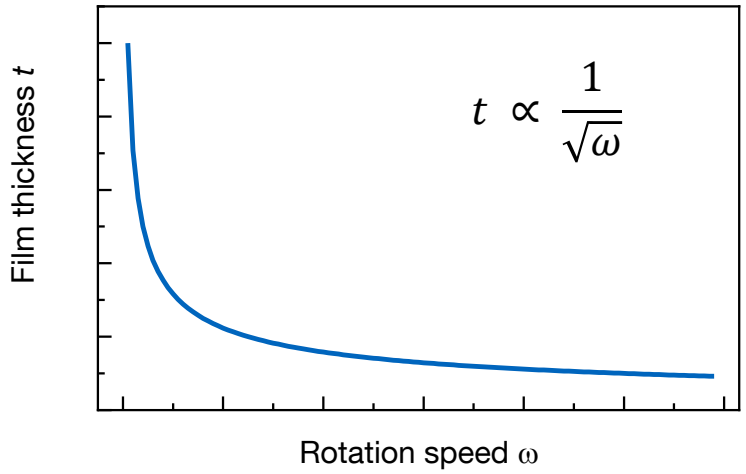

Figure 3.4 Exemplary film thickness spin curve for a solution with constant concentration as a function of spin speed. The equation shows the dependence of the film thickness on the rotation speed.

As described, spin-coating is a simple process, but it has many small details to take care of to get reproducible and uniform thin films in the nm range. The main cause for poor device performance is small particles or aggregates. For this reason, cleaning the substrate thoroughly and filtering the solution before usage is essential to avoid particles and aggregates. Rough surfaces also affect the spin-coating process; therefore, they might need to be prepared accordingly. A detailed description of the spin-coating process, together with tips and tricks, is given in the book from Koch and Rinke called "Photolithography", as well as at the homepage from Ossila.[116, 118]

3.2.2 Physical vapor deposition

Physical vapor deposition (PVD) is a deposition technique where atoms from the source material are thermally vaporized. The vaporized atoms or molecules reach the substrate almost without deflecting through other atoms due to a high vacuum of better than 10^{-4} mbar in the sample chamber.[119] For better film quality and less contamination, a better quality vacuum is needed. Due to the low chamber pressure, the melting point and vapor pressure decrease with increasing temperature, making this method feasible. The two most common heat sources to vaporize the materials are resistive heating, called resistive thermal evaporation (RTE), and electron-beam (E-beam), called E-beam evaporation. Both methods were used in this work. A simplified version of both evaporation techniques is depicted in Figure 3.5 with thermal via resistive heating left and E-beam evaporation on the right side. A detailed description of PVD is provided in the 'Handbook of physical vapor deposition (PVD) processing'.[119]

Resistive thermal evaporation Resistive heating is the most common way to heat materials that vaporize below 1500 °C.[119] Therefore, the material is placed in a boat, crucible, or basket to heat up by the contact with the hot surface. W is a commonly used boat material because of its electric conductivity, high melting point, and low thermal extinction. Resistive heating occurs under low voltages (< 10 V) and very high currents of several hundreds of A.[119]

Electron beam evaporation For E-beam evaporation, a high-energy electron beam is used to heat up the material. Using this method, materials such as insulators, ceramics, or glasses can be deposited. Also, large amounts of materials can be evaporated. The E-beam is generated with a thermionic-emission filament for electron generation, an acceleration voltage, and a magnetic field to focus and deflect the

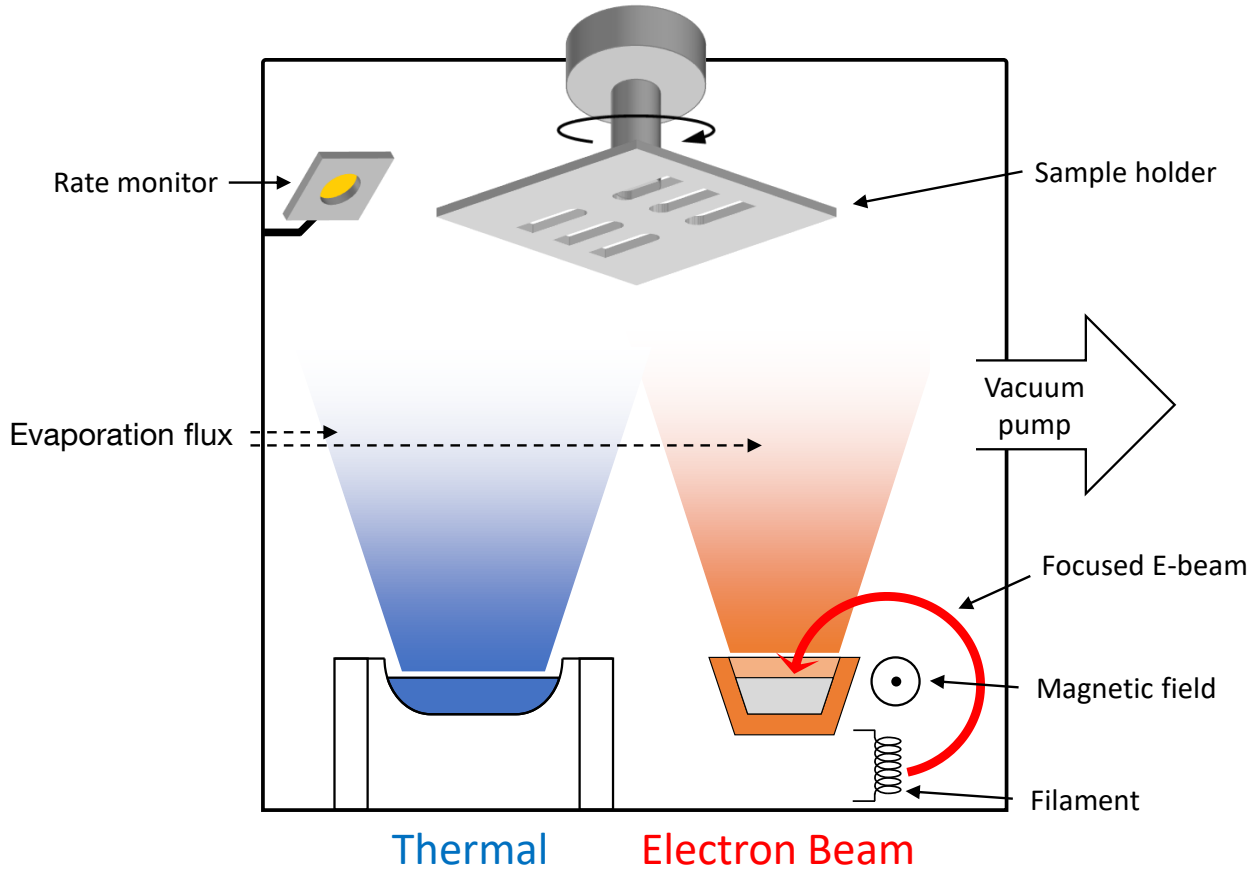

Figure 3.5 Simplified illustration of RTE and E-beam evaporation. The necessary temperature for material evaporation is provided by a resistively heated boat or by an E-beam. The material to deposit becomes evaporated and the resulting evaporation flux condenses on the rotating sample holder. The deposition rate on the sample is monitored by an oscillating quartz rate monitor.

E-beam.[119] The E-beam is focused on the source material to provide the energy to heat it up and evaporate.

In both systems, RTE and E-beam, the deposition is monitored with a quartz crystal rate monitor (QCM). The QCM measures the change in resonant frequency, as the frequency is directly proportional to the added mass.[119] As a result, a rate in $\text{Å}\,\text{s}^{-1}$ can be measured. The evaporation flux of the vaporized material condenses on the sample, which is placed upside-down above the evaporation source. The sample holder usually rotates for increased film homogeneity. The material source can be small compared to the sample size and then a cosine distributed thickness profile can be observed. The distribution of the atoms on the sample surface from a point like source can be described by

$$\frac{dm}{dA} = \frac{E}{\pi r^2} \cos\phi \cos\theta \tag{3.1}$$

with $\frac{dm}{dA}$ is the mass per unit area, E the total mass evaporated, r the distance from the source to the subsrate, ϕ the angle from a line from the source to a point on the substrate, and θ the angle from the normal to the vaporizing surface.[119] From this equation, is clear that big samples show a thickness gradient from the center towards the edges of the sample. In this work, a Univex350 evaporation system from Leybold with a RTE was used to evaporate the top silver electrode of the SiQD-LEDs with a rate < $3\,\text{Å}\,\text{s}^{-1}$. Additionally, a Univex250 from Leybold with RTE for a thin silver outcoupling mirror ($3\,\text{Å}\,\text{s}^{-1}$) and E-beam for SiO_2 deposition ($1.5\,\text{Å}\,\text{s}^{-1}$) was used.

3.2.3 Sputter deposition

Sputtering is a deposition method where thin films are deposited by physically vaporizing atoms from a surface by bombarding with energetic atomic-sized particles such as ions.[119] A schematic representation of the sputtering process is illustrated in Figure 3.6. Radio frequency (RF) magnetron sputtering was used in this work and therefore only described among the many different sputtering techniques. RF sputtering is using a high frequency at the power supply with typically 13.56 MHz, while the reversed part of the cycle eliminates charge buildup on an insulating surface.[120] It further enables the sputtering of insulators in a reactive environment.[120] The magnetron employs a static magnetic field at the cathode to constrain secondary electrons, enhancing the plasma density in the confined area.[120] In Figure 3.6, the RF voltage is applied in the vacuum chamber, and inert Ar gas is inserted. Under the right conditions, the gas breaks down to Ar^+ ions into plasma discharge. The ions are accelerated towards the target and vaporize the target material. The vaporized atoms accumulate at the substrate underneath and a thin film grows.

We used the sputtering process to deposit ITO on SiO_2 to act as an anode in cavity LEDs. In the used Alcatel model A 450 RF magnetron sputtering system, a base pressure of 2×10^{-7} mbar prevailed in the sample chamber, whereas a pressure of 4 µbar was maintained during sputtering due to the inlet of argon. The ITO was then sputtered at 50 W.

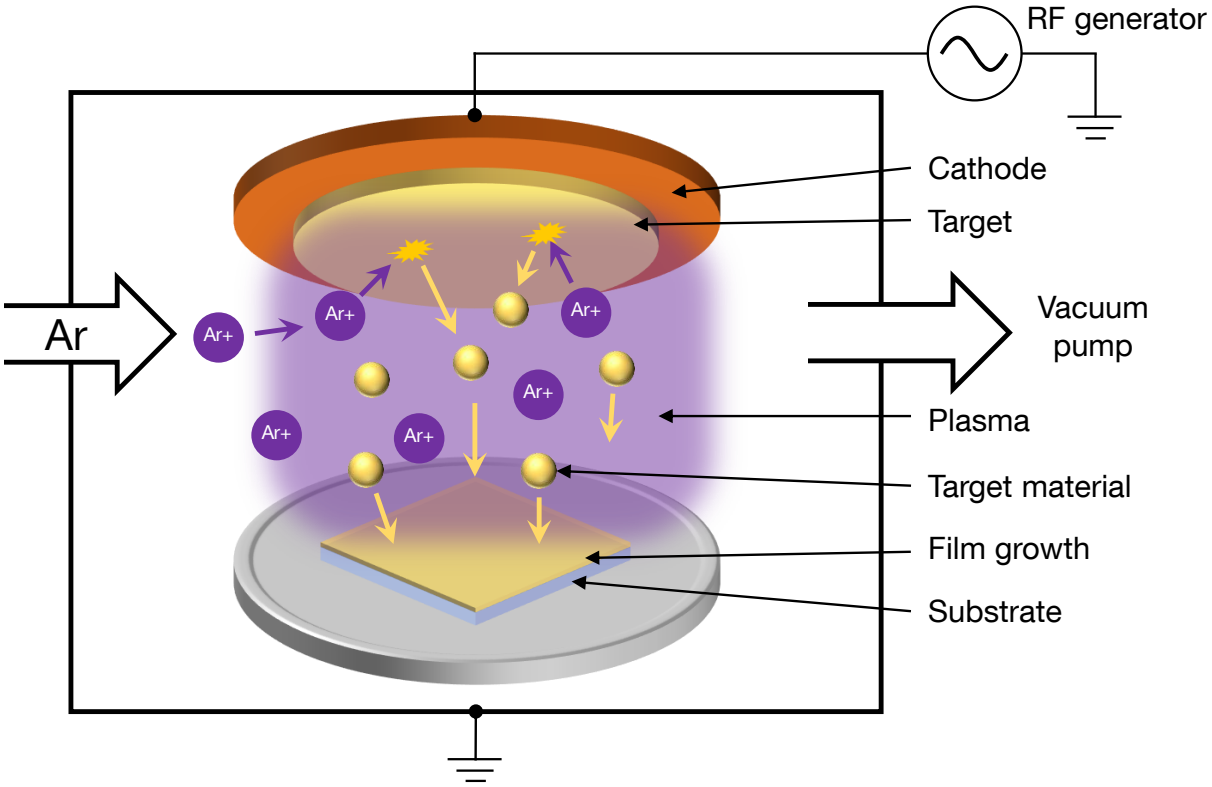

Figure 3.6 A schematic illustration of a RF sputtering process. A RF voltage is applied at the cathode, generating an Ar plasma, which is illustrated in violet color. The Ar+ ions bombard the target material and the vaporised atoms accumulate at the substrate to grow a thin film.

3.3 Material characterization techniques

Surface analysis is essential in research and industry processes to ensure reliable results. This section serves to describe the characterization methods for individual LED layers. First, the morphological meth-

ods intended for layer thickness measurement are described before the optical measurement methods are explained.

3.3.1 Stylus profilometry

Contact-type profilometry with a diamond stylus tip is a conventional measurement method in research and industry. It allows measuring the vertical displacement of, for example films on wafer-scale-sized samples, which is an excellent advantage over other measurement techniques, e.g., atomic force microscopy (AFM, see chapter 3.3.2). The stylus is dragged in contact across the sample's surface and reconstructs the surface morphology with step sizes of 10 nm and below.[99] A stylus with tip sizes in the µm range and made of diamond are commonly used. In our work, a DektakXT stylus profilometer from Bruker was used and the explanation of the function of a profilometer is based on this example. A simplified illustration is shown in Figure 3.7. The used stylus in our setup has a 2 µm tip radius and the stylus force can be set from 1 mg to 15 mg. Due to the tip radius, systematic measurement errors occur and must be taken into account.[121] The sensor head contains the controller and PC feedback mechanism to track the stylus's movement. The whole sample stage can be moved and rotated to align with the features to measure. The thickness measurement of thin layers requires at least one feature where the layer thickness can be measured. In this work, a scratch through the thin film to the substrate was used to measure the film thickness. The height difference d from the material surface to the substrate can then be measured. The measurement of the step profile is illustrated in the figure inset. Typical scratches had an approximate width of 100 µm to exclude a vertical influence of the measuring tip. The samples were measured for at least three scratches to ensure good film homogeneity. For the thin layers in nm regime, we used the lowest stylus force of 1 mg to avoid film damage induced by the diamond tip.

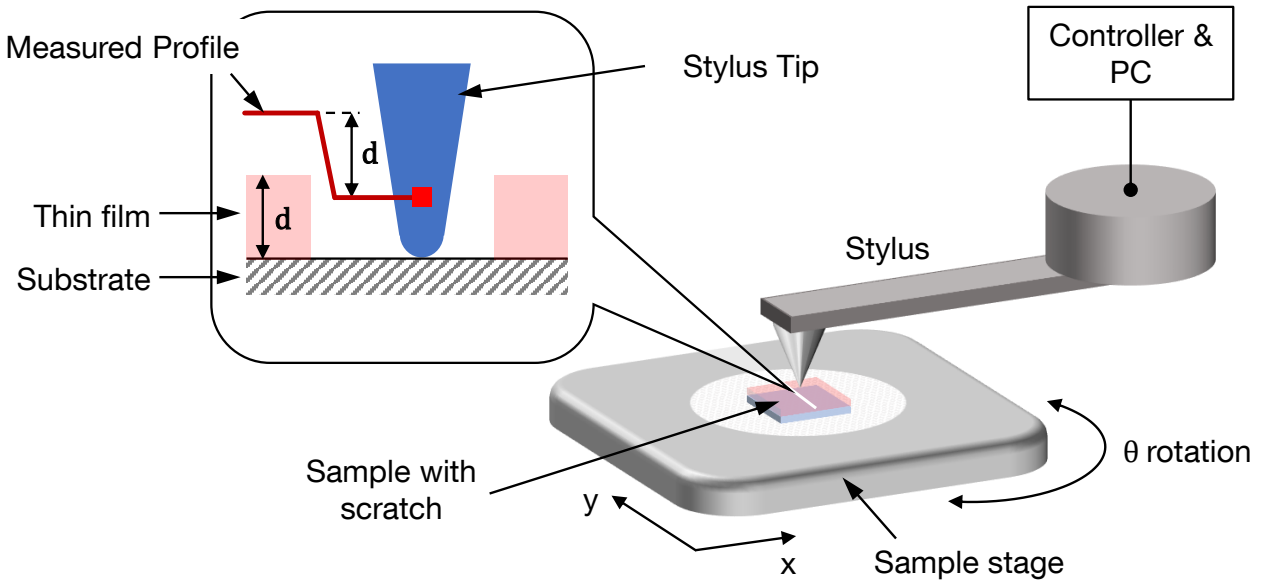

Figure 3.7 Simplified illustration of a stylus profilometer. The stylus rides across the sample and the controller tracks the stylus movement of the surface. The inset shows that in more detail and how the thickness of the film is measured by the displacement of the tip.

3.3.2 Atomic force microscopy

Atomic force microscopy belongs to the family of scanning probe microscopes (SPM), where extremely sharp mechanical probes scan solid surfaces with a tip radius of < 30 nm.[122, 123] Other major types of SPMs, are the scanning tunneling microscope (STM) or the scanning near-field optical microscope

(SNOM).[122] The AFM was first introduced by Binnig et al. in 1986 with a lateral and vertical resolution of $3\,\mathrm{nm}$ and $0.1\,\mathrm{nm}$, respectively.[124] In contrast to the STM, which requires an electrically conductive surface, the AFM can also measure insulating materials, making the AFM the first imaging microscope for conductors and insulators with atomic resolution.[122, 124]

A typical setup of an AFM is illustrated in Figure 3.8. An AFM generates 3-dimensional images of a surface by measuring very small forces (less than $1\,\mathrm{nN}$) on the extremely sharp tip [122–124]. These small forces can be measured by measuring the motion of a very flexible cantilever with an ultra-small mass.[123] Further, an extremely low spring constant is necessary for high vertical and lateral resolution at the small forces and additionally with high resonance frequency ($10\,\mathrm{kHz}$ to $1000\,\mathrm{kHz}$) to minimize the sensitivity of the AFM to surrounding vibration noise.[122, 123] Commercially available cantilevers have a tip radius curvature of commonly $5\,\mathrm{nm}$ to $50\,\mathrm{nm}$ and are batch-fabricated from pure silicon or silicon nitride by applying photolithographic and etching techniques.[122] The surface is usually measured employing a laser beam deflection technique. Using this technique, the laser beam is focused on the reflective cantilever top and is collected by a quadrant detector. Any normal forces (by sensing the bending of the cantilever) and lateral forces (by sensing the angular changes caused by cantilever torsion) deflect the laser beam, change the position of the beam on the detector, and gives a deflection signal to the feedback electronic in the controller.[122, 123] While the sample is held in place, the sharp tip scans line by line in x- and y-direction over the sample. For imaging, the vertical motion (z-direction) gets linked to the x, y-position of the cantilever and generates a topographic image of the scanned area of the surface.[122, 123]

Depending on the application, The AFM can be utilized in numerous measuring modes, such as contact, conductive, tapping, magnetic, force mode, and many more. Tapping mode AFM was mainly used; therefore, it is described and shown in the inset of Figure 3.8 in more detail. In tapping mode AFM, the cantilever oscillates with a specific frequency and a set-point amplitude and is then brought closer than the set-point amplitude to the sample surface for the measurement. During each oscillation cycle, the tip taps the surface for a short time and the amplitude change gives a change in height. Sample damage is mostly avoided in this measuring mode, making it preferable for soft polymer samples. The probe-sample interaction changes not only the amplitude of the oscillation it also results in a phase shift of the oscillation with respect to the freely oscillating cantilever.[122] Attractive forces cause a negative phase shift, while repulsive forces cause a positive phase shift.[122] With the combination of x, y, amplitude change and phase change, the 3D image can be calculated. For all measurements, a Veeco Dimension Icon AFM was utilized.

3.3.3 Ellipsometry

Ellipsometry is a well-established and non-destructive method to measure the refractive index or the thin film thickness of planar solid thin films.[125] It is further able to detect film thicknesses from a few Å to some µm in various environments, which makes it suitable for many industrial applications. Ellipsometry is generally based on the change of the polarization of light, where a linear polarized light beam is reflected by the sample. At the same time, it gets elliptically polarized, which is also the origin of the name. The polarization of the elliptically reflected light depends on the thin film thickness, the angle of incidence, the wavelength, and the dielectric constant of the film.[125] The change in polarization is measured by a rotating analyzer, which is linked to the dielectric properties of the sample. At a particular wavelength, the original s- and p- polarization components r_s and r_p of the incident beam are changing at the interface. The complex reflectance ratio ρ, the amplitude $\tan(\Psi)$ and phase Δ can be calculated using the Fresnel equation that gives a good approximation for thin films[125, 126]

$$\rho = \frac{r_p}{r_s} = \tan(\Psi) \cdot e^{i\Delta} \tag{3.2}$$

where ρ is the complex reflectance ratio of r_p and r_s, which is often described as an amplitude $\tan(\Psi)$ and phase Δ.[126] The change in reflectance is dependent on the dielectric constant, the angle of incidence, the wavelength, and the film thickness.

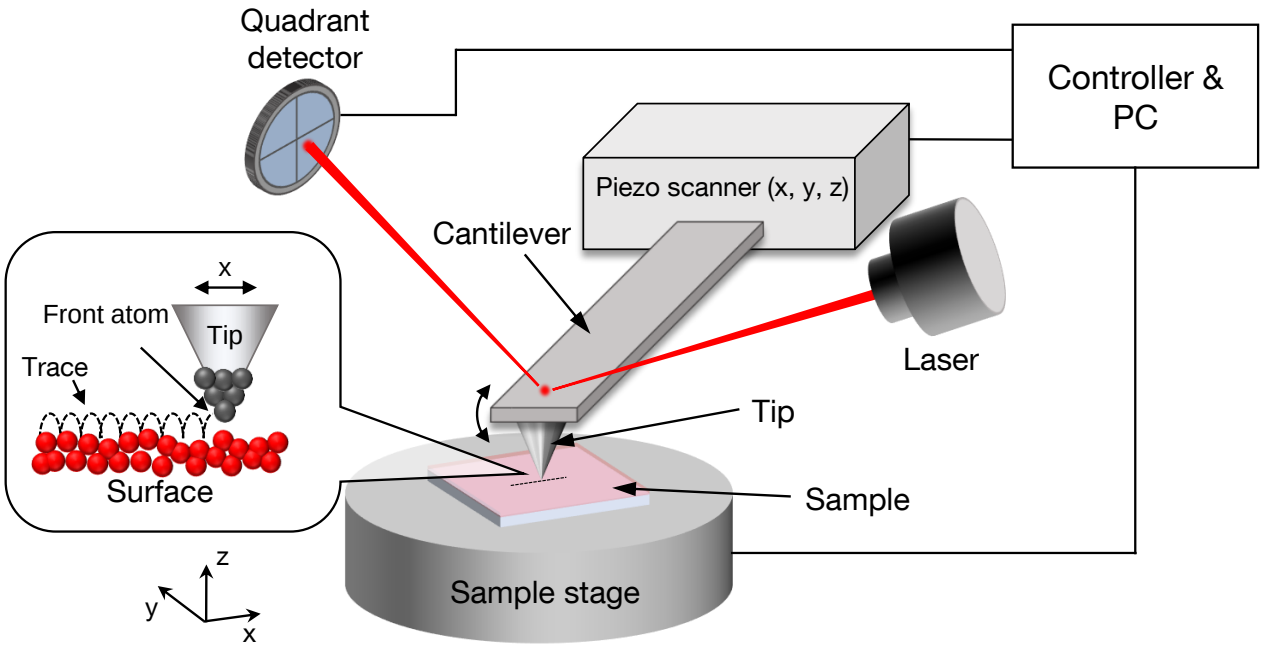

Figure 3.8 Simplified illustration of an AFM. A laser is sensing the deflection of the free cantilever with an extremely sharp tip, while the tip is scanning line by line over the surface of the sample to map the morphology of the sample surface. In tapping mode, the cantilever oscillates in close distance to the surface and taps on the surface for only a short time.

In this work, we employed the ellipsometer to determine the dielectric constants of thin films with a known thickness. For the measurement a Woollam alpha-SE (J. A. Woollam Co. Inc., U.S.A.) under angels of 65°, 70°, and 75° in the wavelength range from 380 nm to 900 nm was used. A more detailed description on the fitting procedure and the measurement data is given in subsection 7.2.3.

3.3.4 Transmission spectroscopy

The optical transmission spectra of thin films have to be recorded for proper characterization in optical devices. Transmission spectroscopy is a standard method to obtain the transmitted spectrum by measuring the light passing through the sample. As light is absorbed or reflected from the sample surface, the intensity of the measured light at the detector will be modulated. Usually, for transparent electrodes or thin films, the transmittance in the green region around 550 nm is evaluated because the human eye is most sensitive there.[7] For optoelectronic devices, the entire spectrum is important due to various layers inside the devices that may have different properties. From a typical measurement, the transmittance T is given by

$$T(\lambda) = \frac{I(\lambda)}{I_0(\lambda)} \tag{3.3}$$

where I is the transmitted light and I_0 is the incident light intensity, both dependent on the wavelength λ.[127, 128] Usually, the sample is deposited on a substrate with its own transmittance. To obtain the pure material transmittance, the setup becomes calibrated with an empty substrate to eliminate this source of error.

In this work, an AvaLight-DH BAL lamp from Avantes was used as the light source to obtain a transmission spectrum in the wavelength from 190 nm to 1200 nm, which was detected by an Avaspec ULS 2048x64 spectrometer.

3.4 Device characterization

Besides controlling the fabrication or material quality, the complete LED device was characterized using various methods. Essential were the measurement techniques for determining the current-voltage profile, the irradiance, the EL spectrum, and the EQE of the SiQD-LEDs. For this purpose, an integrating sphere with a calibrated spectrometer and a photodiode was used. In addition, charge transport properties were investigated via a capacitance-voltage method.

3.4.1 Integrating sphere

An integrating sphere is an optical device that enables to measure the optical radiation. It consists of a hollow sphere that diffusely reflects the light. With an integrating sphere, the basic radiometric quantities of a LED, such as the irradiance and the EL spectrum, can be measured. By combining the sphere with a source measurement unit (SMU), the current-voltage characteristics can be determined and the EQE can be calculated. The used setup in this work is depicted in Figure 3.9. Through the SMU, a voltage or current is applied to the LED, and both current and voltage are measured. The LED was placed at the surface of the sphere and centered at a port, as shown in the side view. The light emitted from the LED was collected by the integrating sphere and fed into a spectrometer via an optical fiber that analyzes the EL spectrum. For the irradiance measurement of the LED, the spectrometer was calibrated with a known reference spectrum across the visible spectrum from 300 nm to 1100 nm.

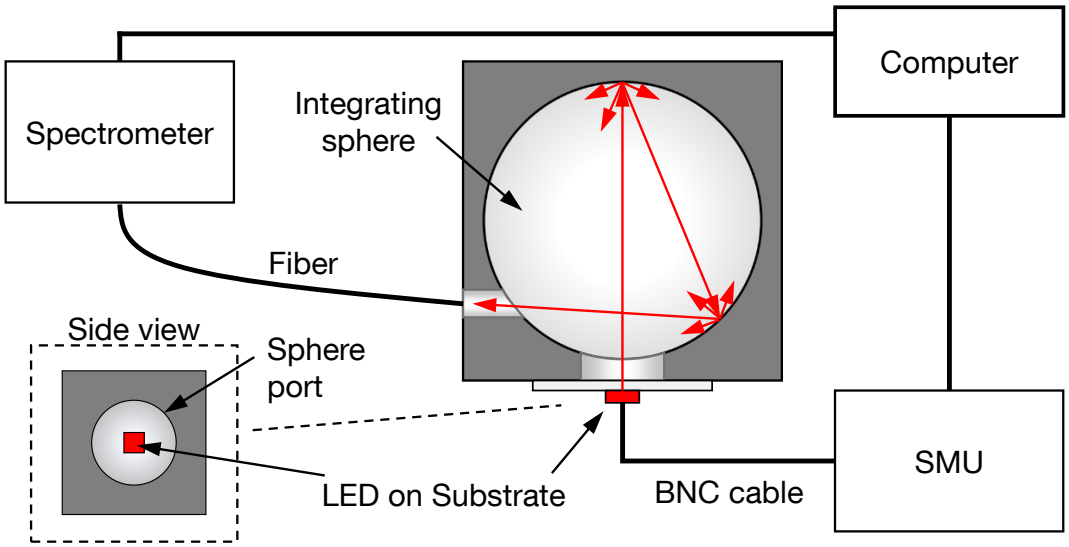

Figure 3.9 Schematic representation of the used integrating sphere setup. The LED was placed centered at one opening at the integrating sphere. The emitted light was diffusely reflected inside the sphere and fed into the fiber to the spectrometer, where the spectrum of the LED is analyzed. A computer controlled both the driving voltage and the spectrometer.

The efficiency of a LED is an important factor for power savings. In an ideal device, every injected electron emits one photon in the active area. In real devices, not every injected electron generates a photon due to material defects acting as non-radiative recombination centers. The ratio between the injected electrons and the generated photons is defined as the internal quantum efficiency (IQE).[8] Furthermore, some generated photons are reabsorbed inside the LED, which is accounted for by the extraction efficiency $\eta_{\text{extraction}}$. The EQE now is defined as IQE $\cdot \eta_{\text{extraction}}$ or by the number of photons N_{photon} emitted into free space divided by the number of injected electrons N_{electron}.[8, 129]

$$EQE = \frac{N_{\text{photon}}}{N_{\text{electron}}} \tag{3.4}$$

To calculate the EQE, the number of electrons need to be known. In general, a constant current I, depends on the electric charge Q and time t by

$$I = \frac{Q}{t} \tag{3.5}$$

With Q as a multiple of the elementary charge q and the number of electrons ($Q = N_{\text{electron}} \cdot q$) and Equation 3.5, the number of electrons N_{photon} can be calculated by

$$N_{\text{electron}} = \frac{I \cdot t}{q} \tag{3.6}$$

In order to calculate the number of photons N_{photon}, the energy at a specific wavelength λ is needed. The optical energy of the measured LED at a given wavelength $E_{\text{total},\lambda}$ is divided by the photon energy $E_{\text{photon},\lambda}$ at that wavelength

$$N_{\text{photon},\lambda} = \frac{E_{\text{total},\lambda}}{E_{\text{photon},\lambda}} \tag{3.7}$$

with $E_{\text{photon},\lambda} = \frac{h \cdot c}{\lambda}$ and $E_{\text{total},\lambda} = P_{\text{total},\lambda} \cdot t$. As a result, $N_{\text{photon},\lambda}$ can be written as

$$N_{\text{photon},\lambda} = \frac{P_{\text{total},\lambda} \cdot t \cdot \lambda}{h \cdot c} \tag{3.8}$$

where $P_{\text{total},\lambda}$ is the optical power at wavelength λ, h is the Planck constant, and c the speed of light. $P_{\text{total},\lambda}$ can be written as irradiance $E_{\text{e},\lambda} \cdot A$ where A is the LED area. Finally, the number of photons at a specific wavelength can be written as

$$N_{\text{photon},\lambda} = \frac{E_{\text{e},\lambda} \cdot A \cdot t \cdot \lambda}{h \cdot c} \tag{3.9}$$

As photons exhibit different energies at different wavelengths in the spectra, and the LED emits at many different wavelengths, the whole spectrum is needed to calculate the total number of photons. By integration of the measured spectrum, the number of photons can be calculated by

$$N_{\text{photon}} = \frac{A \cdot t}{h \cdot c} \int_0^\infty E_{\text{e},\lambda} \lambda \, d\lambda \tag{3.10}$$

Now, Equation 3.6, and Equation 3.10 can be inserted into Equation 3.4, which leads to

$$EQE = \frac{N_{\text{photon}}}{N_{\text{electron}}} = \frac{A \cdot q}{h \cdot c \cdot I} \int_0^\infty E_{\text{e},\lambda} \lambda \, d\lambda \tag{3.11}$$

In this thesis, the typical EQE are in the range of 0.5 % to 1.5 % for SiQD-LEDs. For more evolved LED types, i.e. OLEDs and other QD-LEDs, the EQE is about 25 % and 18 %, respectively.[130]

3.4.2 Electro-optical LED measurement

An alternative way to measure the EQE is using a photodiode instead of the integrating sphere setup. By doing so, the spectral information is lost because the photodiode completely collects the full EL spectrum, but the measurement is high-speed. This is due to the large number of averaging for a good signal-to-noise ratio at a spectrometer versus measuring the photocurrent from the photodiode. The used photodiode measurement setup is schematically depicted in Figure 3.10. It enables the measurement of the EQE of the SiQD-LEDs. The forward-emitted light of the LED is collected by the photodiode at a small distance t_2. The distance t_2 is introduced from the sample holder and t_1 is the substrate thickness of the LED. The lateral dimensions of the quadratic LED l_1 is 3 mm x 3 mm and the large-area photodiode is 10 mm x 10 mm. Because of the centered position of the LED on top and the bigger size of the photodiode, we assumed that the bigger photodiode collects all forward-emitted photons. The photodiode's responsivity was taken

at the average value of the emission spectrum, which was measured individually with a spectrometer. The measured optical power of the LED P_{measured} can be calculated by

$$P_{\text{measured}} = \frac{I_{\text{PD}}}{R(\lambda)} \tag{3.12}$$

with the photocurrent I_{PD} and the responsivity of the photodiode $R(\lambda)$. Due to the air/semiconductor interface, a correction factor is implemented to account for total reflection losses. Under the assumption of lambertian emission from a point source, the optical power density P_{LED} can be written as[8]

$$P_{LED} = P_{\text{measured}} \cdot \frac{S}{A_{\text{sphere}}} \tag{3.13}$$

where S is the surface area of a semisphere, A the surface area of this sphere, r the solid angle, and ϕ_c the critical angle. A can be calculated by

$$\begin{aligned} A_{\text{sphere}} &= 2\pi \cdot r^2 \cdot (1 - \cos\phi_{\text{c}}) \\ \cos\phi_{\text{c}} &= \frac{t_1 + t_2}{r} \end{aligned} \tag{3.14}$$

and S with

$$\begin{aligned} S &= 2\pi \cdot r^2 \\ r &= \sqrt{\frac{l^2}{4} + (t_1 + t_2)^2} \end{aligned} \tag{3.15}$$

By the geometry of the used sample holder, we get a correction factor of 1.63 for the irradiance measurement. Finally, the EQE can be calculated with a slightly alternative version than the integrating sphere equation by

$$EQE = \frac{P_{LED} \cdot \lambda_{\text{mean}} \cdot e}{h \cdot c \cdot I_{LED}} \tag{3.16}$$

where I_{PD} is the measured photodiode current, λ is the mean emission wavelength, e the electron elementry charge, $R(\lambda)$ the photodiode resposivity, h the Planck constant, c the speed of light, and I_{LED} the LED current.

3.4.3 Capacitance-voltage characterization

Capacitance-voltage (CV) characteristics are typically measured with an LCR meter (for inductance [L], capacitance [C], and resistance [R]) for frequencies up to a few MHz. It enables the non-destructive examination of charge injection and kinetics at the interfaces in multilayered devices.[131–134] For this purpose, an alternating voltage is modulated in small-signal behavior with a frequency range of kHz to some MHz onto a possible DC signal and the system response is measured. By knowing the amplitude and phase angle of the complex impedance, all the other AC impedance parameters, i.e. the capacitance and conductance, can be calculated.[135] Due to the large frequency range, processes that occur at various time scales can be monitored with high sensitivity.[136–138] The differential capacitance originates from the small voltage interference dV_{AC} but the additional voltage signal slightly deviates the measurement data.[139] The capacitance at the sample, or device under test (DUT) C_{DUT} in general, can be calculated by

$$C_{\text{DUT}} = \frac{I_{\text{DUT}}}{2\pi f V_{\text{AC}}} \tag{3.17}$$

with I_{DUT} is the current at the DUT, f is the test frequency, and V_{AC} the measured AC voltage.[140]

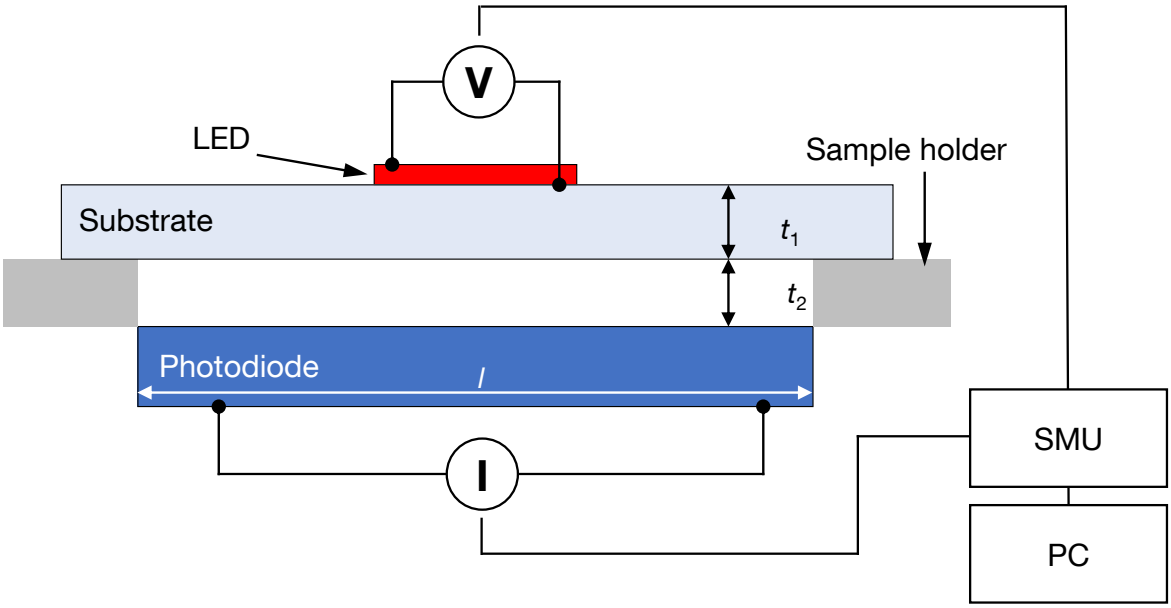

Figure 3.10 Schematic representation of the used photodiode measurement setup. The red highlited LED is sourced by a SMU at the top and bottom electrode. The light is emitted through the substrate and collected by the photodiode. t_1 and t_2 are the edge length of the quadratic LED and photodiode size, respectively.

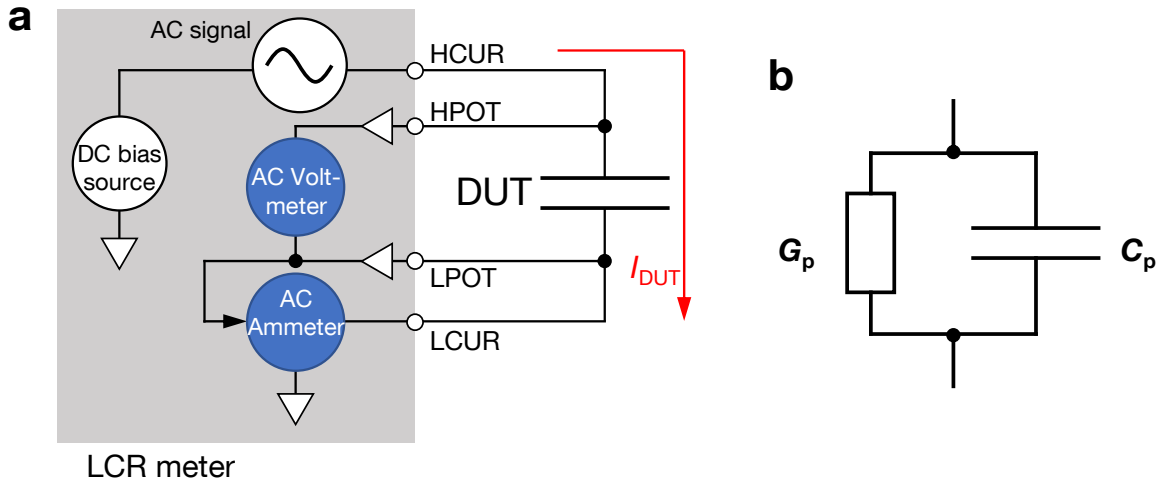

Figure 3.11 a) Principle of LCR measurements: The AC signal is applied at HCUR superimposed on the DC bias signal. The AC voltage is senses between HPOT and LPOT while the AC current is sensed at LCUR. b) Parallel capacitance and conductance model used in this work.

The simplified measurement circuit behind an impedance analyzer can be seen in Figure 3.11a). For the measurement of the AC impedance, the high current terminal (HCUR) supplies an AC voltage. The current and voltage of the device are measured by the low current terminal (LCUR) and the high and low potential terminals (HPOT and LPOT), respectively.[135, 140] Since the amplitude and phase of the output voltage and current signals are synchronized with the input signal, creating a phase-locked loop, any AC impedance parameter can be calculated. There are two common AC impedance models: the parallel model, where results are expressed as a parallel capacitance (C_p) and a parallel conductance (G_p), and the series model, where results are expressed as a series capacitance (C_s) and a series resistance (R_s) [135]. In this work, the parallel model illustrated in Figure 3.11b) was used.

In the conducted impedance measurements, a Keysight LCR Meter E4990A was utilized to sweep the frequency and DC bias while keeping a constant AC voltage to measure capacitance. An automated measurement script was created in Matlab to control the LCR meter and capture the recorded data in a standardized format for analysis.

4 Silicon Quantum Dot Light-Emitting Diodes

This chapter describes the operation of SiQD-LEDs after successful fabrication. Firstly, the principle of operation is explained, followed by the state of the art section that defines different structural influences on the SiQD-LEDs. After a chemical synthesis, the SiQDs are chemically characterized to ensure a suitable quality. The section is followed by the fabrication process of the SiQD-LEDs, whereby the quality of all individual layers is verified. Eventually, an exemplary measurement of a SiQD-LED is presented, and its electro-optical properties are discussed in the context of their performance and stability. This chapter is completed with a presentation of the long-term behavior and inverted LEDs.

4.1 SiQD-LED working principle

This subchapter described the functionality of a SiQD-LED in detail. As mentioned in chapter 2, SiQD-LEDs are a hybrid between organic and inorganic LEDs. Like an OLED, the SiQD-LED is made of several layers to transport the charge carriers into the SiQD layer. The design aims to confine the electrons and holes in the SiQD layer, where they can recombine under the emission of a photon. Leakage at the counter-electrode, where electrons reach the anode and holes the cathode, should also be avoided by choosing a suitable design. In this work, two HTLs and one ETL are used to build a well-working SiQD-LED. The structure from the bottom is ITO|PEDOT:PSS|Poly-TPD|SiQDs|ZnO|Ag and is shown in Figure 4.1. The light emission is through the bottom of the structure. The purpose of each layer and the working principle of the SiQD-LED are schematically illustrated in Figure 4.2.

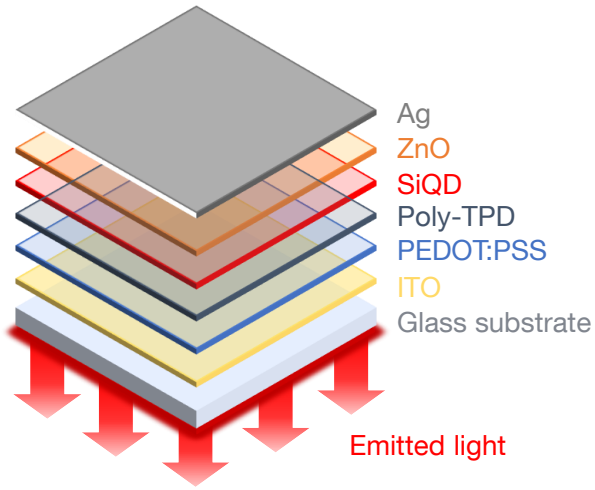

Figure 4.1 Illustration of the SiQD-LED structure. The light emission is directed through the bottom of the structure.

The working principle becomes clearer with the energy diagram in Figure 4.2. The energy levels of HOMO and LUMO of the individual layers are of significant importance for the device performance. The ITO anode is used as a transparent conducting electrode with a low work function of 4.7 eV and is used for hole injection of the LED. The following PEDOT:PSS layer eases the hole injection, smoothens out possible ITO roughness, exhibits high optical transparency, and prevents oxygen diffusion from the ITO into the next semiconducting polymer layer, Poly-TPD.[51] The Poly-TPD layer transports the holes towards the emitting SiQDs without any potential difference to the PEDOT:PSS layer. Poly-TPD with a mobility of

μ_h =2.1 $\times$ 10^{-3} cm^2 V^{-1} s^{-1} to 10^{-4} cm^2 V^{-1} s^{-1} is ideal as a HTL, while the low LUMO energy level of 2.3 eV can efficiently block electrons.[91–94] For this reason, it is also called EBL. On top, the emitting or active SiQD layer is deposited with a HOMO level of 5.7 eV and a LUMO of 3.8 eV.[46] SiQDs have a thin insulating organic layer around their crystalline QD, which is indicated as grey barriers in the figure. This small tunneling barrier exists between all SiQDs and decreases the charge transport. The ZnO layer is used for electron transport and hole blocking at the same time. ZnO exhibits a high electron mobility ($\mu_e \approx 2 \times 10^{-3}$ cm^2 V^{-1} s^{-1}) for good electron transport properties and a low HOMO level of 7.7 eV for hole blocking.[42, 46, 97] The LUMO level of 4.3 eV matches very well with the top silver cathode (4.3 eV).[141]

From Figure 4.2 it becomes clear that the high potential barrier for electron and hole blocking of 1.5 eV and 2 eV enables efficient blocking properties but also prevents charge carrier leakage through the device. This is important because Poly-TPD is also a fluorescent material and the blocking suppresses emission from the transport layer. All other potential steps for holes or electrons from the contacts and the high major charge carrier mobility enable easy charge transport towards the emissive layer without significant voltage drops within the device.

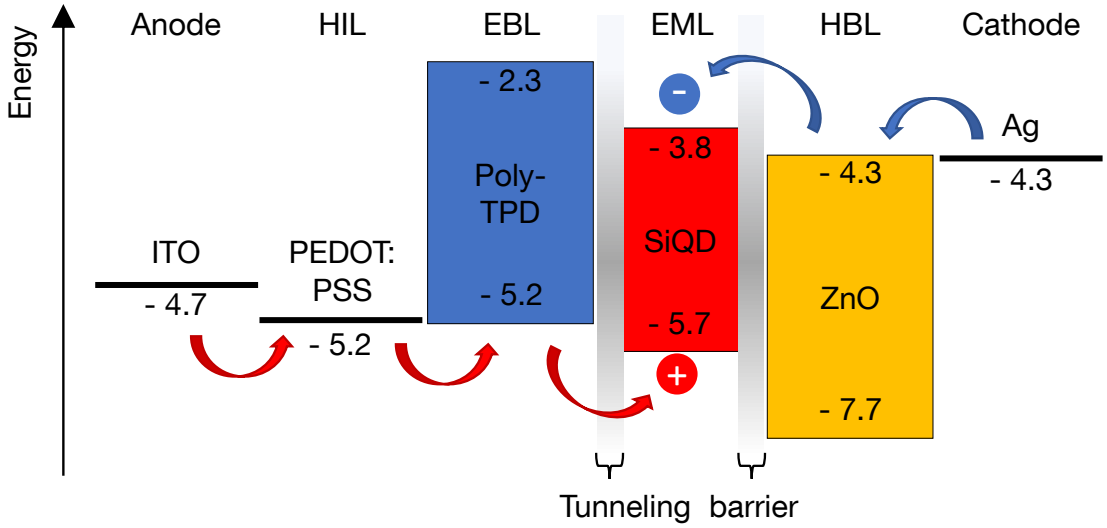

Figure 4.2 Working principle of a SiQD-LED. The HOMO and LUMO levels are indicated and the grey tunneling barriers are between every SiQD in the layer. Holes are injected at the ITO anode, while electrons are injected at the Ag cathode. Both become confined by the blocking layers in the emissive SiQD layer. The figure is adapted with changes and with permission from [99].

4.2 State of the art

Silicon as photonic material has been known for about 30 years and the first SiQDs were studied inside a passivating SiO_2 matrix.[37, 142] Colloidal SiQDs, i.e. freestanding, have been studied in a wide range of concepts, and in LEDs, the research interest is growing. The first near-IR SiQD-LED was presented in 2010 by Cheng et al. with an EQE of 0.6 %.[40] They exploited SiQDs functionalized with dodecene via hydrosilylation and with a size of ~5 nm. The fabricated LEDs showed side emission from the used transport layer MEH-PPV. In their follow-up study one year later, the highest reported peak EQE of 8.6 % was presented.[41] The SiQD were produced using a non-thermal plasma approach and a dodecene functionalization with a SiQD size around 5 nm. The emission wavelength was around 850 nm. Vacuum-deposited Alq3 was used as a hole blocking layer to facilitate recombination in the SiQD layer and suppress side emission.[41] The peak EQE was at a very low optical power of about 0.1 µW cm^{-2} in the infrared region. However, at high current densities, the emission shifted into the visible region and the EQE decreased below 1 %. The 3 nm big SiQDs, comparable to the used SiQD size in this thesis, also showed a high peak

EQE of 6.7 % at an emission wavelength of ca. 730 nm. Similar to the bigger QDs, their EQE falls to 1 % accordingly.

4.2.1 SiQD size impact

The SiQDs emission color can be tuned by the size of the SiQDs across the entire visible spectrum. [143] As a result, SiQDs should be available in all possible colors, but most SiQD-LEDs are in the orange to IR regime.[41, 100] The already mentioned study by Cheng et al., with 3 nm to 5 nm sizes was in the red to IR region.[40, 41] The emission wavelength shifted from 777 nm for the 3 nm SiQD size towards 853 nm for the 5 nm size. The same trend was observed by Puzzo et al., which used 1-decene functionalized SiQDs with sizes of 3.0 nm and 3.2 nm, and could observe a peak emission shift from 645 nm to 685 nm. Maier-Flaig et al. presented a more elaborated study with LED emissions from red to orange color. Allylbenzene capped SiQDs via hydrosilylation with sizes of 1.3 nm, 1.6 nm, and 1.8 nm have been used, while the different sized where achieved via size-separation methods.[49] The LEDs achieve different colors of 680 nm, 650 nm, and 625 nm respectively, which had additionally the positive side effect that the full width at half maximum (FWHM) could be reduced to $\sim$100 nm. Yamanda et al. prepared SiQD-LEDs with SiQDs sized of 2.7 nm, 2.2 nm, 1.9 nm, 1.7 nm, and 1.3 nm.[102] All SiQDs were passivated via hydrosilylation and 1-decene with EL peak emission from 755 nm for the biggest SiQDs to 590 nm for the smallest SiQDs. They observed a decreasing EQE for decreasing SiQD size and justified it with the lower PLQY for the smaller particles.[107] Even smaller SiQDs were used by Xin et al., which presented a SiQD-LED with broadband white emission from SiQD sizes of 0.8 $\pm$ 0.1 nm and 2.4 $\pm$ 0.4 nm, measured by DLS and TEM respectively.[144] Most of the LED emission (77.8 %) stems from the SiQDs themselves, but 20.8 % and 1.4 % come from the poly-TPD and Alq3 layers, which are used as HTL and ETL.

4.2.2 Additional transport and interlayer influence

The most classical approach to increase efficiency is to add additional transport or interlayers. Their task is to improve charge transport or to specifically block one type, either holes or electrons, of charge carriers. The energy level alignment (HOMO and LUMO) of the introduced layers is of importance. Most SiQD-LEDs use PEDOT:PSS in combination with ITO, followed by either Poly-TPD or PVK (poly(9-vinylcarbazole)) as HTL.[41, 46, 49, 100, 145] Liu et al. even used a combination from Poly-TPD and PVK, most likely to improve the electron blocking .[48] Other interlayers thinner than 10 nm have also an impact on the device performance, which has been presented by Gu et al., which introduced HAT-CN[1] and MoO_3 interlayers. A 3 nm thick MoO_3 layer improved the EQE from 0.9 % to 2.6 %.[42] Unwanted photon emission can originate from semiconducting transport or blocking layers. Cheng et al. presented unwanted orange emission of the MEH-PPV HTL under increasing currents as a result of poor charge confinement and electron-hole charge balance.[40] The side emission of multiple materials inside one SiQD-LED can also be used to combine their spectra, thus fabricating a different color LED. As an example, Ghosh et al. achieved white-light emission from a SiQD-LED by combining the red SiQD emission with the blue emission from the used HTL poly-TPD.[43]

Cheng et al. tested three ETL made of TCTA[2], Alq_3, and CBP[3] with electron mobility's from low to high ($<10^{-8}$ cm^2 V^{-1} s, $\sim10^{-6}$ cm^2 V^{-1} s, and $\sim10^{-3}$ cm^2 V^{-1} s)[146–148], which resulted in a peak efficiency range from 4.4 % to 8.6 % for Alq_3.[41] ZnO and TPBi[4] are another widely used ETLs, which yield EQEs of up to 6.2 % in the combination used by Liu et al. with PEDOT:PSS|Poly-TPD|PVK as a hole transport side and ZnO on the electron transport side.[43, 46, 48, 49, 101]

[1] Dipyrazino (2, 3-f:2' ,3 '-h) quinoxaline-2,3,6,7,10,11-hexacarbonitrile (HAT-CN)
[2] Tris(4-carbazoyl-9-ylphenyl)amine (TCTA)
[3] 4,4'-Bis(N-carbazolyl)-1,1'-biphenyl (CBP)
[4] 1,3,5-Tris (N-phenyl-benzimidazole-2yl) (TPBi)

4.2.3 Organic ligand influence

SiQDs are typically deposited from solution to enable cheap fabrication methods. To assure colloidal stability, a surface functionalization is needed.[38] Up to date, various alkyl chains with six[46] eight,[48] ten,[50, 145] and twelve[40, 41] have been functionalized to the silicon surface. Besides achieving colloidal stability, the surface group can improve the charge transport across the single SiQDs. Mastronardi et al. and Liu et al. used allylbenzene-capped and phenylpropyl ligands, which both belong to the conjugated polymers.[48, 149] The conjugation has the advantage that charge transport is enhanced in comparison to the insulating alky chains due to the interparticle $\pi - \pi$ interaction of the polymer.[48, 149] In Liu's study, they could enhance the optical power density of the SiQD-LEDs, due to the increased charge transport of the SiQDs compared to an octyl surface functionalization.[48] Mastronardi et al. directly measured allylbenzene-caped SiQDs' conductivity, which yielded a 9-time greater conductivity than the octyl-capped SiQDs.[48, 149]

Not only the influence of the functionalization but also the surface coverage has an impact on the device performance. The OLR method enhances the current density with less ligand coverage, as shown by Angi et al..[46] They could improve the EQE from $0.006\,\%$ to almost $0.02\,\%$ by using the OLR method instead the HS method.[46] The current density and irradiance increased while the turn-on voltage decreased with the OLR method compared to HS.

4.2.4 Influence of architecture and design

In normal LED designs, ITO serves as the anode and a metal electrode as the cathode. For inverted designs, this is reversed. Inverted design of LEDs or solar cells is common, as it improves the device stability due to the organic interlayer shielding with, for example MoO_3 from air.[101] Yao et al. presented the first inverted design for SiQD-LEDs in 2016.[45] They use ITO and Al as electrodes, but then the electrons are injected at the ITO and holes at the Al. For the hole transport TAPC[5] was used, while for the electron transport ZnO was used. Other groups used CBP as HTL in inverted design SiQD-LEDs.[101, 102, 150] Furthermore, a $10\,\mathrm{nm}$ thick MoO_3 layer before the top electrode was introduced in the studies to increase the work function of the electrode for better hole injection abilities. This MoO_3 combination with Al or Ag is widely used in inverted devices.[151, 152] To increase the work function of the ITO and improve the electron injection, a thin PEI (polyethylenimine) layer can be introduced. Yao et al. used a $2\,\mathrm{nm}$ thin PEI layer that boosted the EQE of the device from $1.1\,\%$ to $2.7\,\%$, which was possible through improved charge balance of electrons and holes.[45] Organic layers tend to degrade upon exposure to oxygen or humidity. Therefore, an all-inorganic approach was started by Ghosh and Shirahata, who used ZnO and WO_3 as ETL and HTL.[44] The inorganic device was able to maintain its EQE of $0.25\,\%$ without any encapsulation for 45 days under harsh conditions with $80\,\%$ humidity. Their approach might lead the way to very stable SiQD-LEDs desired for an industrial application.

4.3 Characterization of SiQDs

In the following, we present the characterization of the used SiQDs. The QDs were functionalized with a hexyl group via the previously mentioned OLR method, which results in lower surface coverage of the SiQDs. In this work, the SiQD synthesis, functionalization, and characterization have been performed by Elisabeth Groß of the chemistry department at TUM. Three main aspects of the SiQDs need to be analyzed in depth as they can alter the LED devices: i) the SiQD-size, ii) their successful functionalization, and iii) their optical properties for their utility in applications.

SiQD size The SiQDs are synthesized via thermolysis from HSQ and subsequently etched to freestanding SiQDs. A detailed description is already given in section 3.1.6. By this method, the etching time in HF

[5] 1,1-Bis[(di-4-tolylamino)phenyl]cyclohexan (TAPC)

controls the size of the QDs. For this reason, size control is an important measure to ensure consistent quality. After the synthesis, the functionalization is performed to passivate the SiQDs immediately. The mean diameter of a typical SiQD sample was determined by transmission electron microscopy (TEM) with a size of $3.5\,\text{nm} \pm 0.67\,\text{nm}$. The corresponding TEM image of hexyl functionalized SiQDs (SiQD-Hex) and the corresponding histogram is shown in Figure 4.3a,b). TEM analysis is widely used to measure the size of any QD, but it has its difficulties for functionalized SiQDs. The functionalized organic ligand might lead to increased SiQD diameter if no care at the size determination is taken. Furthermore, silicon itself gives a low contrast in the image due to its low atomic weight and the small QD size.[153] For this reason, a second method is utilized. Dynamic light scattering (DLS) reveals the hydrodynamic radius of $3.01\,\text{nm} \pm 1.51\,\text{nm}$ (Figure 4.3c)) for the SiQDs. In DLS, the hydrodynamic radius of the SiQDs is measured. The SiQDs are in solution and an incident light beam becomes scattered at the particles, which is measured and analyzed. As a consequence, the mean SiQD diameter is slightly different from the results obtained by TEM and given in a log scale.

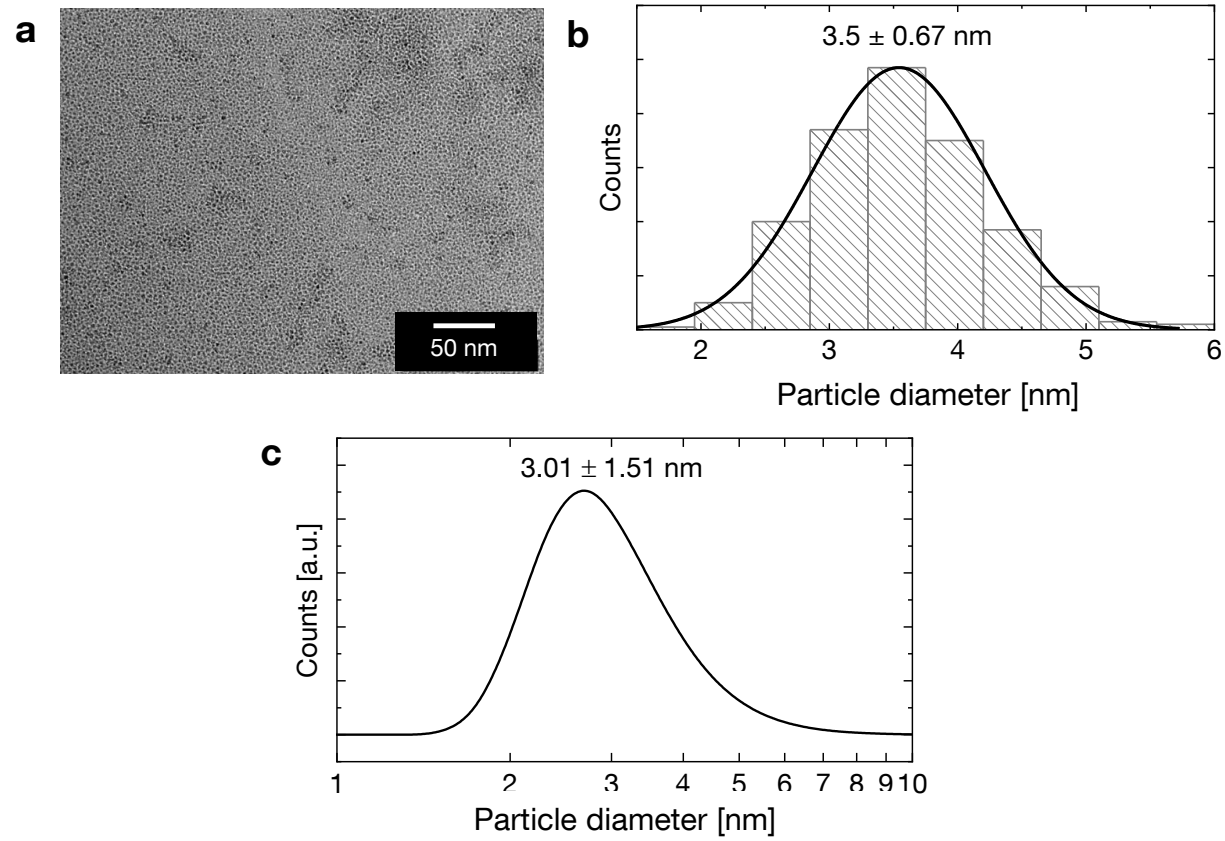

Figure 4.3 a) TEM image of SiQDs with a hexyl functionalization. b) Histogram of the size distribution of SiQDs from the TEM image in a). The measurements result in a SiQD mean diameter of $3.5\,\text{nm} \pm 0.67\,\text{nm}$. c) DLS measurement of the SiQDs, which results in $3.01\,\text{nm} \pm 1.51\,\text{nm}$. The Figure is adapted with permission from [99].

SiQD functionalization The functionalization of the SiQDs is needed to obtain colloidal stability, which is important if a solution-based fabrication method like spin-coating is used.[38] The successful functionalization of the SiQDs can be determined by Fourier transform infrared (FTIR) spectroscopy, where the IR absorption or transmission of a material is measured over a broad spectral range. Different bands in the molecule show peaks at a characteristic wavenumber. Such a transmittance spectrum is given in Figure 4.4a), which confirms the successful functionalization of the SiQD compound. The strong C-H stretching bands (ν(CHx)) at $2800\,\text{cm}^{-1}$ as well as the deformation bands (δ(CHx)) at $1400\,\text{cm}^{-1}$ indicate

the presence of the hexyl surface functionalization. The state of oxidation can be measured by the Si-O stretching band at $1050\,\mathrm{cm}^{-1}$, which is not very pronounced and only minor oxidation can be concluded from it. From the OLR method, some Si-H bands have to be present in the measured spectra. The Si-H stretching band is located at $2100\,\mathrm{cm}^{-1}$ and indicates the presence of the remaining H-termination at $50\,\%$ of the SiQD. Overall, only wanted bands could be detected, which indicates a good quality of the SiQDs with their hexyl functionalization. A detailed analysis of the absolute atomic ratio of the atoms could be provided by XPS (X-ray photoelectron spectroscopy) but lies out of the scope of this thesis.

SiQD optical properties Besides the successful passivation, the optical properties of SiQDs are important for the implementation into SiQD-LEDs. For this reason, the PL spectrum under UV excitation (365 nm, dark blue) was measured in solution. The PL spectra of the SiQDs in Figure4.4b) shows a peak emission maximum at $\sim 710\,\mathrm{nm}$ with a FWHM of $140\,\mathrm{nm}$. In the case of alkyl-capped SiQDs, the mechanism of bandgap emission dominates and results in a single peak as seen here.[38] The SiQD PL emission matches with the size-dependent PL emission maximum of $\sim 710\,\mathrm{nm}$ as reported by other research groups.[153, 154] In addition, the theoretical model of Parks et al. shows that the SiQD size is consistent with the bandgap emission.[155] A photograph of the red PL of SiQDs-Hex in toluene is depicted in Figure 4.4c) and confirms that the colloidal stability is ensured even with a low surface coverage below $50\,\%$ origin from the OLR functionalization method. The UV/Vis absorption spectrum is detected by measuring the broadband light of only the background and subsequently with sample interaction. At the wavelength where an optical transition is possible, the absorption increases. The quartz vial and solvent need to be taken care of. The UV/Vis absorption spectrum for the SiQDs is normalized to the signal strength of 300 nm. The absence of other absorption bands indicates that the sample is free of unsaturated substances or side products.

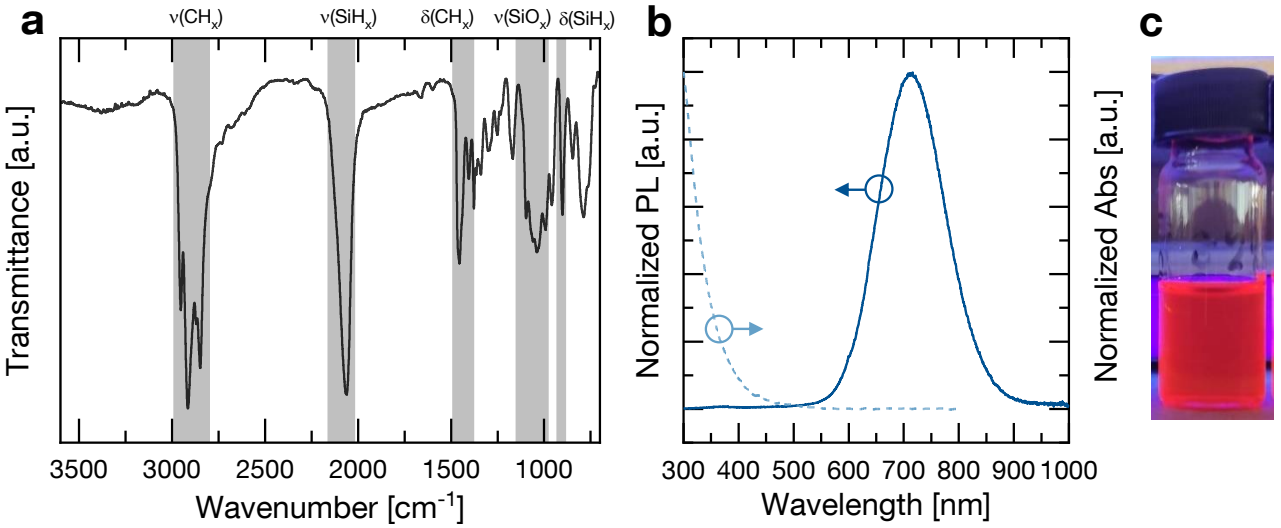

Figure 4.4 a) FTIR spectra of SiQD-Hex, which is normalized to the CH_x signal at $2920\,\mathrm{cm}^{-1}$ and all necessary bands are highlighted in grey. b) Normalized UV/Vis absorption (light blue) and PL spectra of SiQDs, which are measured in diluted form. The absorption starts at 450 nm, while the PL emission is between 550 nm and 900 nm.c) Photograph of the PL of SiQDs diluted in toluene under UV excitation. The Figure is adapted with permission from [99].

4.4 SiQD-LED fabrication

This section describes the SiQD-LED fabrication process schematically depicted in Figure 4.5. One sample exhibits six identical SiQD-LEDs with an area of 3 mm x 3 mm. After substrate cleaning, all layers are

spin-coated after each other with an annealing step in between, and the top electrode is evaporated to finish the device stack. After the fabrication, the LEDs are ready to be measured.

In general, for thin-film devices, for OLEDs or QLEDs in particular, cleanliness is an essential factor that should not be underestimated. Most defects and malfunctions of devices can be traced to some contamination through particles or agglomerates from the fabrication process as the devices are built from layers below 100 nm. Ideally, the LEDs are manufactured under cleanroom conditions to minimize environmental particle contamination. If this is not possible, all attempts must be made to reduce contamination. In our lab facilities, it was not possible to fabricate the SiQD-LEDs in a clean room environment. Nevertheless, a laminar flow box was used for processes at ambient conditions and a nitrogen-filled glovebox with high-efficiency particulate air (HEPA) filters (<0.2 µm) was used for inert conditions. Many contaminants stem from impure materials and for this reason, all solvents were either purchased as high-performance liquid chromatography (HPLC) grade or filtered with a 0.2 µm syringe filter.

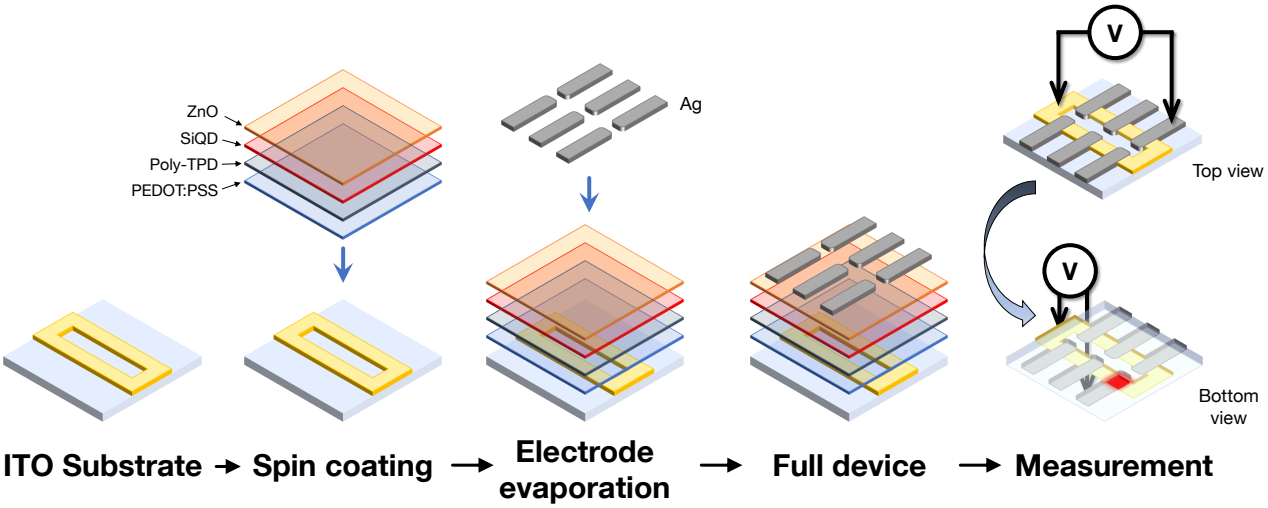

Figure 4.5 SiQD-LED fabrication scheme. After cleaning the ITO substrate, the individual layers of the LED became spin-coated. Afterward, the top electrode was evaporated with a shadow mask to define the LED area. The LED was later measured by applying a voltage.

4.4.1 LED design considerations

All devices were fabricated on a prepatterned ITO (15 Ω/□, 120 nm) glass substrate from Xinyan Technology LTD, which is depicted in Figure 4.6a). A shared ITO anode was utilized that is highlighted by the dashed line in the figure. This design approach caused some difficulties that needed to be taken into account while analyzing the LED data. As the distance from the anode contact to the LED pixel is changing for half of the LEDs, they exhibit a different series resistance, hence a voltage drop. The different voltages caused a variation in LED current, leading to a slightly varying irradiance and EQE. Also, the rather big device area of 3 mm by 3 mm caused a minor voltage drop at each LED pixel from the edges towards the center. Other groups used a much smaller design, which has the advantage that the probability of having a defect in the LED is lower. For example, Cheng et al. used a round LED design which was 1 mm in diameter. Due to the ITO thickness and the resulting step, there are edge effects with high E-fields.[51]

4.4.2 Substrate preparation

For quantum dot LEDs, the used substrates must be perfectly clean to avoid LED defects. These defects are mainly caused by absorbed water, organic impurities, and particles. We used a process where

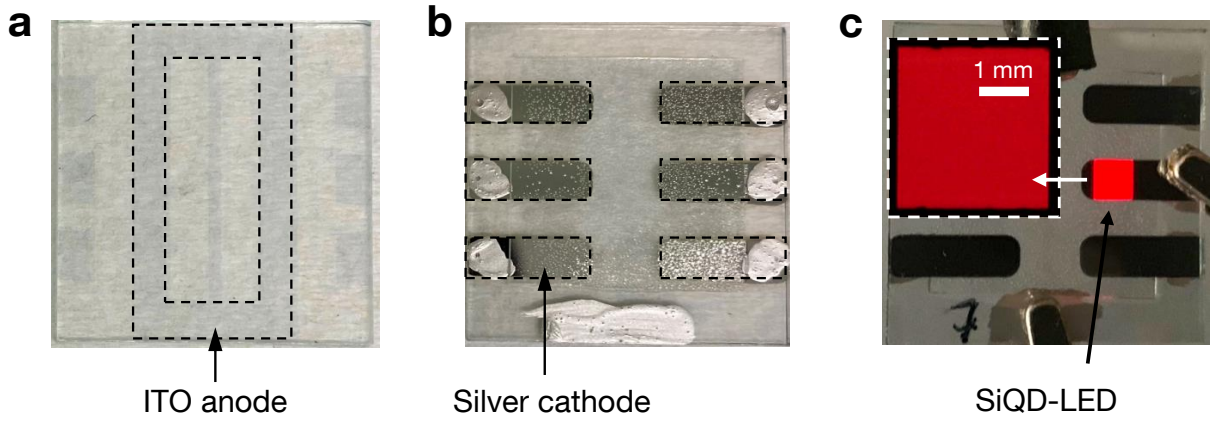

Figure 4.6 a) Photograph of the ITO substrate. The dashed lines highlight the shared ITO anode. b) Photograph of the finished SiQD-LED and the dashed lines highlight the silver cathodes of all six devices. c) Photograph of a turned-on SiQD-LED pixel. The Inset is a zoom of a SiQD-LED to show the high homogeneity of the LEDs.

those problems were minimized and the wettability was increased. In Figure 4.7 the used three-stage-process is illustrated. All washing steps were done inside a preheated bath sonicator. First, the substrates were washed for 10 min in Di-water and lab detergent to remove big particles. Before the samples were immersed in the acetone bath, they were rinsed again with clean Di-water since the washed-off particles remained inside the used beaker. Afterward, the substrates were transferred into acetone to remove any organic impurities on the surface for another 10 min. Acetone leaves stains on the substrates, and therefore, the substrates were transferred into HPLC grade isopropanol to wash away the possible contaminated acetone. After another 10 min in the sonication bath, the substrates were dried strains-free with pressurized nitrogen. To maximize the wetting of the cleaned substrates, we heated all substrates to a temperature of 140 °C for 2 min. This treatment increases the hydrophobic character of the surface, thus improving the wetability.[116] Due to the relative humidity in the laboratory environment, a water film can be adsorbed again on the surface after cleaning. The substrates were used shortly after cooling to room temperature to avoid this.

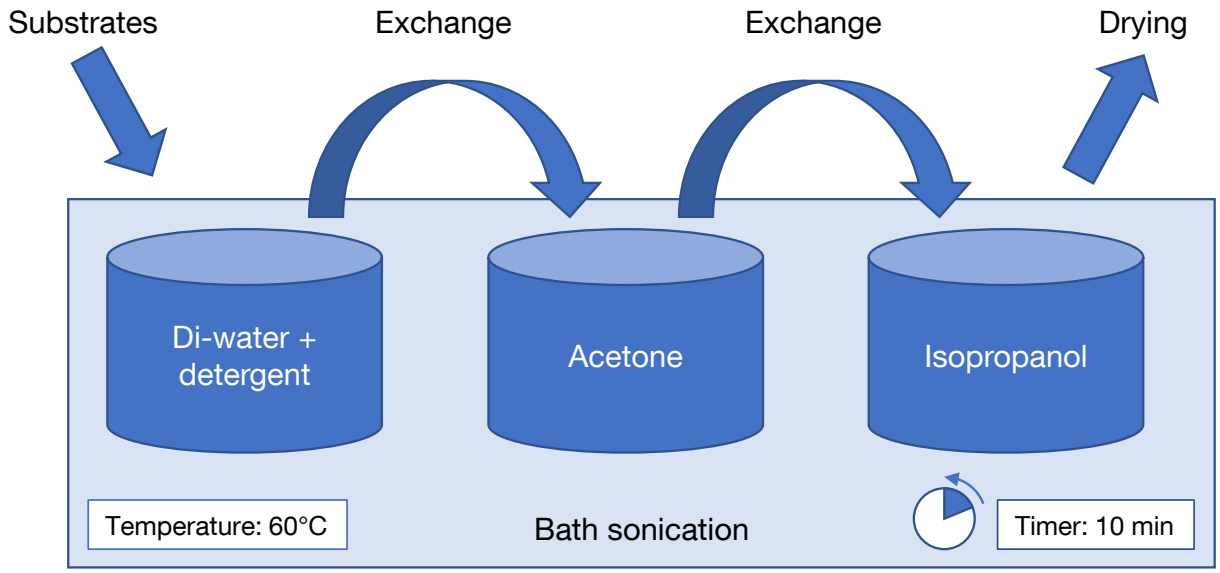

Figure 4.7 Schematic representation of the substrate cleaning process. Each cleaning step is left for 10 min inside the bath sonicator before the exchange. Figure adapted from [116]

There are many more surface activation techniques, such as an oxygen plasma or ozone treatment. However, we avoided those because the wetting of the first organic PEDOT:PSS layer was sufficient. Furthermore, the oxygen plasma treatment can change the work function of the ITO up to $0.5\,\mathrm{eV}$.[156] We measured a work function of $4.7\,\mathrm{eV}$ after cleaning the ITO surface, which is close to the work function of $4.8\,\mathrm{eV}$ measured by ultraviolet photoelectron spectroscopy (UPS) from the manufacturer. The difference can originate from different cleaning processes, which the manufacturer does not further describe.

4.4.3 LED layer deposition

Clean substrates are the basis of good device fabrication. After cleaning, the remaining layers were deposited from solution via spin-coating, and the top electrode was evaporated in a final step. The spin coating parameter are summarized at Table 4.1. Depending on the exact concentrations of the material solutions, the spin speed can vary from batch to batch to deposit the target thickness. All substrates were blown off with pressurized nitrogen just before spin coating to remove any dust particles that could have settled on the substrate during transport from the cleaning to the spin-coater. For the deposition of the HIL layer, PEDOT:PSS was diluted in isopropanol (1:3) and filtered by a $0.45\,\mu\mathrm{m}$ RC syringe filter prior to deposition. The mixing with IPA is important because it increases the wetting of the solution and allows to spin very thin films with a thickness of $20\,\mathrm{nm}$. After deposition and spinning of $\sim$70 µL PEDOT:PSS solution, each sample was annealed for $10\,\mathrm{min}$ at $140\,°\mathrm{C}$ in ambient conditions. This step was performed inside a laminar flow box with HEPA Filter $0.4\,\mu\mathrm{m}$ to minimize particle contamination. After the deposition and annealing, all samples were transferred into a nitrogen-filled glovebox for further processing. Although the glovebox has a HEPA filter (H13) for nitrogen circulation, contamination with other particles inside the shared glovebox could not be excluded. The $10\,\mathrm{nm}$ thick HTL Poly-TPD ($0.5\,\mathrm{wt}\%$, $\sim$50 µL) was deposited and annealed at $140\,°\mathrm{C}$ for $10\,\mathrm{min}$. Multi-layer spin-coating is difficult because the individual layers might dissolve the underlying layer. In the case of PEDOT:PSS, which is usually dissolved in water, other organic solvents are unproblematic.[51] If the same solvent or a similar is used, there might be issues with the bottom layer, for example a mixing at the interface. Afterward, the $35\,\mathrm{nm}$ thick SiQD layer was deposited and annealed at the same temperature and time. Spin coating of colloidal QDs is tricky because they tend to agglomerate while spinning, which results in so-called comets. That is especially the case for static spin coating, where the QDs can settle and the solvent starts to evaporate before any rotation is applied. For this reason, dynamic spin coating was used for the SiQD solution. The sample rotation was started and after three seconds of acceleration, the final spin speed was reached. At that moment, the SiQD solution was deposited in the center of the sample to achieve a homogeneous thin film without any agglomeration. On top, a $25\,\mathrm{nm}$ thick layer of ZnO nanoparticles was deposited by dynamic spin coating with $100\,\mu\mathrm{L}$. Both, The SiQD and ZnO solutions were filtered by a $0.2\,\mu\mathrm{m}$ polytetrafluoroethylene (PTFE) filter prior to usage. The Ag top electrode was thermally evaporated ($3\,\mathrm{Å\,s^{-1}}$, $< 10^{-5}\,\mathrm{mbar}$), defining the $3\,\mathrm{mm}$ x $3\,\mathrm{mm}$ device area by using a shadow mask. The $100\,\mathrm{nm}$ thick silver layer encapsulates the device and acts as a highly reflecting mirror to reflect photons emitted towards the silver layer, increasing the EQE. The PVD system was directly attached to the glovebox system to avoid material degradation. After the evaporation of the top electrode, a thin glass slide ($0.2\,\mathrm{mm}$) was glued on top of the SiQD-LEDs with an Araldite 2011 epoxy to minimize device degradation at ambient conditions. The two-component epoxy was hardened at $80\,°\mathrm{C}$ for $10\,\mathrm{min}$ inside the glovebox. The LEDs were transferred to ambient conditions where the bottom glass side was cleaned. Silver conductive ink was applied to the top electrode and the shared ITO electrode for better mechanical stability for the contact pins in the measurement setup. The ready-to-use SiQD-LEDs were measured after fabrication or stored inside the glovebox to avoid device degradation. A photo of a finished SiQD-LED is depicted in Figure 4.6b).

For the production of reproducible high-quality SiQD LEDs, all parameters must be precisely maintained. Therefore, quality control of the individual layers concerning their thickness, roughness, and optical properties is eminently important. This quality control is described in the following. The thickness of each layer is

Table 4.1 Material deposition table with the spin-coating parameter and the target thickness.

Material	Rotation speed [rps]	Rotation time [s]	Annealing (temp \ time)	Target thickness [nm]
PEDOT:PSS	50	30	140 °C \ 10 min	20 nm
Poly-TPD	67	30	140 °C \ 10 min	10 nm
SiQD	67	30	140 °C \ 10 min	35 nm
ZnO	50	30	140 °C \ 10 min	25 nm

controlled once every fabrication batch, while the other measures depend on the material itself and remain constant.

4.4.4 Thickness and morphology characterization

As already mentioned, the thickness is crucial for the devices. Varying thicknesses can lead to an imbalance between electrons and holes, thus decreasing the efficiency. Another effect is that the recombination zone might be shifted out of the SiQD layer, resulting in unwanted photon emission of for example, poly-TPD.

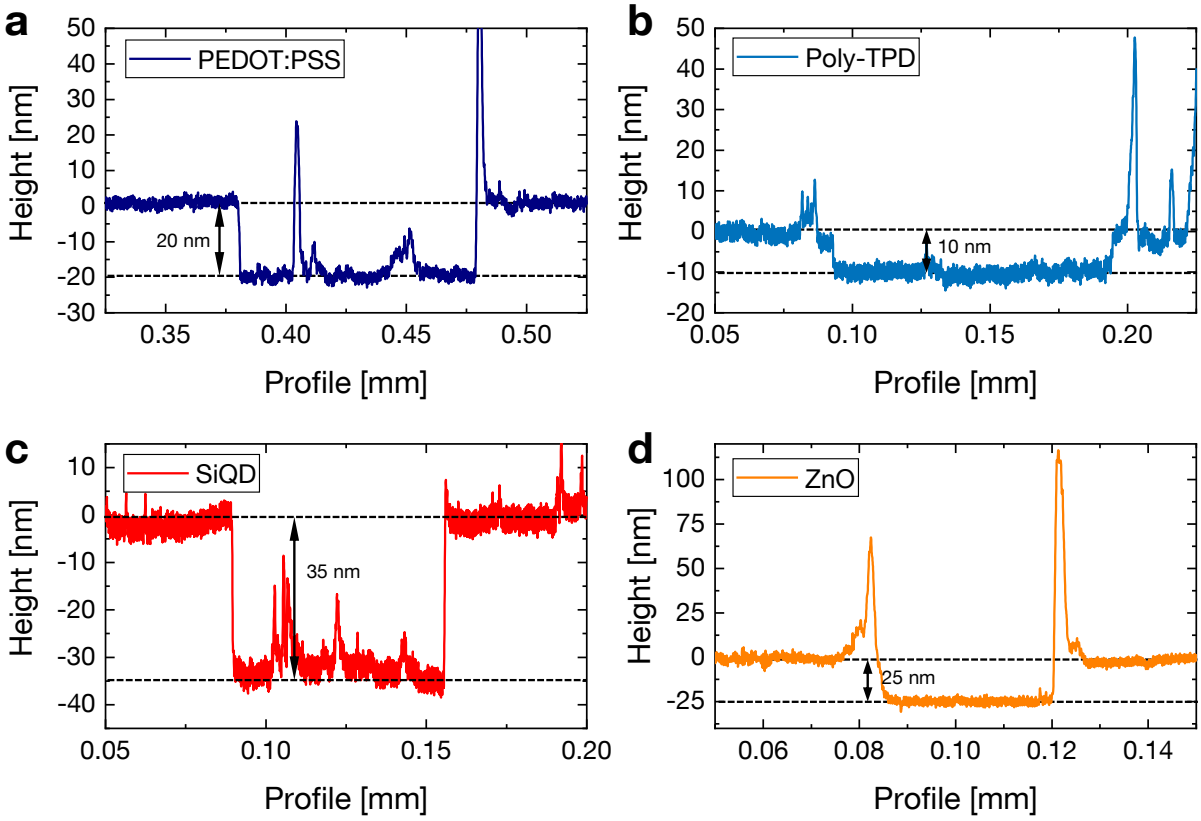

Figure 4.8 Thickness profiles of a) PEDOT:PSS, b) Poly-TPD, c) SiQD, and d) ZnO. The profiles are obtained by stylus profilometry as one example of the three measurements each. The Figure is adapted with permission from [99].

To confirm the correct thickness of each layer in the LED, reference samples were prepared and measured. Glass substrates were cleaned the same way as the ITO substrates of the LEDs to have the same surface properties. Afterward, the individual layers were spin-coated under the same conditions on a separate glass substrate. After the annealing of the reference samples, the layers were scratched and the

profile of this cut is measured as described in subsection 3.3.1. Care had to be taken not to damage the glass, as this would have falsified the thickness measurement. The thickness was monitored on at least three different spots on the sample (center and two sides) with a stylus profilometer and the mean value was taken. Exemplary measurements of each layer are shown in Figure 4.8. The scratch in every profile is about 40 µm to 100 µm wide and much bigger than the stylus tip of 2 µm. Therefore, the tip did not affect the measurements and correct height measurements were taken. The displaced material from the scratch typically caused the high side walls. For the measurement, the flat surfaces are compared and the difference gives the layer's height. Each profile a)-d) shows an acceptable match to the target thickness. PEDOT:PSS and the SiQD profile have some peaks in the scratch that origins from scratching could not be removed with pressurized nitrogen.

After checking the correct layer thickness, it is additionally needed to ensure that the surface roughness is good. For this purpose, the reference samples were further measured with an AFM. The AFM images were taken in tapping mode over an area of 5 µm x 5 µm and are presented in Figure 4.9. The full stack consisting of ITO, PEDOT:PSS, Poly-TPD, SiQDs, and ZnO has been measured to see how the total roughness of all layers was before the top electrode was evaporated. The root mean square (RMS) roughness of each layer was calculated with Gwyddion[158] and big particles (>15 nm, e.g., Poly-TPS bottom right corner) were excluded from the calculation. Overall, the roughness for the ITO, PEDOT:PSS, Poly-TPD, and SiQDs layer was smaller than 1.05 nm. The ZnO layer roughness was about double with 2.2 nm, which might be the reason for the comparable roughness of 2.45 nm for the combined stack. Overall, the images show an excellent uniformity for all layers and smooth out underlying roughness as expected from a solution processable materials.

4.4.5 Optical characterization

Not only is the morphology important for the SiQD-LED, but also the optical behavior of it, hence of the individual layers. Therefore, we measured the transmittance of all layers, as it allowed us to estimate the light escape probability into free space. The rest of the light becomes absorbed inside the LED layers. In Figure 4.10 all transmittance spectra of the LED are shown. As the EL spectrum has its peak emission around 700 nm, ideally, a high transmittance is achieved around that wavelength region. All layers showed a transmittance above 90 % at 700 nm, which is a rather high value and reaches towards a lower wavelength of around 450 nm. Nevertheless, the achieved transmittance resulted in a decreased LED performance because some emitted light becomes directly lost inside the LED and did not contribute to the LED performance. In addition, no light was absorbed from the high band gap HTL and ETL. Their absorption peak is indicated by the sudden decrease of the transmittance at around 400 nm and 380 nm, respectively.

The intensity attenuation could be estimated from the transmittance values for 700 nm. In the estimation, all other loss mechanisms, such as waveguides, reabsorption, etc., inside the LED were neglected. By multiplying the transmittance values from the individual layers below the emissive SiQD layer, the forward emitting intensity attenuation is calculated:

$$T_{\text{total}} = T_{\text{ITO}} \cdot T_{\text{PEDOT:PSS}} \cdot T_{\text{Poly-TPD}} \tag{4.1}$$

When we assume isotropic emission, half of the intensity passes through the bottom LED and the other half is reflected by the top silver electrode (for total reflection) and passes the full LED stack afterwards. By taking the bottom transmittance into account, the attenuation of half of the emission is 93.4 %. The other part is attenuated by the entire stack plus the ZnO layer, which results in 89.9 % and is the theoretical maximum.

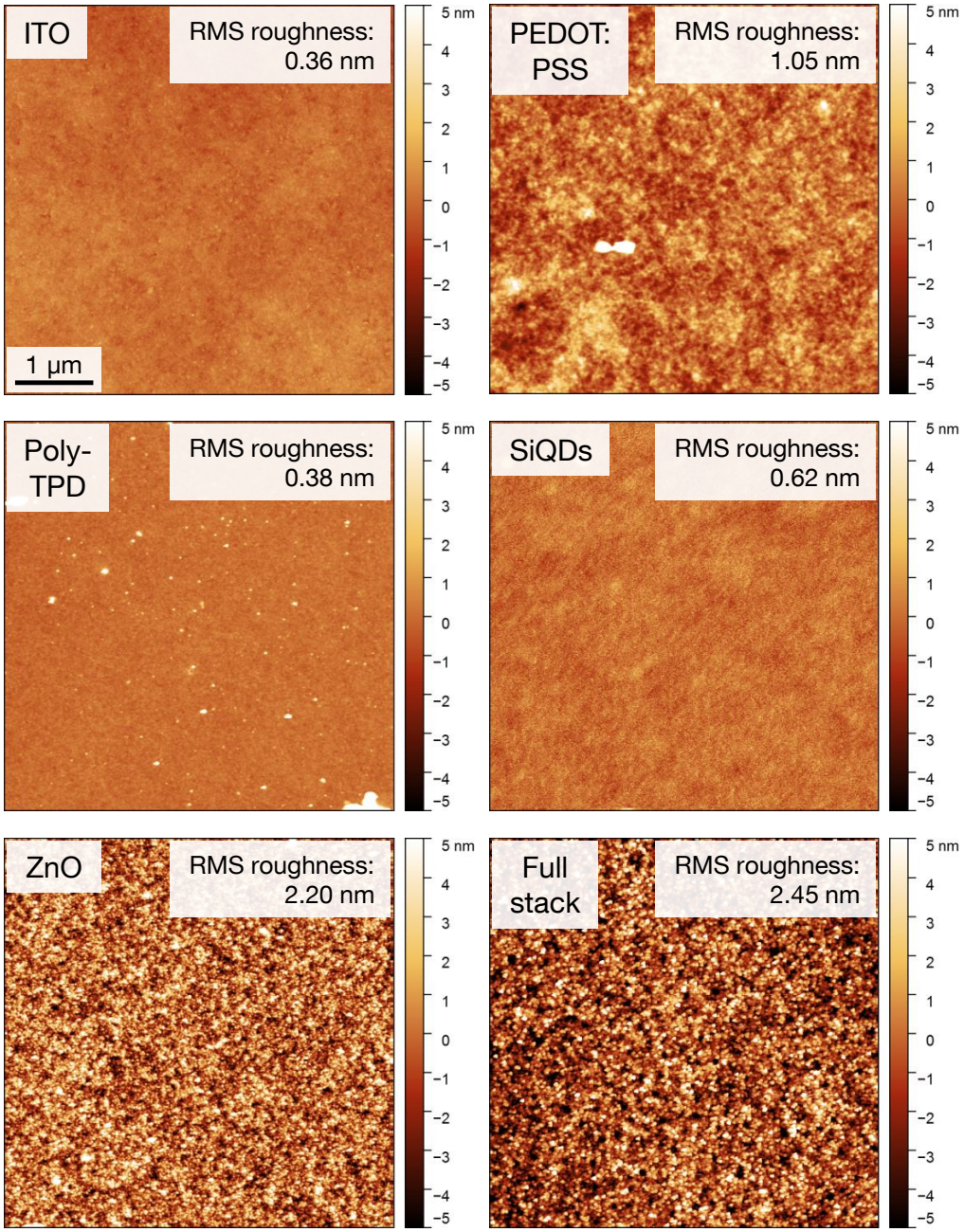

Figure 4.9 5 µm by 5 µm big tapping mode AFM images of each individual LED layer and the full LED stack without the top Ag electrode. The RMS roughness was calculated by excluding big particles >15 nm in the images. The scale bar in the ITO image also applies to all other images. Figure adapted with permission from [157].

4.5 SiQD-LED operation

In this section, the fabricated SiQD-LED was operated and measured. For the LEDs, the key parameters are the turn-on voltage, the maximum irradiance, the EQE, and the emission spectrum. To obtain all parameters, all fabricated SiQD-LEDs were measured one by one on the same day as they were fabricated.

In Figure 4.11, a typical measurement from the electro-optical measurement setup using a photodiode is presented. It allowed us to determine the performance of the LED from the current density (J-V) and the irradiance to calculate the EQE. In Figure 4.11a), the absolute current density as a function of voltage

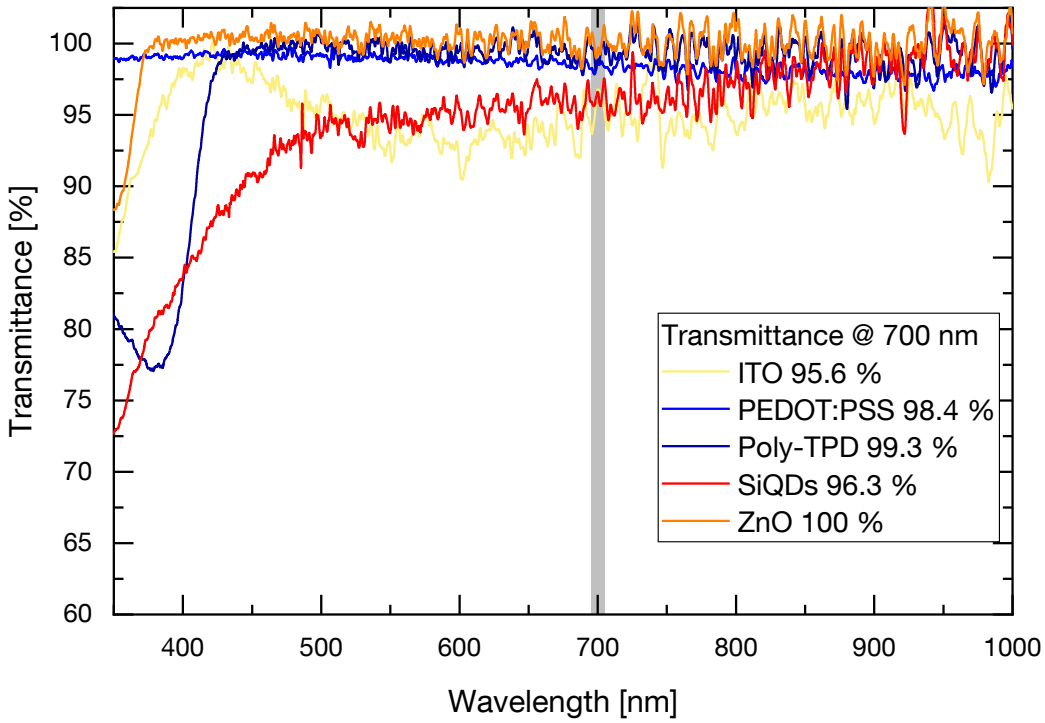

Figure 4.10 Transmittance spectra of all individual LED layers in the wavelength range from 300 nm to 1100 nm. The grey area highlights the wavelength at 700 nm ±5 nm and its mean values are given in the legend.

is plotted. In reverse bias direction, a leakage current below $10\,\mathrm{A\,cm^{-2}}$ was observed. In the forward direction, the SiQD-LED turned on at a voltage around 1.5 V, showing a nice LED current characteristic with current densities up to $1000\,\mathrm{A\,cm^{-2}}$. The downward sweep, in dashed line, drove less current than the forward sweep and showed a higher leakage current in the reverse direction. A possible mechanism for this behavior is the partial degradation of the SiQD-LED in the first measurement. Pinholes and agglomerates in the LED layers conduct more current than proper layers. Hence, the current is degrading on the back sweep. In the reverse direction, the defects cause multiple shunt paths, which increases the leakage current. The second sweep in red showed a reduced conductivity inside the LED. The irradiance of the SiQD-LED is shown in Figure 4.11b). In the reverse direction below 0 V, no emission from the LED was detected, as the injected charge carriers do not reach the active layer. In the forward direction, the SiQD-LED emission increased steeply with voltage, following the current curve and reached a maximum at ≈7.5 V. The inset shows the turn-on of the SiQD-LED at ≈1.5 V with very low irradiances below $0.1\,\mu\mathrm{W\,cm^{-2}}$. For high voltages above 7.5 V, the irradiance degraded after a maximum of $728\,\mu\mathrm{W\,cm^{-2}}$. The second voltage sweep of the LED did not reach the initial irradiance level. As mentioned for the $J-V$ curve, degradation of the LED is possible, especially when the LED is driven into such high voltages as 8 V. Figure 4.11c) shows the calculated EQE, from Equation 3.16, as a function of voltage. After a steep increase in efficiency, the SiQD-LED exhibited an EQE maximum of 0.69 % at 2.8 V. At the maximum EQE value, the irradiance was $52.3\,\mu\mathrm{W\,cm^{-2}}$. For higher voltages, the EQE decreases again towards a value of 0.1 %. The reverse sweep shows a more pronounced curvature, due to the more straight irradiance decrease. Similar to the irradiance was the second sweep lower in EQE.

However, this measurement is one out of a few hundred SiQD-LEDs fabricated and measured during this thesis. The EQE ranges between 0.1 % to 3.4 % with most devices around 1 %. Deviations in efficiency can have multiple reasons. One important factor is the quality of the used SiQDs. As all of the SiQDs, also the HSQ precursor were synthesized by Elisabeth Groß, deviations in the quantum dot QY can have a

big impact on the LED performance. Another factor is the organic ligand shell. When the functionalization of the SiQDs yields unpure educts, the charge transport is prohibited and the efficiency degrades. Bad quality SiQDs also result in a worse film quality after spin coating. Unclean solvents or agglomerates in the diluted material are causing many problems, such as fluctuating layer thickness or agglomerates.

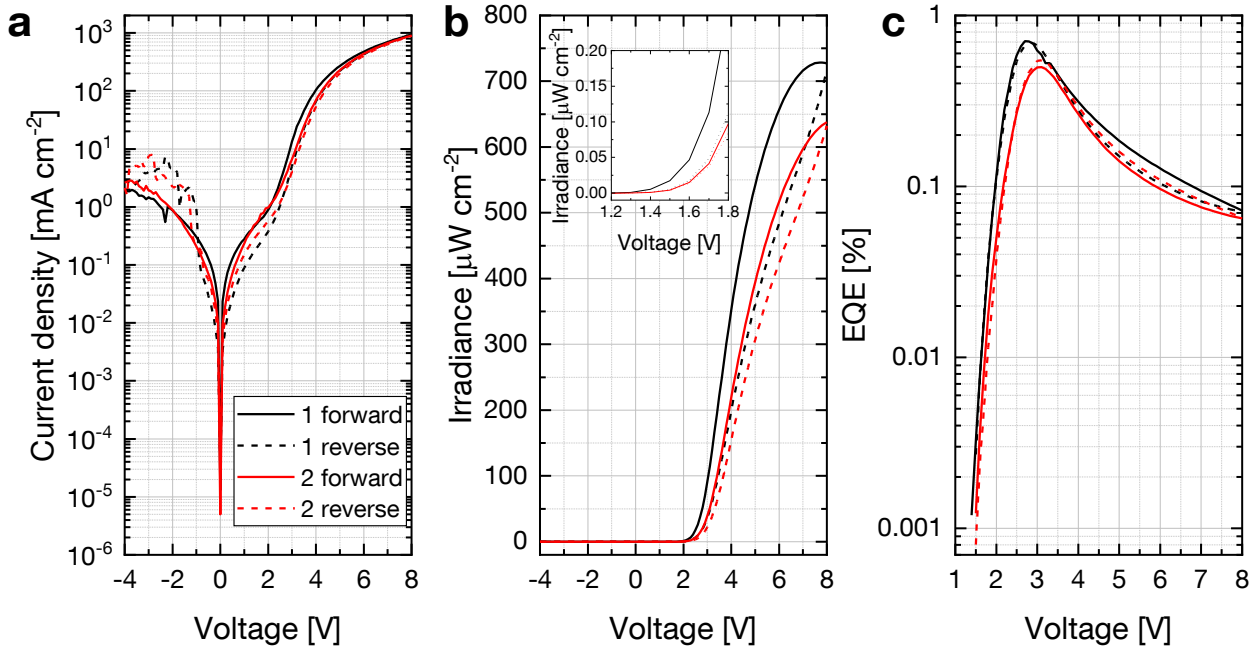

Figure 4.11 $J - L - EQE$ characteristic of a SiQD-LED. a) J as a function of voltage for two consecutive sweeps. The solid line indicates the forward sweep and the dashed line the reverse sweep direction. b) Irradiance plot from the same SiQD LED as in a). The inset shows the turn-on of the LED at around 1.5 V. for both sweeps. c) Calculated EQE of the SiQD-LED. After a steep increase, the maximum of 0.69 % is reached and afterwards, the EQE decreases with increasing voltages. The legend in a) applies to all three plots in the figure.

It is well known for SiQD-LEDs that the EL spectrum is shifting with increasing voltages.[100] In Figure 4.12a) an EL spectrum is plotted for increasing voltages, from turn-on until the peak emission. At the turn-on voltage, the EL emission peak was at 775 nm and blue shifts in wavelength to 735 nm at the maximum irradiance with an applied voltage of 5 V. The black arrow indicates the increase and the shift of the spectrum for increasing voltages. With the voltage, the current increased thus, more charge carriers recombined and as a result, the EL spectrum increased. The red arrow indicates the spectral shift, which is plotted in Figure 4.12b). At the initial turn-on value, no shift was observed, $\Delta\lambda = 0$, and while the peak shifts towards blue, $\Delta\lambda$ became more negative, i.e., shorter wavelength. This behavior is usually attributed to the SiQD-size distribution.[41, 100, 149, 159] For the used SiQD sample, a size distribution was observed by TEM images in Figure 4.3. The SiQDs exhibit different band gaps that determine the emission wavelength, where small SiQDs have a large band gap, and large SiQDs have a smaller band gap.[160] As a result, the SiQD-LEDs exhibited a broad emission spectrum with a FWHM ranging from 111 nm for the turn-on voltage, up to 128 nm at 5 V. The increasing applied voltage excites SiQDs from big to small and therefore, the spectrum broadens to larger energies, i.e., smaller wavelengths.[99] The obtained FWHM was in the same range from 100 nm to 150 nm that had been reported so far in SiQD-LED literature.[43, 100, 102]

Only the mean color, the irradiance, and the EQE of the whole LED can be obtained from the spectrum and the performance measurements. A complementary method uses a luminance camera to gain lateral information about the SiQD-LEDs. Figure 4.13a) shows a microscope image of a SiQD-LED at 5 V that exhibited good homogeneity. The LED appeared very uniform in color and intensity throughout the whole area. However, the image looked different if the LED was recorded with a luminance camera. Figure 4.13b)

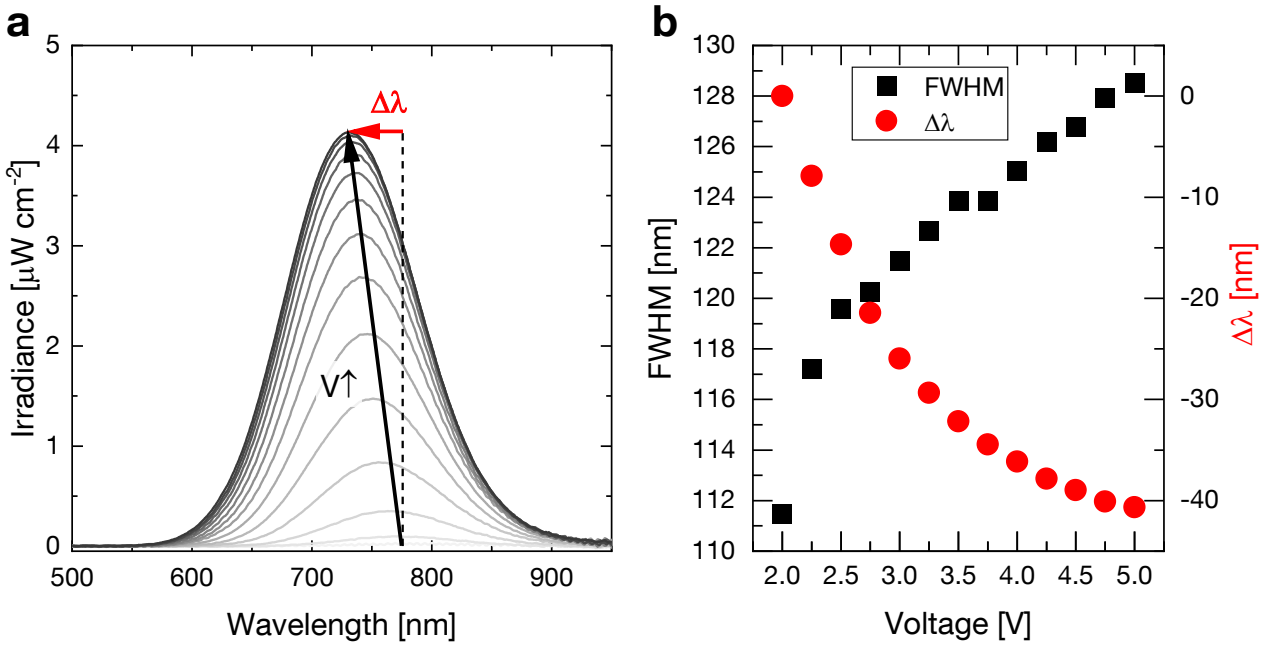

Figure 4.12 a) EL spectra of a single LED for increasing voltages. The higher the applied voltage becomes, the darker the line is printed. The EL peak emission shifts towards lower wavelengths, which is indicated by the red arrow $\Delta\lambda$. b) FWHM and $\Delta\lambda$ for the EL spectra in a). As the EL spectrum is shifting towards a lower wavelength with increasing voltages, the FWHM increases from 111 nm to 128 nm. The Peak position shifts up to 40 nm in the same voltage range. The figure is partially adapted with permission from [99].

shows the image generated by the luminance camera where the intensity decreased towards the center of the SiQD-LED, which is attributed to the voltage drop in the ITO anode. Additionally, there was very high emission at the LED edges or almost no emission around defects, e.g., agglomerates or particles. The deviation becomes even more evident if it is plotted as luminance deviation ΔL from the mean luminance in Figure 4.13c). The edges showed the highest deviation but also agglomerates revealed exciting behavior. From the shape of the so-called comets, one could determine the position of the LED on the sample during the spin-coating process. In this particular case, the rotation center was located on the right side of the LED. From this image, no information about the material can be made, which caused the agglomerates. The thicker material around the comets showed increased luminance. This can be explained as follows. When one or multiple materials are thicker in front of the particle, more current is conducted through it, which increases the emission in that area. The local high currents additionally caused the device to degrade faster in those areas, making agglomerates a good starting point for device failure.

4.5.1 Long-term stability

Lifetime measurements are eminent for industrial display applications. The SiQD-LED design has many organic materials, which can degrade with high currents. Therefore, alternatives for OLEDs are researched, and inorganic QDs become more recognized. Ghosh et al. presented an all-inorganic SiQD LED which could keep its initial EQE for 45 days.[44] Nevertheless, the efficiency was only $0.25\,\%$, which is outperformed by many other SiQD-LEDs.[48, 100] All the LEDs have in common that their surface is functionalized via the hydrosilylation method. As we use the OLR method, which enables higher currents, we compared SiQD-LEDs with both methods to see if the higher current degraded the LED faster.

In Figure 4.14, a long-term measurement is presented with hexyl functionalized SiQDs via OLR and HS method. Angi et al. used the OLR method for SiQD-LEDs and showed that the SiQD-LEDs drive more current, are therefore brighter, and are more efficient compared to the HS functionalized ones.[46] Larger

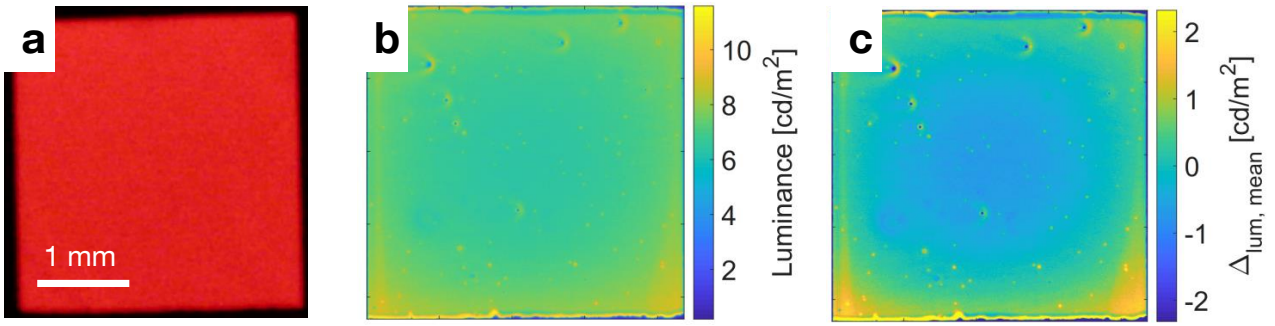

Figure 4.13 a) Microscope image of a SiQD-LED at 5 V showing a good homogeneity. b) Luminance image of the LED at 5 V reveals brighter emission at edges and corners. c) ΔL to mean luminance value of the SiQD-LED in b). The plot shows up to 2.5 cd m^{-2} luminance deviation at edges, corners, and pinholes from the mean value.

currents usually mean an increased risk of device failure due to increased temperatures caused by the Joule-heating. A relatively high current density of 111 mA cm^{-1} was applied to see an effect in a short time range. Figure 4.14 presents that the HS functionalized SiQDs degrade much faster than the OLR ones. The HS QDs reached 50 % of the output intensity after only 20 s. The OLR SiQDs, however, needed 120 s for 50 %. Both values are not very high and need much improvement for industrial applications. However, if the lifetime is defined until complete device failure, almost 10 h lifetime for the OLR SiQDs could be achieved. The HS SiQD-LED did stop working within a few minutes. Nevertheless, the lifetime is still not sufficient for display applications. The group of Maier-Flaig and co-workers performed size-separated studies with SiQDs, that showed improved lifetimes of over 40 h with a more homogeneous size distribution of the SiQDs.[100] They attribute the lifetime improvement to the mono-dispersed SiQDs and the more evenly distributed current. In contrast to the performed measurement in this thesis, they used a very low current density of 1.6 mA cm^{-2}, where the LED is barely turned on. In comparison, we used 111 mA cm^{-2} of applied current density in our measurement, where the LED is visible with bare eyes at ambient light conditions.

To illustrate the degradation effect of the SiQD-LED, we used a OLR functionalized SiQD-LED and applied a high bias of 6 V around the maximum irradiance. A time-lapse image series was performed and the photos in a time interval of 10 s are depicted in Figure 4.15. In the beginning, the LED already showed some dark spots, which might have come from dust particles or agglomerates in the fabrication step. Except for the spots was the emission evenly distributed on the entire LED, but a small comet was present in the center of the device. After 10 seconds, the LED looked already more grainy, and the emission intensity decreased noticeably. The comet in the center of the LED became more pronounced. After 20 s and 30 s, some areas in the center of the LED were no longer illuminated, which seemingly started at the present defects. For example, the areas with a high current density around the comet had higher temperatures and degraded faster. There are several point defects and the intensity is higher at the LED corners and edges than in the center. The Joule heating was enhanced through the high currents, degrading the LED faster than in other areas. After 40 s the dark area became even larger and after 60 s, most of the LED emission is gone. At this point, the LED was almost completely degraded. The LED is brighter at the emission interfaces to the dark spots due to the enhanced current densities there.

4.5.2 Inverted design

Most SiQD-LEDs use ITO as the anode in their device layout and Ag or Al as their cathode. Inverted design LEDs exhibit the ITO as cathode, which has some advantages over the "normal" LED design. Some of these advantages are e.g., lower driving voltages, longer lifetimes, and improved processing techniques for the top layers.[101, 161] For this reason we tested the inverted design, and we additionally tried to keep the same materials for the transport and blocking layers as for the normal architecture. Nevertheless, the

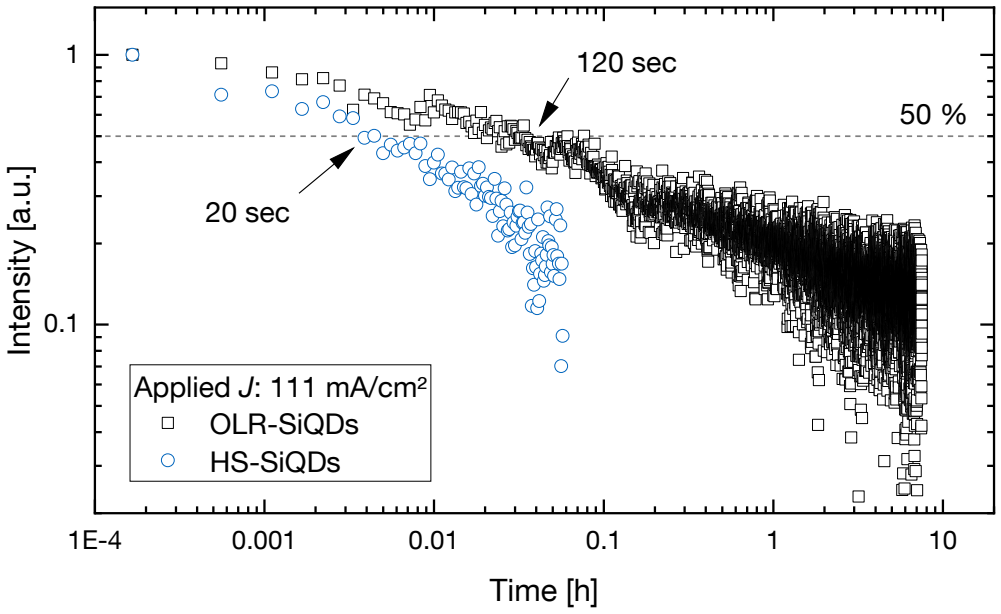

Figure 4.14 Long-term measurement with a constant applied current of $111\,\mathrm{mA\,cm^{-2}}$ for SiQD-LEDs with hexyl surface functionalization. The OLR functionalized SiQDs outlive the HS functionalized SiQDs 6-fold. The dashed line highlights $50\,\%$ of the initial irradiance.

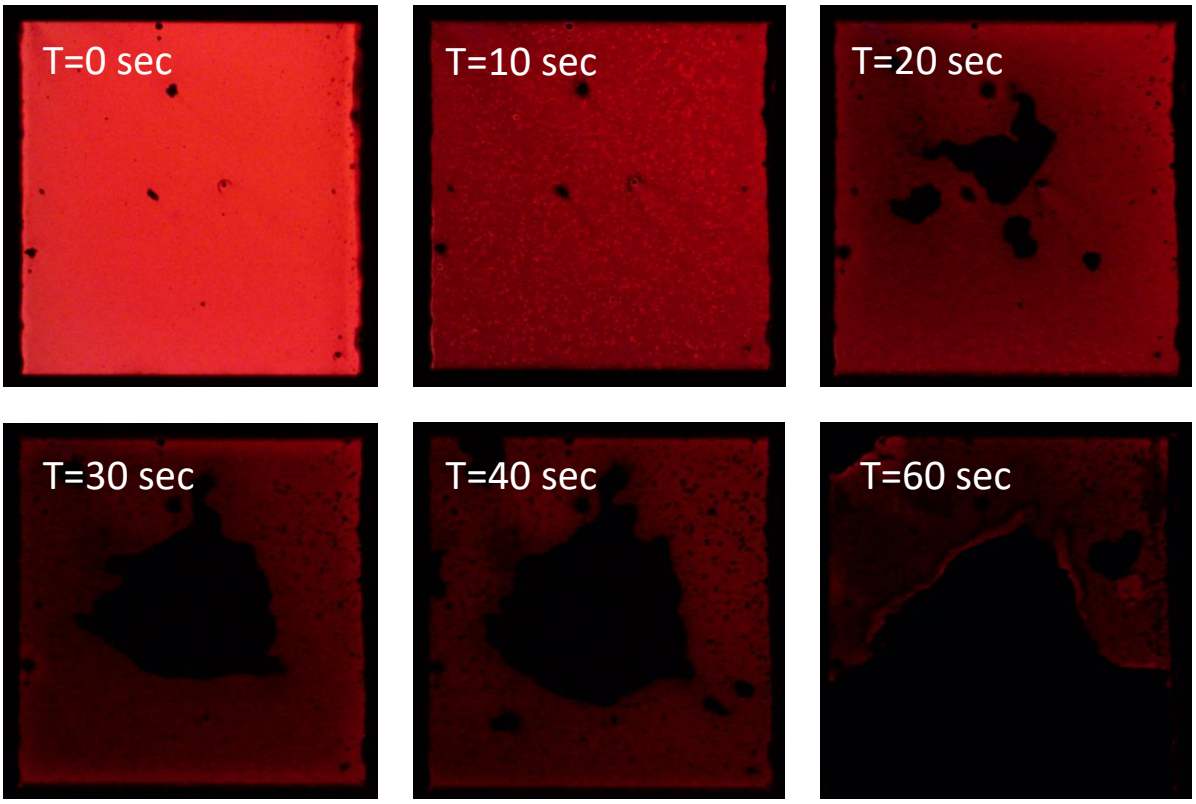

Figure 4.15 Microscope photos of a SiQD-LED at an applied forward bias of $6\,\mathrm{V}$. Each photograph shows the same LED at different times, which is indicated in the top left corner.

electrodes needed to be modified so that charge injection is increased. Usually, the anode has a high work function and the cathode has a low work function. ITO is an excellent transparent electrode and is kept in most inverted LED designs. To make it suitable for electron injection, the work function is modified, which is commonly done with branched PEI.[45] PEI introduces an intrinsic dipole moment on the ITO surface, thus reducing the work function up to $1\,\mathrm{eV}$.[152] Also other conductors can be modified by using PEI. Höfle showed via XPS measurements that the work function of ZnO can be shifted by $0.7\,\mathrm{eV}$ when PEI is spin-coated on top of the ZnO layer.[162] At the anode side, MoO_3 is commonly used to enable hole injection into the device and encapsulated by Al or Ag. [152, 163–165] The MoO_3 interlayer, with its very low conduction and valence band edges of $6.7\,\mathrm{eV}$ and $9.7\,\mathrm{eV}$, favors hole injection into the next layer by increasing the work function of the underlying layers to sufficiently high values.[166, 167]

In Figure 4.16, the proposed energy diagram of the developed design is presented. We decided to test PEI directly on the ITO to increase its work function as well as on the ZnO layer to build a small potential barrier next to the SiQDs to enable more recombination. We decided to use the combination with MoO_3 and Ag on the anode side. For efficient hole blocking and a smoother hole transition to the SiQDs, we test Poly-TPD and PVK. PVK has a bigger band gap which enables better blocking abilities, but at the same time, it has a lower hole mobility than poly-TPD.[93] As we fabricated multiple devices, all possible combinations are added to the diagram. For the fabrication, we used the layer combinations shown in Table 4.2.

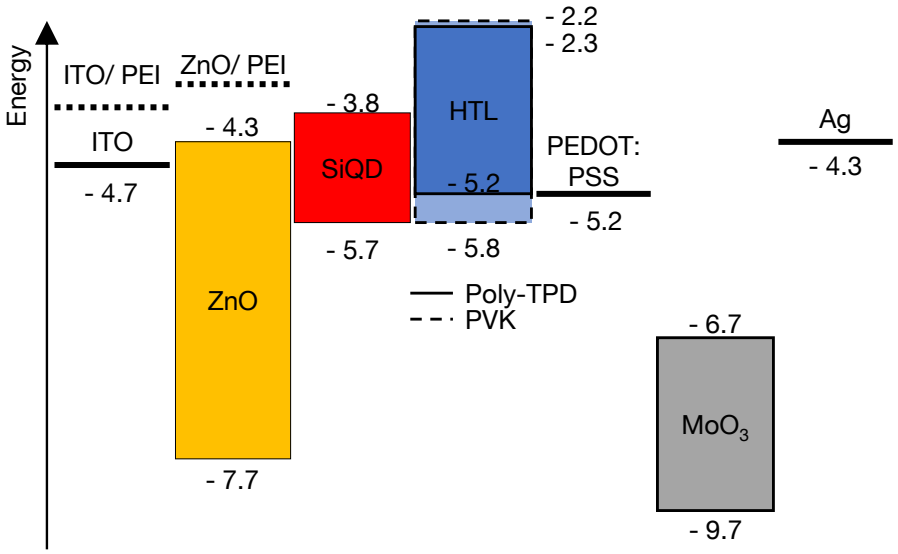

Figure 4.16 Proposed energy diagram of the inverted layout with all possible layers implemented. The fabricated device structure can be taken from Table 4.2.

Table 4.2 Inverted device layouts. The energy diagram can be taken from Figure 4.16.

LED Nr.	PEI	ZnO	PEI	SiQDs	Poly-TPD	PVK	PEDOT:PSS	MoO_3/Ag
1	•	•		•	•			•
2		•	•	•	•			•
3		•		•	•		•	•
4	•	•		•		•		•
5		•	•	•		•		•
6		•		•		•	•	•

Inverted LED fabrication The ITO substrates were cleaned with the same procedure as the normal SiQD-LEDs and directly transferred into the glovebox. Afterwards, the PEI layer was spun cast with 160 rps from a 0.1 wt% in ethanol solution to a 10 nm thick layer. After annealing for 10 min at 140 °C, the 25 nm thick ZnO layer was then deposited on top of the PEI layer or vice versa. After the ZnO layer, the emitting SiQD layer (35 nm,140 °C for 10 min) was deposited. For the inverted devices, we used two polymers, Poly-TPD and the wider band-gap PVK for the HTL and EBL. Poly-TPD was 10 nm thick, while the PVK layer had 20 nm thickness, both annealed at 140 °C for 10 min. The PVK thickness worked well in previous experiments, so we kept it unchanged. PVK was dissolved in DCB with a concentration of 10 mg mL^{-1}. A second HTL layer was deposited for two devices to ease the hole injection from the anode. In those cases, a 20 nm thick PEDOT:PSS layer was used to enhance the hole injection from the anode. Finally, the top electrode was thermally evaporated. The MoO_3 was deposited with a slow rate of 0.2 Å s^{-1} to 0.5 Å s^{-1} to a final thickness of 10 nm. Subsequently, the silver layer with a thickness of 100 nm was evaporated. Afterward, the LEDs were encapsulated with the same method as the normal ones and measured.

In Figure 4.17 the $J-V-Irr-EQE$ characteristics of all inverted devices are shown. In a), the $J-V$ characteristic is depicted, where the solid lines are the three devices with Poly-TPD, and the dashed lines are with PVK. The color of the lines indicates the same transport layer configuration as mentioned in Table 4.2. The PEDOT:PSS LEDs drive the most current through the device, which indicates a good charge injection on both sides of the contacts. The ZnO|PEI combination with PVK has some significant current drops, which most likely originate from local shorts, where much current can flow first and after burning through the current drops. In b), the irradiance is plotted and again, the PEDOT:PSS devices showed the highest irradiance of up to 59 µW cm^{-2}. All other devices reached values below 10 µW cm^{-2}. Further, the different turn-on voltages are well visible. The PVK device's turn-on voltage was shifted towards higher voltages than the Poly-TPD devices. This voltage shift is due to the lower hole mobility of PVK (2.5×10^{-6} cm^2 V^{-1} s^{-1} to 1×10^{-4} cm^2/V/s).[93] The combination with PVK, ZnO, and PEI showed the highest turn-on voltage, but this might originate from the shorts and, therefore, non-perfect charge confinement within the LED layers. In Figure 4.17c) the EQE is depicted in log scale as a function of the applied voltage. All EQEs remain below 0.04 % where the ZnO|PEI device has the highest EQE. The PEI|ZnO devices are the worst with 2×10^{-4} % to 3×10^{-4} %. The high stability of the EQE for the PEDOT:PSS devices might appear due to the improved charge balance and reduced exciton quenching.[168]

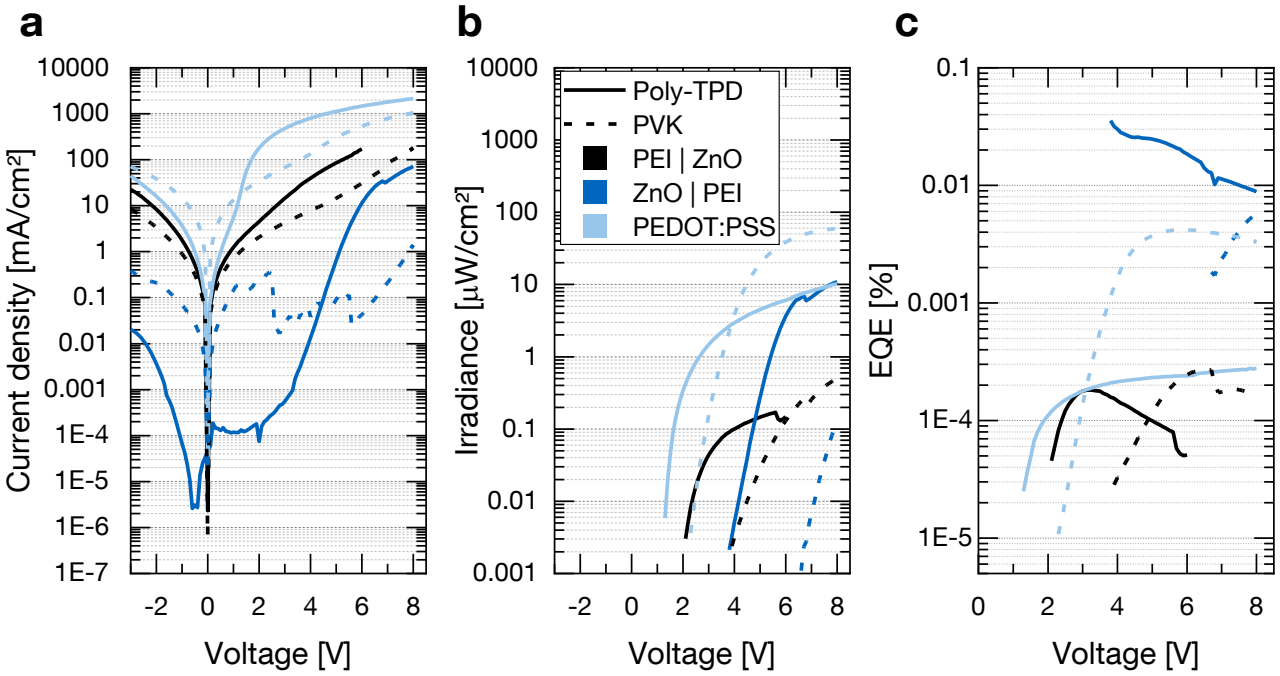

Figure 4.17 a) $J - V$ characteristic of the inverted SiQD-LEDs. The solid lines represent the Poly-TPD LEDs and the dashed lines the PVK LEDs.

5 Surface Engineering of SiQDs for LEDs

A major advantage of SiQDs is the well researched and established surface chemistry, allowing researchers to functionalize many different molecules onto the silicon surface. Organic ligands are essential for SiQD-LED fabrication because they ensure colloidal stability.[169] The most drastic effect of a surface functionalization is most likely the change of the emission color, presented by Dasog et al..[38] Other ligands like conjugated molecules can improve the charge transport, but most groups use alkyl groups of various length.[40, 46, 48, 50] It is well known that the charge transport between the SiQDs is limited by the tunneling through the insulating alkyl ligands.[170] On one side, the ligands are necessary to ensure colloidal stability, but on the other side, they limit the charge transport between the SiQDs, making them undesirable. Attempts have been made to remove the ligands of other QDs after deposition by burning them away but the practical aspect in a multi-layer device is very limited.[171] For this reason, an in-depth study on the effect of alkyl ligand length is needed but lacking in the literature. We investigated the length effect of alkyl ligands by analyzing three different alkyl chain lengths, hexyl, octyl, and dodecyl (C_6, C_8, and C_{12}) as SiQD surface functionalization. All of them have been widely used in SiQD-LEDs, but a comprehensive study is missing.[40, 46, 48] We used the standard stack layout and varied the organic group in the LEDs to see the length effect. The results of this investigation were published in the journal *Advanced photonics research* with the title 'Surface Engineering of Silicon Quantum Dots: Does the Ligand Length Impact the Optoelectronic Properties of Light-Emitting Diodes?'.[99]

5.1 Chemical analysis of SiQDs with hexyl, octyl, and dodecyl surface ligands

For a good comparison of the three different LEDs, the different SiQDs must be of equal quality. Therefore, the functionalization quality of the SiQDs was controlled by FTIR, thermal gravimetric analysis (TGA), PL, and absorption measurements to verify the successful functionalization combined with low oxidation and the same QD size. The SiQDs were synthesized the same way described in section 3.1.6 and functionalized with the OLR method.

5.1.1 Fourier-transform infrared spectroscopy

By the use of FTIR spectroscopy, the successful functionalization of each surface ligand and the degree of oxidation can be tested. However, only the functionalization's presence and quality can be confirmed, not the amount on the SiQDs. In Figure 5.1, the obtained transmittance spectra of all three SiQD compounds are presented. All spectra were normalized to the CH_x signal at $2920\,\mathrm{cm}^{-1}$. This allows us to make relative statements about the strength of the individual peaks. The grey areas highlight the important modes in the measurements. The presence of the alky chains were indicated by the strong $C-H$ stretching bands ($\nu(CH_x)$) at $2800\,\mathrm{cm}^{-1}$ as well as the deformation bands ($\delta(CH_x)$) at $1400\,\mathrm{cm}^{-1}$. In all three samples, only minor oxidation was observed at $1050\,\mathrm{cm}^{-1}$ via the $Si-O_x$ stretching. The relative intensity of the $\nu(Si-H_x)$ stretching band ($2100\,\mathrm{cm}^{-1}$) decreases from hexyl to dodecyl due to longer chain lengths. Longer chains like dodecyl need more space and prevent functionalization in the immediate surrounding area.

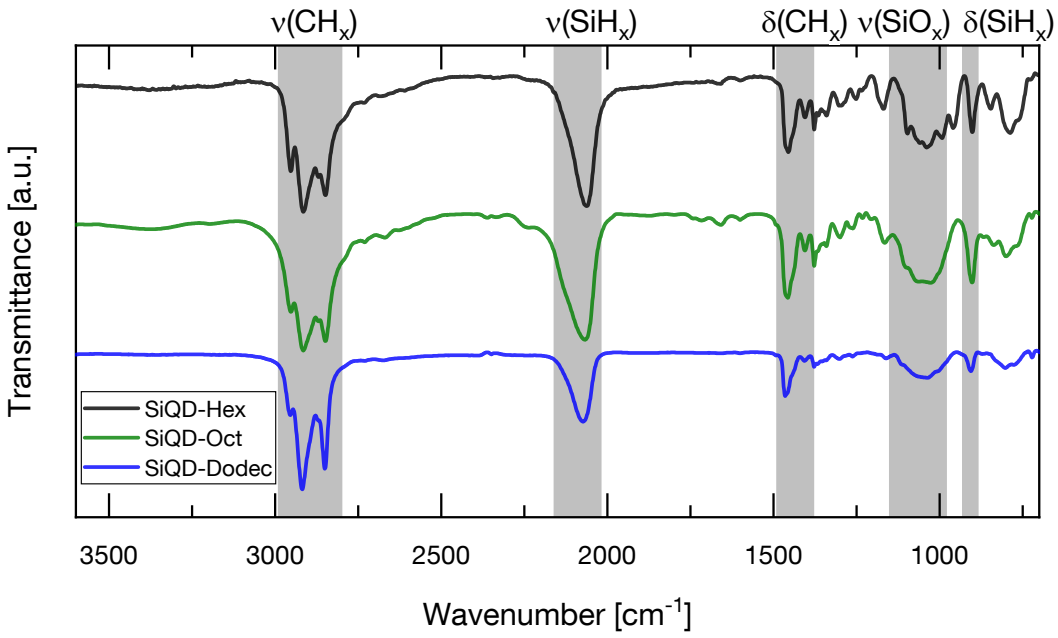

Figure 5.1 Normalized FTIR spectrum of hexyl, octyl, and dodecyl functionalized SiQDs to the CH_x signal at $2920\,cm^{-1}$. The gray area indicates the corresponding bands, which are named above. Only minor oxidation at the $Si-O_x$ stretching is observed for all samples. The relative intensity of the Si-H stretching is decreasing from SiQD-Dodec to SiQD-Hex. The Figure is reprinted with permission from [99].

5.1.2 Thermal gravimetric analysis

TGA measures the weight of a sample over time while heating it at a known rate. As the chamber heats up, the SiQD sample's organic parts burn away. By operating in an inert atmosphere, no reaction can occur, leaving the inorganic sample behind. The TGA measurements were carried out inside a glovebox with a heat rate of $10\,min^{-1}$ from 30 °C to 750 °C under an argon flow of $20\,ml\,min^{-1}$. The measurement results are presented in Figure 5.2. While heating the sample, the removal of the organic ligands was observed between 250 °C to 400 °C for all three functionalized samples, i.e. SiQD-Hex, SiQD-Oct, and SiQD-Dodec. The H-terminated reference sample showed only minor mass loss across the whole temperature range because SiQD-H does not have an organic shell. The mass loss of $5\,\%$ can be explained by minor solvent residues in the sample preparation process. According to the theory, the long chain lost more weight than the shorter ones. SiQD-Hex and SiQD-Oct showed a relative mass loss of $24\,\%$ and $25\,\%$, whereas SiQD-Dodec lost $41\,\%$. Minor solvent residues can again explain the small discrepancy between the short SiQD-Hex and the SiQD-Oct sample.

In the following step, the surface coverage was determined by combining the TGA results with the computational model by Avarmov et al..[172] From the OLR functionalization method a theoretical maximum of $50\,\%$ surface coverage is possible.[46, 47] SiQD-Hex and SiQD-Dodec exhibit a surface coverage slightly above $40\,\%$, whereas the lowest surface coverage of $33\,\%$ is determined for the SiQD-Oct sample. These results are lower than the aforementioned maximum surface coverage of $50\,\%$ due to steric hindrance.[173]

5.1.3 UV/Vis and PL spectroscopy

PL spectroscopy was conducted using an Avantes AvaSpec 2048 spectrometer, coupled with a Prizmatix light source ($365\,nm$ excitation) and an Avantes CUV-FL-UV/vis cuvette holder. A quartz cuvette with diethyl ether as a solvent was used for the measurements. The PL spectra in Figure 5.3a) showed an almost identical peak emission for all three ligands at $710\,nm$. The same peak emission confirmed that the

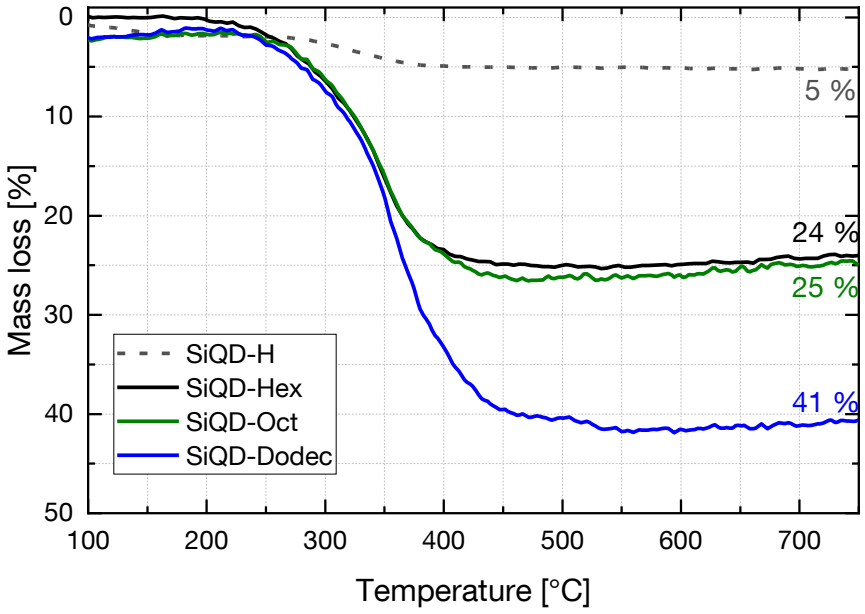

Figure 5.2 TGA of SiQDs without, SiQD-H, and with surface functionalization, SiQD-Hex, SiQD-Oct, and SiQD-Dodec. The H-terminated quantum dots lose almost no mass while the mass loss increases with weight from 24 % up to 41 %. The figure is adapted with permission from [99].

different length alkyl functionalization introduced no wavelength shift. The minor difference of a few nm might also come from a minimal size variation of the SiQDs during the etching process. Overall does the PL emission was consistent to other groups with a SiQD size of 3.5 nm $\pm$ 0.67 nm which was determined by TEM in section 4.3.[153, 154] The FWHM is $\sim$140 nm for all samples and shows the big size distribution of the SiQDs. UV/VIS-spectroscopy was conducted within the 200 nm to 800 nm range and normalized to the signal at 300 nm. The normalized spectra are depicted in Figure 5.3b). The absorption is the same for all three kinds and strongly decreases with wavelength. At 450 nm practically no absorption is present. The featureless absorption shows no contamination of the sample, which would be visible if other absorption bands would be present.

5.2 SiQD-LED electric-optical characterization

In this subsection, we investigate the influence of the ligand's length on the performance of the SiQD-LEDs. For this reason, three identical LEDs were built, in which only the surface functionalization of the SiQDs was modified. As a consequence, the impact of the ligand length can be directly compared. The SiQD-LED performances were measured with the integrating sphere setup to have, within one measurement, information about the power output and the EL spectrum. In total, we investigated thirteen SiQD-Hex LEDs, seven SiQD-Oct LEDs, and five SiQD-Dodec LEDs to account for sample variation and have a statistically more relevant data set. The different number for the three functionalizations is due to the fact that through fabrication issues, some SiQD-LEDs could not be used for the analysis. The increasing ligand length made it harder to achieve homogeneous film thicknesses, as they caused much more agglomeration and comets than the short hexyl chain. For example, the spin coating probabilities of SiQD-Dodec are much worse than the shorter ligands; therefore, the active layer tends to agglomerate during spin coating. The effect of enhanced agglomeration in the finished SiQD-LED and an image of such a SiQD-Dodec reference layer is depicted in Figure 5.4. Consequently, the unusable samples were sorted out as they could not be compared.

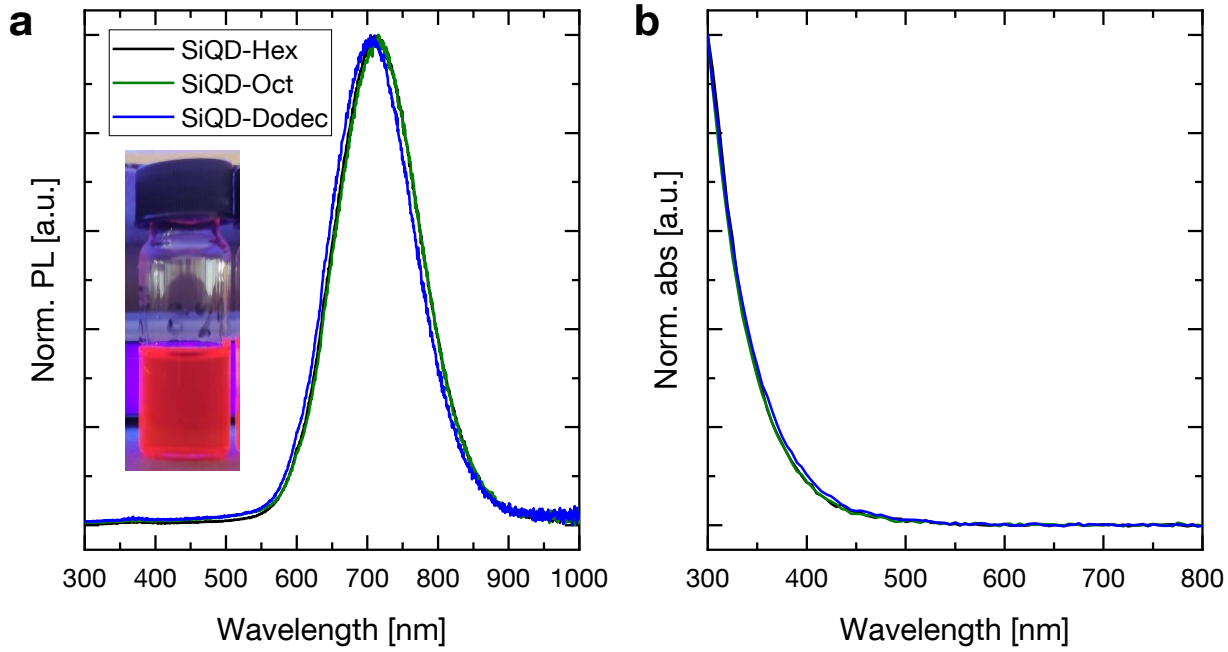

Figure 5.3 a) PL emission spectrum and b) absorption curve of SiQDs in diethyl ester. The PL emission peak of all three SiQD kinds is at around 710 nm. The featureless absorption decreases for wavelength below 400 nm. The legend of a) applies also to b). The figure is adapted with permission from [99]

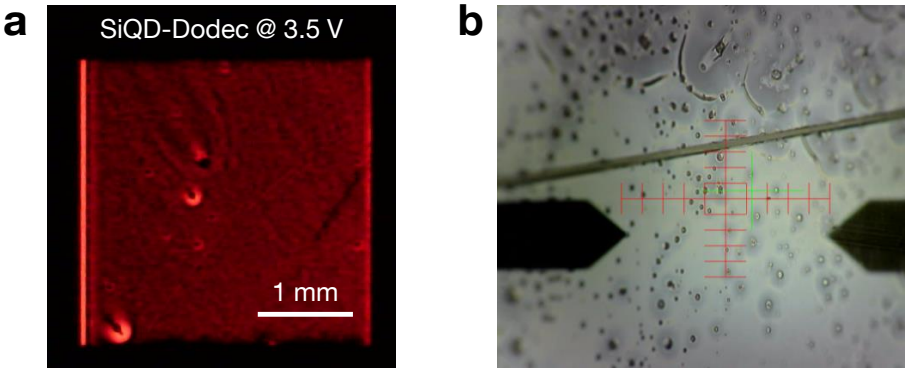

Figure 5.4 a) Photograph of a SiQD-Dodec LED with clearly visible defects from the fabrication process. b) Image of the SiQD-Dodec reference layer at the stylus profilometry. The agglomeration is clearly visible throughout the whole image.

The $J-V-Irr-EQE$ measurements were summarized in Figure 5.5. In a) and b), the mean value was calculated and plotted by the line, whereas all single data points are shown in the EQE plot. The SiQD-Hex and SiQD-Oct samples were biased from -3 V to 6 V and the SiQD-Dodec samples from -3 V to 14 V, both with a voltage step size of 0.25 V. The mean current densities are plotted in Figure 5.5a) and the standard deviation is given in voltage steps of 0.25 V. Under reverse bias, J is mainly influenced by pinholes and other defects inside each LED, which spreads over almost one order of magnitude.[51, 174] Nevertheless, the shorter ligand has a higher leakage, indicating a better charge transport. In the forward bias direction, a current onset at 2 V is clearly visible for SiQD-Hex and SiQD-Oct LEDs with a linearization for higher voltages. The short SiQD-Hex drives a higher current density (669 mA cm^{-1}) than the intermediate SiQD-Oct (391 mA cm^{-1}). The current onset of Dodec-LEDs is at 4 V but remains in an exponential increase at low current densities below 3.5 mA cm^{-1} even for very high voltages of up to 14 V. The differences in

current density arise from the different lengths of the surface functionalization at the SiQDs. The surface ligand provides a tunneling barrier between two SiQDs, which scales with the ligand length l.[160, 170] As a result, the current through the device is attenuated by the barrier.

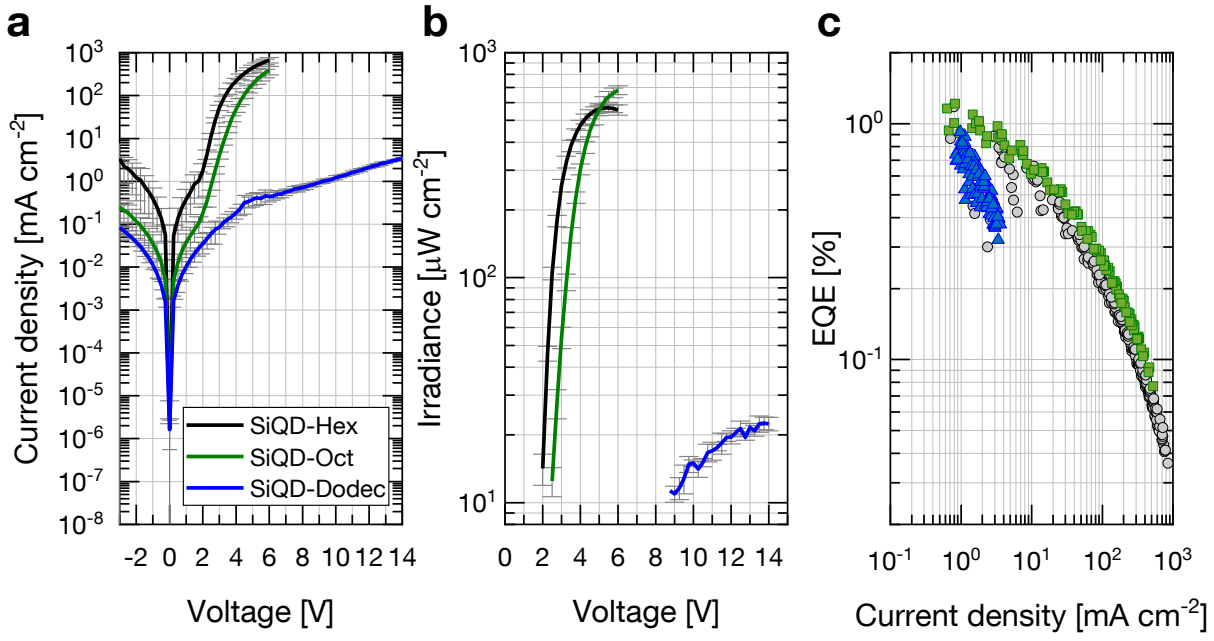

Figure 5.5 $J-L-EQE$ characteristic for varying ligand length SiQD-LEDs. The lines represent the mean values of the same surface functionalization in a) and b) and the legend in a) applied to all plots in this figure. a) $J-V$ characteristics of the three different SiQD-LED types. Hex and Oct drive much more current than the long Dodec-LED. b) Irradiance as a function of applied voltage. Hex-LEDs turn on at the lowest voltages. Oct-LEDs turn on at slightly elevated voltages compared to SiQD-Hex, while SiQD-Dodec needs voltages above 9 V for the turn-on. For irradiance, SiQD-Oct outperforms the SiQD-Hex LEDs by $\sim$120 µW cm^{-2} with a mean maximum of 681 µW cm^{-2}. c) Calculated EQE values as a function of current density. At low J at 1 mA cm^{-2}, the EQE is roughly the same for all three ligand types. With increasing current density, the EQE decreases. The figure is adapted and partially reprinted from [99] with permission.

Figure 5.6a) schematically shows two SiQDs with their simplified organic shell. The intra-QD distance d can be calculated by double the ligand length and the corresponding band diagram is depicted below. With increasing ligand length l, d widens and the carrier mobility deteriorates.[175] With the assumption of dense packing, the SiQD-to-SiQD distance is approximately two times the molecule length measured in the software Chem3D 19.1 from PerkinElmer Inc. The distances are 1.26 nm, 1.76 nm, and 2.74 nm for SiQD-Hex, SiQD-Oct, and SiQD-Dodec, respectively.

During device operation, space charges are induced, which lead to a space-charge-limited-current (SCLC) in the device.[176] An illustration of this effect is shown in Figure 5.6b). At the top, the injected charge carriers (CCs) can freely traverse from the left contact through the SiQDs to the other contact at the right side, establishing the current I_1. In the bottom schematic, some CCs become localized at the SiQDs, through the ligand barriers or defects and build up space charges that reduce the current. As a result, I_2 is smaller than I_1. Pfaehler et al. described SCLC transport in OLR-functionalized SiQD-Hex electrode devices, along with a high density of trap states.[176] The presence of traps is described in chapter 6.3 later in this thesis. Furthermore, SCLC is observed in many other SiQD-LED devices with alkyl surface ligands.[43, 44, 50, 102] To minimize the current attenuation through the insulating alkyl chains, conjugated molecule systems, with π–π stacking for enhanced CC conduction, have been implemented.[48, 149] Nevertheless, the introduced π–π stacking of allylbenzene enhanced the charge transport but at the same

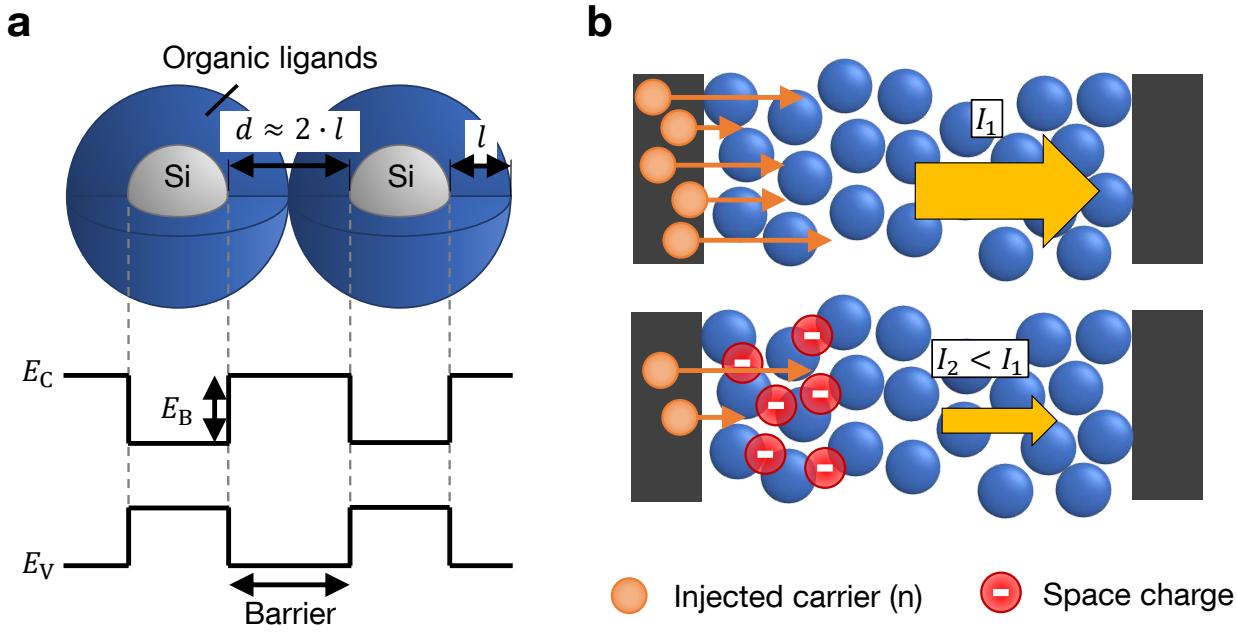

Figure 5.6 a) Schematic representation of the organic ligand shell and how it affects the charge transport in the active layer. b) Schematic of the SCLC in the active SiQD layer. The figure is merged and reprinted with permission from [99].

time caused an electron/hole imbalance in the SiQD layer, which ultimately decreased the EQE.[48, 177] To avoid the unbalanced electron/hole concentration, tailored HTL and ETL layer thicknesses are needed.

In Figure 5.5b), the irradiance is plotted as a function of applied voltage. Measurement values below the turn-on irradiance of $10\,\mu W\,cm^{-2}$ are not shown for clarity. The high turn-on irradiance was chosen because then the SiQD-LED was visible with bare eyes and bright enough for usage in other applications. One advantage of cutting away the data below the threshold is that the threshold voltage V_T can be read directly. For the three LED types, V_T was 2 V, 2.5 V, and 9 V for SiQD-Hex, SiQD-Oct, and SiQD-Dodec LEDs, respectively. The threshold voltage of SiQD-Hex and SiQD-OCt LEDs were still in the same range as SiQD-LEDs of other groups that defined the turn-on irradiances below $100\,nW\,cm^{-1}$, which is not visible with bare eyes.[41, 48] Their low turn-on values were chosen because the efficiency at very low currents is usually higher and therefore, they were able to present high EQEs at $5\,\mu W\,cm^{-2}$ and $0.1\,\mu W\,cm^{-2}$ but with a limited practical approach.[41, 48] The maximum irradiances I_{max} for SiQD-Hex, SiQD-Oct, and SiQD-Dodec LEDs, were $628\,\mu W\,cm^{-2}$, $734\,\mu W\,cm^{-2}$, and $25\,\mu W\,cm^{-2}$, respectively. Interestingly, the octyl ligand LEDs exhibited the highest irradiance. At 5 V, a crossover of the irradiance to the SiQD-Hex LEDs occurs because the irradiance of the SiQD-Hex starts to degrade while the SiQD-Oct is still increasing. For voltages higher than 5 V, the recombination rate for Oct LEDs was higher at high voltages than the rate for Hex LEDs. A possible reason for this behavior is that the CC localization becomes insufficient for Hex LEDs for high voltages. Hence, the irradiance degrades. In the Oct LEDs, the injected electrons and holes are better localized because the electron tunneling is limited by the potential barrier formed by the ligands.[160] SiQD-Oct had a higher tunneling barrier than SiQD-Hex. Additionally, Liu et al. showed that the potential barrier around SiQDs with organic ligands is lower for electrons than for holes. [160] That resulted in a lower tunneling probability for holes than for electrons and caused an imbalance of CCs in the SiQDs, thus affecting the recombination rates.[160] From SiQD-Dodec LEDs, we observed a very low irradiance because the long dodecyl ligand suppressed most charge transport and only a small amount of CCs did recombine in the SiQDs.

In Figure 5.5c), the calculated EQE (Equation 3.11) at each voltage step is shown as a function of current density. All SiQD-LEDs showed a comparable EQE of around $1\,\%$ for low current densities right

after the turn-on. The peak values of the EQE for the individual samples were $1.33\,\%$ for Hex, $1.48\,\%$ for Oct, and $0.92\,\%$ for Dodec QD LEDs. As for the irradiance, the SiQD-Oct showed the highest EQE value of all LEDs. For increased current densities, the EQE decreased, whereas the EQE of SiQD-Oct remained higher than the others for elevated J. As mentioned in the irradiance description, the radiative recombination was enhanced by an optimized CC confinement in the SiQDs with the octyl ligand. Similar to the irradiance and current density showed the Dodec LEDs the lowest EQE of all compared devices.

5.3 Electroluminescence spectral characterization

In this section, the ligand influence on the EL spectra is investigated. In the previous section, we observed an optical power attenuation of the SiQD-Dodec LEDs, whereas the SiQD-Oct LEDs could even improve the optical output compared to the SiQD-Hex LEDs. In chapter 4.5, a blue-shift and a peak broadening of the EL spectrum with increasing driving voltages was described. All those observations were made with a SiQD-Hex LED, which is now complemented by observations of SiQD-Oct and SiQD-Dodec LEDs.

In Figure 5.7, the normalized EL spectra for increasing driving voltages of a SiQD-Hex LED are shown. At the turn-on voltage the peak was at a wavelength of $790\,\mathrm{nm}$ and blue shifted to $731\,\mathrm{nm}$ at $5\,\mathrm{V}$. Additionally was the normalized PL spectrum with its peak at $712\,\mathrm{nm}$ and a FWHM of $140\,\mathrm{nm}$ of the SiQDs plotted in red. As the applied voltage to the LED was increased, the EL spectra moved towards the PL one, decreasing the difference between them. We note that the PL was measured in dilute solution prior device fabrication. Wood et al. showed that alloyed ZnO and SnO_2 QDs that measured PL in diluted and solid form differ and explained it by the QD interactions in films.[178] Furthermore, the emission spectra in solution were slightly blue-shifted and broadened compared to their solid layer PL measurement.[178, 179] Nevertheless, the difference is usually a few nm and not a few tens of nm as present in Figure 5.7. Hence, a different mechanism is causing the gap between the spectra. As PL and EL are excited differently, we suspected the excitation mechanism in combination with the organic ligand shell to influence the behavior.

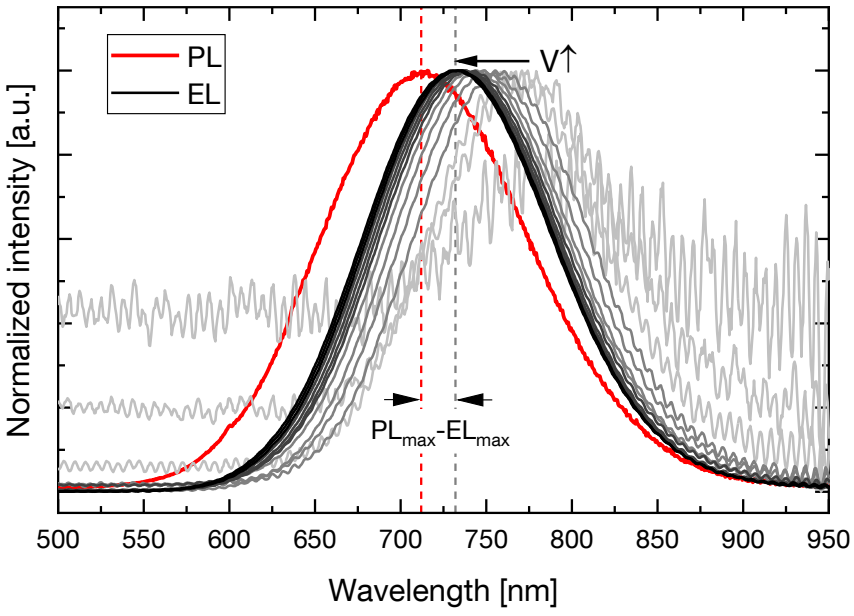

Figure 5.7 Normalized EL of a SiQD-Hex LED under increasing applied voltages. With increasing voltage, the line color becomes darker. The top arrow indicates the EL shift of the spectrum. The corresponding PL spectra is shown in red and the distance of the PL_{max} to the EL_{max} is exemplary shown for $5\,\mathrm{V}$.

In Figure 5.8 the EL spectra metrics, i.e. the FWHM and their PL_{max} to EL_{max}, are plotted for increasing voltages and all SiQD-LEDs fabricated. Similar to the previous figure, only EL spectra where the LED had an irradiance above $10\,\mu W\,cm^{-2}$ were selected and analyzed. In Figure 5.8a), the FWHM SiQD-Hex and SiQD-Oct LEDs started with $110\,nm$ and $115\,nm$ for voltages of $2\,V$ and $2.5\,V$, respectively. The SiQD-Dodec LEDs turned on at $9\,V$ and already exhibited a higher initial FWHM of $\sim 130\,nm$. Without exception, the FWHM for all LEDs increased with voltage. The SiQD-Dodec LED data points show a higher deviation than the other two LED types due to low intensity and noisy EL spectra. As a result, the FWHM of the SiQD-Dodec LEDs reached values of up to $150\,nm$, which was even broader than the FWHM of the PL measurement. The broad spectra are caused by the size distribution of the SiQDs and a broader EL spectrum would conclude that the size distribution had changed or that not all SiQDs were excited in the PL measurement. In the PL measurement, an adequate UV excitation source of $365\,nm$ was used, leaving only a high noise level for single peaks as the reason for the bigger FWHM. The mean value was still the same as the PL FWHM of $140\,nm$. When the EL and PL reach the same FWHM value, one can assume that all SiQDs are activated via the injected CCs. For the SiQD-Dodec samples, this happens at $12\,V$, whereas SiQD-Hex and SiQD-Oct do not broaden that far before device failure.

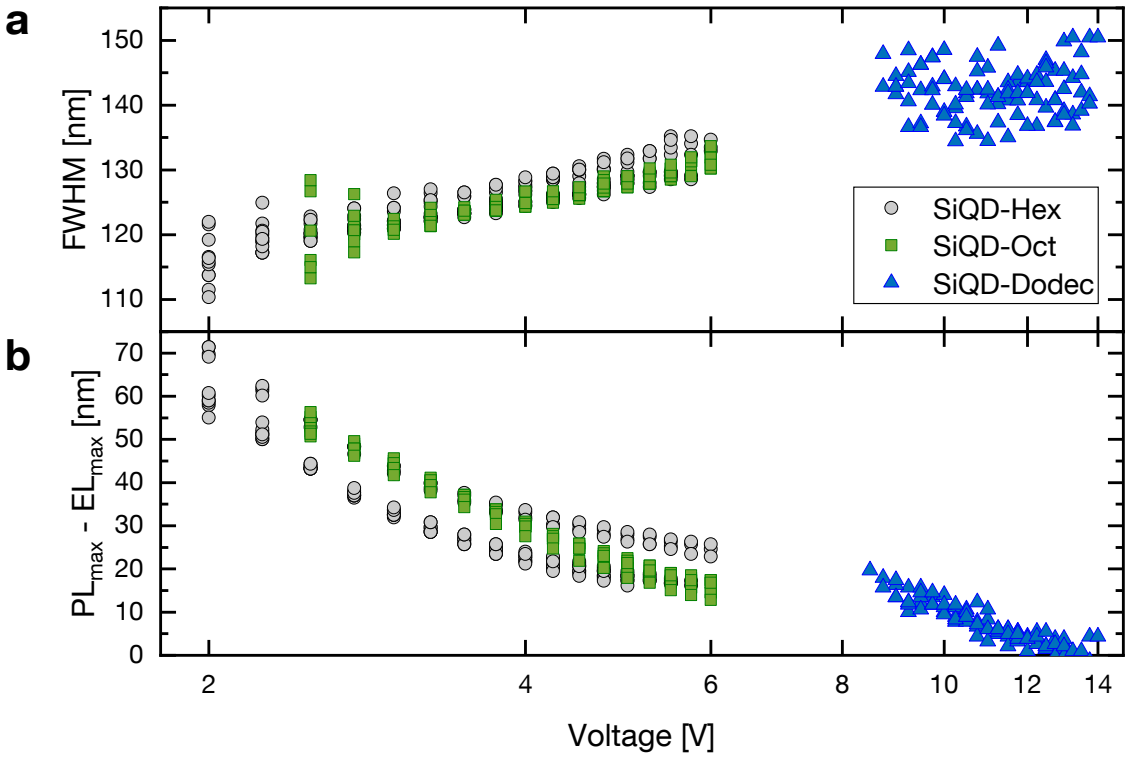

Figure 5.8 a) FWHM of EL spectrum for all SiQD-LEDs as a function of the applied voltage. The legend applies to all plots in the figure. b) Difference between the peak position of the PL and the EL spectrum. With increasing voltage, the difference decreases towards zero. In both plots, the data points are shifted towards higher voltages with a longer ligand length. The figure is merged and adopted from [99] with permission.

Figure 5.8b), compares the peak position difference between PL and EL emission. Therefore, the value of the EL peak at a given voltage was subtracted from the PL peak position and that difference was plotted over the applied voltage, as depicted in Figure 5.7. The spectra position equalizes with increasing voltage for all three ligand types. At the turn-on of the LEDs, the difference was $71\,nm$ at $2\,V$, $56\,nm$ at $2.5\,V$, and $19\,nm$ at $8.5\,V$ for SiQD-Hex, SiQD-Oct, and SiQD-Dodec LEDs, respectively. All three types approached the PL position, which was eventually reached, when PL_{max}-$EL_{max} = 0$. The SiQD-Hex LEDs reached their minimum value of $16\,nm$ at $5\,V$ and SiQD-Oct reached their minimum also at $6\,V$ with $12\,nm$. For the

SiQD-Dodec LEDs, the EL and PL spectrum match for voltages above 12 V. At that voltage, the FWHM became as big as the PL spectrum, which means that all SiQDs were excited.

Where do the EL blue shift and the broadening of the EL spectrum come from? The EL blue shift is usually attributed to the band-filling effect and the size distribution of the SiQDs.[41, 100, 149, 159, 180] The band-filling effect is a phenomenon where the charge carriers fill up the energy bands from the bottom. With an increase in carrier concentration, the higher energy charge carriers increase, which causes a blue shift to higher energies (lower wavelength) of the spectrum.[181] This also holds for a size distribution of SiQDs. The schematic in Figure 5.9 visualizes the size effect on the FWHM and the EL peak position. Large SiQDs exhibit a smaller band gap than smaller SiQDs as a result of the quantum size effect and is called band gap widening.[155, 182, 183] For a PL measurement, the SiQDs are excited via typically UV irradiation with a high enough energy to excite all QDs at the same time. Inside a LED, the applied voltage provides the excitation energy and at low voltages, the CCs do not exhibit enough energy to excite all SiQD sizes. In that case, only the big SiQDs with a small band gap emit photons at a high wavelength. With increasing voltage, the CCs provide enough energy to excite smaller SiQDs, and the larger band gap QDs emit at higher energies (lower wavelength). Consequently, the spectrum is broadening and due to the shifted emission mean value, the EL spectrum is also blue shifting. For SiQDs with their organic ligand shell, the insulating alkyl ligands suppress the charge transport to the SiQDs for certain energies until the voltage is high enough to pass the barrier. For increasing ligand length, more energy in the form of voltage is required to surpass that barrier. Additionally to the described broadening effect, phonon coupling with the organic ligand or dangling bonds can occur on the surface and further broaden the spectrum.[184] This effect becomes even stronger when driving LEDs at higher voltages, as an enhanced phonon concentration is increased by Joule heating.[185]

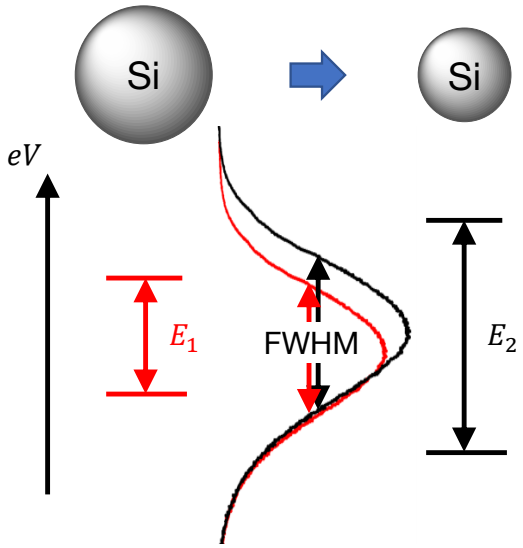

Figure 5.9 Schematic illustration of how the reduction of the SiQD affects the emission spectrum. Large SiQDs have a low band gap as shown in red, while smaller sized SiQDs exhibit a larger band gap. For a size distribution of SiQDs, the FWHM increases with more higher band gap SiQDs. The figure is reprinted from [99].

In summary, in this chapter, the SiQDs were functionalized with hexyl, octyl, and dodecyl ligands in order to find a performance maximum of the SiQD-LEDs. The octyl ligand showed the highest irradiance and EQE among the three tested SiQD functionalizations. Additionally showed the SiQD-LEDs a spectral influence on the ligands. With increasing ligand length, the blue-shift and spectral broadening increased.

6 Capacitance Measurements of SiQD-LEDs

In this chapter, the effect of charge transport on the capacity behavior of the SIQD-LEDs is analyzed with the help of capacitance-voltage ($C-V$) measurements. This becomes important as the SiQD-LED shall be used for high frequency display applications. $C-V$ is a powerful technique where an AC signal is superimposed on a DC bias and the electrical response, so the capacitance and conductance of a device can be recorded as a function of AC frequency.[186–188] They also enable an insight into the working mechanism of the LEDs, as charge injection and kinetics can be studied in a non-destructive manner[132–134] and processes that occur at various time scales can be monitored with high sensitivity.[136–138] The analyzed SiQD-LEDs are fabricated with the same layout and are of the same quality as in the previous chapters, extending the gained knowledge. Within our measurements, shown in Figure 6.1, we see a normal LED behavior in a-c). In the capacitance measurement in d), we found a not expected negative capacitance (NC) in the SiQD-LED. In the following chapter, we will discuss and explain the physical mechanisms behind the NC in our hexyl functionalized SiQD-LED sample as well as in a dodecyl functionalized SiQD-LED. This chapter and its results were published in the *IEEE Photonics Journal* with the title 'Revealing the Negative Capacitance Effect in Silicon Quantum Dot Light-Emitting Diodes via Temperature-Dependent Capacitance-Voltage Characterization' under a Creative Commons Attribution 4.0 Licence.[189]

6.1 Capacitance introduction

In the capacitance measurement in Figure 6.1 we observed a gradual increase of the capacitance C up to a maximum at approximately $2\,\mathrm{V}$. For higher voltages, the capacitance decreased rapidly and even reached negative values above $2.8\,\mathrm{V}$. The highest NC magnitude was reached at ca. $3.4\,\mathrm{V}$ from where the magnitude decreased further on. What caused the negative value and how does capacitance work in LEDs?

In general, differential capacitance C can be measured and is defined as $C = \frac{\mathrm{d}Q}{\mathrm{d}V}$, where Q is the change in charge that occurs because of a change in voltage V.[139] In Figure 6.1d), the capacitance behavior can be explained until the NC with the well-known pn-junction theory, where the capacitance generally consists of a depletion and diffusion capacitance C_{diff}.[7] The former is related to space charges while the latter is influenced by injected carriers. At low biases, the active region is fully depleted and the voltage-independent geometrical capacitance dominates. Together with an increase in bias, charge carriers are injected and accumulate, hence increasing the capacitance, which follows the expected behavior of the diffusion capacitance C_{diff} which is described by:

$$C_{\mathrm{diff}} = \frac{q^2}{2k_{\mathrm{B}}T} \cdot (L_{\mathrm{p}} p_{\mathrm{n0}} + L_{\mathrm{n}} n_{\mathrm{p0}}) \cdot e^{\frac{qV_{\mathrm{f}}}{k_{\mathrm{B}}T}}, \tag{6.1}$$

where q is elementary charge, k_{B} is Boltzmann constant, T is junction temperature, L_{p} and L_{n} are diffusion lengths of holes and electrons, respectively, p_{n0} is hole concentration in p-doped region in thermal equilibrium, n_{p0} is electron concentration in n-doped region in thermal equilibrium, and V_{f} is forward bias voltage. It can be seen from Equation 6.1 that the diffusion capacitance is positive and increases with the voltage. C_{diff} is proportional to the DC current level ($\propto \exp(qV_f/k_BT)$, so it becomes especially important at low frequencies and under forward-bias conditions.[7] This is true for the SiQD-LED until the capacitance starts to decrease.

OLEDs and hybrid organic/inorganic QLEDs differ structurally from inorganic pn-diodes, as they usually consist of several stacked layers for hole and electron transport instead of doped regions. Therefore, we

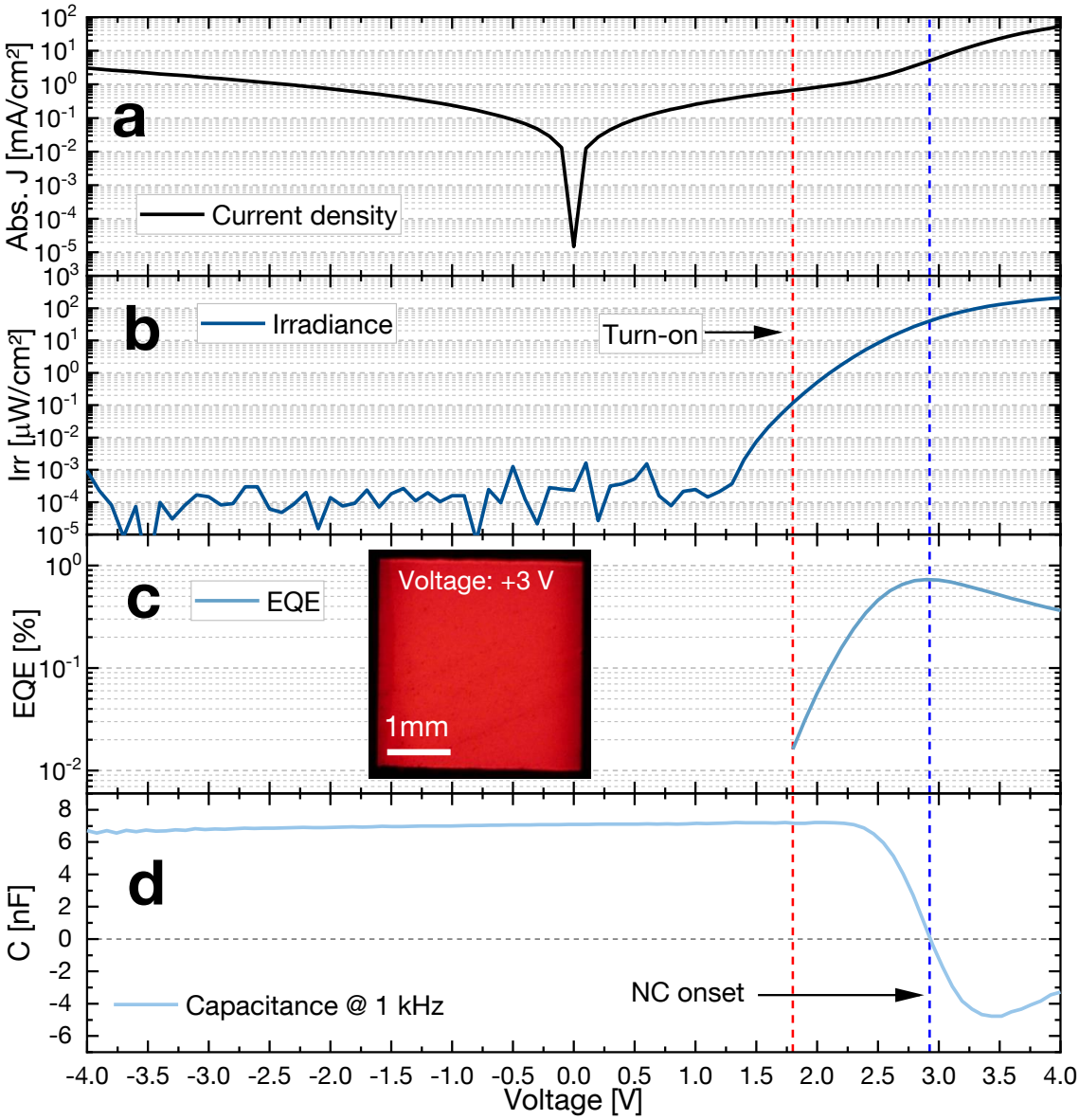

Figure 6.1 a) $J-V$ characteristic of a hexyl functionalized SiQD-LED for absolute J values from -4 V to 4 V. b) The irradiance shows no emission in reverse direction and increase up to 209 µW cm^{-2} at 4 V. c) EQE calculated from a) and b) after the turn-on, which is at 0.1 µW cm^{-2} and indicated by the red dashed line. d) Device capacitance as a function of voltage, which slightly increases until it suddenly drops and reaches a negative value. At ca. 3.5 V it increases again. The inset shows the SiQD-LED at 3 V. The figure is adapted with permission from [189].

can also assume them in an ideal capacitor as a plate capacitor. Following their capacitance can be described by

$$C = \epsilon_0 \epsilon_r \frac{A}{d}, \tag{6.2}$$

where ϵ_0 is the vacuum permittivity, ϵ_r the permeability of the material, A is the LED area, and d is the material thickness. A serial connection of the individual capacitors between the two electrodes was used to calculate the total geometric capacitance $C_{\text{SiQD-LED}}$ of the SiQD-LED.

Table 6.1 Capacitance calculation

Material	Thickness [nm]	n	ϵ_r	Capacitance [nF]
PEDOT:PSS	20	1.56	2.43	9.68
Poly-TPD	10	1.84	3.39	13.51
SiQD	35	2.03	4.12	16.42
ZnO	25	1.58	2.50	9.96

$$\frac{1}{C_{\text{SiQD-LED}}} = \frac{1}{C_{\text{PEDOT:PSS}}} + \frac{1}{C_{\text{Poly-TPD}}} + \frac{1}{C_{\text{SiQD}}} + \frac{1}{C_{\text{ZnO}}} \tag{6.3}$$

We measured the refractive index n with ellipsometry and calculated the relative permittivity by $\epsilon_r = n^2 - k^2$ in order to get an estimation of the geometric capacitance of our LEDs.[125] A more detailed description is provided in subsection 7.2.3. We used the values of n at the same position as the SiQD-LED emission peak at 710 nm, and $k = 0$. Our calculation results are summarized in the table 6.1. Using the obtained values, the theoretical capacitance $C_{\text{SiQD-LED}}$ was calculated to 2.69 nF. At reverse bias and low frequencies, the geometric capacitance dominates the behavior and can be read directly from the $C - V$ measurements. For the measurement in Figure 6.1d) at 1 kHz, the geometric capacitance was 6.5 nF to 6.7 nF, which was about 2.5 times higher than the calculated geometric capacitance. The deviations may occur from inhomogeneous layer thicknesses, pinholes inside the LED or an imprecise fabricated LED area because of the used shadow mask to evaporate the top silver electrode.

6.2 Negative capacitance in SiQD-LEDs

The phenomena of NC is not unknown, and in many optoelectronic devices such as GaN LEDs,[190] solar cells,[191] p-i-n Si photodiodes,[192] OLEDs,[193], quantum well infrared detectors,[194], or multi quantum well-based LEDs,[195] a negative capacitance has already been observed. However, a negative capacitance is not predicted by Shockley's theory, which only describes increasing diffusion capacitance as seen in the previous section.[196] The NC was therefore often attributed to parasitic inductance due to instrumental problems or false equipment calibration.[188, 190] Nevertheless, capacitance measurements can reproduce the NC effect, which would not be possible for a measurement artifact.[190] This leads us to the open question of where the NC measurements originate from.

So far, many different theories have been developed to explain the NC. The classical electronic interpretation of the NC is a lag of current behind the voltage as the bias changes.[188, 194] Mathematically this is expressed as a positive-valued time derivative of the transient current response to a voltage step.[188, 197] Laux and Hess managed to quantitatively explain the NC by introducing a new equivalent circuit model in which all current contributions were included and the boundary conditions were revisited.[198] Nevertheless, the physical origin remained unclear. Bisquert et al. explained the phenomenon via an electron injection model through interfacial states in OLEDs.[191] Others have attributed the effect to high-level injection, conductivity modulation, minority carrier injection, slow transient time of injected carriers, or charge trapping.[190, 193–195] Bimolecular recombination, self-heating, and energetic disorder have also been considered as responsible mechanisms.[138] To validate any of those theories, $C - V$ measurements were used, which remain as the key in order to understand the effect of negative capacitance. Of particular importance is the capacitance behavior at varying temperature and frequency modulations, because the effect is not completely understood.[199]

6.2.1 NC explanation theory

The connection between light emission and NC in Figure 6.1 led us to assume that e-h injection, recombination and the NC appearance are somehow related.[195, 200, 201]. A potential physical mechanism

leading to NC can be derived if we consider the presence of traps. Electrons/holes in (deep) traps have a finite probability of being thermally re-emitted into the conduction/valence band. The characteristic time scale τ_{trap} of this thermal emission or release from a defect to the conduction band is given by [202]

$$\tau_{\text{trap}} = \gamma^{-1} exp(\frac{\Delta E}{k_B T}) \tag{6.4}$$

where γ is the attempt-to-escape frequency with $\gamma = N_{\text{C,V}} v_{\text{th}} \sigma_{\text{n,p}}$, $N_{\text{C,V}}$ is the conduction/valence band effective density of states, v_{th} the thermal velocity, and $\sigma_{\text{n,p}}$ the electron/hole capture cross-section.[203–205] ΔE is the energy difference of the trap energy level to the conduction/valence band ($\Delta E = E_{\text{C,V}} - E_{\text{trap}}$).[206]

In capacitance measurements, the AC frequency determines which trap levels are probed when an AC signal is applied. Thus, there is a maximum frequency at which the defect states can respond to the voltage modulation. The probed trap states need to meet the condition $\omega_{\text{AC}} * \tau_{\text{trap}} = 1$ with the angular frequency of the AC signal ($\omega_{\text{AC}} = 2\pi f_{\text{AC}}$), where f_{AC} is the measurement frequency.[205, 206] Using this condition, an energy level known as demarcation [204, 206–210] can be determined by rearranging equation 6.4:

$$E_\omega = \Delta E = k_B T \ln(\frac{\gamma}{\omega_{\text{AC}}}) \tag{6.5}$$

This energy is also called cut-off [139, 210] or thermal activation energy [211, 212] but for the rest of this work, E_ω will be referred to as demarcation energy. A schematic representation of the demarcation energy is given in Figure 6.2. Trapped charges whose energy levels lie above the red energy will be able to contribute to the capacitance signal.[139, 187, 204, 206, 207, 213] This condition practically translates to the thermal emission rate $e_{\text{n,p}}$ being larger than the frequency of the AC signal, i.e. $e_{\text{n,p}} > \omega_{\text{AC}}$.[54, 139] Traps energetically below E_ω will be "frozen" with respect to the AC signal since their capture and emission rates are lower than the modulating frequency.[210, 214, 215] The Fermi level that controls the state occupancy determines the upper energy limit of the traps contribution. States far above the Fermi level are empty and therefore cannot be charged or discharged with the AC modulation, whereas charges in deep traps are also not probed since they are fully occupied.[216] So, only trapped charges between the demarcation and Fermi levels can produce an additional capacitance signal.[207, 217] As the Fermi level position moves in the gap with the AC modulation, as an effect of barrier height modulation, traps can charge and discharge, resulting in a capacitance variation.[194] Furthermore, the same combination of (ω, T) might probe different energies for different traps.[139]

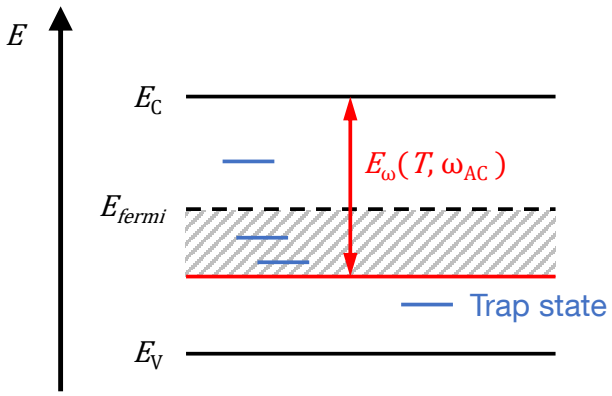

Figure 6.2 Schematic representation of the band diagram to understand the demarcation energy effect. If the demarcation energy E_ω is big enough to cross the Fermi level, as shown in this case, trap states can be charged and discharged. The grey shaded area represents the energy area where charges can be charged and discharged. The figure is adapted from [189].

The effect of NC in Figure 6.1d) can be explained using the demarcation energy formalism. At low forward bias, holes and electrons are slowly injected into the device and accumulate at the interfacial layers,

i.e. at the HBL and EBL, respectively, as shown in Figure 6.3. Trapped carriers in the SiQDs are also being re-emitted to the conduction band at increasing voltages, contributing to free charge distribution, thus increasing capacitance. As the voltage is high enough to excite the SiQDs and carriers recombine radiatively, charges emitted from trap levels are consumed irreversibly.[192, 218] In the capacitance measurement at the end of one AC modulation cycle, the equilibrium defect population of the charge carriers is disturbed as equilibrium lags behind the voltage, resulting in negative capacitance (blue line). A compensatory current is then induced to re-establish the equilibrium and the NC magnitude decreases again. So the responsible mechanism for NC is trap-mediated recombination,[136, 138, 219, 220] where the consumption rate (recombination) is faster than the replenishment rate (charge injection) of the charge carriers.[136, 137, 187, 195, 199, 201, 221]

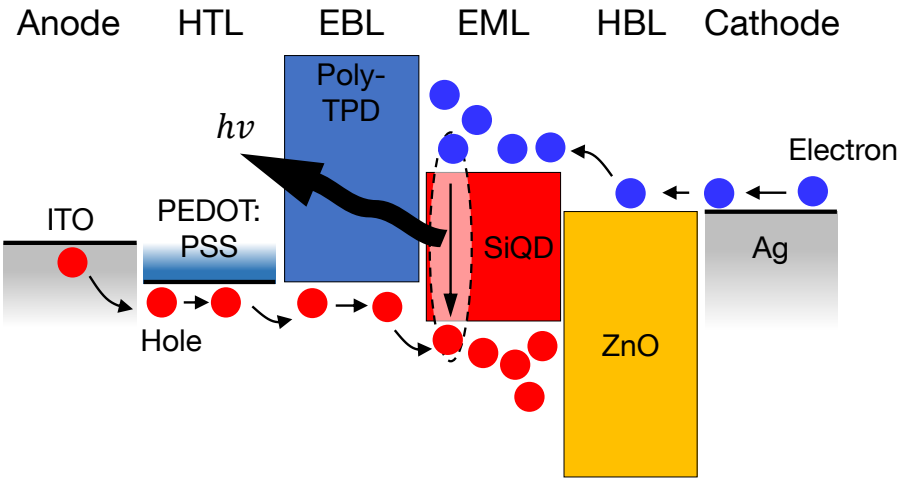

Figure 6.3 Schematic representation of the accumulation of the injected electrons (blue circles) and holes (red circles) at the interface between the active SiQD layer and the HBL and EBL, respectively. The electron and holes recombine under the emission of a photon in the EML when a high enough voltage was reached. The figure is adapted with minor changes from [189].

6.3 Proof of trap states

The presence of trap states in the device is essential if the presented theory of the demarcation energy holds. This section briefly explains what trap states are and verifies the existence of traps in the SiQD-LEDs. Traps are defect states in molecular crystals or organic semiconductors originating from structural imperfections of the crystal or chemical impurities during synthesis.[222, 223] For the SiQDs as an inorganic semiconductor, trap states can originate from point defects, dislocations and many more.[52] Defects create localized states that are distributed within the material's band gap and can be categorized into two groups based on their energetic depth: shallow and deep traps. Shallow trap states are energetically near the band edge and have a trapping energy of a few $k_{\mathrm{B}}T$, whereas deep traps lie deep in the band gap away from the band edges. Traps can capture charge carriers and, depending on their energetic position, either thermally re-emit them into their corresponding band (for shallow traps), in a process called detrapping, or become non-radiative recombination centers (for deep traps).[54, 186]

SiQDs are known to have high trap densities as they are not fully crystalline.[224] Around a Si core, SiQDs exhibit a non-crystalline surface shell which is more prone to defects hence trap states.[183] Traps can be traced in a $I-V$ measurement where they manifest in a hysteretic behavior.[186]

6.3.1 Hysteretic J-V

A SiQD-LED functionalized with a hexyl ligand was studied at room temperature (20 °C) with respect to their current density-voltage ($J-V$) behavior. A voltage from $-4\,\mathrm{V}$ to $4\,\mathrm{V}$ was sourced and the current density was calculated by dividing the measured current by the nominal LED area of $3\,\mathrm{mm}$ x $3\,\mathrm{mm}$. Two voltage sweeps with a step size of $0.1\,\mathrm{V}$ and a rate of $0.1\,\mathrm{V\,s^{-1}}$ were consecutively performed, forward sweep and reverse sweep, and are presented in Figure 6.4. A minor shift of the zero crossing is observed between both curves. This hysteretic behavior can be attributed to the presence of slowly responding traps in the system.[223, 225] During the forward sweep, charge carriers become trapped at the semiconductor/blocking layer interface and get released in the reverse sweep. This delay leads to a differential current and therefore causes a shift in the $J-V$ curves.[186]

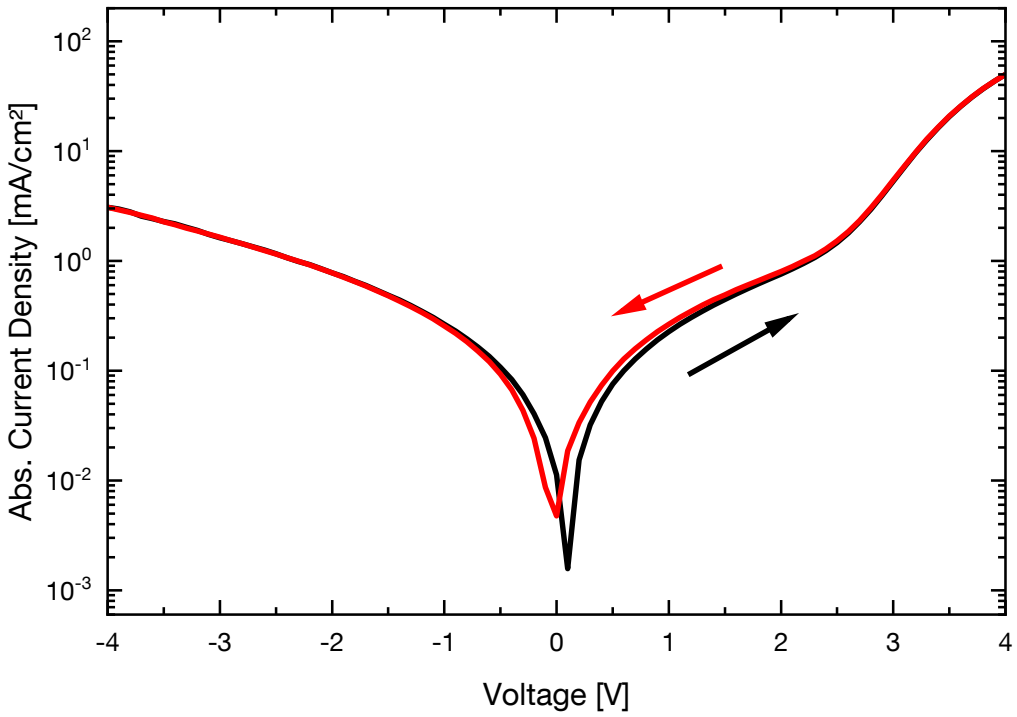

Figure 6.4 $J-V$ curve of the SiQD-Hex sample with the forward measurement starting at $-4\,\mathrm{V}$ in black and the reverse sweep in red, starting at $4\,\mathrm{V}$. The figure is reprinted from[189].

6.3.2 log-log J-V

The hysteresis behavior shown in Figure 6.4 is a good trap indication, but it might also originate from other factors. To gain further proof, the $J-V$ measurement is plotted in a log-log scale in Figure 6.5 because a SCLC is expected, which has been previously presented for SiQDs by Pfähler et al..[176] Two linear regimes were identified in the measurement of the SiQD-Hex sample. At low voltages (red region I), the graph can be described with Ohmic behavior since J rises (almost) linearly with voltage. The slight deviation of the slope from unity is attributed to the shape of the DOS distribution.[226] Region II (green) started shortly after the device turn-on and was characterized by a power law dependence ($J \propto V^m$, $m \approx 8$), which was attributed to the presence of exponentially distributed trap energy states.[227–230] This current transport is called trap-assisted SCLC, where the injected charge is larger than the intrinsic charge and traps affect the charge transport. As mentioned before, trap states can capture carriers leading

to a reduction in free charge carrier density and thus current. As the voltage increases, the Fermi level shifts towards the band edge and fills empty trap states. These now filled states cannot trap further charge carriers and current will increase faster than quadratic until all traps are filled.[223, 230] As the voltage further increases, carrier injection increases until all traps are filled, and the transport of remaining carriers can be free of the influence of traps. This behavior is described in the $J-V$ plot by a slope of $m=2$ and indicates the trap-free SCLC region [186, 229–231] described by the Mott-Gurney law [51]

$$j = \frac{9}{8}\varepsilon_r \varepsilon_0 \mu \frac{V^2}{d^3} \tag{6.6}$$

where μ is the charge carrier mobility, ε_r the material's relative permitivity, ε_0 the vacuum permitivity, V the applied voltage, and d the sample thickness. In the measured SiQD-Hex sample, only the Ohmic conduction regime and the trap-assisted SCLC current transport could be observed. With the high density of trap centers and an exponent of $m=8$, the measurements were in a similar range to Pfähler et al.[176] who measured exponents of up to $m=8.6$ for pure SiQDs in nanogap electrodes. The comparable fitting result strongly indicated trap states in the SiQD-LEDs.

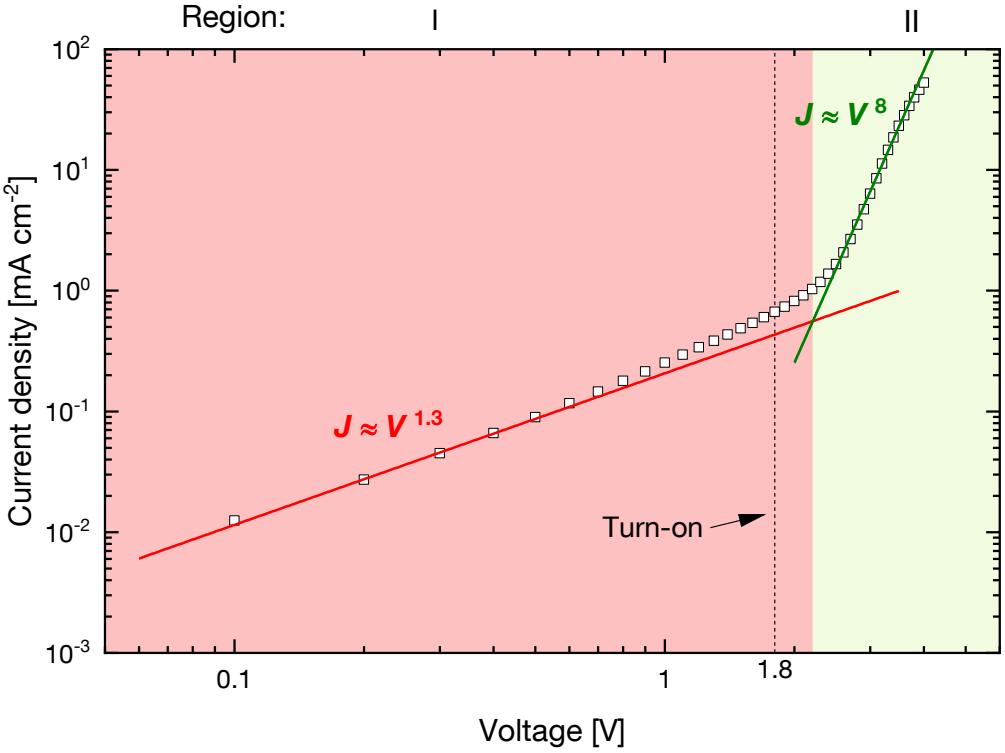

Figure 6.5 Log-log representation of $J-V$ characteristics of a SiQD-Hex LED. Two distinct regimes, I and II, are highlighted in red and green color for Ohmic transport in region I and trap-assisted SCLC in region II. The LED turn-on is given as a reference line.

6.4 C-V measurement results

According to the explanation and theory of the NC in chapter 6.2.1, the demarcation energy depends on the frequency and temperature. Therefore, we investigate the capacitance of the LEDs for a range of frequencies followed by the same measurements at different temperatures.

6.4.1 Frequency sweep

From an electrical point of view, NC can be described as an inductance-like behavior; nevertheless, NC cannot be treated as a classical inductance.[195] In that case, NC would increase with frequency and a magnetic field would also be observed.[188, 197] We observed a different behavior for increasing frequency in our sample, which is depicted in Figure 6.6. The capacitance remained relatively constant around 6.7 nF in reverse bias and low biases until the turn-on voltage at around 2 V. From the turn-on voltage on, the capacitance decreased rapidly and reached negative values until a negative maximum at 3 V. For further increasing voltage, the magnitude decreased again. Varying the frequency of the modulation voltage allowed probing the device at different demarcation energies.[208] Slowly responding traps cannot follow the AC signal with increasing frequency and are consequently frozen out. Trapped carriers closer to the conduction band became thermally re-emitted and the amount of defect contribution to free charge carriers was reduced, thus less accumulation was observed.[211, 232] As a consequence, fewer formerly trapped carriers were consumed during recombination, and a smaller compensatory current was required, which reduced the NC in magnitude. At high frequencies, trapping and detrapping occur rapidly, so a stationary accumulation of charges becomes difficult [197] and re-establishing equilibrium after recombination takes less time.[218] The voltage shift of the capacitance curve towards larger voltages with increasing frequency is also explained via the demarcation energy. As the frequency was increased, E_ω became reduced and only shallow states contributed to the capacitance signal. To compensate for the loss in the free carrier density due to freezing of deeper trap states, a higher voltage was needed for the same capacitance.

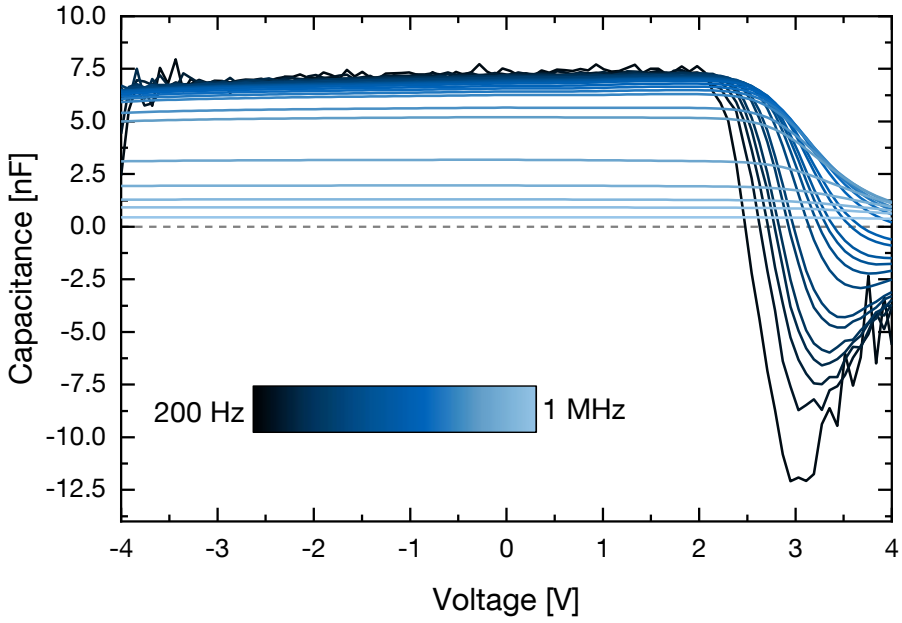

Figure 6.6 $C - V$ characteristics of the SiQD-Hex LED probed at different AC signal frequencies from 200 Hz to 1 MHz. The phenomenon on negative capacitance is observed at the onset of recombination at around 2 V. As the frequency increases, the positive peak decreases, and at the same time, the negative capacitance value decrease and the curve shifts to higher voltages. The black color represents low frequencies, the green medium, and the blue color high frequencies. The figure is reprinted from [189].

6.4.2 Temperature sweep

The demarcation energy is dependent on frequency and temperature (Equation 6.5). For this reason, we performed the same $C - V$ measurements at different temperatures to further validate the demarcation

energy theory. For the measurements, we exploited a climatic chamber with temperatures ranging from -40 °C to 60 °C in 20 °C steps as a test environment.

Temperature dependent C-V The results for the $C-V$ measurements of the SiQD-Hex sample at a probing frequency of 1 kHz are presented in Figure 6.7. Three effects were identified with increasing temperature from -40 °C to 60 °C: i) the positive capacitance peak decreased, ii) the magnitude of the NC was decreasing, and iii) the whole $C-V$ curve shifted towards lower voltages. E_ω from increased as a consequence of the increased temperature, as schematically shown in Figure 6.8. In the system, deeper trap states were able to contribute to the capacitance. With more free charge carriers in the system, the recombination was enhanced at a fixed rate, reducing the positive peak (Figure 6.7b)) and reaching the NC at lower voltages. The increasing temperature should also have a higher negative capacitance response. However, we saw the opposite trend in the presented sample in Figure 6.7c). Other temperature-driven effects can explain this phenomenon. We hypothesize that field-assisted escape processes of free charge carriers out of the quantum dots dominated over trap-mediated recombination. Hence, the number of charge carriers available for radiative recombination was reduced at higher voltages. As a result of increasing charge carrier escape, e-h recombination was reduced, which led to a decrease in the NC signal.[195, 211]

Generally, processes such as Poole-Frenkel emission and phonon-assisted tunneling, which facilitate the escape of carriers out of the quantum dot, are enhanced at high temperatures. Poole-Frenkel emission refers to the lowering of the potential barrier around a charged trap that allows carriers to cross the barrier.[233] In Figure 6.9 the NC onset frequency is plotted against the square root of the applied voltage. The linear fit in the log plot correlates to the Poole-Frenkel model, which describes that the electron emission is increasing exponentially with the square root of the applied bias.[193, 234, 235] In phonon-assisted tunneling, a carrier can tunnel by emitting or absorbing a phonon.[235] These processes compete against charge injection, recombination, and detrapping.

Temperature driven effects on LED performance Additionally to the $C-V$ temperature sweep, the LED performance was obtained at each temperature. In the $J-V$ characteristics in Figure 6.10a), we observed higher current densities with increasing temperatures. More thermally excited carriers from the valence band and were flowing through the SiQD-LED, thus increasing the current density. A similar behavior was seen for the irradiance (Figure 6.10)b), which increased with increasing temperature. The higher current provided more charge carriers and resulted in more recombination. As a result, did the turn-on voltage shift towards lower voltages. In Figure 6.10c) the EQE defined as $EQE = \frac{N_{\text{photons}}}{N_{\text{electrons}}}$ is plotted as a function of the voltage. We observed the same picture as for the irradiance for low voltages, but the highest maximum peak was observed for the EQE at -40 °C. Since more charges are mobile at higher temperatures, $N_{\text{electrons}}$ increased, and consequently, the EQE decreased. As thermal escape is also enhanced, radiative recombination becomes less efficient. The shift of the maximum EQE towards lower voltages coincided with the voltage shift of the $C-V$ curve in the same direction in Figure 6.6, which further strengthen the theory that the NC is caused by charge injection and recombination effects. Moreover, the carrier mobility decreases with decreasing temperature, and a higher voltage is required to maintain a certain amount of light output. [236] We observed that for biases up to 2.5 V the higher the temperature the higher the EQE. At higher voltages, this behavior is reversed and coincides with the SCLC with traps regime. As the bias was further increased, more charges flowed and became trapped at defect levels, thus reducing the amount of free charge available.

Spectrum under temperature We measured the EL spectra at a forward voltage of 4 V as a function of temperature in Figure 6.11a). We observed that the EL spectrum shifted towards higher wavelengths with increasing temperature. The peak wavelength is additionally depicted in Figure 6.11b) together with the corresponding current density. The current density remains constant for all temperatures, except the

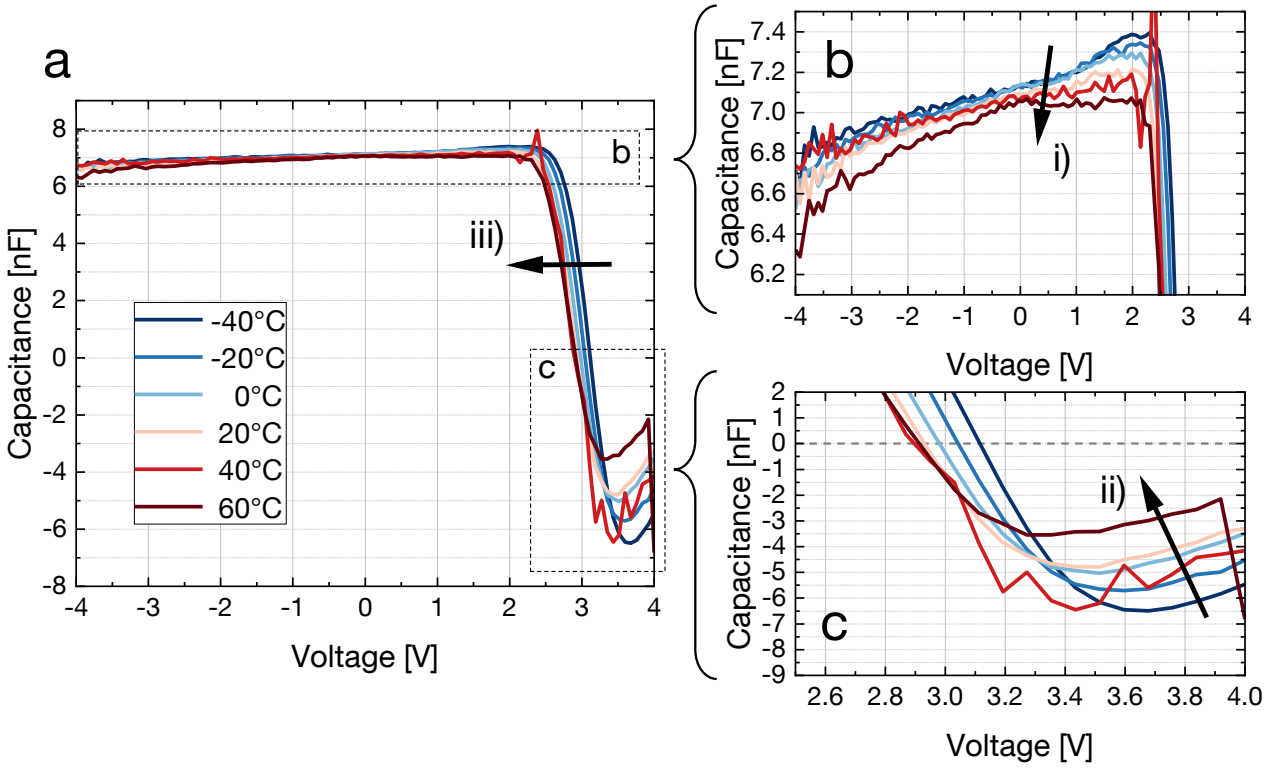

Figure 6.7 a) $C-V$ characteristics of the SiQD-Hex LED probed at different temperatures and fixed AC signal frequency of 1 kHz. b) Zoom-in to the positive peak reduction of the capacitance. c) Zoom-in to the NC, which also becomes smaller in magnitude with increasing temperature. The phenomenon of accumulation and negative capacitance is reduced at higher temperatures. This can be attributed to increased carrier thermal escape with higher temperatures. The figure is reprinted with permission from [189].

measurement at -20 ℃. The spectral shift is then introduced with the temperature change, not with a higher or lower current. The PL spectrum of SiQDs also changes with temperature, which was accounted to the band gap widening effect.[182]

6.5 Dodecyl functionalized SiQD-LEDs

The demarcation energy explained the behavior of the hexyl functionalized SiQD-LED well. Nevertheless, in a previous publication,[99] we showed that the organic ligand impacts the LED performance and for this reason, a second functionalization was tested. We fabricated SiQD-LED with a longer dodecene alkyl chain on the SiQDs to further test the theory and see if the surface functionalization influences the capacitance behavior too. The $C-V$ curve at room temperature in Figure 6.12a) for the same frequency range, revealed the three same effects as the SiQD-Hex sample. With increasing frequency, the curve shifts to higher voltages and the positive and negative capacitance peaks are reduced in magnitude. All effects are in agreement with the presented demarcation theory. The amplitude of the peaks is higher than for the SiQD-Hex sample. That indicates more charge accumulation in the LED.

6.5.1 Temperature sweep

The temperature-dependent capacitance behavior at 1 kHz is shown in Figure 6.12b). As the temperature increased, the magnitude of the negative capacitance decreased as in the SiQD-Hex sample while the positive capacitance peak increased, which is the reversed trend. The curves are also shifted to lower

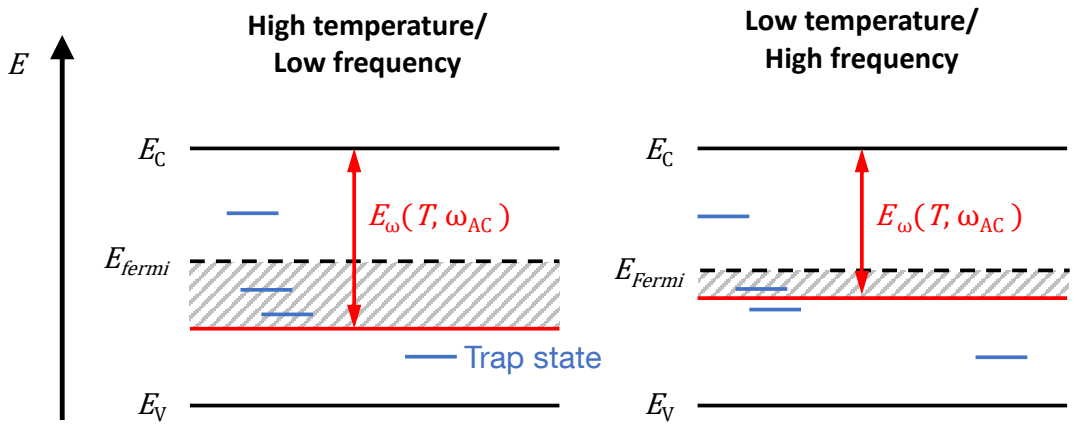

Figure 6.8 Schematic illustration of the temperature and frequency effect on the demarcation energy. The combination of a high temperature and low frequency results in a big E_ω while low temperatures and high frequencies result in a low E_ω.

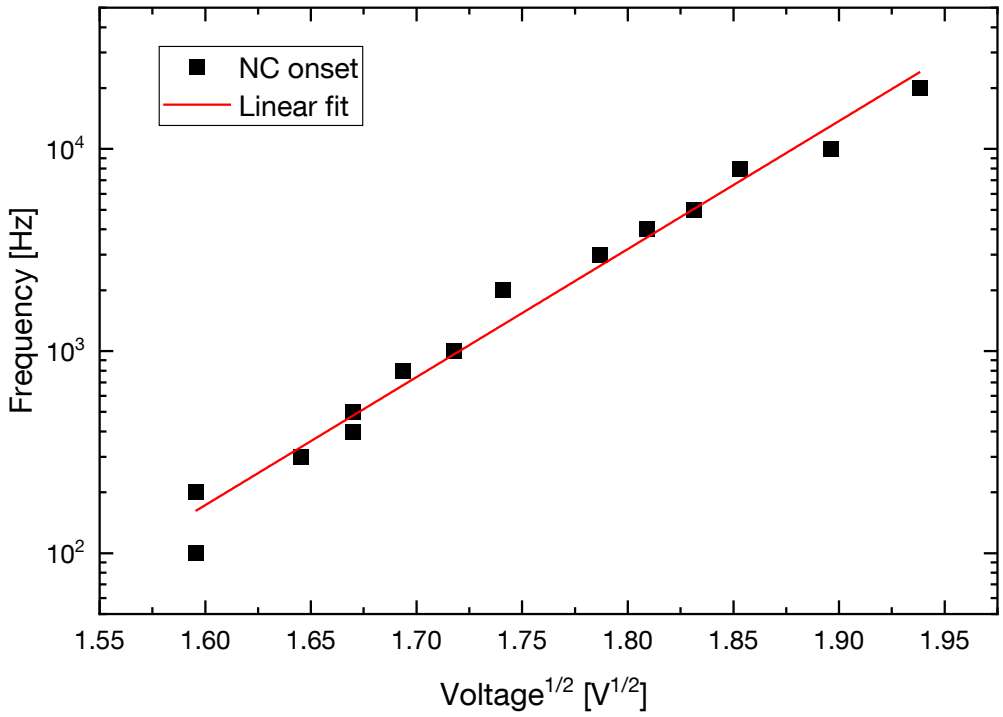

Figure 6.9 Frequency of NC onset as a function of voltage$^{1/2}$. The red line is a linear fit to the data and indicates Poole-Frenkel emission in SiQD LEDs.

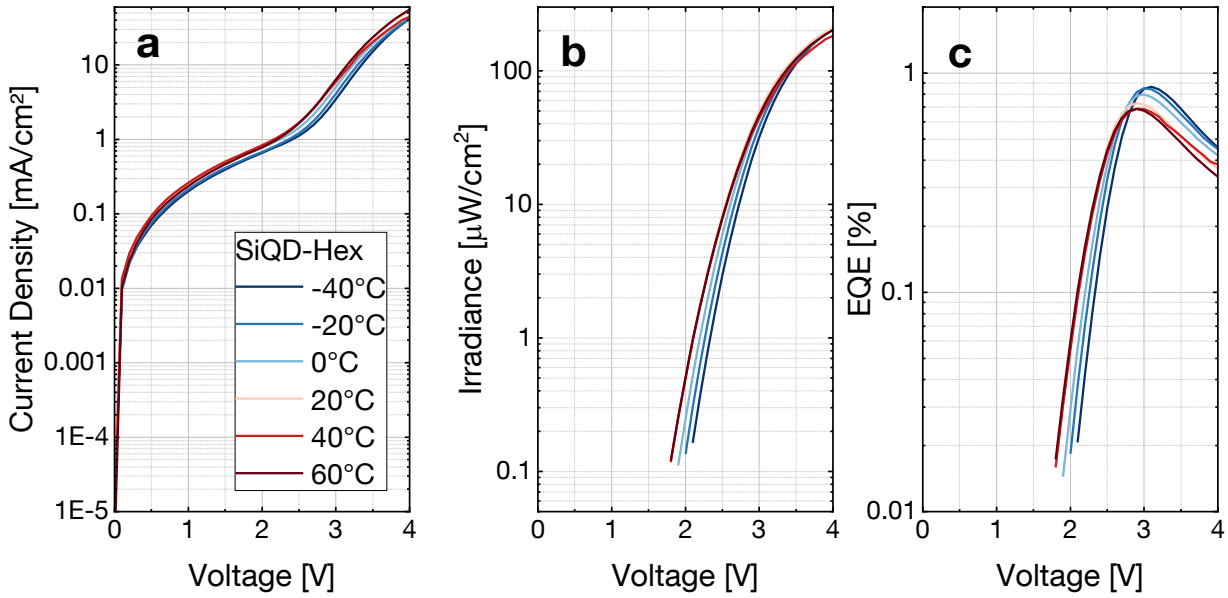

Figure 6.10 a) $J - V$ characteristic of hexyl LED for all temperatures. The inset shows the $J - V$ temperature dependence in detail. b) Irradiance and c) EQE dependence. For low temperatures, the irradiance is lower but the EQE is increased. The measurement for 40 ℃ is a bit off. The figure is reprinted with permission from [189].

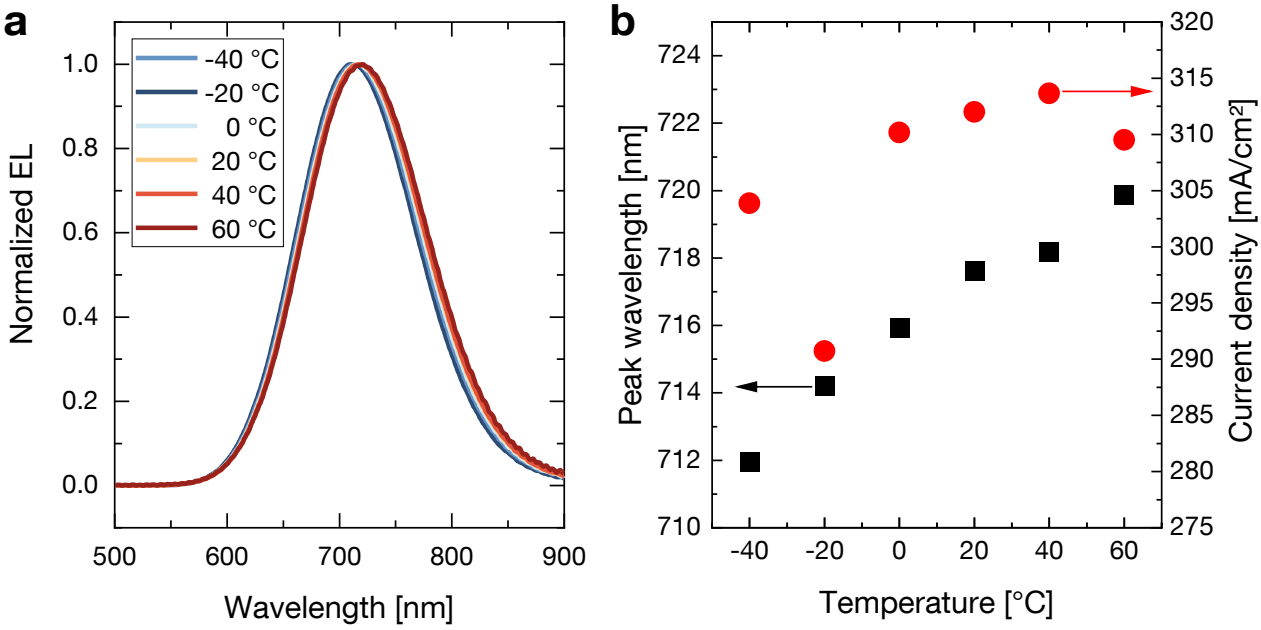

Figure 6.11 a) Normalized EL spectra at different temperatures. b) Peak wavelength as black squares as function of temperature on the left axis is increasing with temperature. The corresponding current density is plotted in red circles.

voltages with higher temperatures. The explanation behind the voltage shift is similar as presented in the case of the SiQD-Hex LED. The trend of the positive capacitance, however, is opposite and agrees with Equation 6.4 whereas the negative capacitance of the SiQD-Dodec and SiQD-Hex samples are similar. The discrepancy in the positive capacitance peak was explained by comparing the properties of the two

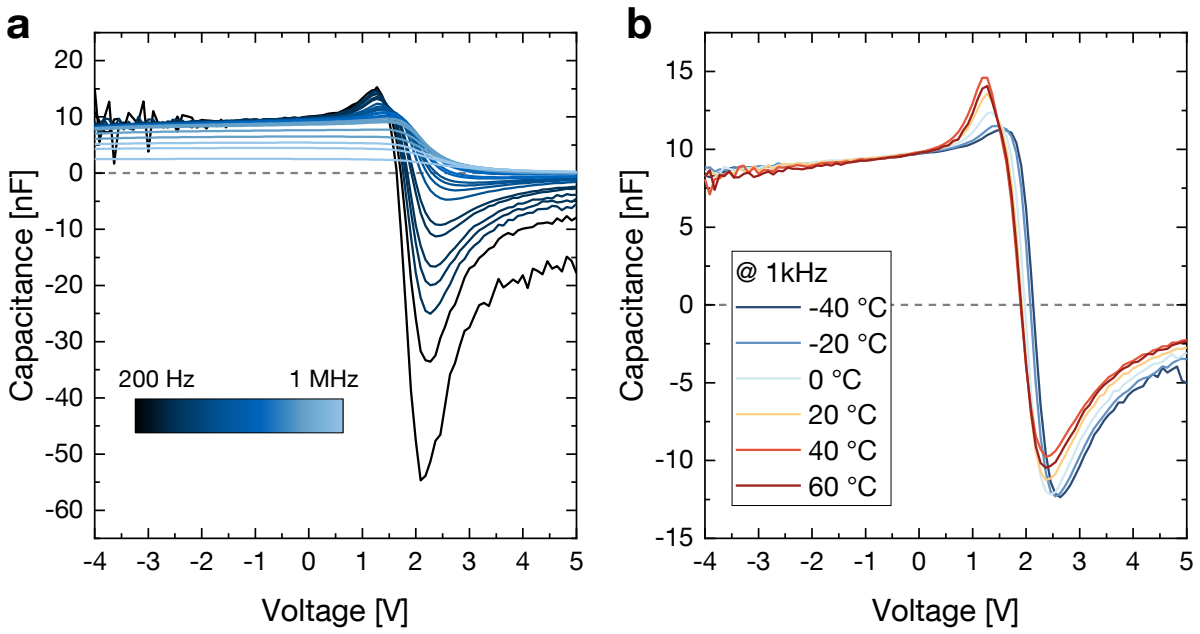

Figure 6.12 a) $C-V$ curve of the dodecyl sample at 20 ℃ for frequencies from 200 Hz up to 1 MHz. The phenomenon of negative capacitance is observed at the onset of recombination. As the frequency increases, the positive and negative capacitance decrease and the curve shifts to higher voltages. b) $C-V$ characteristics of the SiQD-Dodec sample probed at a frequency of 1 kHz for varying temperatures. The positive capacitance peak increases as the temperature increases, while the magnitude of the negative capacitance decreases. The curve is also shifted to lower voltages with higher temperatures. The figure is reprinted with permission from [189].

functionalizations. QLEDs with a dodecyl functionalization show improved charge carrier localization because the potential barrier width is larger, which reduces the electron tunneling.[99] In addition was the capacitance peak located at a lower applied voltage, hence the field assisted escape processes did not play a big role there. Since charges are more localized with longer ligands, increased temperature leads to increased charge accumulation due to higher carrier energy, thus increasing positive capacitance with temperature.[237] Furthermore, as temperature increased and more thermally generated carriers were in the system, the replenishment of the emptied trap states due to recombination happened faster than the recombination rate, thus negative capacitance decreased.

6.5.2 log-log J-V

As with the Hex-sample, we also examined the dodecene samples in a double logarithmic $J-V$ representation, shown in Figure 6.13. Three distinct regions were observed compared to the two regions for the hex LED. After the trap-assisted region with a linear fitting exponent of $m = 7.7$, the slope of the curve flattened out towards a smaller exponent of $m = 2.1$. This indicated the beginning of trap-free SCLC. The gradual transition between the trap-assisted SCLC and the trap-free region indicates an energetic distribution of trap energies.[236] The dodecene sample drives more current due to enhanced pinhole density as shown by the inset in Figure 6.13. Hence, the traps are filled faster than in the hex sample and the dodecene sample reached SCLC.

6.5.3 LED performance

The $J-V$ behavior of the SiQD-Dodec LED showed a current increase with temperature, similar to the SiQD-Hex LED, as shown in Figure 6.14a). A more pronounced effect was observed for the irra-

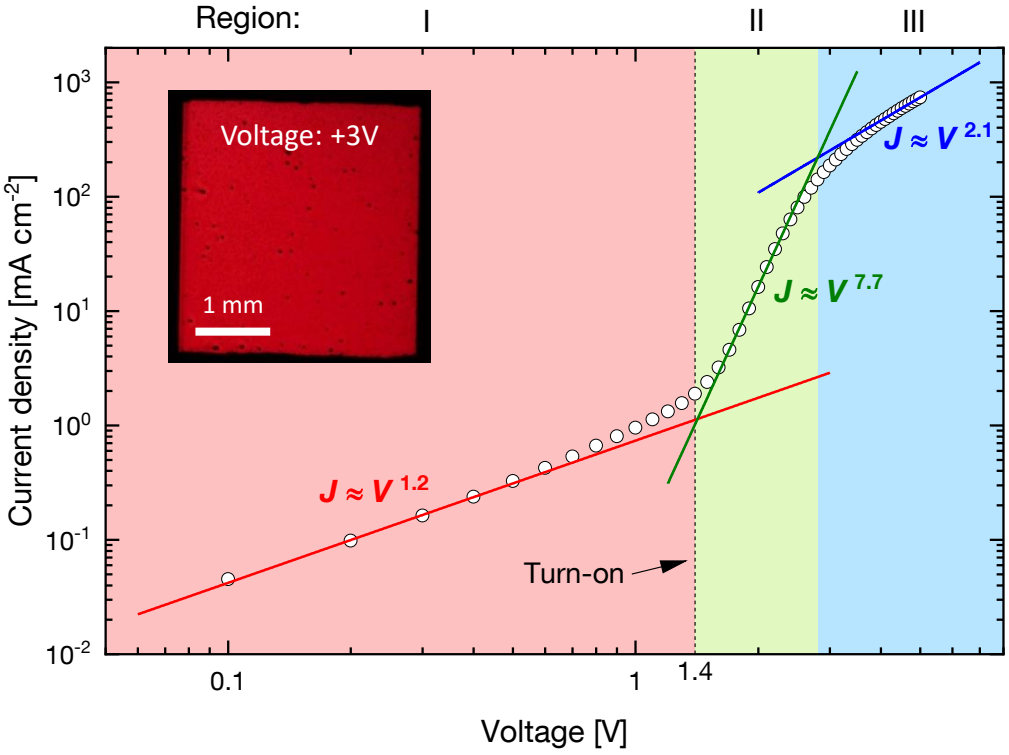

Figure 6.13 Double logarithmic plot of the $J-V$ curve for the dodecene LED and the colored lines are a linear fit to the data in each region. Three regions are highlighted with color, i.e. region I in red represents the ohmic behavior, region II in green the trap-assisted SCLC, and region III in blue the trap-free SCLC. The inset shows a microscope photo of the dodecene SiQD-LED. The figure is reprinted with permission from [189].

diance and EQE. At $2.6\,\mathrm{V}$ the temperature dependence reversed and lower temperatures resulted in a higher irradiance and EQE. $2.6\,\mathrm{V}$ was also the voltage at which current transport transitioned from trap-assisted SCLC to trap-free SCLC. This crossover indicates that even though more charges are injected (Figure 6.14)a). The device efficiency decreased at higher voltages which was attributed to increased non-radiative recombination.[197]

6.6 Comparison of Hex and Dodec capacitance curves

A direct comparison of the SiQD-Hex and SiQD-Dodec LED is plotted in Figure 6.15. In a), the capacitance characteristics of both are shown after normalizing them to their capacitance value at $-4\,\mathrm{V}$. We observed that the onset of negative capacitance is at a lover voltage for the dodecene sample due to the different currents driven through the LEDs. The magnitude of the positive and negative capacitance in SiQD-Dodec LED showed an increase of up to $64\,\%$, compared to Hex LED with a $7\,\%$ capacitance increase. Dodecyl confined charges more efficiently impeding the transport of carriers to the next SiQD, so positive capacitance builds up more.[197] The combination of the increased accumulation with longer recombination lifetimes led to larger NC values of the dodecene sample.[159] In Figure 6.15b), the dC/dV is shown. The higher negative peak of the dodecene sample suggests a faster capacitance decay, resulting from a faster charge carrier consumption in the LED.

In this chapter, the kinetic behavior of SiQD-LEDs was examined and a negative capacitance was observed. The NC was explained with the charging and uncharging of trap states and the demarcation energy. This deeper device understanding helps to build improved SiQD-LEDs in the future.

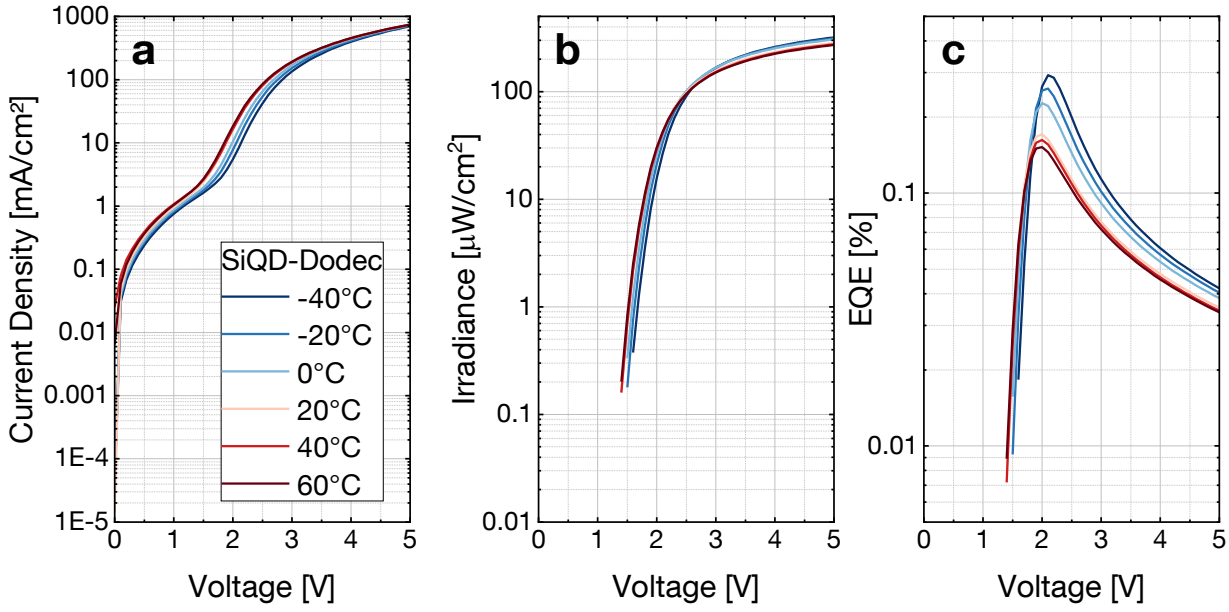

Figure 6.14 Electrical characteristics of the SiQD-Dodec sample probed at different temperatures. The current density in a) and the irradiance in b) increase with increasing temperature. At a crossover voltage of ca. 2.6 V, the irradiance behavior reverses and decreases with increasing temperature. The same crossover effect with temperature was observed for the EQE in c). The Figure is reprinted with permission from [189].

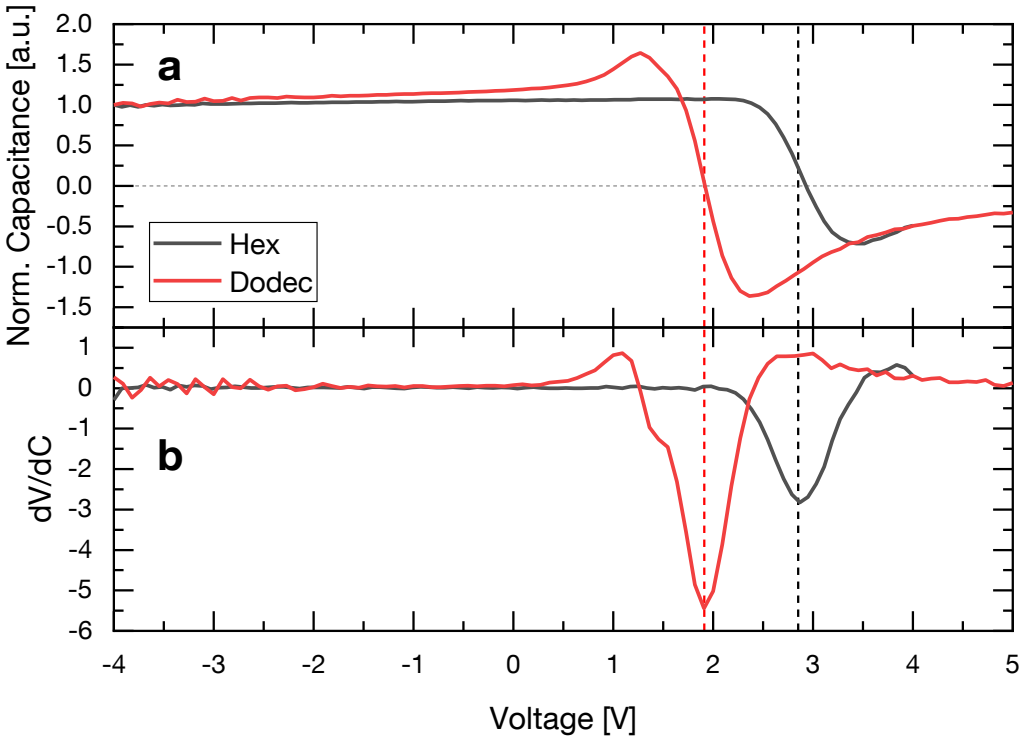

Figure 6.15 Characteristics of the normalized capacitance of the SiQD-Hex and SiQD-Dodec QLEDs. In the case of dodecyl, more accumulation and a larger magnitude of negative capacitance are observed.

7 Fabry-Pérot Resonator Built-in SiQD-LED

One limiting factor of LEDs for display applications is the EL spectral width. In the case of SiQD-LEDs, the spectral width stems from the size distribution of the SiQDs. Separation methods such as size-selective precipitation were established to target mono-dispersed SiQDs and to narrow down the spectral width. Maier-Flaig and co-workers showed that these size-selected SiQDs enable spectral thinning, however, the EL FWHM remains at ca. $100\,\mathrm{nm}$.[49] Although the size-separated SiQDs enable more stable LEDs compared to non-size-separated SiQD-LEDs, the EL remains still too broad for display applications, and alternatives are sought to achieve the required spectral purity of $\leq 50\,\mathrm{nm}$ emission bandwidths. While the thinning approach via size-selection of the SiQDs does not work well enough, the spectral width can also be reduced by engineering the LED structure. Fabry-Pérot (FP) resonators enable spectral narrowing and tuning with very high purity. They consist of a planar structure with two parallel reflective surfaces. The FP structure behaves like a wavelength filter as it forms a standing wave of light inside the optical cavity through constructive and destructive interference. While this filtering approach was demonstrated for SiQDs by Amans et al., who used a dielectric distributed Bragg reflector (DBR) to narrow the SiQD PL emission, the fragile, complex multilayer structure is impractical for device applications.[238] Later, Hryciw and co-workers later demonstrated a sandwiched SiQD-containing silicon-rich oxide between two reflective metallic layers (i.e., silver).[239] That is a more straightforward approach compatible with LED fabrication as it only requires a few additional fabrication steps. Cheong et al. established a similar FP cavity of SiQD-polymer hybrids/blends and successfully narrowed down the PL linewidth from > $100\,\mathrm{nm}$ to ca. $9\,\mathrm{nm}$.[240] Despite the advances in their presented structure, the optically driven structures are not suitable for self-emitting LEDs and an electronically driven system needs to be explored. Recently, Zhang et al. presented a study with an inorganic distributed feedback (DFB) LED and employed SiQDs inside an oxide film with an EL peak at $638\,\mathrm{nm}$ and a FWHM of $33\,\mathrm{nm}$. However, by using fabrication methods such as an time-consuming electron-beam lithography, their device remains impractical.[241]

The existing SiQD-LED layout from the previous chapters can be implemented into a FP resonator structure to build a cavity SiQD-LED (cLED). Therefore, two additional layers are needed to complete an LED-driven FP resonator, a second semi-transparent mirror to confine the cavity and a transparent spacer layer to tune the spectral emission. The proposed cavity device structure is schematically illustrated in Figure 7.1. The bottom silver mirror and the SiO_2 layer were added below the device to complete the full cavity and govern spectral tuning ability. In contrast to the normal SiQD-LEDs where prestructured ITO substrates were used, the ITO layer was sputtered on top of the spacer layer.

The results presented in this chapter are published in the journal *Advanced Optical Materials* with the title 'Colloidal Silicon Quantum Dot-Based Cavity Light-Emitting Diodes with Narrowed and Tunable Electroluminescence'.[157] Therefore, the following chapter describes the process in detail and were in close collaboration with I. T. Cheong from the University of Alberta. The contribution of this thesis was mainly the fabrication, measurements, and design of experiments for the cavity based SiQD-LEDs, whereas I. T. Cheong contributed with the chemistry part, simulations, and detailed spectral analysis.

7.1 Fabry-Pérot resonator theory

The Fabry-Pérot resonator relies on an arrangement of two highly reflecting mirrors. The light is multiple reflected at both mirror surfaces and the resonant wavelength λ_m is outcoupled. The wavelength depends on the cavity's optical path length, which is a function of the thickness, refractive index, and penetration

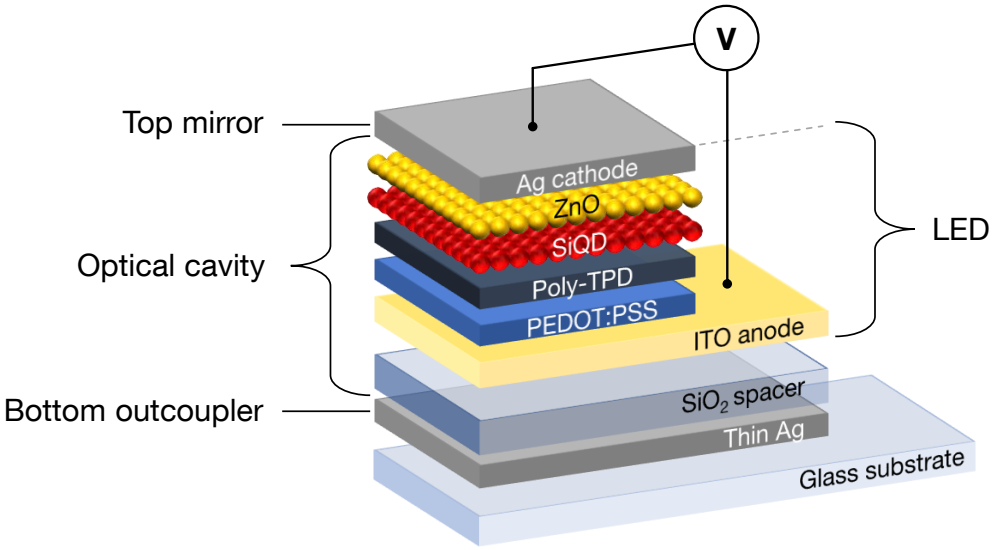

Figure 7.1 Schematic FP cavity device structure. Additional SiO_2 and a bottom Ag layer are implemented compared to the normal LED. The bottom Ag layer acts as a semi-transparent outcoupling mirror while the SiO_2 is used as a transparent spacer for spectral tuning. The SiQD-LED is driven between the ITO anode and the top silver cathode.

depth at the mirror surfaces. Through the Fabry-Pérot equation, the resonant wavelength λ_m can be calculated by [240, 242]

$$\lambda_m = \frac{2}{m}(\sum_i \eta_i d_i \cdot \cos\alpha + 2L_{pen,\alpha}) \tag{7.1}$$

where m is an integer indicating the mode number, η_i the refractive index of layer i, d_i the thickness of layer i, α the detection angle, and $L_{pen,\alpha}$ the penetration depth into the metal mirrors. If the penetration depth and the induced phase change are neglected, the total optical pathlength $\sum_i \eta_i d_i$ of the cavity is calculated by

$$\begin{aligned}\sum_i \eta_i d_i = \eta_{SiO_2} d_{SiO_2} + \eta_{ITO} d_{ITO} + \eta_{PEDOT:PSS} d_{PEDOT:PSS} \\ + \eta_{Poly-TPD} d_{Poly-TPD} + \eta_{SiQD} d_{SiQD} + \eta_{ZnO} d_{ZnO},\end{aligned} \tag{7.2}$$

where the indices correspond to each layer of the structure. Some parts of the electromagnetic wave become absorbed by the metallic mirrors and the phase shift at the interface is neither 0 nor π.[242] This phase shift is also interpreted as the penetration depth L_{pen} of the electromagnetic wave. The penetration depth into the metallic mirrors (i.e., Ag) can be calculated according to Ma [242]

$$L_{pen} = \frac{\lambda(\pi - \beta)}{4\pi} \tag{7.3}$$

where $\beta = \arctan[\mathrm{Im}(r)/\,\mathrm{Re}(r)]$ and r is the reflection coefficient.[242]

To get a good first approximation of the outcoupling modes, we neglected the penetration length into the metal mirror and investigated the cavity normal to the surface (i.e., $cos\alpha = 1$). We kept in mind that the penetration depth neglection caused a small calculation error in the end result. With both assumptions, Equation 7.1 can be rewritten to a form where the resonant mode is only dependent on η_i and d_i:

$$\lambda_m = \frac{2}{m}(\sum_i \eta_i d_i) \tag{7.4}$$

Other metrics are important to successfully show improved spectral properties despite the peak emission wavelength. Besides the well-known FWHM, the free spectral range (FSR), the quality factor Q, and the finesse F are used to compare the performance of cLEDs.

Full width at half maximum The full width half maximum (FWHM, $\Delta\lambda$) gives the bandwidth at the half maximum of a peak. The FWHM can be detected graphically from the spectral peak, whereas the wavelength interval can be converted from nm into frequency $\Delta\nu_{\text{FWHM}}$ by:

$$\Delta\nu = \frac{c}{\lambda^2}\Delta\lambda, \tag{7.5}$$

where c is the speed of light and λ is the peak wavelength.

Free spectral range The free spectral range (FSR) is the spacing in wavelength between two following modes. The wavelength interval (λ_{FSR}) can be calculated by

$$\lambda_{\text{FSR}} = \lambda_{\text{m+1}} - \lambda_{\text{m}}, \tag{7.6}$$

where λ_{m} is the wavelength of mode m and $\lambda_{\text{m+1}}$ is the wavelength of the subsequent mode m+1 mode. The wavelength interval can also be converted into frequency interval ν_{FSR} by using,

$$\nu_{\text{FSR}} = \frac{c}{\lambda_{\text{FSR}}} \tag{7.7}$$

Quality factor The quality factor (Q) is a dimensionless parameter that describes the ratio of the resonant frequency to the bandwidth of the cavity resonance. A high Q factor indicates low damping at the resonance frequency and a stable oscillation within a small range of frequencies (i.e., narrower bandwidth). Q can be calculated by:

$$Q = \frac{\lambda}{\Delta\lambda} \tag{7.8}$$

with λ as the mode wavelength and $\Delta\lambda$ as the FWHM of the mode.[243]

Finesse The finesse F is the relation of how narrow the resonant peak is in relation to its frequency distance, which is calculated with the FSR and the FWHM in the frequency regime:

$$F = \frac{\nu_{\text{FSR}}}{\Delta\nu_{\text{FWHM}}} \tag{7.9}$$

7.2 Cavity layer properties

In the following, the properties of the SiQD-cLEDs are presented. The differences and challenges compared to normal SiQD-LEDs are exemplified in detail. As already mentioned, the SiQD-LED implemented in the Fabry–Pérot resonators of Figure 7.1. FP resonators' top and bottom mirrors are typically made of dielectric mirrors (DBR) or thin metallic layers. DBR mirrors consist of multiple alternating high and low refractive index semiconductor or dielectric layers.[244] Due to the high number of layers and the rising manufacturing complexity, we used metallic mirrors. However, a DBR mirror can exhibit a higher reflectivity of close to $100\,\%$.[244] For metal mirrors, both the reflectivity and the absorbance of the mirrors depend on the thickness of the metal layer.[245] For the FP resonator in this thesis, a thin Ag layer was chosen because the top electrode of the SiQD-LED is already made of an Ag layer. Due to the stacked structure

with Ag and SiO_2 layers as first layers, the ITO layer itself must be sputtered on top of those layers. As a result, it differs from the standard ITO layer, which will be characterized in the chapter. The remaining LED structure, layer thicknesses, and materials remained unchanged. Nevertheless, for calculating the optical path length, the refractive indices are needed and obtained by ellipsometry.

7.2.1 Silver reflectivity

FP resonators need one fully reflective mirror, while the second mirror has to be semi-transparent. In SiQD LEDs, the cathode consists of a thick silver layer of 100 nm, which advantageously has a very high reflectivity. Therefore, it was multi functional and used as a mirror and for electron injection simultaneously. For the semi-transparent second mirror, a thin Ag layer with thicknesses of 40 nm, 45 nm, and 50 nm have been tested to confine the cavity.

In the fabrication process, the glass substrate was cleaned the same way as the industrial ITO substrate. On the clean substrate, the Ag layer was deposited using thermal evaporation. Afterward, the reflectivity was measured in normal to the layer using a reflection probe and is presented in Figure 7.2. The data was measured by using a Thorlabs Ag mirror (PF10-03-P01) as a reference. The 100 nm thick Ag layer exhibited the highest reflectivity, whereas the thinnest 40 nm showed the lowest value. For low wavelengths below 450 nm, the reflectivity is better than the reference mirror, hence a value above 100 % was reached. After a drastic drop in reflectivity at ca. 450 nm, it gradually increases with wavelength. The reflectivity data at around 700 nm is presented in Table 7.1, due to the SiQD emission peak around that wavelength. In addition to the reflectivity R, we calculated the transmittance T of each silver layer by using the equation [8]

$$T = 1 - R \tag{7.10}$$

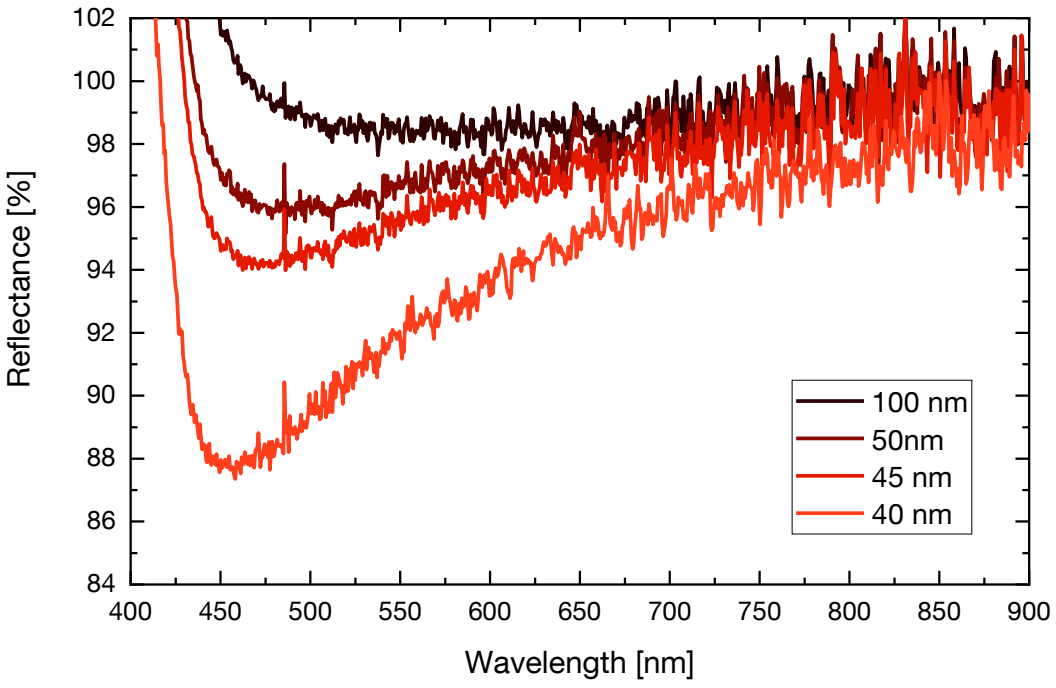

Figure 7.2 Reflectance spectra of silver thin films with 40 nm, 45 nm, 50 nm, and 100 nm.

Table 7.1 Reflactance R and transmittance T at a wavelength of 700 nm for all measured silver layers.

Ag	100 nm	40 nm	45 nm	50 nm
R	99 %	96.1 %	97.8 %	98.5 %
T	1 %	3.9 %	2.2 %	1.5 %

7.2.2 Sputtered ITO anode

The ITO anode was deposited on top of the thin silver film and SiO_2 spacer layer. RF sputtering with Ar as the gas source was employed for deposition. A shadow mask was used during the sputtering process to combine the ITO deposition and structuring in a single step. The shadow mask had a U-shape with 3 mm wide openings to achieve the same structure as the industrial ITO. The important metrics of the sputtered ITO are the transmittance and the sheet resistance, which were 85.7 % and 48 Ω/□ respectively. The transmittance of the sputtered ITO was lower than the industrial (95.6 %) and the sheet resistance was higher (48 Ω/□ to 15 Ω/□), which made the self-sputtered ITO anode worse than the industrial ITO anode. Generally, a high transmittance enhances the optical output of the LED, while the sheet resistance affects the serial resistance of the LED. The sheet resistance causes a voltage drop before the LED and increases the turn-on voltage.

Another important parameter of the ITO electrode is the work function W_F. Only if the ITO and the next layer's work function are similar, they form an Ohmic contact, which eases the charge injection into the device. The industrial ITO substrate had a work function of 4.7 eV that results in a small potential barrier to the PEDOT:PSS ($W_F = 5.2$ eV). The work function of the sputtered ITO electrode was obtained by a Kelvin probe measurement. The measurement was calibrated by a highly oriented pyrolytic graphite (HOPG) measurement. In Figure 7.3, the result is shown. After an initial drift, it showed a work function of 4.92 eV. The measured work function of our sputtered ITO is 0.22 eV higher than the industrial one and improves the charge injection of holes into the PEDOT:PSS layer. Nevertheless, this positive effect is canceled out by the three times worse sheet resistance and the lower transmittance.

ITO anode reference device

To prove the suitability of the sputtered ITO electrode for LED fabrication, a sputtered ITO SiQD-LED was compared to an industrial ITO SiQD-LED. The results of the two SiQD-LEDs are shown in Figure 7.4, where the self-sputtered ITO is colored black and the industry ITO red. For the $J-V$ curve in Figure 7.4a), three characteristics for the sputtered black curve are recognized in comparison to the industry ITO. Firstly, an increased current in the reverse direction, secondly, a higher current flow for small voltages, and thirdly, a reduced current in the forward direction. The first two points were caused by an increased leakage current, which was assigned to surface roughness or agglomeration in the fabrication. The purchased ITO layers were bought polished at the top side to minimize surface roughness, whereas the sputtered ITO layers were directly used after sputtering without further treatment. The third point, the current deviation in the forward bias regime, was caused by the higher sheet resistance of the sputtered ITO. According to Kirchhoff's voltage law, the voltage across the diode and series ITO resistance adds up, hence introducing a flatter slope to the $J-V$ curve.[8] The irradiance curve in Figure 7.4b) showed a lower irradiance with an increasing gap between the two ITO LEDs for increasing voltages. The maximum irradiance for the sputtered ITO LED was 474 µW cm^{-2}, which was lower than for the industry ITO LED with a maximum at 780 µW cm^{-2}. Despite the differences, both devices showed the same turn-on voltage at 1.5 V, highlighted in the inset. The EQE in Figure 7.4c) shows the EQE curves. The EQE of the sputtered LED increased less strongly to a maximum of 0.34 %, whereas the industrial ITO LED reached an EQE of 0.79 %. Also, at the starting point where the turn-on irradiance is reached is the industrial ITO EQE higher than the sputtered one, which is caused by the higher leakage current for low forward voltages(Nr.2 in Figure 7.4a)). The EQE maximum has also shifted from 2.95 V to 3.6 V for the sputtered ITO. After the maximum EQE, the

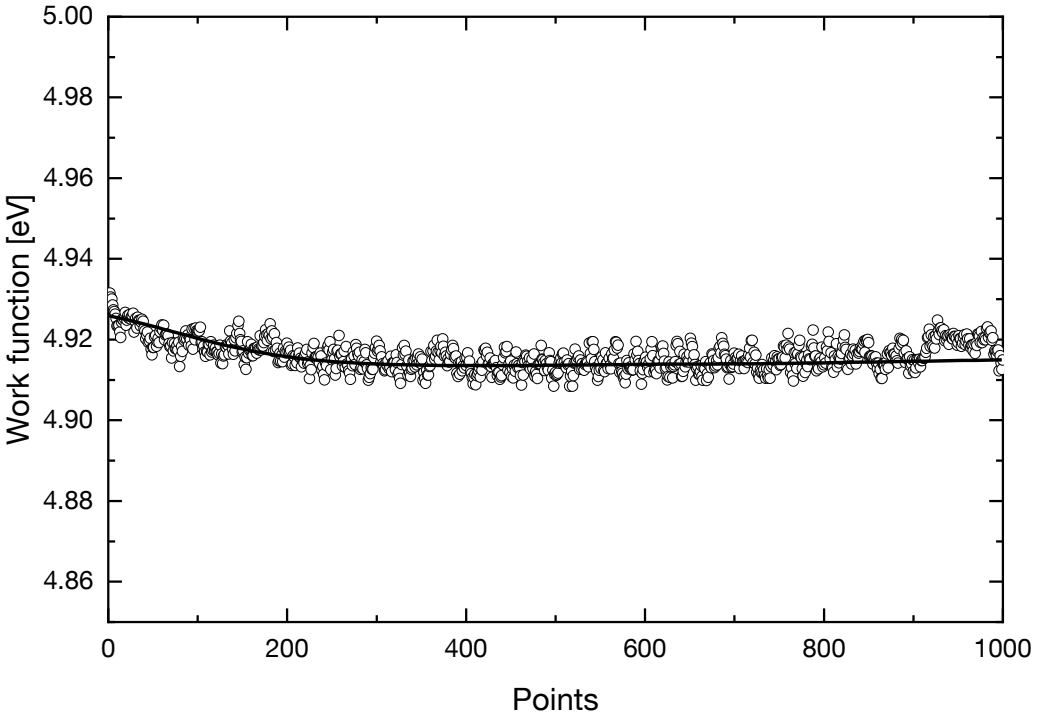

Figure 7.3 Work function of sputtered ITO measured for 1000 points. After an initial decrease, the W_F remains constant at $\sim$4.92 eV.

decrease is not as pronounced as for the industrial ITO and for even higher applied voltages above 4 V, the self-sputtered ITO showed a higher EQE than the industrial one.

ITO edge effects

As mentioned in the previous section, the ITO was used as sputtered without further treatment. For this reason, an investigation of the structural and optical properties has been performed with profilometry and a luminance camera. A profile across the ITO structure is shown in Figure 7.5a). The target structure, width and height are highlighted by the dashed lines. The real profile across the ITO electrode was broader and became thinner at the edges. There were also peaks of up to 50 nm on the surface, which might cause short circuits. The ITO structure broadened at the edges as a result of the used shadow mask for the sputtering process. By a non-perfect edge contact of the shadow mask, some ITO became sputtered underneath the mask and the structure gradually broadened. Furthermore, the used shadow mask was curling up over time by the amount of sputtering depositions. The sputtered ITO and the mask material exhibited different thermal material coefficients, and during sputtering the layers are expanded at different rates. As a result, the mask was lifted up from the sample and deteriorated the ITO edge definition. To avoid a big gap, the mask was held in place magnetically, nevertheless, the slight gradient at the edges could not be prevented. In contrast to the sputtered ITO, a profile of the industrial ITO is shown in Figure 7.5b). The profile showed sharp edges and a smoother surface than the sputtered one. The sharp edges were obtained by a standard photolithography process. In the case of the SiQD-cLED fabrication, photolithography was impossible due to the device's underlying Ag and SiO_2 layer. The adhesion of the Ag layer and the porosity of the SiO_2 prevented using ultrasonic baths for sample cleaning after a photolithography step. Furthermore, the excess ITO is usually etched by HCl, which is also a component of a silver etching solution (HNO_3:HCl:H_2O, 1:1:1).[116, 246] This prohibited the use of an ITO etch. After fabricating

SiQD-LEDs with both ITO layers, their luminescence behavior in the area was investigated. Luminance images of both sputtered and industrial SiQD-LEDs are depicted in Figure 7.5c) and d) with an applied voltage of 5 V. In c) a mean luminance of 6.71 cd cm^{-1} was detected. The intensity decreased towards the edges of the ITO strip, coinciding with the height gradient in the sputtered ITO profile. The thinner ITO exhibited a higher resistance, i.e. less conductive, resulted in a smaller current density. The luminance behaved similar to the current density and resulted in a non homogeneous luminance distribution. In contrast to that is the luminance distribution of the industrial ITO LED, where a higher mean luminance was obtained with 7.10 cd cm^{-1} and a lower standard deviation of 0.77 cd cm^{-1} compared to 0.88 cd cm^{-1}. The homogeneous luminance distribution is beneficial for the lifetime due to the equally distributed current in the lateral direction.

7.2.3 Refractive indices of individual cLED materials

The SiQD-cLED consists of many different layers with varying refractive indices and thicknesses. For the calculation of the cavity mode by using Equation 7.4, the correct optical pathlength is essential. For this reason, the refractive index n_i of each material and layer was measured. The thickness was obtained by stylus profilometry as described previously. The measurements of the refractive indices were performed with an ellipsometer under different angles (65°, 70°, and 75°) for at least three samples each. Silicon wafers with a native oxide layer were used as substrates. The measurements for the refractive indices n are shown in Figure 7.6a) in the visible wavelength regime from 400 nm to 900 nm. For all materials except the ITO layer, a Cauchy model $n(\lambda) = A + B/\lambda^2 + C/\lambda^4$ with A, B, and C as constants and λ as the wavelength was used to fit the measurement data. The Cauchy model fitted most of the data, as it performs well for transparent thin films.[247] The extinction coefficient k was 0 for all Cauchy fits. The ITO layer was fitted with a Drude-Lorentz model because as a metal oxide the Cauchy model does not fit

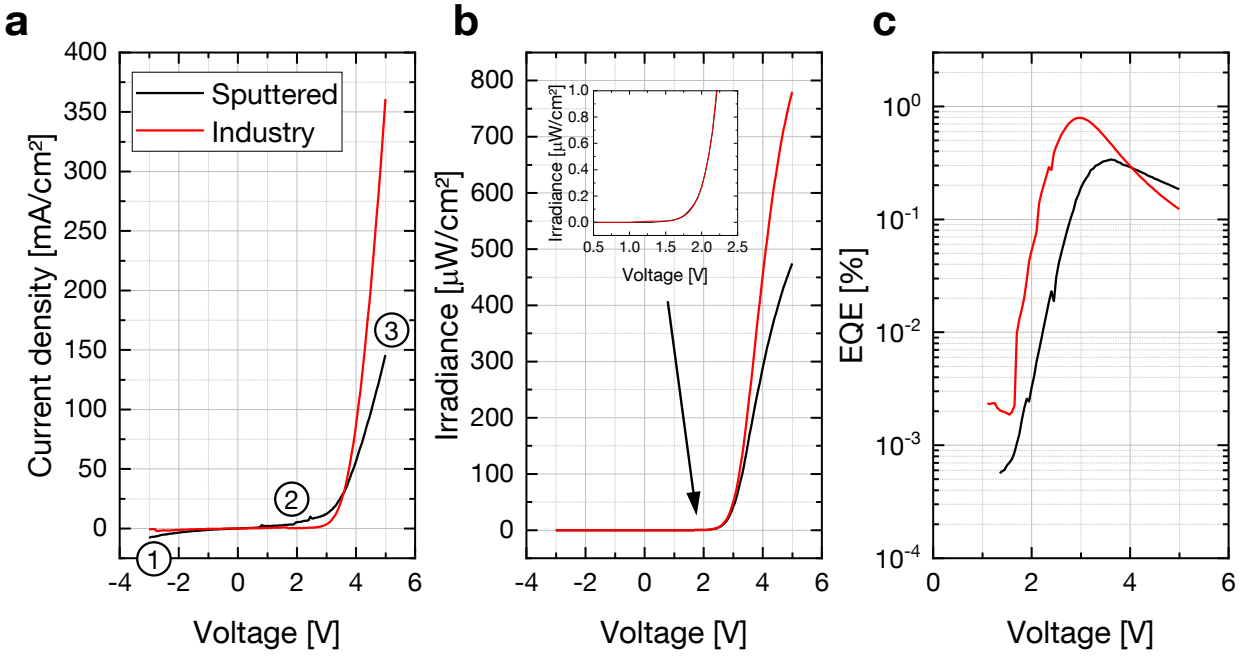

Figure 7.4 Comparison of the self-sputtered LED in black color and the purchased industrial LED in red color. a) $J-V$ characteristic of both LEDs. At (1) and (2), a higher leakage current is observed for the sputtered ITO. At (3), a ∼200 mA cm^{-2} lower J is driving through the LED at 5 V. The legend applies to all three plots. b) The irradiance of the self-sputtered ITO LED is maximum at 474 µW cm^{-2} compared to 780 µW cm^{-2} for the industrial, while the turn-on voltage is 1.5 V for both. c) The EQE maximum is lower for the self-sputtered LED (0.34 % to 0.79 %). For voltages above 4 V, the sputtered ITO shows superior EQE.

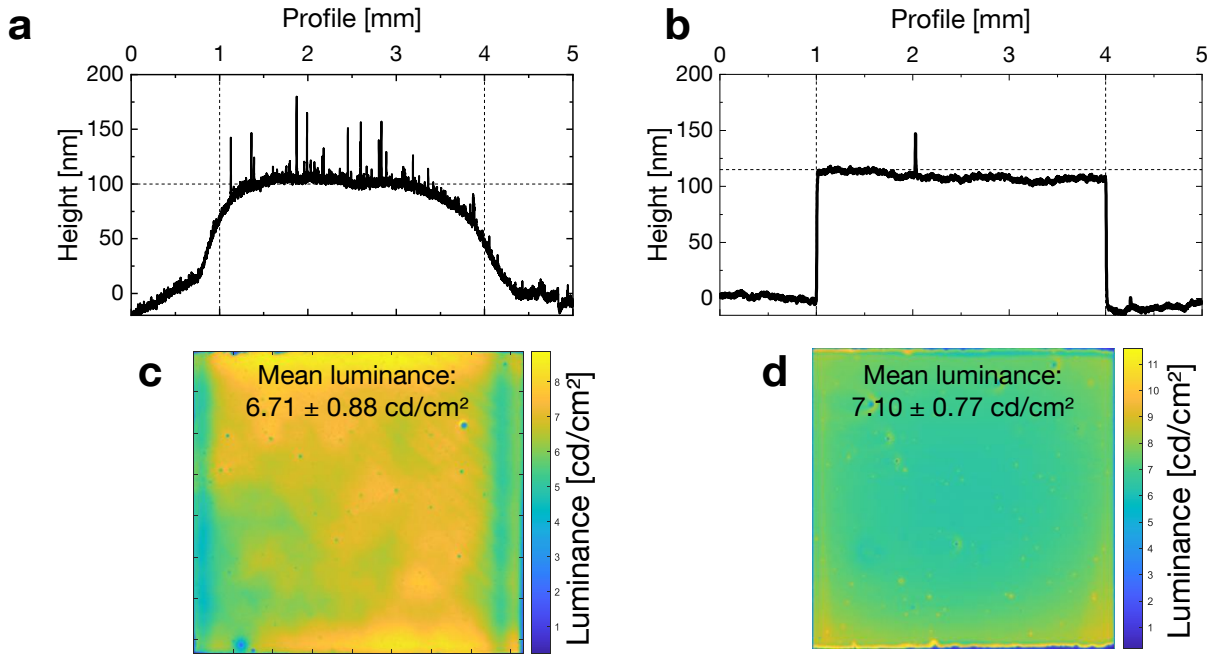

Figure 7.5 a) Height profile obtained by stylus profilometry from a sputtered ITO sample. The dashed lines show the aimed profile width and height. b) Profile of an industrial ITO structure that matched the manufacturers width and height. c) The luminance camera measurement shows a decrease of luminance towards the edges, where the ITO becomes thinner. d) Luminance image of an LED with industrial ITO. It shows a higher luminance and fewer edge effects, which also reduces the standard deviation (SD) in comparison to the image in c).

well enough.[248] The values at 700 nm are presented in Table 7.2, which match well to literature, except for the SiQD layer. Our Cauchy fit resulted in a n of 1.92, whereas Choi et al. obtained a value between 1.48 and 1.59.[249] One has to mention that they used various annealing temperatures and thicknesses to measure the SiQD layer, which explains the discrepancy between their values and ours.

Table 7.2 The table gives the refractive index n of each material used in the cLED. The values are taken at a wavelength of 700 nm. The literature values $n_{\text{Literature}}$ are also at the same wavelength.

	SiO_2	ITO	PEDOT:PSS	Poly-TPD	SiQDs	ZnO
n	1.46	1.96	1.51	1.78	1.92	1.58
$n_{\text{Literature}}$	1.47 [247]	1.83 [248]	1.49 [250]	1.74 [251]	1.59 [249]	1.62 [252]

7.2.4 Layer transmittance

Transmittance is essential for LEDs, especially for cLEDs. In normal SiQD-LEDs, the emitted photons must pass through the transport layers once, while in the cavity structure, it takes several round trips between the two silver mirrors. Each time the photons pass a layer, some light is absorbed by the layer and reduces the overall light output. On top of the thin outcoupling silver mirror, a SiO_2 optical spacer layer was evaporated to tune the optical path length and as an insulating barrier to avoid current leakage through the silver. The transmittance of all layers is presented in Figure 7.6b). As mentioned, the SiO_2 layer is added with a transmittance of 99.4 % and the sputtered ITO layer exhibited a lower transmittance of 85.7 % than the industrial one. The values were recorded at 700 nm and all other layers, i.e. PEDOT:PSS, Poly-TPD, SiQD, and ZnO, remained unchanged. When the emitted photons travel from one mirror to the other mirror and pass the whole cLED stack, then only 80.2 % is transmitted or 19.8 % of the intensity is lost per round trip. Thus, the cLED will lose intensity with every cycle the light travels.

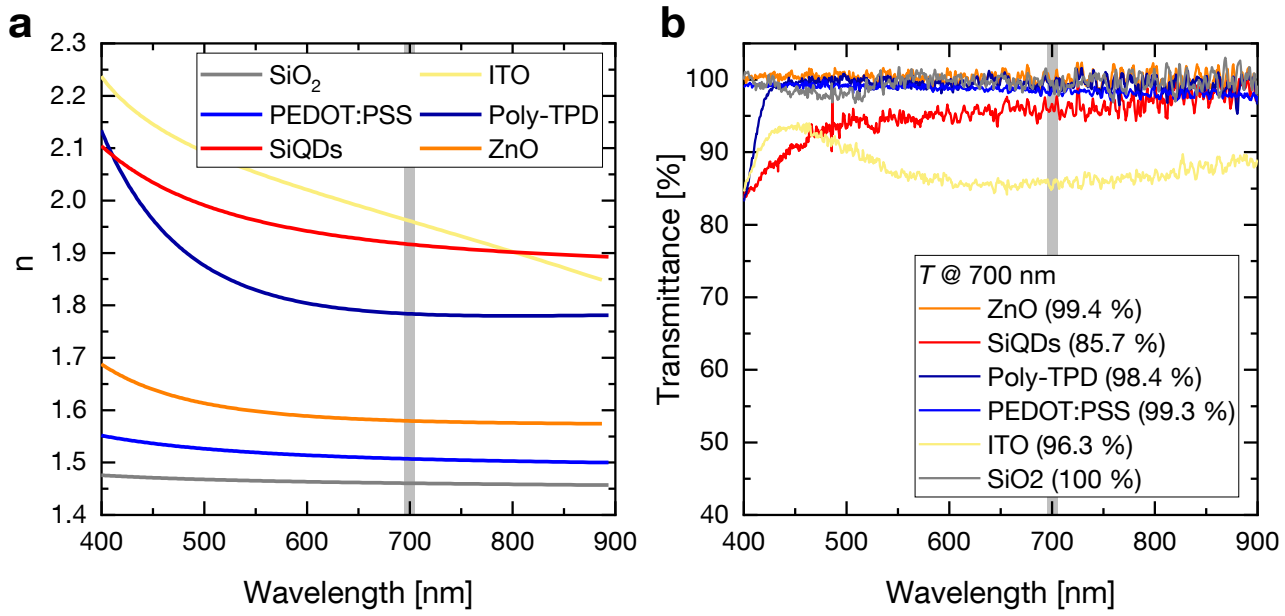

Figure 7.6 a) Fitting results of the refractive indices n for all individual cLED layers in the visible wavelength regime. b) Transmittance in the visible range for all layers. The grey area highlights 700 nm±5 nm, which is about the EL emission of the SiQD-LED in both plots

7.3 Normal SiQD-LED reference devices

To validate the SiQD-cLED devices, reference devices without a cavity were made to see the normal output of the SiQD-LEDs. Therefore, the ITO was sputtered on a bare substrate to have the same device without the bottom Ag outcoupling mirror and SiO_2 spacer. Six control LEDs were fabricated and the performance results are illustrated in Figure 7.7.

The current density is plotted as a function of voltage in Figure 7.7a). The mean value and the standard deviation were added to each measurement point as a blue dashed line. The J deviation of all six LEDs is not even one order of magnitude, which proved the good reproducibility of the SiQD-LEDs. For the same LEDs, the irradiance is illustrated with the standard deviation in b). For high voltages, the maximum irradiance spread was about 200 µW cm^{-2}. Nevertheless, the current density and irradiance showed the expected LED behavior with good irradiance values. The high irradiance was important because of the losses of each photon round trip inside the cLEDs. In Figure 7.7c), the EL spectrum of control LED 3 for positive applied voltages from2 V to 5 V is depicted. As for all other SiQD-LEDs shown in the chapter 4, the spectrum peak emission is blue-shifting with increasing applied voltages. In d), the FWHM of the EL spectrum is given for the same voltages and also reveals the FWHM broadening characteristic. Again, the broadening of the EL spectrum is denoted by the size distribution of the SiQDs. From 120 nm at the turn-on, the EL broadens up to 148 nm at 4.5 V. Overall, the reference LEDs showed sufficient irradiance, essential for fabricating SiQD-cLEDs.

7.4 Reflectivity of cavity LEDs

To verify the optical properties and the successful fabrication of the SiQD-cLEDs, the optical cavity properties, i.e. the reflectivity spectra, were investigated. For this purpose, every cLED was measured using a reflection probe, where the broadband light input is multiply reflected by the cavity and only the light at the cavity modes are transmitted back to the spectrometer. This is a destruction free approach to validate the

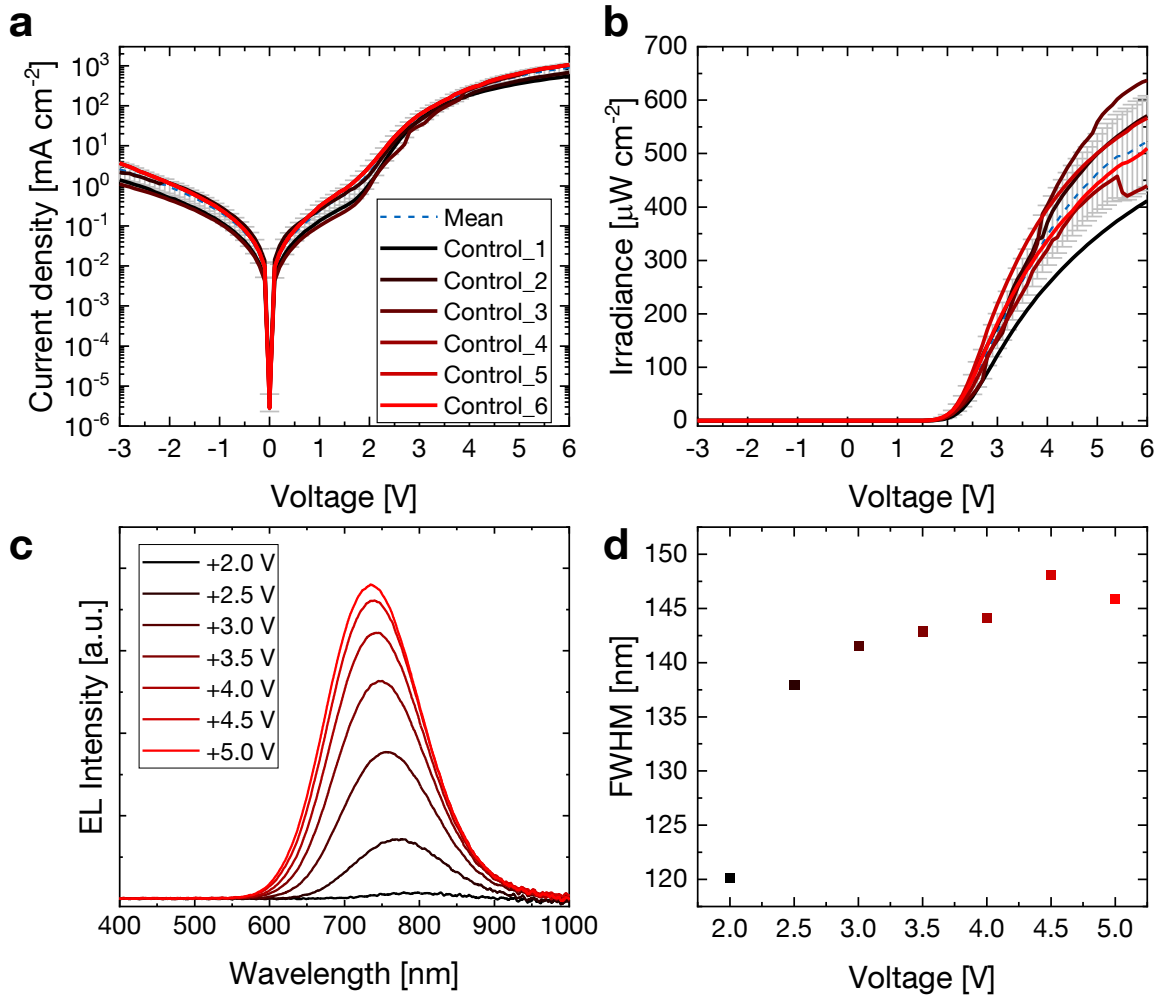

Figure 7.7 Reference LEDs with sputtered ITO. a) Current densities as a function of the applied voltage. The legend also applies to b). The grey bars represent the standard deviation of the mean for each voltage. b) Irradiance measurements as function of the voltage. c) EL spectrum of control LED 3 from the turn-on until the maximum emission at 5 V. As usual, the EL spectrum shifts towards a lower wavelength, i.e. higher energies. d) FWHM of the EL spectra in c) as a function of voltage. With increasing voltage, the spectrum broadens.

correct cavity length, tuned by the SiO_2 spacer layer. By using Equation 7.4, the refractive indices, and the thickness of the layers with SiO_2 thicknesses between 200 nm to 500 nm, the cavity modes were estimated and compared with the measured reflectance spectra in Figure 7.8a). The reflection spectra showed a consistent reflection with multiple peaks at the cavity modes, where the light is coupled out. The estimated modes m = 2–6 were indicated by the circle at each SiO_2 thickness and the vertical dashed lines.

An offset in wavelength of the calculated modes to the measured modes was observed and presented in Figure 7.8b). The mean deviation of the real and the estimated modes are between 34 nm and 43 nm for all modes in the visible regime. For the mode calculation, the penetration depth effect in the silver layers was neglected and caused some deviation from the real behavior. If the penetration depth is included, the emission modes shift towards lower wavelengths for thinner cavities, while for thicker cavities, the modes shift towards higher wavelength.[242] Furthermore, layer thickness variations, roughness, tilt, and curvature introduced in the fabrication process cause mode shifting due to the changing optical pathlength.[253] A common source of non homogeneous film thicknesses is the cosine distribution of the PVD process, used for SiO_2 deposition.[119] The relevant modes for SiQD-cLEDs are m = 2 and m = 3, because they match the emission range of the SiQD-LED from ca. 550 nm to 980 nm. For those two modes, the mean

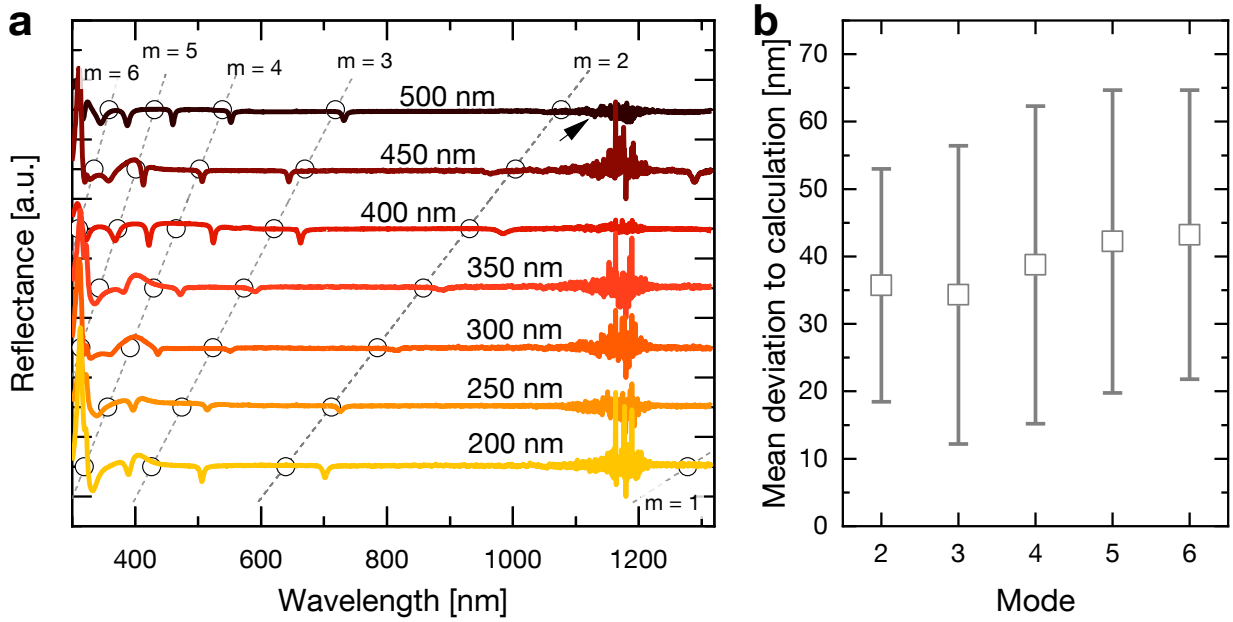

Figure 7.8 a)Reflection spectra of full cavities with a 50 nm silver outcoupler. The dashed lines represent the estimated modes in the spectrum corresponding to each SiO_2 spacer thickness. The arrow at 500 nm indicates mode 2. b) Mean deviation per mode for all thicknesses of the calculated modes to the measured modes in a).

deviation is 36 nm for m = 2 and 34 nm for m = 2. Even if the cavity's optical path length is not perfect, the cLED emission is strong enough to detect a signal.

In order to show the color tuning ability, we compared the mode m = 2 in the EL spectral range of the normal SiQD-LED. Suitable emission with SiO_2 spacer thickness and m = 2 were from 200 nm to 350 nm. We analyzed the position, the FWHM, and FSR of the corresponding reflectance spectra with m = 2 in the region of interest and presented the results in the appendix in Table 1. All spectral peaks exhibited a FWHM below 25 nm, presuming an optically FWHM reduction of the EL (120 nm) by a factor of at least 4.8. Furthermore, with increasing film thickness, the FSR was inclining for each SiO_2 thickness. That means a better spectral purity was achieved when the SiO_2 spacer became thicker and the mode FSR increased.

7.5 Electroluminescene spectra of full cavity devices

The FP cavity is built to reduce the spectral linewidth, i.e. the FWHM, of the SiQD-LEDs. To show the effect of the SiQD-cLED, the EL spectrum of a reference LED was compared to a cLED with a 40 nm silver outcoupler and a 350 nm thick SiO_2 spacer layer. Through the reflectance analysis in the appendix in Table 1, the emission modes are known at wavelengths of 606 nm and 898 nm for m = 2 and m = 3, respectively. The EL spectra with increasing applied voltages of a normal SiQD-LED are shown in Figure 7.9a) and EL spectra of the cLED are presented in Figure 7.9b). The normal SiQD-LED EL spectrum was blue-shifted with increasing voltages and exhibited a broad spectral distribution. In contrast, the EL spectrum of the cLED with modes at m = 2 and m = 3 only increased in amplitude, and no blue shift was observed. The cavity modes were located at 638 nm for m = 3 and 950 nm for m = 2, which is shown in detail in the inset. For further illustration of the stable wavelength emission, photographs of both LED types were made for increasing voltages and are depicted in Figure 7.9c) and d). For the photos, a higher voltage range from 4 V up to 8 V was needed to have sufficient cLED emission for the camera to detect any image. In c) the normal SiQD-LED color was changing from 4 V towards a more orange appearance at 8 V, while in d) the

cLED color remained red for the entire voltage range. The peak of mode m = 2 is in the IR region and exhibited very little intensity, so in the photographs only the mode m = 3 is visible.

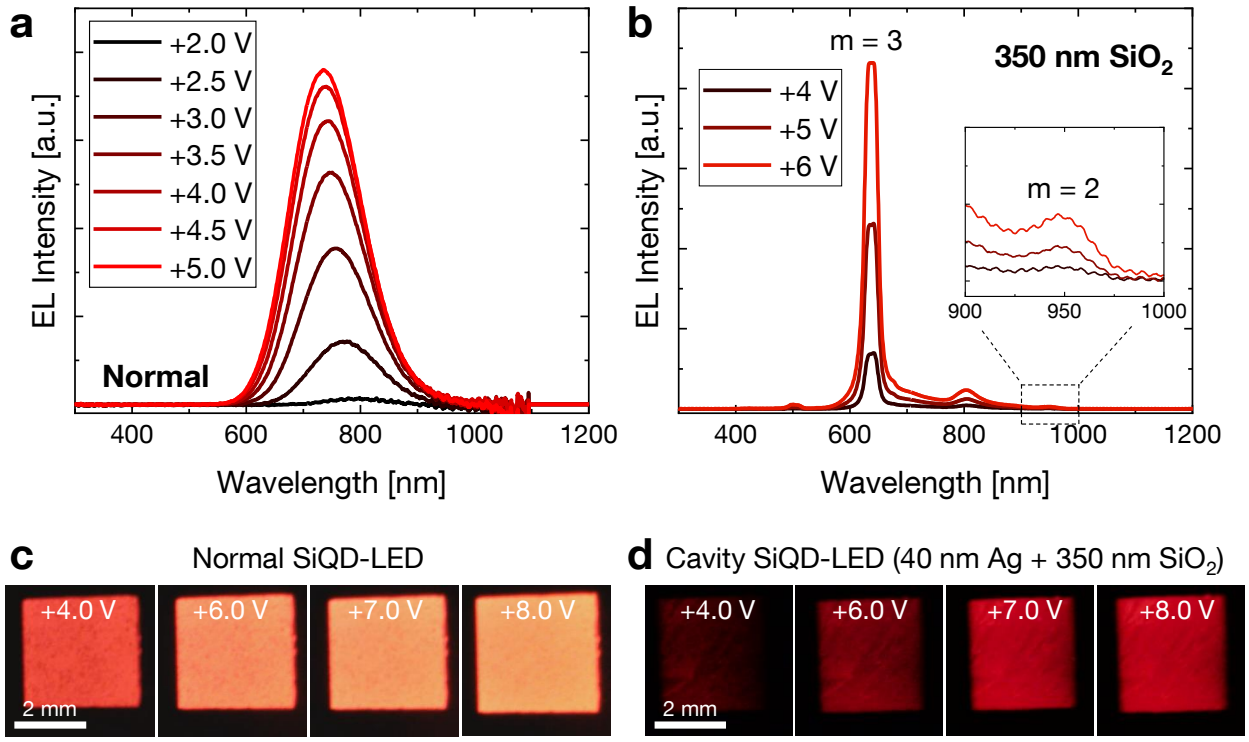

Figure 7.9 a) EL spectrum for increasing voltages of a normal LED. b) EL spectrum of a cavity SiQD-LED with a SiO_2 spacer of 350 nm and 40 nm silver outcoupler. The inset shows the EL emission at 2.5 V and the mode number m is given above the corresponding peak. c) Photographs of the LED in a). The color changes from red to a more orange emission. d) Photographs of the cavity SiQD-LED, where no color change is visible for higher applied voltages.

Another cLED with the same thickness as in Figure 7.9b) was fabricated to account for sample variations. Due to fabrication variations, the cavity turns out to be thicker than the nominal thickness, the emission peak shifts red towards higher wavelengths, while when the cavity becomes thinner, the mode emission shifts blue toward lower wavelengths. After the fabrication and measurement, both samples were compared. Their EL spectra are depicted in Figure 7.10 and demonstrated the described effect. Two strong modes at 638 nm for cLED-1 and 890 nm for cLED-2 are shown in front of the normal LED emission. On top as a blue line, the simulated spectrum for the cavity device was added with cavity modes at 619 nm and 941 nm. In the case of the 350 nm SiO_2 thickness, m = 2 or m = 3 can dominate the emission depending on the actual thickness. For cLED-1, m = 3 was dominating because the LED emission exhibits higher intensity at 638 nm than at 950 nm, where m = 2 is present. On the other hand, for cLED-2, m = 2 exhibited a higher intensity due to its position at 890 nm with a small emission peak at m = 3 at 602 nm.

The relevant modes for applications are in the spectral range of the SiQD-LED, which is between 550 nm and 950 nm. All other modes are not visible due to the lack of SiQD excitation. To illustrate the spectral tuning effect for different spacer thicknesses, we fabricated cavity devices with 50 nm increasing step size from 200 nm to 500 nm. Their EL spectra are illustrated in Figure 7.11. For the cavities, m = 2 and m = 3 are relevant and plotted separately for clarity. Emission peaks with m = 2 spread from 650 nm to 950 nm, while the emission with m = 3 were from 600 nm to 700 nm. In both cases, a blue shift with decreasing spacer thickness was observed, which was expected from Equation 7.4. For the 450 nm SiO_2 spacer sample, two emission peaks were observed. The mode at 625 nm correlated to mode 3 and the mode at 950 nm correlated to mode 2. The two modes illustrated the limits of the normal SiQD-LED emission. Some other

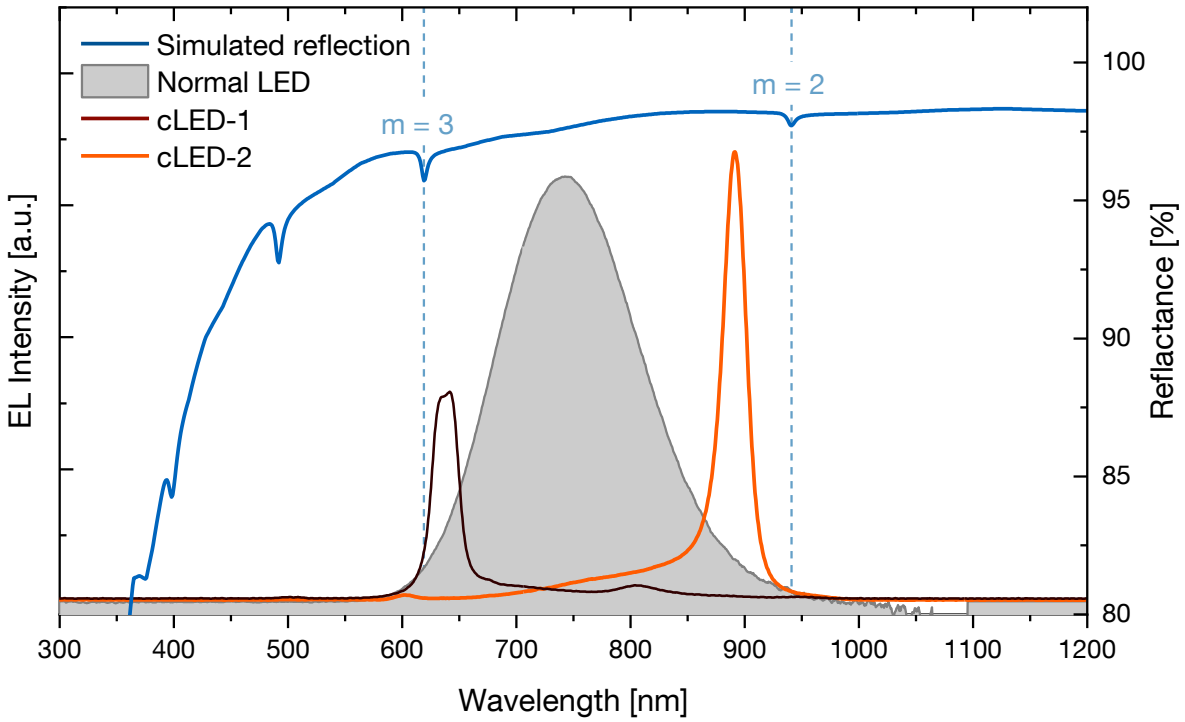

Figure 7.10 EL spectra of two cLEDs with a 350 nm thick SiO_2 spacer and a normal SiQD-LED at the bottom. The simulated reflectance is plotted on top.

EL spectra exhibited an additional broadband emission to the mode. As already mentioned, the delicate fabrication process can cause defects and the broad emission was leakage emission from the SiQD-LED. In Table 2 in the appendix, the emission peaks were analyzed for the highest intensity concerning their FWHM and the Q-factor. Unlike what was presented in Table 1 for the optical reflectance spectra in the appendix, the modes for the EL had a much higher FWHM around 25 nm to 40 nm but with one peak of 105 nm. So far, a FWHM below 10 nm as presented by Cheong et al. could not be achieved, but the reduction from 140 nm to low tens of nm was possible so far.[240] The broad emission also decreases the Q-factor as a measure of the cavity quality.

The FP cavity approach worked, but the broad spectral emission remained an issue that needs further analysis. The big deviation between the optical reflectance and EL emission modes can be caused by multiple effects. Two main parts are probably the optical excitation for the reflectance measurements. For the reflection measurements, a fiber-coupled reflection probe was used, where the six excitation fibers and one detection fiber were merged into one probe with hexagonal orientation and the detection fiber in the center. A Image is given in the appendix in Figure 1. All fibers exhibited a diameter of 400 µm. For the reflection measurements, the single detection fiber was used but for the EL measurements, the six outer fibers were used to enhance the incoming light, thus increasing the signal-to-noise ratio. For this reason, the EL spectrum measurement is more spread across the cLED area and slight thickness variations or defects can decrease the cavity quality and eventually cause the mode to broaden. The thickness profile in Figure 7.12 was measured over a range of 3.3 mm with a 300 µm step size in between the single profiles. The nominal thickness of the full cavity stack is 740 nm as the sum of all single layers (50 nm+400 nm+100 nm+20 nm+10 nm+35 nm+25 nm+100 nm=740 nm). In an ideal device, the thickness would be constant with sharp edges. In the obtained measurement, however, the thickness of the device varies by $\pm$10 nm and becomes thinner at the edge, until the profile does not detect any ITO of the LED at

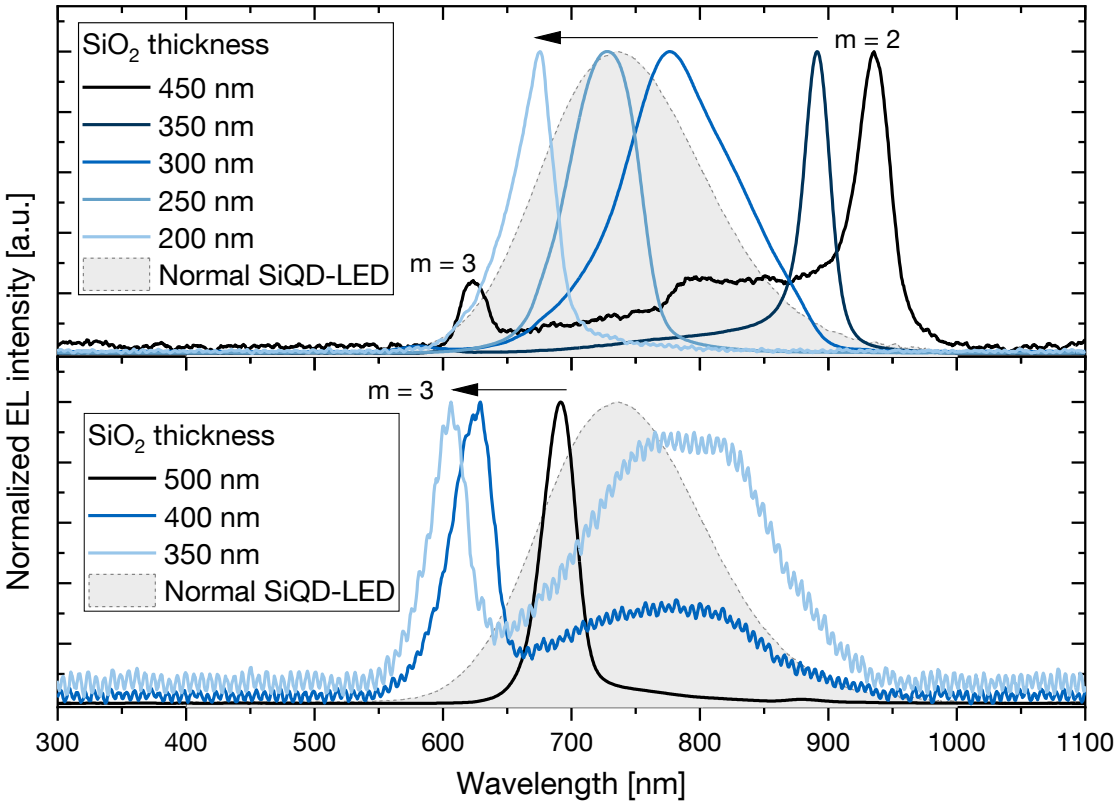

Figure 7.11 EL spectra of all cavity spacer thickness with a 40 nm thick silver outcoupling mirror. In the top graph, mode m = 3 is shown and in the bottom m = 2. For the 450 nm thick SiO_2 spacer, we identify two peaks, one m = 2 at 950 nm and m = 3 at 625 nm. The SiQD-LED excitation is plotted as a grey area in the background.

3 mm. The height difference besides the ITO structure to the cavity center should be 100 nm but it is only about 70 nm, which was explained by edge effects of the structured ITO strip during spin coating.

Ag outcoupler effect

So far, the FP cLEDs with an Ag outcoupler of 40 nm have been presented. In the last section, the spectral purity of the mode emission did not meet the expectations. Higher reflective mirrors should improve the quality of the EL spectrum because the resonant confinement correlates to the energy storage of photons inside the optical cavity. For this reason, SiQD-cLEDs with 40 nm, 45 nm, and 50 nm Ag outcoupler were fabricated and the thickness effect was investigated. As shown in the previous section 7.2.1, the Ag outcoupler reflectivity increases from 96.1 % for 40 nm to 97.8 % and 98.5 % for 45 nm and 50 nm Ag thickness. To show this effect, SiQD-cLEDs with a 500 nm thick SiO_2 spacer were fabricated with different Ag thicknesses. In Figure 7.13a), the reflectance spectra of the cLEDs are depicted. The relevant mode is m = 3, which centers around 709 nm $\pm$ 26 nm, which is labeled in the figure. The analysis of the reflectance spectra is presented in the appendix in Table 3. The FSR was in a similar range between 333 nm for the two thinner Ag layers (40 nm and 45 nm) and 348 nm for 50 nm Ag for all thicknesses at the resonance mode 3, allowing only one resonant mode within the SiQD emission spectrum. In Figure 7.13b), the EL spectra of the cLEDs are depicted for the same 500 nm SiO_2 spacer thickness with an applied bias of 4 V. The cLED emitted with m = 3 around a wavelength of 695 nm $\pm$ 18 nm. Minor leakage emission was observed due to film inhomogeneity discussed in the previous sections. By increasing the Ag thickness, the resonant peak should shift towards a lower wavelength for a few nm in accordance with Ma et al..[242] However, in our

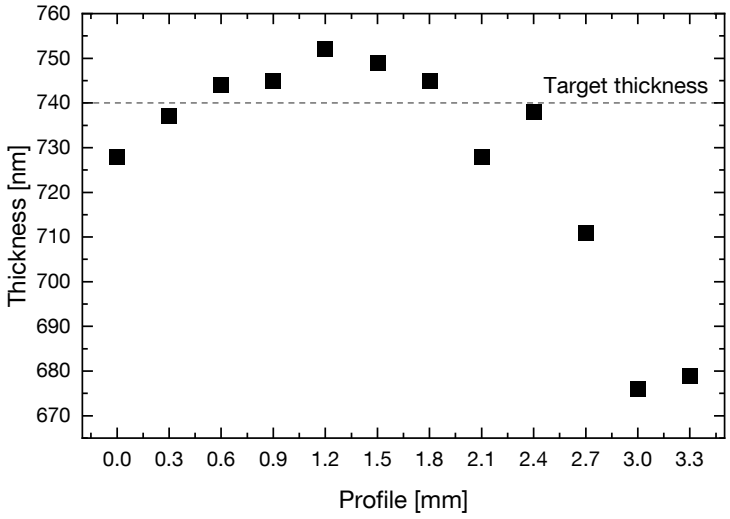

Figure 7.12 Thickness profile across a SiQD-cLED with a 50 nm silver layer and a 400 nm SiO_2 spacer. The step size in between the measurements was 300 µm and the dashed line indicates the theoretical cLED thickness.

measurement data, we did not observe a trend between the peak shift and the silver thickness, which is due to the film inhomogeneity. Nevertheless, the emission bandwidth was narrowed by approx. 24 % with a FWHM of 23 nm and 24 nm than the initial for the 45-cLED and 50-cLED when compared to the 40-cLED with a FWHM of 31 nm.

The Table 4 in the appendix displays the metrics of the three EL spectra. With a thicker Ag layer, the FWHM was decreasing below 31 nm from ca. 140 nm and the Q-factor was increasing to 29.7 for the 50 nm Ag thin film. The Finesse improved with the thicker 50 nm Ag layer by almost 30 % to 61.6. Overall the thicker Ag outcoupler improved the cavity metrics in combination with superior leakage suppression.

7.5.1 Angle-dependent EL spectra

Fabry-Pérot cavity devices show a narrow emission cone than non-cavity devices because the emission is more normally directed to the mirror surfaces.[238] In this case, the emission spectrum of the cLEDs should decline very fast with the detection angle. To test this behavior, the cLED sample was mounted on a rotation stage and the reflectance probe was placed at a short distance, enough to enable the sample rotation. A SiQD-cLED with a 500 nm thick SiO_2 spacer and a 50 nm thick silver outcoupler was used due to its good quality measures. The measurements were conducted at an applied voltage of 5 V to achieve sufficient emission of the cLED and for detection angles of up to 20°. The EL spectra are shown in Figure 7.14. For 0° detection angle or normal, the emission m = 3 at 682 nm and some leakage emission (600 nm to 850 nm) were present. Afterward, the angel was increased in 5° steps by rotation of the sample. The mode emission was decreasing with higher angles, and after 15°, only leakage emission was detected. This narrow emission cone is in accordance with previous publications.[238] Additional to the decreasing intensity, the mode was slightly blue shifting (< 5 nm) with increasing detection angles, which was also in accordance with Equation 7.1 and seen previously for PL emission devices.[240, 254, 255]. Whereas the mode emission was angular dependent, the broad background emission showed no angular dependence.

7.5.2 SiQD-cLED performance

So far, the successful narrowing of the EL spectrum in FP cavity LEDs has been presented. The 50-500 cLEDs showed one narrow mode emission without any leakage. This section presents the performance

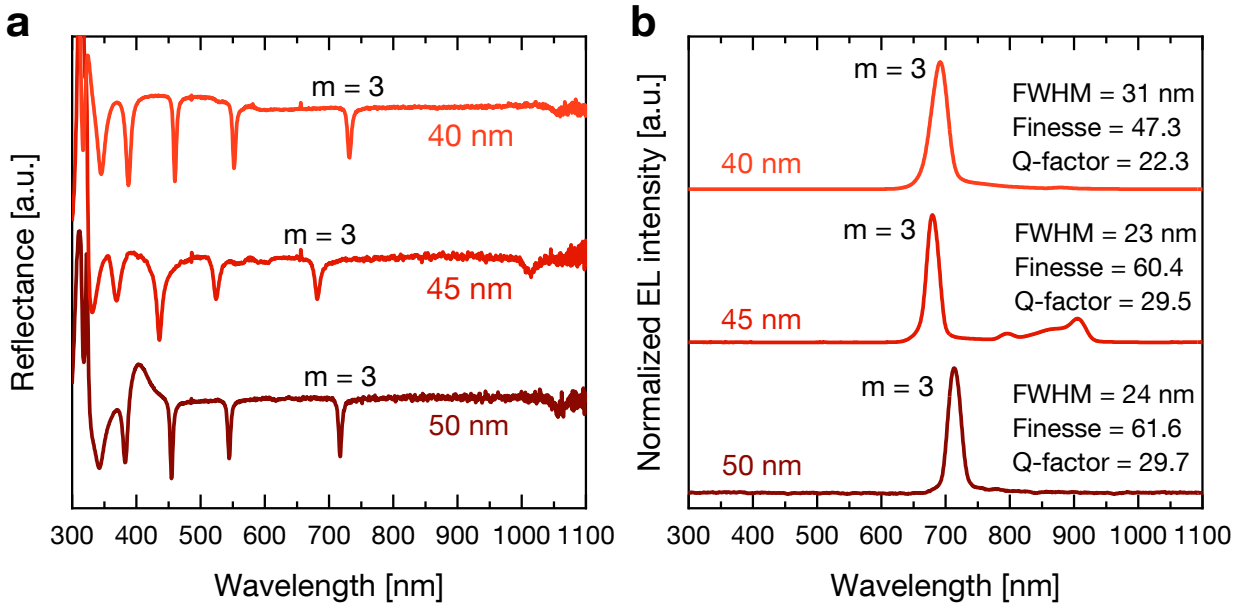

Figure 7.13 Reflectance spectra of cLEDs with 40 nm, 45 nm, and 50 nm Ag outcoupler thickness in a) and the corresponding normalized EL spectra of the same cLEDs in b). All cLEDs were fabricated with a SiO_2 spacer of 500 nm. The FWHM, Finesse and Q-factor were calculated for the EL spectrum for m = 3. The figure is merged and adapted from [157].

of such a 50-500 cLED for increasing voltages. In Figure 7.15, the EL spectrum of the cLED is shown. It exhibited a mode emission around the center wavelength of 713 nm under different applied voltages (i.e. 2 V to 4.5 V) and a Q-factor of ca. 30. In contrast to the normal SiQD-LED, the spectral width was tremendously reduced from ca. 140 nm to ca. 23 nm, but the turn-on voltage was 3.5 V, which is higher than the normal SiQD-LED (<2 V). For the spectral measurements, a voltage step size of 0.5 V was used, which can artificially increase the turn-on voltage but gave benefits in the form of device stability.

In Figure 7.16, the $J-V$, irradiance and EQE of two cLEDs with a 50 nm Ag outcoupler and a SiO_2 spacer of 500 nm are shown. For comparison with the normal SiQD-LEDs, the mean values of the six reference LEDs (Figure 7.7) were added to the graphs. Figure 7.16a) shows the $J-V$ curve of two cLEDs. The cLED curve hardly showed diode behavior for the reverse and low bias regime. The current density in reversed direction and under low applied biases was much higher than the normal LED. J is equalized from a voltage of ca. 3.5 V and higher for cLED-1. The big difference in J for low voltages most likely comes from defects in the individual LED layers. This is further strengthened by the sudden decrease in J for both cLEDs at ca. 3 V, where an agglomerate degraded irreversibly and the current is distributed evenly afterward. In contrast to the cLEDs, the normal LED showed almost no leakage and an exponential increase after turn-on. The irradiance is shown in b) and the normal LED increased exponentially at 2 V, whereas the cLEDs increased linearly at 3 V and 4 V, respectively. The irradiance increase coincidences to start after the current drop in J and reached maximum values of 36 µW cm^{-2} and 60 µW cm^{-2}, respectively. The EQE is depicted in Figure 7.16c), and the cLEDs exhibited a maximum EQE of 0.004 %, which is about two orders of magnitude smaller than the maximum EQE of the normal LED (0.53 %). As mentioned in subsection 7.2.4, the intensity is attenuated with every round trip of a photon and the internal quantum efficiency is to be assumed in the same range as the normal LED. Interestingly, the cLEDs EQE did not decrease after the maximum. After a steep increase at the turn-on, the EQE remained almost constant for all other voltages from 4 V for both cLED samples. At the same time, the EQE of the normal SiQD-LED decreased from its maximum down towards 0.041 % at 8 V, a reduction to

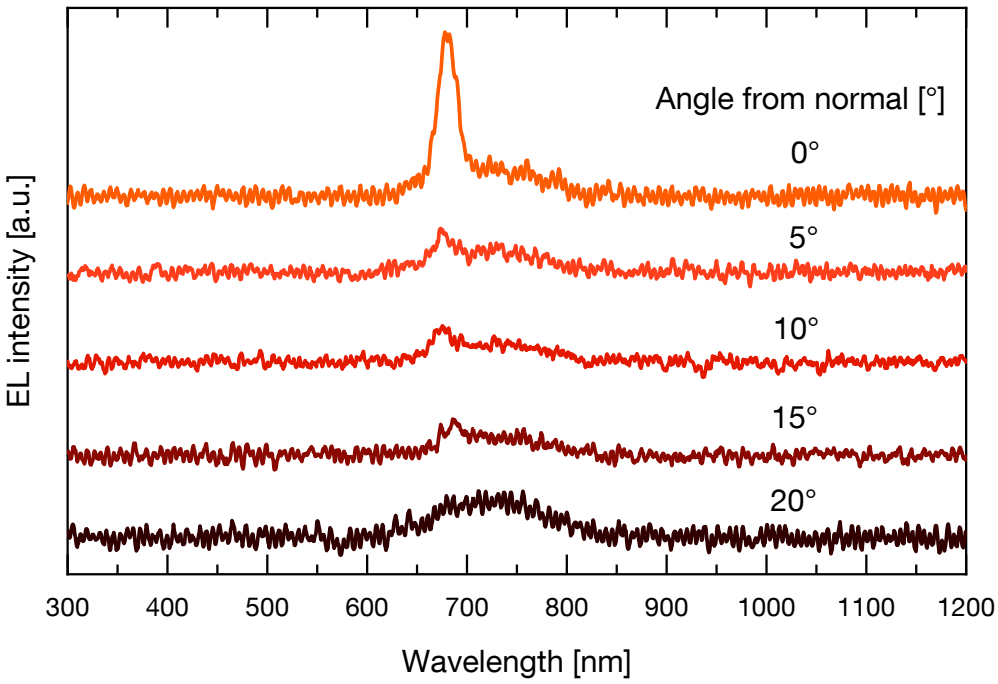

Figure 7.14 Angle-dependent EL spectra of cLED with a 500 nm SiO_2 spacer and a 50 nm thick outcoupler silver layer. The applied voltage was 5 V for all measurements and the spectra are plotted with an offset for clarity. The mode intensity at surface normal (0°) is decreasing with increasing detection angle and after 15° no mode emission is detected. The figure is reprinted from [157].

a tenth. The EQE plateau and missing peak can be explained by the higher leakage current of the cLEDs and the non-exponential irradiance increase.

Both, the low irradiance and low EQE of the cLEDs can be attributed to the low transmittance of the 50 nm Ag outcoupler at the visible wavelength. The high reflectivity needed to fabricate well working cLEDs reduced at the same time the optical output. Brighter SiQDs via a different functionalization method or an output coupler with higher transmittance (e.g. WO_3/W) could improve the cLED intensity.[256–258]

To summarize this chapter, the broad SiQD-LED emission was drastically reduced by the implementation into a Fabry-Pérot resonant cavity. The improved FWHM was as low as 24 nm and could be tuned from orange-red to infrared by adjusting the distance between the semi-transparent outcoupling mirror and the highly reflective device cathode. The approach enables much better control of the emission color for using SiQD-LEDs in future display applications.

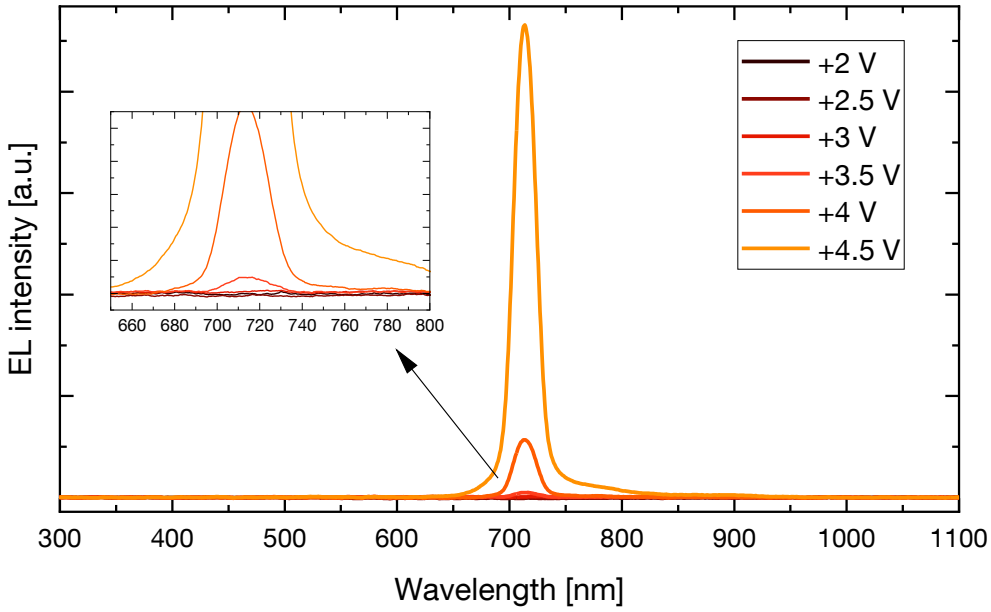

Figure 7.15 EL spectrum of a 50-500 cavity for increasing bias voltages from 2 V to 4.5 V. The turn-on voltage is 3.5 V, which can be seen in the inset. No spectral shift of the peak wavelength at 713 nm was observed for increasing voltages

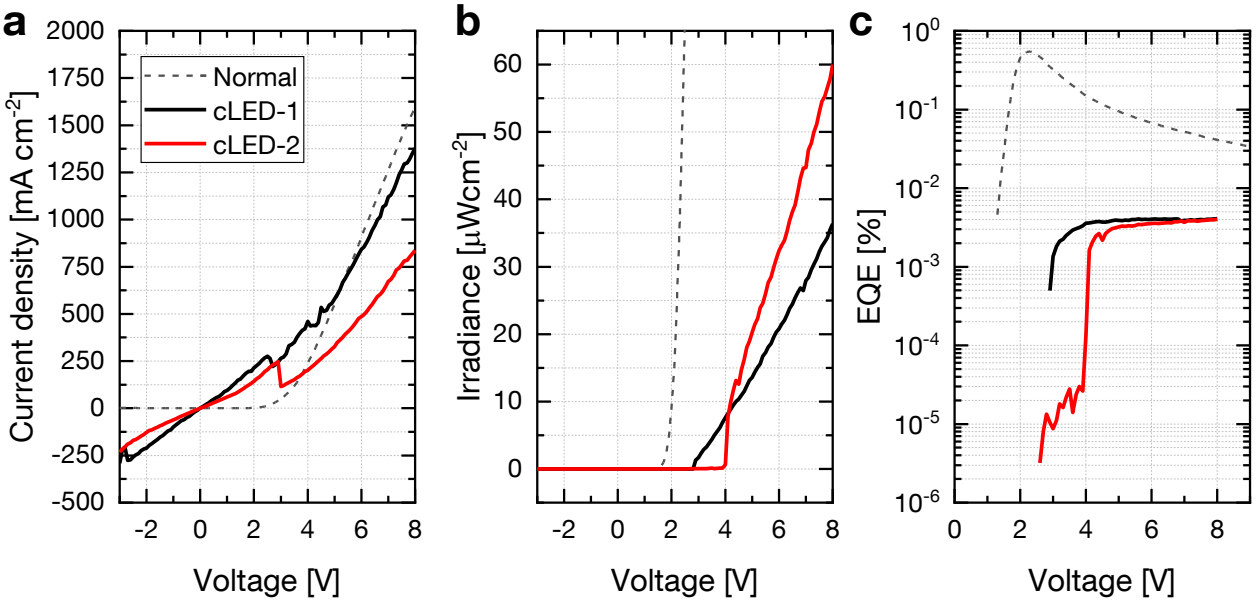

Figure 7.16 Performance measurements of cLEDs with 50 nm Ag outcoupler and 500 nm SiO_2 spacer thickness. The gray dashed line indicates the mean value of the normal reference LED from Figure 7.7. a)The $J-V$ curve is showing a much higher J for the cLEDs than for the normal ones at the reverse and low bias regime. b) Irradiance as function of voltage reveals that the turn-on of the cLEDs happens at higher voltages and the maximum irradiance only reaches 60 µW cm^{-2} at 8 V. c) EQE of cLEDs is 0.004 % about 1 V after turn-on but remains constant for increasing voltages.

8 Summary and Outlook

8.1 Summary

The most used QDs in QLEDs are based on rare and toxic materials such as In, Cd, and Pb, while their amount should be minimized in electronics devices. In the search for non-toxic materials with good optoelectronic qualities for QLED applications, SiQDs are a very promising candidate. In this thesis, we reported on the fabrication, characterization, and engineering of SiQD-LEDs as an upcoming alternative to nowadays used QLEDs. The SiQDs were synthesized from HSQ with a size of ca. 3 nm and functionalized via the OLR method with a hexyl, octyl, or dodecyl alkyl chain in the department of chemistry.

In the beginning, a brief overview of the theoretical background and the used materials are given to understand the challenges and possibilities of hybrid organic/inorganic SiQD-LEDs. Afterward, the fabrication method of such LEDs, like spin-coating or PVD, was discussed. A SiQD-LED consists in this thesis of stacked thin films in the nm range; they were the ITO anode on a glass substrate, the HTLs PEDOT:PSS and Poly-TPD, followed by the SiQD EML, and the ETL made of ZnO. All layers were encapsulated by an Ag cathode, which was vacuum deposited. Apart from the electrodes, all SiQD-LED layers were deposited from solution via spin-coating and the finished devices exhibited a size of 3 mm by 3 mm, defined by the overlap of the electrodes. To ensure repeatability and excellent quality, a reference layer of each material was further controlled every time a SiQD-LED batch was fabricated. Consequently, the thickness was controlled by stylus profilometry to ensure the same device properties. The RMS surface roughness of each layer and the whole LED stack was determined by AFM below 2.5 nm and the optical characterizations revealed high transmittance values above 90 % for all layers, while the Ag electrode was highly reflective.

When a forward voltage was applied to the fabricated SiQD-LEDs, the red-colored emission reached high irradiances of several hundred µW cm^{-2} with peak EQEs around 1 %. The irradiance and EQE were strongly depended on the SiQD batch, wherein the QY can vary from batch to batch due to the synthesis. The EL spectrum depends on the SiQD size and the ca. 3 nm big SiQDs implemented into SiQD-LEDs showed a peak emission around 700 nm with a FWHM of up to 140 nm. The SiQD-LEDs showed a turn-on voltage at around 1.5 V and the EL spectrum shifted towards a lower wavelength while broadening with increasing voltages. Both effects were caused by the size distribution of the SiQDs. Additionally, a lateral intensity gradient was observed in the LED pixel, which resulted from the voltage drop across the ITO anode. The presented SiQD-LEDs showed a lifetime of up to 10 h under high current densities of 111 mA cm^{-1}. Further, inverted SiQD-LEDs with multiple layouts have been analyzed but exhibited much lower irradiances and EQEs than the normal SiQD-LEDs. Their irradiance remained below 60 µW cm^{-2} and the EQEs exhibited maximum values of 0.03 %. Nevertheless, an improved EQE stability, compared to the normal layout, was observed for two devices using PEDOT:PSS as HIL.

In chapter 4, an important topic to improve the SiQD-LED performance was investigated: the effect of the surface ligands on the SiQD-LEDs. We focused on the widely used alky chains, hexyl, octyl, and dodecyl, as functionalization on the SiQDs and how they influence the SiQD-LED optoelectronic performance. At the beginning, the consistent SiQD quality of all three functionalized SiQD samples was ensured and proved that the different ligand length did not influence their intrinsic optical properties. After the fabrication of several SiQD-LEDs for the different ligands, their current density and the irradiance were measured and the EQE was calculated. The increasing ligand length reduced the current in the forward direction through the SiQD-LED by several orders of magnitude. The same effect, albeit to a lesser extent, was observed in the reverse direction. The decreasing current was attributed to the SCLC effect, where the longer ligand exhibited higher potential barriers between the SiQDs, which resulted in a higher degree of

charge localization. The turn-on voltage increased with ligand length from 2 V for SiQD-Hex, to 2.5 V for SiQD-Oct, and 9 V for SiQD-Dodec LEDs. The medium-sized octyl ligand showed the highest irradiance of 734 µW cm^{-2} due to the optimized ratio between charge transport and charge confinement. The same result was observed for the EQE, where the maximum EQE of SiQD-Oct was 1.48 %, SiQD-Hex was 1.33 %, and SiQD-Dodec was 0.92 %. Despite the performance difference, the EL spectrum of all SiQD-LEDs blue-shifted and broadened under increasing voltage. This was related to the band-filling effect and the SiQD-size distribution. For EL, the excitation energy is provided by the applied voltage, and with increasing voltage, the bigger QDs (higher wavelength) are excited at lower voltages than the smaller QDs (lower wavelength). Additionally, the induced potential barrier of the ligands strongly impacted the blue shift and the broadening of the EL spectrum by changing the charge transport properties. The longer the ligand, the more the blue shift and broadening occurred. By selecting the optimum ligand length in the study, we were able to tune the activated SiQD size and therefore, the shape of the emission spectrum. Additionally, when high-performance SiQD-LEDs are needed short ligands are preferred, whereas a trad-off is needed between color tuning and high optical power and efficiency.

In chapter 5, the working mechanism and charge kinetics were in-depth investigated and a non-expected capacitance behavior was detected for hexyl and dodecyl functionalized SiQD-LEDs. A negative capacitance was observed when the SiQD-LEDs were swept in voltage at a given frequency. The NC was explained with the help of trap states and the demarcation energy, and the latter described the temperature and frequency-dependent trapping and detrapping of trap states in the SiQD-LEDs. Together with the recombination process, the NC can be described. First, the presence of trap states was proved by the analysis of the $J - V$ characteristic in a double log scale. Therein, distinct linear regions were identified, which depend on their fitting coefficient m accounted for an Ohmic region ($m \approx$1), a trap-assisted SCLC ($m >$2), and a trap-free SCLC ($m \approx$2). Second, a frequency sweep showed that the NC was reduced and shifted towards higher voltages for increasing frequencies. The temperature sweep from $-$40 °C to 60 °C showed a decrease in charge carrier accumulation for the SiQD-Hex LED, a reducing NC amplitude, and a voltage shift towards lower voltages. In contrast, the SiQD-Dodec sample also showed the NC amplitude reduction and the voltage shift, but at the same time, an increased charge carrier accumulation with increasing temperatures. This behavior was caused by the better confinement probabilities of the longer ligand. The results provide a deeper understanding of functionalized SiQDs inside LEDs to improve their future efficiency. Additionally can the results be used as a starting point of high frequency switching behavior in display applications.

The broadband emission spectrum of SiQD-LEDs remained a key challenge for their usage in display applications. Chapter 6 presented the successful implementation of SiQD-LEDs into a Fabry-Pérot cavity resonator to narrow the initial broad emission of 140 nm to ca. 23 nm. The narrow emission cone makes SiQD-LEDs a real alternative to other toxic QLEDs. An FP resonator consists of two parallel mirrors, where light constructively and destructively interferes and only a specific wavelength, a mode, is coupled out. This wavelength can be tuned by adjusting the distance between the two mirrors. In the used approach, an Ag semi-transparent mirror and a SiO_2 spacer layer were added below the normal SiQD-LED layout to complete the FP cavity. For this reason, the ITO anode was sputtered on the underlying layers. The sputtered ITO values for transmittance and sheet resistance were worse than the industrial ITO substrates used for the non-cavity SiQD-LEDs, but its work function was better aligned to the PEDOT:PSS layer. The fabricated reference LEDs with the sputtered ITO showed a lower efficiency and brightness than the industrial ITO electrodes, but they were sufficient for the fabrication of SiQD-cLEDs. The successful cLED fabrication was confirmed by the obtained mode emission. In operation and by adjusting the SiO_2 spacer thicknesses, the mode emission was tuned from red-orange (ca. 600 nm) to IR (ca. 900 nm). Additionally, the SiQD-cLEDs revealed improved wavelength resilience under increasing applied voltages. By increasing the Ag outcoupler thickness from 40 nm to 50 nm in a cLED with a 500 nm thick SiO_2 spacer layer, the finesse and the Q-factor were further enhanced up to 61.6 and 29.7, and the emission spectrum was narrowed down to ca. 24 nm. Angle-dependent measurements demonstrated a narrowed emission cone of only 15°. The cLED performance was examined for a 50-500 cLED. The high current density in

reverse and the low voltage region indicated a high density of defects inside the device. Furthermore, the turn-on voltage was higher for the cLEDs as compared to the normal one and only reached a maximum of $60\,\mu W\,cm^{-2}$, whereas the normal SiQD-LED exhibited several hundred $\mu W\,cm^{-2}$. The cLED EQE was only about $0.004\,\%$ but remained at a constant value for increasing voltages. Overall, SiQD-cLEDs were shown for the first time, employing an FP resonator.

In this thesis, several topics have been addressed to bring SiQD-LEDs further towards the usage in industrial applications and to be a widely used alternative to their toxic counterpart QDs. The provided studies highlighted the importance of the surface ligands on SiQDs that strongly influence their behavior and have been so far only a minor part of the research. By choosing the desired ligand, the device performance and their charge carrier kinetics can change as shown in the capacitance measurements with a hexyl and dodecyl ligand SiQD-LED. Furthermore, a way to drastically reduce the spectral bandwidth of SiQD-LEDs has been presented with the implementation into the FP resonators. Altogether, the results achieved and the research obstacles to tackle can only be a starting point for high-power and narrow-emission SiQD-LEDs in the future.

8.2 Outlook

Despite the fundamental achievements in this thesis, there are many more points to tackle to make SiQD-LEDs a real competitor to the current QLED technology. Some of the following steps can help to improve the SiQD-LEDs and to minimize the development gap to the QLED state of the art.

Lifetime remains a big issue in SiQD-LEDs, and sufficient charge transport can limit the self-heating and prolongs the SiQD-LEDs life. The importance of the surface ligands of SiQDs has already been emphasized for their charge transport properties, and conjugated molecules have been presented to improve charge transport. Instead, we used a hexyl functionalization to reduce the insulating barrier between the SiQDs and even shorter alkyl chains can be used. Butyl capped SiQDs are also colloidal stable and might improve the charge transport even further.[259] Another approach to enhance the charge transport would be a ligand exchange on the SiQDs or the elimination of those after deposition so that no insulating barrier is present or highly conductive functionalization concepts are enabled. Then the electrical characterization of SiQD layers needs to be performed, and the interface charge transfer needs to be studied. A positive effect would be that the turn-on voltage can be reduced due to the minimized serial resistance, which allows turn-on voltages even below $1.5\,V$. The better charge transport of the SiQD layer also reduces the device's heating and ultimately enhances the LED lifetime. As a consequence, a better blocking layer as the currently used Poly-TPD and ZnO might be needed to suppress the charge transport to the opposite electrode. Another approach to utilizing the surface functionalization was presented by Dasog et al., who used the functionalization to change the emission color of the SiQDs from red to blue by keeping the same SiQD size.[38] Angi et al. showed that the spectrum could be shifted $\sim 115\,nm$ towards an even higher wavelength by introducing conjugated alkynyl(aryl) surface groups. Those two references show that the emission of same-sized SiQDs can be tuned by adjusting the surface group throughout the entire visible spectrum from blue (alkyl amine) to even near IR emission (alkynyl(aryl)).[38, 260] This approach can be used to produce white light SiQD-LEDs. So far a combined emission from transport layers and the SiQDs by Ghosh [43] combined with blue Poly-TPD emission and from Xin [144] combined with Poly-TPD and Alq3. Mixing different size SiQDs might be tempting but the smaller band gap QDs might not be excited due to the lower energy states in the bigger SiQDs. None of them use pure SiQD emission to generate white light.

We presented a SiQD-LED with a spectral bandwidth of ca. $24\,nm$, by the implementation of a Fabry-Perérot structure. To make optical outcoupling structures obsolete, the spectral bandwidth of the SiQDs themselves must improve. That way the optical attenuation in the resonator is removed and the emission is stronger. The broad emission is caused by the size distribution of the SiQDs after synthesis and represents the quantum confinement effect. Mastronardi used size-selective precipitation to get size-separated SiQDs, which Maier-Flaig tested in SiQD-LEDs.[49, 261] Despite their great efforts, the FWHM remained

still above 100 nm. More sensitive cascade centrifugation steps can be tested to resolve the size distribution further, but then large amounts of SiQDs are needed to gain an amount usable for device fabrication. This approach seem to be unpractical and therefore a more precise synthesis method with better size control is more realistic. The same-sized SiQDs also benefit for the device lifetime, as also presented by Maier-Flaig et al., which prolonged the LED lifetime to above 40 h.[49] This might be even enhanced by a combination of an improved surface ligand and size-separated SiQDs to fabricate extremely stable SiQD-LEDs.

In conclusion, SiQDs-LEDs can find their way into commercial products only if the following problems are overcome. The efficiency, lifetime, and spectral emission need to be improved in a way not to decrease one of the others. By solving them, SiQD-LEDs have a chance in some commercial applications and if not, SiQDs have big potential in other research topics.

List of Figures

List of Tables

Bibliography

[1] J. Y. Tsao and P. Waide, “The world’s appetite for light: Empirical data and trends spanning three centuries and six continents,” *LEUKOS*, vol. 6, no. 4, pp. 259–281, 2010.

[2] *COMMISSION REGULATION (EU) 2019/2020: laying down ecodesign requirements for light sources and separate control gears pursuant to Directive 2009/125/EC of the European Parliament and of the Council and repealing Commission Regulations (EC) No 244/2009, (EC) No 245/2009 and (EU) No 1194/2012*, ser. Official Journal of the European Union, 2019. [Online]. Available: https://eur-lex.europa.eu/legal-content/EN/TXT/PDF/?uri=CELEX:32019R2020&from=EN

[3] European Union, “Eur-lex - 32005l0032 - en - eur-lex,” 2005. [Online]. Available: https://eur-lex.europa.eu/legal-content/DE/ALL/?uri=CELEX:32005L0032

[4] H. J. Round, “A note on carborundum,” *Electric World*, vol. 49, p. 309, 1907. [Online]. Available: https://archive.org/details/electricalworld49newy/page/309/mode/1up

[5] O. V. Lossev, “Cii. luminous carborundum detector and detection effect and oscillations with crystals,” *The London, Edinburgh, and Dublin Philosophical Magazine and Journal of Science*, vol. 6, no. 39, pp. 1024–1044, 1928.

[6] N. Holonyak and S. F. Bevacqua, “Coherent (visible) light emission from $Ga(As_{1-x}P_x)$ junctions,” *Applied Physics Letters*, vol. 1, no. 4, pp. 82–83, 1962.

[7] S. M. Sze and K. N. Kwok, *Semiconductor Devices Physics and Technology*, 3rd ed. John Wiley & Sons, Inc, 2006. [Online]. Available: https://onlinelibrary.wiley.com/doi/book/10.1002/0470068329

[8] E. F. Schubert, *Light-emitting diodes*, 2nd ed. Cambridge University Press, 2006.

[9] S. Nakamura, T. Mukai, and M. Senoh, “Candela–class high–brightness ingan/algan double–heterostructure blue–light–emitting diodes,” *Applied Physics Letters*, vol. 64, no. 13, pp. 1687–1689, 1994.

[10] “The nobel prize in physics 2014,” Stockholm, 07.10.2014. [Online]. Available: https://www.nobelprize.org/uploads/2018/06/press-25.pdf

[11] V. C. Bender, T. B. Marchesan, and J. M. Alonso, “Solid-state lighting: A concise review of the state of the art on led and oled modeling,” *IEEE Industrial Electronics Magazine*, vol. 9, no. 2, pp. 6–16, 2015.

[12] J. Y. Tsao, H. D. Saunders, J. R. Creighton, M. E. Coltrin, and J. A. Simmons, “Solid-state lighting: an energy-economics perspective,” *Journal of Physics D: Applied Physics*, vol. 43, no. 35, p. 354001, 2010.

[13] S. Scholz, D. Kondakov, B. Lüssem, and K. Leo, “Degradation mechanisms and reactions in organic light-emitting devices,” *Chemical Reviews*, vol. 115, no. 16, pp. 8449–8503, 2015.

[14] A. Bernanose, M. Comte, and P. Vouaux, “Sur un nouveau mode d’émission lumineuse chez certains composés organiques,” *Journal de Chimie Physique*, vol. 50, pp. 64–68, 1953.

[15] A. Bernanose, “Electroluminescence of organic compounds,” *British Journal of Applied Physics*, vol. 6, no. S4, pp. S54–S55, 1955.

[16] M. Pope, H. P. Kallmann, and P. Magnante, “Electroluminescence in organic crystals,” *The Journal of Chemical Physics*, vol. 38, no. 8, pp. 2042–2043, 1963.

[17] W. Helfrich and W. G. Schneider, “Recombination radiation in anthracene crystals,” *Physical Review Letters*, vol. 14, no. 7, pp. 229–231, 1965.

[18] C. W. Tang and S. A. VanSlyke, “Organic electroluminescent diodes,” *Appl. Phys. Lett.*, vol. 51, no. 12, pp. 913–915, 1987.

[19] J. H. Burroughes, D. D. C. Bradley, A. R. Brown, R. N. Marks, K. Mackay, R. H. Friend, P. L. Burns, and A. B. Holmes, “Light-emitting diodes based on conjugated polymers,” *Nature*, vol. 347, no. 6293, pp. 539–541, 1990.

[20] M. Bale, J. C. Carter, C. J. Creighton, H. J. Gregory, P. H. Lyon, P. Ng, L. Webb, and A. Wehrum, “Ink-jet printing: The route to production of full-color p-oled displays,” *Journal of the Society for Information Display*, vol. 14, no. 5, p. 453, 2006.

[21] A. Sandström, A. Asadpoordarvish, J. Enevold, and L. Edman, “Spraying light: ambient-air fabrication of large-area emissive devices on complex-shaped surfaces,” *Advanced Materials*, vol. 26, no. 29, pp. 4975–4980, 2014.

[22] R. Abbel, I. de Vries, A. Langen, G. Kirchner, H. t’Mannetje, H. Gorter, J. Wilson, and P. Groen, “Toward high volume solution based roll-to-roll processing of oleds,” *Journal of Materials Research*, vol. 32, no. 12, pp. 2219–2229, 2017.

[23] S.-M. Lee, J. H. Kwon, S. Kwon, and K. C. Choi, “A review of flexible oleds toward highly durable unusual displays,” *IEEE Transactions on Electron Devices*, vol. 64, no. 5, pp. 1922–1931, 2017.

[24] J. Božek, M. Grgić, and B. Zovko-Cihlar, Eds., *Proceedings ELMAR-2013: 55th International Symposium ELMAR-2013, 25-27 September 2013, Zadar, Croatia*. Zadar, Croatia: Croatian Society Electronics in Marine - ELMAR, 2013. [Online]. Available: http://ieeexplore.ieee.org/servlet/opac?punumber=6647891

[25] M. Dong and L. Zhong, “Chameleon: a color-adaptive web browser for mobile oled displays,” in *MobiSys’11*, A. Agrawala, M. D. Corner, and D. Wetherall, Eds. [New York]: ACM, 2011, p. 85.

[26] R. Rossetti, S. Nakahara, and L. E. Brus, “Quantum size effects in the redox potentials, resonance raman spectra, and electronic spectra of cds crystallites in aqueous solution,” *The Journal of Chemical Physics*, vol. 79, no. 2, pp. 1086–1088, 1983.

[27] A. I. Ekimov, A. Efros, and A. A. Onushchenko, “Quantum size effect in semiconductor microcrystals,” *Solid State Communications*, vol. 56, no. 11, pp. 921–924, 1985.

[28] M. Liu, N. Yazdani, M. Yarema, M. Jansen, V. Wood, and E. H. Sargent, “Colloidal quantum dot electronics,” *Nature Electronics*, vol. 4, no. 8, pp. 548–558, 2021.

[29] J. Kwak, W. K. Bae, D. Lee, I. Park, J. Lim, M. Park, H. Cho, H. Woo, D. Y. Yoon, K. Char, S. Lee, and C. Lee, “Bright and efficient full-color colloidal quantum dot light-emitting diodes using an inverted device structure,” *Nano Letters*, vol. 12, no. 5, pp. 2362–2366, 2012. [Online]. Available: https://pubs.acs.org/doi/10.1021/nl3003254

[30] Yu-Ho Won, Oul Cho, Taehyung Kim, Dae-Young Chung, Taehee Kim, Heejae Chung, Hyosook Jang, Junho Lee, Dongho Kim, and Eunjoo Jang, “Highly efficient and stable inp/znse/zns quantum dot light-emitting diodes,” *Nature*, vol. 575, pp. 634–638, 2019.

[31] P. O. Anikeeva, J. E. Halpert, M. G. Bawendi, and V. Bulović, "Electroluminescence from a mixed red-green-blue colloidal quantum dot monolayer," *Nano Lett*, vol. 7, no. 8, pp. 2196–2200, 2007.

[32] M. Nam, S. Lee, J. Park, S.-W. Kim, and K.-K. Lee, "Development of hybrid photovoltaic cells by incorporating cuins 2 quantum dots into organic photoactive layers," *Japanese Journal of Applied Physics*, vol. 50, no. 6, p. 06GF02, 2011.

[33] J. R. Heath, J. J. Shiang, and A. P. Alivisatos, "Germanium quantum dots: Optical properties and synthesis," *The Journal of Chemical Physics*, vol. 101, no. 2, pp. 1607–1615, 1994.

[34] M. Dasog, J. Kehrle, B. Rieger, and J. G. C. Veinot, "Silicon nanocrystals and silicon-polymer hybrids: synthesis, surface engineering, and applications," *Angewandte Chemie International Edition*, vol. 55, no. 7, pp. 2322–2339, 2016. [Online]. Available: http://doi.wiley.com/10.1002/anie.201506065

[35] S. Y. Lim, W. Shen, and Z. Gao, "Carbon quantum dots and their applications," *Chemical Society Reviews*, vol. 44, no. 1, pp. 362–381, 2015.

[36] *DIRECTIVE 2002/95/EC OF THE EUROPEAN PARLIAMENT AND OF THE COUNCIL of 27 January 2003: on the restriction of the use of certain hazardous substances in electrical and electronic equipment*, ser. Official Journal of the European Union, 2003. [Online]. Available: https://eur-lex.europa.eu/legal-content/EN/TXT/PDF/?uri=CELEX:32002L0095&from=DE

[37] L. T. Canham, "Silicon quantum wire array fabrication by electrochemical and chemical dissolution of wafers," *Applied Physics Letters*, vol. 57, no. 10, pp. 1046–1048, 1990. [Online]. Available: http://aip.scitation.org/doi/10.1063/1.103561

[38] M. Dasog, G. B. de los Reyes, L. V. Titova, F. A. Hegmann, and J. G. C. Veinot, "Size vs surface: tuning the photoluminescence of freestanding silicon nanocrystals across the visible spectrum via surface groups," *ACS Nano*, vol. 8, no. 9, pp. 9636–9648, 2014. [Online]. Available: http://pubs.acs.org/doi/10.1021/nn504109a

[39] Q. Li, T.-Y. Luo, M. Zhou, H. Abroshan, J. Huang, H. J. Kim, N. L. Rosi, Z. Shao, and R. Jin, "Silicon nanoparticles with surface nitrogen: 90% quantum yield with narrow luminescence bandwidth and the ligand structure based energy law," *ACS Nano*, vol. 10, no. 9, pp. 8385–8393, 2016.

[40] K.-Y. Cheng, R. Anthony, U. R. Kortshagen, and R. J. Holmes, "Hybrid silicon nanocrystal−organic light-emitting devices for infrared electroluminescence," *Nano Letters*, vol. 10, no. 4, pp. 1154–1157, 2010.

[41] ——, "High-efficiency silicon nanocrystal light-emitting devices," *Nano Letters*, vol. 11, no. 5, pp. 1952–1956, 2011.

[42] W. Gu, X. Liu, X. Pi, X. Dai, S. Zhao, L. Yao, D. Li, Y. Jin, M. Xu, D. Yang, and G. Qin, "Silicon-quantum-dot light-emitting diodes with interlayer-enhanced hole transport," *IEEE Photonics Journal*, vol. 9, no. 2, p. 4500610, 2017. [Online]. Available: http://ieeexplore.ieee.org/document/7858634/

[43] B. Ghosh, Y. Masuda, Y. Wakayama, Y. Imanaka, J.-i. Inoue, K. Hashi, K. Deguchi, H. Yamada, Y. Sakka, S. Ohki, T. Shimizu, and N. Shirahata, "Hybrid white light emitting diode based on silicon nanocrystals," *Advanced Functional Materials*, vol. 24, no. 45, pp. 7151–7160, 2014. [Online]. Available: http://doi.wiley.com/10.1002/adfm.201401795

[44] Ghosh and Shirahata, "All-inorganic red-light emitting diodes based on silicon quantum dots," *Crystals*, vol. 9, no. 8, p. 385, 2019.

[45] L. Yao, T. Yu, L. Ba, H. Meng, X. Fang, Y. Wang, L. Li, X. Rong, S. Wang, X. Wang, G. Ran, X. Pi, and G. Qin, "Efficient silicon quantum dots light emitting diodes with an inverted device structure," *Journal of Materials Chemistry C*, vol. 4, no. 4, pp. 673–677, 2016. [Online]. Available: http://xlink.rsc.org/?DOI=C5TC03064A

[46] A. Angı, M. Loch, R. Sinelnikov, J. G. C. Veinot, M. Becherer, P. Lugli, and B. Rieger, "The influence of surface functionalization methods on the performance of silicon nanocrystal leds," *Nanoscale*, vol. 10, no. 22, pp. 10 337–10 342, 2018. [Online]. Available: http://xlink.rsc.org/?DOI=C7NR09525B

[47] I. M. D. Höhlein, A. Angı, R. Sinelnikov, J. G. C. Veinot, and B. Rieger, "Functionalization of hydride-terminated photoluminescent silicon nanocrystals with organolithium reagents," *Chemistry – A European Journal*, vol. 21, no. 7, pp. 2755–2758, 2015. [Online]. Available: https://chemistry-europe.onlinelibrary.wiley.com/doi/full/10.1002/chem.201405555

[48] X. Liu, S. Zhao, W. Gu, Y. Zhang, X. Qiao, Z. Ni, X. Pi, and D. Yang, "Light-emitting diodes based on colloidal silicon quantum dots with octyl and phenylpropyl ligands," *ACS Applied Materials & Interfaces*, vol. 10, no. 6, pp. 5959–5966, 2018. [Online]. Available: https://pubs.acs.org/doi/10.1021/acsami.7b16980

[49] F. Maier-Flaig, J. Rinck, M. Stephan, T. Bocksrocker, M. Bruns, C. Kübel, A. K. Powell, G. A. Ozin, and U. Lemmer, "Multicolor silicon light-emitting diodes (sileds)," *Nano Letters*, vol. 13, no. 2, pp. 475–480, 2013. [Online]. Available: http://pubs.acs.org/doi/10.1021/nl3038689

[50] B. Ghosh, T. Hamaoka, Y. Nemoto, M. Takeguchi, and N. Shirahata, "Impact of anchoring monolayers on the enhancement of radiative recombination in light-emitting diodes based on silicon nanocrystals," *J. Phys. Chem C*, vol. 122, no. 11, pp. 6422–6430, 2018.

[51] A. Köhler and H. Bässler, *Electronic Processes in Organic Semiconductors*. Weinheim, Germany: WILEY–VCH Verlag, 2015. [Online]. Available: https://onlinelibrary.wiley.com/doi/book/10.1002/9783527685172

[52] M. Grundmann, *The Physics of Semiconductors*, 3rd ed., ser. Graduate Texts in Physics. Cham: Springer International Publishing, 2016. [Online]. Available: http://link.springer.com/10.1007/978-3-319-23880-7

[53] D. K. Schroder, *Semiconductor Material and Device Characterization*. Hoboken, NJ, USA: John Wiley & Sons, Inc, 2005. [Online]. Available: http://doi.wiley.com/10.1002/0471749095

[54] G. L. Miller, D. V. Lang, and L. C. Kimerling, "Capacitance transient spectroscopy," *Annual Review of Materials Science*, vol. 7, no. 1, pp. 377–448, 1977.

[55] W. Heisenberg, "Über den anschaulichen inhalt der quantentheoretischen kinematik und mechanik," *Zeitschrift fr Physik*, vol. 43, no. 3-4, pp. 172–198, 1927.

[56] D. J. Griffiths, *Introduction to quantum mechanics*. Cambridge University Press, 1994.

[57] E. Schrödinger, "An undulatory theory of the mechanics of atoms and molecules," *Physical Review*, vol. 28, no. 6, pp. 1049–1070, 1926.

[58] J. Clayden, S. Warren, N. Greeves, and P. Wothers, *Organic chemistry*, 2nd ed. Oxford: Oxford Univ. Press, 2012.

[59] Wollrab, *Organische Chemie: Eine Einführung für Lehramts- und Nebenfachstudenten*, 4th ed., ser. Springer-Lehrbuch. Berlin: Springer Berlin Heidelberg, 2014.

[60] R. M. Metzger, *Unimolecular and Supramolecular Electronics I*. Berlin, Heidelberg: Springer Berlin Heidelberg, 2012, vol. 312.

[61] D.-D. Zhang, J.-L. Xu, and H.-B. Sun, "Toward high efficiency organic light–emitting diodes: Role of nanoparticles," *Advanced Optical Materials*, p. 2001710, 2021.

[62] A. Miller and E. Abrahams, "Impurity conduction at low concentrations," *Physical Review*, vol. 120, no. 3, pp. 745–755, 1960.

[63] L. Li and H. Kosina, "Charge transport in organic semiconductor devices," in *Organic Electronics*, ser. Advances in Polymer Science, T. Grasser, G. Meller, and L. Li, Eds. Berlin, Heidelberg: Springer Berlin Heidelberg, 2010, vol. 223, pp. 301–323.

[64] W. Shockley, "The theory of p-n junctions in semiconductors and p-n junction transistors," *Bell System Technical Journal*, vol. 28, no. 3, pp. 435–489, 1949.

[65] J. Rose, S. Bradbury, I. Bond, P. Ogden, A. Price, R. Oliver, and Y. F. Khassen, "Driving led in a nanosecond regime by a fast operational amplifier." [Online]. Available: https://arxiv.org/pdf/1011.1954

[66] V. D. Trong, C. T. Anh, N. D. Cuong, P. H. Binh, C. T. Truong, and A. T. Pham, "Frequency dependence of negative capacitance in light-emitting devices," in *2012 Fourth International Conference on Communications and Electronics (ICCE 2012)*. Piscataway NJ: IEEE, 2012, pp. 44–47.

[67] "Technologie im detail: Quantum dots von samsung," 6/14/2022. [Online]. Available: https://news.samsung.com/de/technologie-im-detail-quantum-dots-von-samsung

[68] K.-S. Cho, E. K. Lee, W.-J. Joo, E. Jang, T.-H. Kim, S. J. Lee, S.-J. Kwon, J. Y. Han, B.-K. Kim, B. L. Choi, and J. M. Kim, "High-performance crosslinked colloidal quantum-dot light-emitting diodes," *Nature Photonics*, vol. 3, no. 6, pp. 341–345, 2009.

[69] S. Coe-Sullivan, "Quantum dot developments," *Nature Photonics*, vol. 3, no. 6, pp. 315–316, 2009.

[70] M. Lu, J. Guo, S. Sun, P. Lu, J. Wu, Y. Wang, S. V. Kershaw, W. W. Yu, A. L. Rogach, and Y. Zhang, "Bright cspbi3 perovskite quantum dot light-emitting diodes with top-emitting structure and a low efficiency roll-off realized by applying zirconium acetylacetonate surface modification," *Nano Lett*, vol. 20, no. 4, pp. 2829–2836, 2020.

[71] X. Jin, C. Chang, W. Zhao, S. Huang, X. Gu, Q. Zhang, F. Li, Y. Zhang, and Q. Li, "Balancing the electron and hole transfer for efficient quantum dot light-emitting diodes by employing a versatile organic electron-blocking layer," *ACS Applied Materials and Interfaces*, vol. 10, no. 18, pp. 15 803–15 811, 2018.

[72] H. Y. Kim, Y. J. Park, J. Kim, C. J. Han, J. Lee, Y. Kim, T. Greco, C. Ippen, A. Wedel, B.-K. Ju, and M. S. Oh, "Transparent inp quantum dot light-emitting diodes with zro 2 electron transport layer and indium zinc oxide top electrode," *Advanced Functional Materials*, vol. 26, no. 20, pp. 3454–3461, 2016.

[73] A. P. Alivisatos, "Perspectives on the physical chemistry of semiconductor nanocrystals," *The Journal of Physical Chemistry*, vol. 100, no. 31, pp. 13 226–13 239, 1996.

[74] A. D. Yoffe, "Semiconductor quantum dots and related systems: Electronic, optical, luminescence and related properties of low dimensional systems," *Advances in Physics*, vol. 50, no. 1, pp. 1–208, 2001.

[75] A. M. Smith and S. Nie, “Semiconductor nanocrystals: structure, properties, and band gap engineering,” *Accounts of Chemical Research*, vol. 43, no. 2, pp. 190–200, 2010.

[76] M. G. Bawendi, M. L. Steigerwald, and L. E. Brus, “The quantum mechanics of larger semiconductor clusters ("quantum dots"),” *0066426X*, vol. 41, no. 1, pp. 477–496, 1990.

[77] L. E. Brus, “Electron–electron and electron–hole interactions in small semiconductor crystallites: The size dependence of the lowest excited electronic state,” *The Journal of Chemical Physics*, vol. 80, no. 9, pp. 4403–4409, 1984.

[78] F. Divsar, *Quantum Dots: Fundamental and Applications*. IntechOpen, 2020.

[79] L. Brus, “Electronic wave functions in semiconductor clusters: experiment and theory,” *The Journal of Physical Chemistry*, vol. 90, no. 12, pp. 2555–2560, 1986.

[80] J. R. Chelikowsky and M. L. Cohen, “Electronic structure of silicon,” *Physical Review B*, vol. 10, no. 12, pp. 5095–5107, 1974.

[81] D. J. L. Pavesi and Lorenzo, “Silicon fundamentals for photonics applications,” in *Silicon photonics*, ser. Physics and astronomy online library. Berlin and Heidelberg and New York: Springer, (2004), vol. 94, pp. 1–50.

[82] S. Furukawa and T. Miyasato, “Three-dimensional quantum well effects in ultrafine silicon particles,” *Japanese Journal of Applied Physics*, vol. 27, no. Part 2, No. 11, pp. L2207–L2209, 1988.

[83] Furukawa and Miyasato, “Quantum size effects on the optical band gap of microcrystalline si:h,” *Physical review. B, Condensed matter*, vol. 38, no. 8, pp. 5726–5729, 1988.

[84] H. Takagi, H. Ogawa, Y. Yamazaki, A. Ishizaki, and T. Nakagiri, “Quantum size effects on photoluminescence in ultrafine si particles,” *Applied Physics Letters*, vol. 56, no. 24, pp. 2379–2380, 1990.

[85] D. Kovalev, H. Heckler, M. Ben-Chorin, G. Polisski, M. Schwartzkopff, and F. Koch, “Breakdown of the k -conservation rule in si nanocrystals,” *Physical Review Letters*, vol. 81, no. 13, pp. 2803–2806, 1998.

[86] Hybertsen, “Absorption and emission of light in nanoscale silicon structures,” *Physical Review Letters*, vol. 72, no. 10, pp. 1514–1517, 1994.

[87] X. Crispin, S. Marciniak, W. Osikowicz, G. Zotti, A. W. D. van der Gon, F. Louwet, M. Fahlman, L. Groenendaal, F. de Schryver, and W. R. Salaneck, “Conductivity, morphology, interfacial chemistry, and stability of poly(3,4-ethylene dioxythiophene)-poly(styrene sulfonate): A photoelectron spectroscopy study,” *Journal of Polymer Science Part B: Polymer Physics*, vol. 41, no. 21, pp. 2561–2583, 2003.

[88] J. Chen, W. Cranton, and M. Fihn, “Handbook of visual display technology,” *00309346*, 2016.

[89] T. M. Brown, J. S. Kim, R. H. Friend, F. Cacialli, R. Daik, and W. J. Feast, “Built-in field electroabsorption spectroscopy of polymer light-emitting diodes incorporating a doped poly(3,4-ethylene dioxythiophene) hole injection layer,” *Applied Physics Letters*, vol. 75, no. 12, pp. 1679–1681, 1999.

[90] Ossila, “Pedot:pss | ph1000, ai4083, htl solar & htl solar 3, f hc solar,” 6/15/2022. [Online]. Available: https://www.ossila.com/en-eu/products/pedot-pss?variant=30366225236064

[91] Solaris Chem, “poly-tpd | sol2420 | solaris chem | cas: 472960-35-3,” 1/3/2022. [Online]. Available: https://solarischem.com/product/poly-tpd-sol2420?wcmlc=CAD

[92] W. W. Zhu, S. Xiao, and I. Shih, "Field-effect mobilities of polyhedral oligomeric silsesquioxanes anchored semiconducting polymers," *Applied Surface Science*, vol. 221, no. 1-4, pp. 358–363, 2004.

[93] L. Lan, B. Liu, H. Tao, J. Zou, C. Jiang, M. Xu, L. Wang, J. Peng, and Y. Cao, "Preparation of efficient quantum dot light-emitting diodes by balancing charge injection and sensitizing emitting layer with phosphorescent dye: Journal of materials chemistry c, 7(19), 5755-5763," *J. Mater. Chem. C*, vol. 7, no. 19, pp. 5755–5763, 2019.

[94] Q. J. Sun, B. H. Fan, Z. A. Tan, C. H. Yang, Y. F. Li, and Y. Yang, "White light from polymer light-emitting diodes: Utilization of fluorenone defects and exciplex," *Applied Physics Letters*, vol. 88, no. 16, p. 163510, 2006.

[95] K. Zilberberg, J. Meyer, and T. Riedl, "Solution processed metal-oxides for organic electronic devices," *J. Mater. Chem. C*, vol. 1, no. 32, p. 4796, 2013.

[96] N. Tiwale, S. P. Senanayak, J. Rubio-Lara, Y. Alaverdyan, and M. E. Welland, "Optimization of transistor characteristics and charge transport in solution processed zno thin films grown from zinc neodecanoate," *Electronic Materials Letters*, vol. 15, no. 6, pp. 702–711, 2019.

[97] S.-H. Liao, H.-J. Jhuo, Y.-S. Cheng, and S.-A. Chen, "Fullerene derivative-doped zinc oxide nanofilm as the cathode of inverted polymer solar cells with low-bandgap polymer (ptb7-th) for high performance," *Advanced Materials*, vol. 25, no. 34, pp. 4766–4771, 2013. [Online]. Available: http://doi.wiley.com/10.1002/adma.201301476

[98] C.-C. Tu, L. Tang, J. Huang, A. Voutsas, and L. Y. Lin, "Visible electroluminescence from hybrid colloidal silicon quantum dot-organic light-emitting diodes," *Applied Physics Letters*, vol. 98, no. 21, p. 213102, 2011.

[99] J. Mock, E. Groß, M. J. Kloberg, B. Rieger, and M. Becherer, "Surface engineering of silicon quantum dots: Does the ligand length impact the optoelectronic properties of light–emitting diodes?" *Advanced Photonics Research*, vol. 2, no. 9, p. 2100083, 2021. [Online]. Available: https://onlinelibrary.wiley.com/doi/full/10.1002/adpr.202100083

[100] F. Maier-Flaig, C. Kübel, J. Rinck, T. Bocksrocker, T. Scherer, R. Prang, A. K. Powell, G. A. Ozin, and U. Lemmer, "Looking inside a working siled," *Nano Lett*, vol. 13, no. 8, pp. 3539–3545, 2013.

[101] B. Ghosh, H. Yamada, S. Chinnathambi, İ. N. G. Özbilgin, and N. Shirahata, "Inverted device architecture for enhanced performance of flexible silicon quantum dot light-emitting diode," *The Journal of Physical Chemistry Letters*, vol. 9, no. 18, pp. 5400–5407, 2018. [Online]. Available: https://pubs.acs.org/doi/10.1021/acs.jpclett.8b02278

[102] H. Yamada, N. Saitoh, B. Ghosh, Y. Masuda, N. Yoshizawa, and N. Shirahata, "Improved brightness and color tunability of solution-processed silicon quantum dot light-emitting diodes," *J. Phys. Chem C*, vol. 124, no. 42, pp. 23 333–23 342, 2020.

[103] J. Derr, K. Dunn, D. Riabinina, F. Martin, M. Chaker, and F. Rosei, "Quantum confinement regime in silicon nanocrystals," *Physica E: Low-dimensional Systems and Nanostructures*, vol. 41, no. 4, pp. 668–670, 2009. [Online]. Available: https://linkinghub.elsevier.com/retrieve/pii/S1386947708004153

[104] X. Cheng, S. B. Lowe, P. J. Reece, and J. J. Gooding, "Colloidal silicon quantum dots: from preparation to the modification of self-assembled monolayers (sams) for bio-applications," *Chem. Soc. Rev.*, vol. 43, no. 8, pp. 2680–2700, 2014. [Online]. Available: http://xlink.rsc.org/?DOI=C3CS60353A

[105] S. Morozova, M. Alikina, A. Vinogradov, and M. Pagliaro, "Silicon quantum dots: Synthesis, encapsulation, and application in light-emitting diodes," *Frontiers in chemistry*, vol. 8, p. 191, 2020.

[106] L. Mangolini, E. Thimsen, and U. Kortshagen, “High-yield plasma synthesis of luminescent silicon nanocrystals,” *Nano Lett*, vol. 5, no. 4, pp. 655–659, 2005.

[107] L. Mangolini, D. Jurbergs, E. Rogojina, and U. Kortshagen, “Plasma synthesis and liquid-phase surface passivation of brightly luminescent si nanocrystals,” *Journal of Luminescence*, vol. 121, no. 2, pp. 327–334, 2006.

[108] X. Chen, X. Zhang, L.-Y. Xia, H.-Y. Wang, Z. Chen, and F.-G. Wu, “One-step synthesis of ultrasmall and ultrabright organosilica nanodots with 100% photoluminescence quantum yield: Long-term lysosome imaging in living, fixed, and permeabilized cells,” *Nano Lett*, vol. 18, no. 2, pp. 1159–1167, 2018.

[109] L. Mangolini, “Synthesis, properties, and applications of silicon nanocrystals,” *Journal of Vacuum Science & Technology B, Nanotechnology and Microelectronics: Materials, Processing, Measurement, and Phenomena*, vol. 31, no. 2, p. 020801, 2013.

[110] S.-M. Liu, S. Sato, and K. Kimura, “Synthesis of luminescent silicon nanopowders redispersible to various solvents,” *Langmuir*, vol. 21, no. 14, pp. 6324–6329, 2005.

[111] S.-M. Liu, Yang, S. Sato, and K. Kimura, “Enhanced photoluminescence from si nano-organosols by functionalization with alkenes and their size evolution,” *Chemistry of Materials*, vol. 18, no. 3, pp. 637–642, 2006.

[112] C. M. Hessel, E. J. Henderson, and J. G. C. Veinot, “Hydrogen silsesquioxane: A molecular precursor for nanocrystalline si−sio2 composites and freestanding hydride-surface-terminated silicon nanoparticles,” *Chemistry of Materials*, vol. 18, no. 26, pp. 6139–6146, 2006. [Online]. Available: https://pubs.acs.org/doi/10.1021/cm0602803

[113] C. M. Hessel, D. Reid, M. G. Panthani, M. R. Rasch, B. W. Goodfellow, J. Wei, H. Fujii, V. Akhavan, and B. A. Korgel, “Synthesis of ligand-stabilized silicon nanocrystals with size-dependent photoluminescence spanning visible to near-infrared wavelengths,” *Chemistry of Materials*, vol. 24, no. 2, pp. 393–401, 2012.

[114] Z. Yang, M. Iqbal, A. R. Dobbie, and J. G. C. Veinot, “Surface-induced alkene oligomerization: does thermal hydrosilylation really lead to monolayer protected silicon nanocrystals?” *Journal of the American Chemical Society*, vol. 135, no. 46, pp. 17 595–17 601, 2013.

[115] U. R. Kortshagen, R. M. Sankaran, R. N. Pereira, S. L. Girshick, J. J. Wu, and E. S. Aydil, “Nonthermal plasma synthesis of nanocrystals: Fundamental principles, materials, and applications,” *Chemical Reviews*, vol. 116, no. 18, pp. 11 061–11 127, 2016.

[116] C. Koch and T. J. Rinke, *Photolithography: Basics of Microstructuring*, 1st ed. Microchemicals GmbH, 2017.

[117] D. W. Schubert and T. Dunkel, “Spin coating from a molecular point of view: its concentration regimes, influence of molar mass and distribution,” *Materials Research Innovations*, vol. 7, no. 5, pp. 314–321, 2003.

[118] Ossila, “Spin coating: Complete guide to theory and techniques,” 6/15/2022. [Online]. Available: https://www.ossila.com/en-eu/pages/spin-coating

[119] D. M. Mattox, *Handbook of Physical Vapor Deposition (PVD) Processing*, 2nd ed. William Andrew Publishing-Elsevier, 2010.

[120] K. Seshan, *HANDBOOK OF THIN-FILM DEPOSITION PROCESSES AND TECHNIQUES Principles, Methods, Equipment and Applications*, 2nd ed. Norwich, NY: William Andrew Publishing, 2002. [Online]. Available: https://is.muni.cz/el/1431/jaro2017/F4280/um/Handbook_of_Thin-Film_Deposition_ed-Seshan-Krishna.pdf

[121] D.-H. Lee and N.-G. Cho, "Assessment of surface profile data acquired by a stylus profilometer," *Measurement Science and Technology*, vol. 23, no. 10, p. 105601, 2012.

[122] G. H. Michler, *Electron Microscopy of Polymers*. Berlin, Heidelberg: Springer Berlin Heidelberg, 2008. [Online]. Available: http://link.springer.com/10.1007/978-3-540-36352-1

[123] B. Bhushan, Ed., *Handbook of Nanotechnology*, 3rd ed. Berlin, Heidelberg: Springer Berlin Heidelberg, 2010. [Online]. Available: http://link.springer.com/10.1007/978-3-642-02525-9

[124] G. Binnig, C. F. Quate ", E. L. Gi, and C. Gerber, "Atomic force microscope," *Physical review letters*, vol. 56, no. 9, pp. 930–934, 1986.

[125] K. Hinrichs and K.-J. Eichhorn, *Ellipsometry of functional organic surfaces and films*, second edition ed., ser. Springer series in surface sciences. Cham, Switzerland: Springer, 2018, vol. Volume 52.

[126] E. D. Palik, *Handbook of optical constants of solids: Volume 1*, 1st ed. Orlando: Academic Press, 1985. [Online]. Available: http://gbv.eblib.com/patron/FullRecord.aspx?p=328563

[127] H. Kuzmany, *Solid-State Spectroscopy*. Berlin, Heidelberg: Springer Berlin Heidelberg, 1998. [Online]. Available: http://link.springer.com/10.1007/978-3-662-03594-8

[128] H.-H. Perkampus, *UV-VIS Spectroscopy and Its Applications*, ser. Springer Lab Manuals. Berlin, Heidelberg: Springer Berlin Heidelberg, 1992. [Online]. Available: https://ebookcentral.proquest.com/lib/kxp/detail.action?docID=6532745

[129] S. Watanabe, N. Yamada, M. Nagashima, Y. Ueki, C. Sasaki, Y. Yamada, T. Taguchi, K. Tadatomo, H. Okagawa, and H. Kudo, "Internal quantum efficiency of highly-efficient inxga1−xn-based near-ultraviolet light-emitting diodes," *Applied Physics Letters*, vol. 83, no. 24, pp. 4906–4908, 2003.

[130] Y. Shirasaki, G. J. Supran, M. G. Bawendi, and V. Bulović, "Emergence of colloidal quantum-dot light-emitting technologies," *Nature Photonics*, vol. 7, no. 1, pp. 13–23, 2013. [Online]. Available: http://www.nature.com/articles/nphoton.2012.328

[131] S. Ali, S. Chang, M. Imran, Q. Shi, Y. Chen, and H. Zhong, "Impedance spectroscopy: A versatile technique to understand solution–processed optoelectronic devices," *physica status solidi (RRL) – Rapid Research Letters*, vol. 13, no. 5, p. 1800580, 2019.

[132] S. Nowy, W. Ren, A. Elschner, W. Lövenich, and W. Brütting, "Impedance spectroscopy as a probe for the degradation of organic light-emitting diodes," *Journal of Applied Physics*, vol. 107, no. 5, p. 054501, 2010.

[133] K. M. Nimith, N. S. Sterin, P. P. Das, G. Umesh, and M. N. Satyanarayan, "Capacitance and impedance spectroscopy studies of polymer light emitting diodes based on meh-ppv:bt blends," *Synthetic Metals*, vol. 250, pp. 99–103, 2019.

[134] G. Zaiats, S. Ikeda, and P. V. Kamat, "Optimization of the electron transport layer in quantum dot light-emitting devices," *NPG Asia Materials*, vol. 12, no. 1, 2020.

[135] L. Stauffer, "C-v measurement tips, tricks, and traps," 2011. [Online]. Available: https://download.tek.com/document/CVMeasTipsWP.pdf

[136] E. Ehrenfreund, C. Lungenschmied, G. Dennler, H. Neugebauer, and N. S. Sariciftci, “Negative capacitance in organic semiconductor devices: Bipolar injection and charge recombination mechanism,” *Applied Physics Letters*, vol. 91, no. 1, p. 012112, 2007.

[137] F. Ebadi, N. Taghavinia, R. Mohammadpour, A. Hagfeldt, and W. Tress, “Origin of apparent light-enhanced and negative capacitance in perovskite solar cells,” *Nature Communications*, vol. 10, no. 1, p. 1574, 2019.

[138] Q. Niu, N. I. Crăciun, G.-J. A. H. Wetzelaer, and P. W. M. Blom, “Origin of negative capacitance in bipolar organic diodes,” *Physical Review Letters*, vol. 120, no. 11, p. 116602, 2018.

[139] J. Heath and P. Zabierowski, “Capacitance spectroscopy of thin-film solar cells,” in *Advanced Characterization Techniques for Thin Film Solar Cells*, D. Abou-Ras, T. Kirchartz, and U. Rau, Eds. Weinheim, Germany: Wiley-VCH Verlag GmbH & Co. KGaA, 2016, pp. 93–119.

[140] Keithley Instruments, “User manual,” 2017. [Online]. Available: https://download.tek.com/manual/4200-900-01K_Feb2017_User.pdf

[141] B. J. Hopkins and J. C. Riviere, “Work function values from contact potential difference measurements,” *British Journal of Applied Physics*, vol. 15, no. 8, pp. 941–946, 1964. [Online]. Available: https://iopscience.iop.org/article/10.1088/0508-3443/15/8/309/meta

[142] P. Mutti, G. Ghislotti, S. Bertoni, L. Bonoldi, G. F. Cerofolini, L. Meda, E. Grilli, and M. Guzzi, “Room–temperature visible luminescence from silicon nanocrystals in silicon implanted sio 2 layers,” *Applied Physics Letters*, vol. 66, no. 7, pp. 851–853, 1995.

[143] A. Gupta, M. T. Swihart, and H. Wiggers, “Luminescent colloidal dispersion of silicon quantum dots from microwave plasma synthesis: Exploring the photoluminescence behavior across the visible spectrum,” *Advanced Functional Materials*, vol. 19, no. 5, pp. 696–703, 2009.

[144] Y. Xin, K. Nishio, and K.-i. Saitow, “White-blue electroluminescence from a si quantum dot hybrid light-emitting diode,” *Applied Physics Letters*, vol. 106, no. 20, p. 201102, 2015.

[145] D. P. Puzzo, E. J. Henderson, M. G. Helander, Z. Wang, G. A. Ozin, and Z. Lu, “Visible colloidal nanocrystal silicon light-emitting diode,” *Nano Letters*, vol. 11, no. 4, pp. 1585–1590, 2011.

[146] J.-W. Kang, S.-H. Lee, H.-D. Park, W.-I. Jeong, K.-M. Yoo, Y.-S. Park, and J.-J. Kim, “Low roll-off of efficiency at high current density in phosphorescent organic light emitting diodes,” *Applied Physics Letters*, vol. 90, no. 22, p. 223508, 2007.

[147] R. G. Kepler, P. M. Beeson, S. J. Jacobs, R. A. Anderson, M. B. Sinclair, V. S. Valencia, and P. A. Cahill, “Electron and hole mobility in tris (8–hydroxyquinolinolato–n1,o8) aluminum,” *Applied Physics Letters*, vol. 66, no. 26, pp. 3618–3620, 1995.

[148] N. Matsusue, Y. Suzuki, and H. Naito, “Charge carrier transport in red electrophosphorescent emitting layer,” *Japanese Journal of Applied Physics*, vol. 45, no. 7, pp. 5966–5969, 2006.

[149] M. L. Mastronardi, E. J. Henderson, D. P. Puzzo, Y. Chang, Z. B. Wang, M. G. Helander, J. Jeong, N. P. Kherani, Z. Lu, and G. A. Ozin, “Silicon nanocrystal oleds: Effect of organic capping group on performance,” *Small*, vol. 8, no. 23, pp. 3647–3654, 2012. [Online]. Available: http://doi.wiley.com/10.1002/smll.201201242

[150] H. Yamada and N. Shirahata, “Silicon quantum dot light emitting diode at 620 nm,” *Micromachines*, vol. 10, no. 5, 2019.

[151] H. H. Kim, S. Park, Y. Yi, D. I. Son, C. Park, D. K. Hwang, and W. K. Choi, “Inverted quantum dot light emitting diodes using polyethylenimine ethoxylated modified zno,” *Scientific Reports*, vol. 5, p. 8968, 2015.

[152] Y. Zhou, C. Fuentes-Hernandez, J. Shim, J. Meyer, A. J. Giordano, H. Li, P. Winget, T. Papadopoulos, H. Cheun, J. Kim, M. Fenoll, A. Dindar, W. Haske, E. Najafabadi, T. M. Khan, H. Sojoudi, S. Barlow, S. Graham, J.-L. Brédas, S. R. Marder, A. Kahn, and B. Kippelen, “A universal method to produce low-work function electrodes for organic electronics,” *Science (New York, N.Y.)*, vol. 336, no. 6079, pp. 327–332, 2012.

[153] Y. Yu, G. Fan, A. Fermi, R. Mazzaro, V. Morandi, P. Ceroni, D.-M. Smilgies, and B. A. Korgel, “Size-dependent photoluminescence efficiency of silicon nanocrystal quantum dots,” *J. Phys. Chem C*, vol. 121, no. 41, pp. 23 240–23 248, 2017.

[154] T. Helbich, M. J. Kloberg, R. Sinelnikov, A. Lyuleeva, J. G. C. Veinot, and B. Rieger, “Diaryliodonium salts as hydrosilylation initiators for the surface functionalization of silicon nanomaterials and their collaborative effect as ring opening polymerization initiators,” *Nanoscale*, vol. 9, no. 23, pp. 7739–7744, 2017. [Online]. Available: http://xlink.rsc.org/?DOI=C7NR01559C

[155] N. M. Park, C. J. Choi, T. Y. Seong, and S. J. Park, “Quantum confinement in amorphous silicon quantum dots embedded in silicon nitride,” *Physical Review Letters*, vol. 86, no. 7, pp. 1355–1357, 2001.

[156] D. J. Milliron, I. G. Hill, C. Shen, A. Kahn, and J. Schwartz, “Surface oxidation activates indium tin oxide for hole injection,” *Journal of Applied Physics*, vol. 87, no. 1, pp. 572–576, 2000.

[157] I. T. Cheong, J. Mock, M. Kallergi, E. Groß, A. Meldrum, B. Rieger, M. Becherer, and J. G. C. Veinot, “Colloidal silicon quantum dot–based cavity light–emitting diodes with narrowed and tunable electroluminescence,” *Advanced Optical Materials*, vol. 11, no. 1, p. 2201834, 2022.

[158] D. Nečas and P. Klapetek, “Gwyddion: an open-source software for SPM data analysis,” *Central European Journal of Physics*, vol. 10, pp. 181–188, 2012.

[159] L. Wang, C. Lu, J. Lu, L. Liu, N. Liu, Y. Chen, Y. Zhang, E. Gu, and X. Hu, “Influence of carrier screening and band filling effects on efficiency droop of ingan light emitting diodes,” *Optics Express*, vol. 19, no. 15, pp. 14 182–14 187, 2011.

[160] X. Liu, Y. Zhang, T. Yu, X. Qiao, R. Gresback, X. Pi, and D. Yang, “Optimum quantum yield of the light emission from 2 to 10 nm hydrosilylated silicon quantum dots,” *Particle & Particle Systems Characterization*, vol. 33, no. 1, pp. 44–52, 2016.

[161] J. K. Noh, M. S. Kang, J. S. Kim, J. H. Lee, Y. H. Ham, J. B. Kim, and S. Son, “17.1: Invited paper: Inverted oled,” *SID Symposium Digest of Technical Papers*, vol. 39, no. 1, p. 212, 2008.

[162] S. Höfle, “Flüssigprozessierte organische tandem-leuchtdioden,” Dissertation, Karlsruher institut für technologie (Kit), 2015.

[163] Y.-H. Kim, T.-H. Han, H. Cho, S.-Y. Min, C.-L. Lee, and T.-W. Lee, “Polyethylene imine as an ideal interlayer for highly efficient inverted polymer light-emitting diodes,” *Advanced Functional Materials*, vol. 24, no. 24, pp. 3808–3814, 2014.

[164] B. A. E. Courtright and S. A. Jenekhe, “Polyethylenimine interfacial layers in inverted organic photovoltaic devices: Effects of ethoxylation and molecular weight on efficiency and temporal stability,” *ACS Applied Materials and Interfaces*, vol. 7, no. 47, pp. 26 167–26 175, 2015.

[165] F. J. Zhang, D. W. Zhao, Z. L. Zhuo, H. Wang, Z. Xu, and Y. S. Wang, "Inverted small molecule organic solar cells with ca modified ito as cathode and moo3 modified ag as anode," *Solar Energy Materials and Solar Cells*, vol. 94, no. 12, pp. 2416–2421, 2010.

[166] J. Meyer, S. Hamwi, M. Kröger, W. Kowalsky, T. Riedl, and A. Kahn, "Transition metal oxides for organic electronics: energetics, device physics and applications," *Advanced Materials*, vol. 24, no. 40, pp. 5408–5427, 2012.

[167] Y. Zhao, J. Chen, W. Chen, and D. Ma, "Poly(3,4-ethylenedioxythiophene):poly(styrenesulfonate)/moo 3 composite layer for efficient and stable hole injection in organic semiconductors," *Journal of Applied Physics*, vol. 111, no. 4, p. 043716, 2012.

[168] N. C. Giebink and S. R. Forrest, "Quantum efficiency roll-off at high brightness in fluorescent and phosphorescent organic light emitting diodes," *Physical Review B*, vol. 77, no. 23, 2008.

[169] M. Dasog, Z. Yang, S. Regli, T. M. Atkins, A. Faramus, M. P. Singh, E. Muthuswamy, S. M. Kauzlarich, R. D. Tilley, and J. G. C. Veinot, "Chemical insight into the origin of red and blue photoluminescence arising from freestanding silicon nanocrystals," *ACS Nano*, vol. 7, no. 3, pp. 2676–2685, 2013.

[170] A. Salomon, T. Boecking, C. K. Chan, F. Amy, O. Girshevitz, D. Cahen, and A. Kahn, "How do electronic carriers cross si-bound alkyl monolayers?" *Physical Review Letters*, vol. 95, no. 26, p. 266807, 2005.

[171] M. Drndić, M. V. Jarosz, N. Y. Morgan, M. A. Kastner, and M. G. Bawendi, "Transport properties of annealed cdse colloidal nanocrystal solids," *Journal of Applied Physics*, vol. 92, no. 12, pp. 7498–7503, 2002.

[172] P. V. Avramov, D. G. Fedorov, P. B. Sorokin, L. A. Chernozatonskii, and M. S. Gordon, "New symmetric families of silicon quantum dots and their conglomerates as a tunable source of photoluminescence in nanodevices." [Online]. Available: https://arxiv.org/pdf/0709.2279

[173] L. Scheres, B. Rijksen, M. Giesbers, and H. Zuilhof, "Molecular modeling of alkyl and alkenyl monolayers on hydrogen-terminated si(111)," *Langmuir : the ACS journal of surfaces and colloids*, vol. 27, no. 3, pp. 972–980, 2011.

[174] M. Nagai, "Impact of particulate contaminants on the current leakage defect in oled devices," *Journal of The Electrochemical Society*, vol. 154, no. 12, p. J387, 2007.

[175] C.-W. Jiang and M. A. Green, "Silicon quantum dot superlattices: Modeling of energy bands, densities of states, and mobilities for silicon tandem solar cell applications," *Journal of Applied Physics*, vol. 99, no. 11, p. 114902, 2006.

[176] S. Pfaehler, A. Angı, D. Chryssikos, A. Cattani-Scholz, B. Rieger, and M. Tornow, "Space charge-limited current transport in thin films of alkyl-functionalized silicon nanocrystals," *Nanotechnology*, vol. 30, no. 39, p. 395201, 2019. [Online]. Available: https://iopscience.iop.org/article/10.1088/1361-6528/ab2c28

[177] P. O. Anikeeva, J. E. Halpert, M. G. Bawendi, and V. Bulović, "Quantum dot light-emitting devices with electroluminescence tunable over the entire visible spectrum," *Nano Lett*, vol. 9, no. 7, pp. 2532–2536, 2009.

[178] V. Wood, M. J. Panzer, J.-M. Caruge, J. E. Halpert, M. G. Bawendi, and V. Bulović, "Air-stable operation of transparent, colloidal quantum dot based leds with a unipolar device architecture," *Nano Lett*, vol. 10, no. 1, pp. 24–29, 2010.

[179] G. Konstantatos and E. H. Sargent, *Colloidal quantum dot optoelectronics and photovoltaics*. Cambridge: Cambridge University Press, 2013.

[180] T. Mukai, M. Yamada, and S. Nakamura, "Characteristics of ingan-based uv/blue/green/amber/red light-emitting diodes," *Japanese Journal of Applied Physics*, vol. 38, no. Part 1, No. 7A, pp. 3976–3981, 1999.

[181] T. Numai, *Fundamentals of semiconductor lasers*, 2nd ed., ser. Springer series in optical sciences. Tokyo and Heidelberg and New York (N.Y.) [etc.]: Springer, 2015, vol. 93.

[182] M. Jakob, M. Javadi, J. G. Veinot, A. Meldrum, A. Kartouzian, and U. K. Heiz, "Ensemble effects in the temperature-dependent photoluminescence of silicon nanocrystals," *Chemistry - A European Journal*, 2019. [Online]. Available: http://doi.wiley.com/10.1002/chem.201804986

[183] A. N. Thiessen, M. Ha, R. W. Hooper, H. Yu, A. O. Oliynyk, J. G. C. Veinot, and V. K. Michaelis, "Silicon nanoparticles: Are they crystalline from the core to the surface?" *Chemistry of Materials*, vol. 31, no. 3, pp. 678–688, 2019. [Online]. Available: http://pubs.acs.org/doi/10.1021/acs.chemmater.8b03074

[184] I. Sychugov, A. Fucikova, F. Pevere, Z. Yang, J. G. C. Veinot, and J. Linnros, "Ultranarrow luminescence linewidth of silicon nanocrystals and influence of matrix," *ACS Photonics*, vol. 1, no. 10, pp. 998–1005, 2014.

[185] G. Krikun and K. Zojer, "Impact of thermal transport parameters on the operating temperature of organic light emitting diodes," *Journal of Applied Physics*, vol. 125, no. 8, p. 085501, 2019.

[186] H. F. Haneef, A. M. Zeidell, and O. D. Jurchescu, "Charge carrier traps in organic semiconductors: a review on the underlying physics and impact on electronic devices," *J. Mater. Chem. C*, vol. 8, no. 3, pp. 759–787, 2020.

[187] K. Bansal, "Electrical and optical investigations of the condensed matter physics of junction diodes under charge carrier injection," Dissertation, Indian Institute of Science Education and Research - Pune, Pune, 2014.

[188] M. Ershov, H. C. Liu, L. Li, M. Buchanan, Z. R. Wasilewski, and A. K. Jonscher, "Negative capacitance effect in semiconductor devices," *IEEE Transactions on Electron Devices*, vol. 45, no. 10, pp. 2196–2206, 1998.

[189] J. Mock, M. Kallergi, E. Groß, M. Golibrzuch, B. Rieger, and M. Becherer, "Revealing the negative capacitance effect in silicon quantum dot light-emitting diodes via temperature-dependent capacitance-voltage characterization," *IEEE Photonics Journal*, vol. 14, no. 4, pp. 1–9, 2022.

[190] L.-f. Feng, C.-y. Zhu, Y. Chen, Z.-b. Zheng, and C.-d. Wang, "Mechanism of negative capacitance in leds," *Optoelectronics Letters*, vol. 1, no. 2, pp. 127–130, 2005.

[191] J. Bisquert, "A variable series resistance mechanism to explain the negative capacitance observed in impedance spectroscopy measurements of nanostructured solar cells," *Physical chemistry chemical physics : PCCP*, vol. 13, no. 10, pp. 4679–4685, 2011.

[192] K. Bansal, M. Henini, M. S. Alshammari, and S. Datta, "Dynamics of electronic transitions and frequency dependence of negative capacitance in semiconductor diodes under high forward bias," *Applied Physics Letters*, vol. 105, no. 12, p. 123503, 2014.

[193] L. S. C. Pingree, B. J. Scott, M. T. Russell, T. J. Marks, and M. C. Hersam, "Negative capacitance in organic light-emitting diodes," *Applied Physics Letters*, vol. 86, no. 7, p. 073509, 2005. [Online]. Available: https://aip.scitation.org/doi/full/10.1063/1.1865346

[194] A. G. U. Perera, W. Z. Shen, M. Ershov, H. C. Liu, M. Buchanan, and W. J. Schaff, "Negative capacitance of gaas homojunction far-infrared detectors," *Applied Physics Letters*, vol. 74, no. 21, pp. 3167–3169, 1999.

[195] E.-M. Bourim and J. in Han, "Size effect on negative capacitance at forward bias in ingan/gan multiple quantum well-based blue led," *Electronic Materials Letters*, vol. 12, no. 1, pp. 67–75, 2016.

[196] Y. Li, C. D. Wang, L. F. Feng, C. Y. Zhu, H. X. Cong, D. Li, and G. Y. Zhang, "Elucidating negative capacitance in light-emitting diodes using an advanced semiconductor device theory," *Journal of Applied Physics*, vol. 109, no. 12, p. 124506, 2011.

[197] C. Blauth, P. Mulvaney, and T. Hirai, "Negative capacitance as a diagnostic tool for recombination in purple quantum dot leds," *Journal of Applied Physics*, vol. 125, no. 19, p. 195501, 2019.

[198] S. E. Laux and K. Hess, "Revisiting the analytic theory of p-n junction impedance: improvements guided by computer simulation leading to a new equivalent circuit," *IEEE Transactions on Electron Devices*, vol. 46, no. 2, pp. 396–412, 1999.

[199] M. Guan, L. Niu, Y. Zhang, X. Liu, Y. Li, and Y. Zeng, "Space charges and negative capacitance effect in organic light-emitting diodes by transient current response analysis," *RSC Adv*, vol. 7, no. 80, pp. 50 598–50 602, 2017.

[200] G. Garcia-Belmonte, H. J. Bolink, and J. Bisquert, "Capacitance-voltage characteristics of organic light-emitting diodes varying the cathode metal: Implications for interfacial states," *Physical Review B*, vol. 75, no. 8, 2007.

[201] L.-f. Feng, J. Wang, C.-y. Zhu, H.-x. Cong, Y. Chen, and C.-d. Wang, "Experimental study of negative capacitance in leds," *Optoelectronics Letters*, vol. 1, no. 2, pp. 124–126, 2005.

[202] S. S. Hegedus and E. A. Fagen, "Midgap states in a –si:h and a –sige:h p – i – n solar cells and schottky junctions by capacitance techniques," *Journal of Applied Physics*, vol. 71, no. 12, pp. 5941–5951, 1992.

[203] R. Herberholz, T. Walter, and H. W. Schock, "Density of states in cuin(sse) 2 thin films from modulated photocurrent measurements," *Journal of Applied Physics*, vol. 76, no. 5, pp. 2904–2911, 1994.

[204] E. von Hauff, "Impedance spectroscopy for emerging photovoltaics," *J. Phys. Chem C*, vol. 123, no. 18, pp. 11 329–11 346, 2019.

[205] E. Kask, T. Raadik, M. Grossberg, R. Josepson, and J. Krustok, "Deep defects in cu2znsns4 monograin solar cells," *Energy Procedia*, vol. 10, pp. 261–265, 2011.

[206] L. Xu, J. Wang, and J. W. P. Hsu, "Transport effects on capacitance-frequency analysis for defect characterization in organic photovoltaic devices," *Physical Review Applied*, vol. 6, no. 6, 2016.

[207] J. A. Carr, "The identification and characterization of electronic defect bands in organic photovoltaic devices," Dissertation, Iowa State University, 2014. [Online]. Available: https://dr.lib.iastate.edu/entities/publication/701662f6-6ae9-4386-8543-f8f2a12a8890?utm_source=lib.dr.iastate.edu%2Fetd%2F13853&utm_medium=PDF&utm_campaign=PDFCoverPages

[208] P. P. Boix, G. Garcia-Belmonte, U. Muñecas, M. Neophytou, C. Waldauf, and R. Pacios, "Determination of gap defect states in organic bulk heterojunction solar cells from capacitance measurements," *Applied Physics Letters*, vol. 95, no. 23, p. 233302, 2009.

[209] T. Walter, R. Herberholz, C. Müller, and H. W. Schock, "Determination of defect distributions from admittance measurements and application to cu(in,ga)se 2 based heterojunctions," *Journal of Applied Physics*, vol. 80, no. 8, pp. 4411–4420, 1996.

[210] M. Anutgan and I. Atilgan, "Forward bias capacitance spectroscopy for characterization of semiconductor junctions: Application to a-si:h p-i-n diode," *Applied Physics Letters*, vol. 102, no. 15, p. 153504, 2013.

[211] K. Bansal and S. Datta, "Temperature dependent reversal of voltage modulated light emission and negative capacitance in algainp based multi quantum well light emitting devices," *Applied Physics Letters*, vol. 102, no. 5, p. 053508, 2013.

[212] E.-M. Bourim and J. in Han, "Electrical characterization and thermal admittance spectroscopy analysis of ingan/gan mqw blue led structure," *Electronic Materials Letters*, vol. 11, no. 6, pp. 982–992, 2015.

[213] O. A. Soltanovich and E. B. Yakimov, "Analysis of the temperature dependence of the capacitance-voltage characteristics of ingan/gan multiple quantum well light-emitting structures," *Semiconductors*, vol. 47, no. 1, pp. 162–168, 2013.

[214] O. Armbruster, C. Lungenschmied, and S. Bauer, "Investigation of trap states and mobility in organic semiconductor devices by dielectric spectroscopy: Oxygen-doped p3ht:pcbm solar cells," *Physical Review B*, vol. 86, no. 23, 2012.

[215] J. M. Montero, J. Bisquert, G. Garcia-Belmonte, H. J. Bolink, and E. M. Barea, "Interpretation of capacitance spectra and transit times of single carrier space-charge limited transport in organic layers with field-dependent mobility," *Physica Status Solidi (a)*, vol. 204, no. 7, pp. 2402–2410, 2007.

[216] N. D. Nguyen, M. Schmeits, and H. P. Loebl, "Determination of charge-carrier transport in organic devices by admittance spectroscopy: Application to hole mobility in α -npd," *Physical Review B*, vol. 75, no. 7, 2007.

[217] T. Muntasir and S. Chaudhary, "Understanding defect distributions in polythiophenes via comparison of regioregular and regiorandom species," *Journal of Applied Physics*, vol. 118, no. 20, p. 205504, 2015.

[218] K. Bansal and S. Datta, "Voltage modulated electro-luminescence spectroscopy to understand negative capacitance and the role of sub-bandgap states in light emitting devices," *Journal of Applied Physics*, vol. 110, no. 11, p. 114509, 2011.

[219] C. Y. Zhu, L. F. Feng, C. D. Wang, H. X. Cong, G. Y. Zhang, Z. J. Yang, and Z. Z. Chen, "Negative capacitance in light-emitting devices," *Solid-State Electronics*, vol. 53, no. 3, pp. 324–328, 2009.

[220] C. D. Wang, C. Y. Zhu, G. Y. Zhang, J. Shen, and L. Li, "Accurate electrical characterization of forward ac behavior of real semiconductor diode: Giant negative capacitance and nonlinear interfacial layer," *IEEE Transactions on Electron Devices*, vol. 50, no. 4, pp. 1145–1148, 2003.

[221] N. C. Chen, P. Y. Wang, and J. F. Chen, "Low frequency negative capacitance behavior of molecular beam epitaxial gaas n-low temperature-i-p structure with low temperature layer grown at a low temperature," *Applied Physics Letters*, vol. 72, no. 9, pp. 1081–1083, 1998.

[222] J. Sworakowski, "On the origin of trapping centres in organic molecular crystals," *Molecular Crystals and Liquid Crystals*, vol. 11, no. 1, pp. 1–11, 1970.

[223] W. Brütting, S. Berleb, and A. G. Mückl, "Device physics of organic light-emitting diodes based on molecular materials," *Organic Electronics*, vol. 2, no. 1, pp. 1–36, 2001.

[224] T. Ono, Y. Xu, T. Sakata, and K.-i. Saitow, "Designing efficient si quantum dots and leds by quantifying ligand effects," *ACS Applied Materials and Interfaces*, vol. 14, no. 1, pp. 1373–1388, 2022.

[225] P. H. Nguyen, S. Scheinert, S. Berleb, W. Brütting, and G. Paasch, “The influence of deep traps on transient current–voltage characteristics of organic light-emitting diodes,” *Organic Electronics*, vol. 2, no. 3-4, pp. 105–120, 2001.

[226] G. A. H. Wetzelaer, M. Kuik, H. T. Nicolai, and P. W. M. Blom, “Trap-assisted and langevin-type recombination in organic light-emitting diodes,” *Physical Review B*, vol. 83, no. 16, 2011.

[227] S. Diaham and M.-L. Locatelli, “Space-charge-limited currents in polyimide films,” *Applied Physics Letters*, vol. 101, no. 24, p. 242905, 2012.

[228] A. S. Sarkar and S. K. Pal, “Exponentially distributed trap-controlled space charge limited conduction in graphene oxide films,” *Journal of Physics D: Applied Physics*, vol. 48, no. 44, p. 445501, 2015.

[229] V. Coropceanu, J. Cornil, D. A. da Silva Filho, Y. Olivier, R. Silbey, and J.-L. Brédas, “Charge transport in organic semiconductors,” *Chemical Reviews*, vol. 107, no. 4, pp. 926–952, 2007.

[230] M. A. Rafiq, “Carrier transport mechanisms in semiconductor nanostructures and devices,” *Journal of Semiconductors*, vol. 39, no. 6, p. 061002, 2018.

[231] S.-K. Kim and Y.-S. Kim, “Charge carrier injection and transport in qled layer with dynamic equilibrium of trapping/de-trapping carriers,” *Journal of Applied Physics*, vol. 126, no. 3, p. 035704, 2019.

[232] P. Chattopadhyay and B. RayChaudhuri, “Frequency dependence of forward capacitance-voltage characteristics of schottky barrier diodes,” *Solid-State Electronics*, vol. 36, no. 4, pp. 605–610, 1993.

[233] J. Furlan, Z. Gorup, A. Levstek, and S. Amon, “Thermally assisted tunneling and the poole–frenkel effect in homogenous a-si,” *Journal of Applied Physics*, vol. 94, no. 12, p. 7604, 2003.

[234] W. Brütting, H. Riel, T. Beierlein, and W. Riess, “Influence of trapped and interfacial charges in organic multilayer light-emitting devices,” *Journal of Applied Physics*, vol. 89, no. 3, p. 1704, 2001.

[235] O. Mitrofanov and M. Manfra, “Poole-frenkel electron emission from the traps in algan/gan transistors,” *Journal of Applied Physics*, vol. 95, no. 11, pp. 6414–6419, 2004.

[236] P. Blom and M. de Jong, “Electrical characterization of polymer light-emitting diodes,” *IEEE Journal of Selected Topics in Quantum Electronics*, vol. 4, no. 1, pp. 105–112, 1998.

[237] M. Zhang, F. Guo, S. Lei, T. Zhong, B. Xiao, C. Liu, L. Wang, J. Chen, Q. You, J. Liu, and R. Yang, “Positive temperature dependence of the electroluminescent performance in a colloidal quantum dot light-emitting diode,” *Dyes and Pigments*, vol. 195, p. 109703, 2021.

[238] D. Amans, S. Callard, A. Gagnaire, J. Joseph, F. Huisken, and G. Ledoux, “Spectral and spatial narrowing of the emission of silicon nanocrystals in a microcavity,” *Journal of Applied Physics*, vol. 95, no. 9, pp. 5010–5013, 2004.

[239] A. Hryciw, J. Laforge, C. Blois, M. Glover, and A. Meldrum, “Tunable luminescence from a silicon-rich oxide microresonator,” *Advanced Materials*, vol. 17, no. 7, pp. 845–849, 2005.

[240] I. T. Cheong, W. Morrish, W. Sheard, H. Yu, B. Tavares Luppi, L. Milburn, A. Meldrum, and J. G. C. Veinot, “Silicon quantum dot-polymer fabry-pérot resonators with narrowed and tunable emissions,” *ACS Applied Materials and Interfaces*, 2021.

[241] Y.-C. Zhang, Z.-Y. Yu, F.-Y. Ma, X.-Y. Xue, K.-X. Liu, J. Sun, S.-Y. Wang, and M. Lu, “Observation of distributed feedback lasing in silicon nanocrystals under electrical pumping,” *Results in Physics*, vol. 39, p. 105734, 2022.

[242] F. Ma and X. Liu, “Phase shift and penetration depth of metal mirrors in a microcavity structure,” *Applied Optics*, vol. 46, no. 25, pp. 6247–6250, 2007. [Online]. Available: https://www.osapublishing.org/ao/viewmedia.cfm?uri=ao-46-25-6247&seq=0

[243] A. Dodabalapur, L. J. Rothberg, R. H. Jordan, T. M. Miller, R. E. Slusher, and J. M. Phillips, “Physics and applications of organic microcavity light emitting diodes,” *Journal of Applied Physics*, vol. 80, no. 12, pp. 6954–6964, 1996.

[244] S. Kasap and P. Capper, Eds., *Springer handbook of electronic and photonic materials*, 2nd ed., ser. Springer Handbooks. Cham, Switzerland: Springer, 2017.

[245] L. P. Schuler, J. S. Milne, J. M. Dell, and L. Faraone, “Mems-based microspectrometer technologies for nir and mir wavelengths,” *Journal of Physics D: Applied Physics*, vol. 42, no. 13, p. 133001, 2009.

[246] M. Hoheisel, A. Mitwalsky, and C. Mrotzek, “Microstructure and etching properties of sputtered indium—tin oxide (ito),” *Physica Status Solidi (a)*, vol. 123, no. 2, pp. 461–472, 1991.

[247] L. Gao, F. Lemarchand, and M. Lequime, “Refractive index determination of sio_2 layer in the uv/vis/nir range: spectrophotometric reverse engineering on single and bi-layer designs,” *Journal of the European Optical Society: Rapid Publications*, vol. 8, 2013.

[248] R. J. Moerland and J. P. Hoogenboom, “Subnanometer-accuracy optical distance ruler based on fluorescence quenching by transparent conductors,” *Optica*, vol. 3, no. 2, p. 112, 2016.

[249] J.-K. Choi, S. Jang, H. Sohn, and H.-D. Jeong, “Tuning of refractive indices and optical band gaps in oxidized silicon quantum dot solids,” *Journal of the American Chemical Society*, vol. 131, no. 49, pp. 17 894–17 900, 2009.

[250] C.-W. Chen, S.-Y. Hsiao, C.-Y. Chen, H.-W. Kang, Z.-Y. Huang, and H.-W. Lin, “Optical properties of organometal halide perovskite thin films and general device structure design rules for perovskite single and tandem solar cells,” *Journal of Chemestry A*, vol. 3, no. 17, pp. 9152–9159, 2015.

[251] A. Senes, R. A. J. Janssen, and S. C. J. Meskers, *Orientation of transition dipole moments in solution processed small molecular emitters*. Eindhoven: Technische Universiteit Eindhoven, 2018.

[252] C. Stelling, C. R. Singh, M. Karg, T. A. F. König, M. Thelakkat, and M. Retsch, “Plasmonic nanomeshes: their ambivalent role as transparent electrodes in organic solar cells,” *Scientific reports*, vol. 7, no. 1, p. 42530, 2017. [Online]. Available: https://www.nature.com/articles/srep42530#Sec11

[253] C. Huber, “Micromechanical tunable fabry-pérot interferometers with membrane bragg mirrors based on silicon/silicon carbonitride,” Dissertation, Karlsruher Institut für Technologie, 2019.

[254] T. Creazzo, B. Redding, E. Marchena, R. Hao, J. Murakowski, S. Shi, and D. W. Prather, “Distributed bragg reflector enhancement of electroluminescence from a silicon nanocrystal light emitting device,” *Thin Solid Films*, vol. 518, no. 15, pp. 4394–4398, 2010.

[255] A. B. Djurisić and A. D. Rakić, “Organic microcavity light-emitting diodes with metal mirrors: dependence of the emission wavelength on the viewing angle,” *Applied Optics*, vol. 41, no. 36, pp. 7650–7656, 2002.

[256] E. A. Weiss, “Designing the surfaces of semiconductor quantum dots for colloidal photocatalysis,” *ACS Energy Letters*, vol. 2, no. 5, pp. 1005–1013, 2017.

[257] Z. Wang, X. Wang, S. Cong, J. Chen, H. Sun, Z. Chen, G. Song, F. Geng, Q. Chen, and Z. Zhao, “Towards full-colour tunability of inorganic electrochromic devices using ultracompact fabry-perot nanocavities,” *Nature Communications*, vol. 11, no. 1, p. 302, 2020.

[258] J. Chen, Z. Wang, Z. Chen, S. Cong, and Z. Zhao, “Fabry-perot cavity-type electrochromic supercapacitors with exceptionally versatile color tunability,” *Nano Lett*, vol. 20, no. 3, pp. 1915–1922, 2020.

[259] K. Dohnalová, A. N. Poddubny, A. A. Prokofiev, W. D. de Boer, C. P. Umesh, J. M. J. Paulusse, H. Zuilhof, and T. Gregorkiewicz, “Surface brightens up si quantum dots: direct bandgap-like size-tunable emission,” *Light, science & applications*, vol. 2, no. 1, pp. e47–e47, 2013.

[260] A. Angı, R. Sinelnikov, H. H. Heenen, A. Meldrum, J. G. C. Veinot, C. Scheurer, K. Reuter, O. Ashkenazy, D. Azulay, I. Balberg, O. Millo, and B. Rieger, “The influence of conjugated alkynyl(aryl) surface groups on the optical properties of silicon nanocrystals: photoluminescence through in-gap states,” *Nanotechnology*, vol. 29, no. 35, p. 355705, 2018. [Online]. Available: http://stacks.iop.org/0957-4484/29/i=35/a=355705?key=crossref.9b974761168bca0662cf43da9b7489f8

[261] M. L. Mastronardi, F. Maier-Flaig, D. Faulkner, E. J. Henderson, C. Kübel, U. Lemmer, and G. A. Ozin, “Size-dependent absolute quantum yields for size-separated colloidally-stable silicon nanocrystals,” *Nano Letters*, vol. 12, no. 1, pp. 337–342, 2012. [Online]. Available: https://pubs.acs.org/doi/10.1021/nl2036194

Appendix

Table 1 Analysis of reflectance spectra for cLEDs and 40 nm Ag outcoupler. Table reprinted from [157]

SiO_2 thickness [nm]	Center wavelength [nm]	FWHM [nm]	FSR ($\lambda_{m+1} - \lambda_m$) [nm]	Resonance mode
200	329	13	51	5
	380	13	113	4
	493	8	196	3
	689	13		2
250	335	25	68	5
	403	10	106	4
	509	8	238	3
	747	12		2
300	332	17	47	6
	379	12	87	5
	466	8	119	4
	585	9	239	3
	879	16		2
350	340	16	51	6
	391	9	89	5
	480	6	126	4
	606	8	292	3
	898	14	314	2
	1213	7		1

Table 2 EL spectra analysis of cLEDs corresponding to the mode emission peaks in Figure 7.11.

SiO_2 thickness [nm]	Applied voltage [V]	Center wavelength [nm]	FWHM	Resonance mode	Q-factor
500	4	691	30	3	23
450	4	935	34	2	28
		624	26	3	24
400	7.5	626	39	3	16
350-1	7.5	606	36	3	17
350-2	4	891	25	2	36
300	5.5	778	105	2	7
250	4	728	63	2	12
200	7	675	39	2	17

Table 3 Reflectance spectra analysis of cLEDs with 500 nm SiO_2 spacer and different Ag outcoupler thickness.

Ag thickness [nm]	Center wavelength [nm]	FSR ($\lambda_{m+1} - \lambda_m$) [nm]	FSR [THz]	Resonance mode
40	338	41	7391	7
	378	69	4347	6
	447	90	3317	5
	538	164	1824	4
	702	333	900	3
	1035			2
45	331	38	7963	7
	369	67	4455	6
	436	88	3422	5
	524	158	1900	4
	682	333	900	3
	1015			2
50	318	65	4634	7
	383	72	4172	6
	455	90	3341	5
	545	173	1737	4
	717	348	862	3
	1065			2

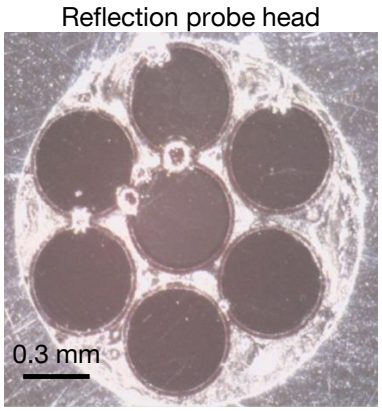

Figure 1 Photo of the reflection probe. The six outer fibers are usually used for illumination and the inner fiber is used for measurements.

Table 4 EL spectra analysis of 500 nm SiO_2 cLEDs and an applied voltage of 4 V. The table is adapted from [157].

Ag thickness [nm]	Center wavelength [nm]	FWHM [nm]	Mode number	Q-factor	Finesse
40	691	31	3	22.3	47.3
45	679	23	3	29.5	60.4
50	713	24	3	29.7	61.6

Publications

1. I. Cheong, J. Mock, M. Kallergi, E. Groß, B. Rieger, M. Becherer, and J. Veinot, “Colloidal Silicon Quantum Dot Cavity Light-Emitting Diode with Narrowed and Tunable Electroluminescence”, Advanced Optical MAterials, vol.11, no.1, 2201834, 2022.

2. J. Mock, M. Kallergi, E. Groß, M. Golibrzuch, B. Rieger, and M. Becherer, “Revealing the Negative Capacitance Effect in Silicon Quantum Dot Light-Emitting Diodes Via Temperature-Dependent Capacitance-Voltage Characterization”, IEEE Photonics Journal, vol. 14, no. 4, pp. 1-9, Art no. 8237309, 2022.

3. J. Mock, E. Groß, M. Kloberg, B. Rieger, and M. Becherer, “Surface Engineering of Silicon Quantum Dots: Does the Ligand Length Impact the Optoelectronic Properties of Light-Emitting Diodes?”, Advanced Photonics Research, vol. 2, no. 9, p. 2100083, 2021.

4. A. Stathis, M. Stavrou, I. Papadakis, J. Mock, M. Kloberg, M. Becherer, A. Lyuleeva-Husemann, and S. Couris, “Silicon Nanosheets: A Promising 2D Material with Strong Ultrafast Nonlinear Optical Response”, Journal of Physical Chemistry C, vol. 125, no. 33, pp. 18510–18516, 2021.

5. M. Stavrou, I. Papadakis, A. Stahis, M. Kloberg, J. Mock, T. Kratky, S. Günther, B. Rieger, M. Becherer, A. Lyuleeva-Husemann, and S. Couris, “Silicon Nanosheets versus Graphene Nanosheets: A Comparison of Their Nonlinear Optical Response”, Journal of Physical Chemistry Letters, vol. 12, no. 2, pp. 815–821, 2021.

6. Y. Goliya, A. Rivadeneyra, J. Salmeron, A. Albrecht, J. Mock, M. Haider, J. Russer, B. Cruz, P. Eschlwech, E. Biebl, M. Becherer, and P. Lugli, “Next generation antennas based on screen-printed and transparent silver nanowire films”, Advanced Optical Materials, vol. 7, no. 21, p. 1900995, 20195.

7. S. Kernbichl, M. Reiter, J. Mock, and B. Rieger, “Terpolymerization of β-butyrolactone, epoxides, and CO_2: chemoselective CO_2-switch and its impact on kinetics and material properties”, Macromolecules, vol. 52, no. 21, pp. 8476-8483, 2019.

8. J. Mock, M. Bobinger, C. Bogner, P. Lugli, and M. Becherer, “Aqueous Synthesis, Degradation, and Encapsulation of Copper Nanowires for Transparent Electrodes”, Nanomaterials, vol. 8, no. 10, p. 767, 2018.

9. M. Bobinger, P. La Torraca, J. Mock, M. Becherer, L. Cattani, L. Larcher, and P. Lugli, “Solution-processing of Copper Nanowires for Transparent Heaters and Thermo-Acoustic Loudspeakers”, in IEEE Transactions on Nanotechnology, pp. 940–947, 2018.

Cover page

1. Cover page of special issue: Ion N. Mihailescu (Ed.), "Synthesis and Modification of Nanostructured Thin Films", MDPI - Multidisciplinary Digital Publishing Institute, 2020.

Acknowledgements

At this point I want to thank a lot of people who made this thesis what it has become. First of all and most important, my parents and my siblings who always believed in me. Without their help and support, this work would look totally different or would never had happened.

As good manners would have it, I thank Dr.-Ing. habil. Markus Becherer, my boss and supervisor, for all of this. He enabled this position to me and highly supported me throughout the years. It was challenging to both of us to handle the distance between the ZEI in Garching and the city center campus, but the phone line always worked. In the very last months, he moved into the new electrical engineering building in Garching. We learned many new things, much chemistry, together working on silicon quantum dot LEDs.

Next are the two most important collaborators, Elisabeth (Elli) Groß and Marc Kloberg for all the samples they've made for me to work with. Thanks for the good times at ATUMS meetings, conferences, and workshops. They stand for all other people at their chair or within the ATUMS project. All of them helped with their good conversations and good ideas, and helping out with their measurement equipment.

Now to my colleges at the chair, Matthias, Martina, and Valentin. We always worked on completely different topics, but I enjoyed the time with you and learned at least some basics of of the stuff you guys do. As the last real Nano member, I have to thank the Nano Sauf und Plausch group of Marius Loch, who guided me through the basics of the SiQD-LEDs and had the idea which started all this, Marco Bobinger, who convinced me to start all this here, Andreas Albrecht, and Florin Loghin for their help and fun times at the beginning at the ZEI. Not to forget Alina Lyuleeva-Husemann as ATUMS introducer and mentor.

A big thank goes to all the students I've supervised during their Ingenieurpraxis, Bachelor thesis, Forschungspraxis, and Masterthesis. That were Tarik Pljevljakovic, Michael Schreiber, Delakshan Srikanthan, Jonas Peis, Bernhard Hamacher, Felix David, and especially Karim Ruvalcaba, Elisabeth Groß, and Maira Kallergi. All of them contributed in one or the other way to the outcome of this work but the latter three spend a long time together with me in the lab. I hope you also had some fun.

Without the people of this group, I would have had not much time to do research. The people worked with on a daily basis and who kept everything organized: Katrin, Susi, Rainer, Anika and especially Rosi, who was also located at the ZEI for two days.

An international research project would be nothing without the internationals. I'd like to thank all people who I met in Canada and want to especially highlight Emily, Charles, Frank, Al, and John. They hosted me in their labs and toughed me some cool laser and Thz physics, opened their lab for sample preparation, or came to Garching to build some cavity LEDs.

Finally, I would like to thank all those I have forgotten so far. This was not intentional and in no way diminishes their contribution.